"Characterisation and evaluation of porphyrins for the development of a proto-type vapour sensor"

Alfredo Flores Gutiérrez

University of Sheffield

September 2014

A thesis submitted for the degree of Doctor of Philosophy at the University of Sheffield

Department of Physics and Astronomy

Hicks Building

Hounsfield Road

Abstract

This thesis describes the influence of VOCs and NO_2 (the analytes) on thin porphyrin films and examines the feasibility of utilising this behaviour in a sensing device. LB films of porphyrins exhibit intense optical absorption bands in the region from 400 to 800 nm. These molecules experience a significant change in their optical absorption properties as a result of exposure to appropriate analytes because the analytes bind to the porphyrins and distort their electronic energy levels. This principle has been adopted as the basis for a simple gas detection system. In-situ optical measurements have been performed to quantify the response of the films in a stream of gas of specified analyte concentration and their subsequent recovery. The sensing properties of a family of porphyrins exposed to analytes have been systematically evaluated.

Both metalled and free base porphyrins have shown response to a variety of analytes. A range of zinc porphyrins were exposed to amines, showing a large response to the analytes. Free base porphyrins showed a large response to carboxylic acids and nitrogen dioxide. It was expected that the porphyrins containing strong electron donating properties within their side groups would show a high response to analytes. Nevertheless, the interaction of porphyrin-analyte is not only limited to the electron donating nature of the side groups but also depends on the porphyrin-porphyrin interactions. Strong porphyrin-porphyrin interactions led to densely packed films; limiting the access of the analyte to the porphyrin binding sites. AFM analysis has shown that an open structure leads to a higher sensor response. Hence, a combination of the electron donating nature within the side groups and an open structure would be required to register a high sensor response.

The response of the sensing material has been improved by incorporating optically transparent host materials which disperse the porphyrin molecules and reduce detrimental aggregation on the monolayers. The expansion of various families of free base porphyrin monolayers upon the exposure to trifluoroacetic acid has been studied by developing a quartz crystal microbalance to determine how exposure to acid influences the molecular orientation on the Langmuir surface, and after deposition onto a substrate. Upon exposure, protonation of the porphine caused Coulombic repulsion between the molecules. This led to a new polar and charged system. The reorientation of the porphyrin molecules showed a lower density of the monolayers, reducing the initial pre-exposed aggregated state.

This thesis also presents a vapour chamber design which uses LB films of porphyrin as a sensitizer and a paired LED/photo detector as a transducer. This low cost sensor system is capable of the detecting different gaseous analytes. Regularly, absorption of porphyrins are modelled by the Langmuir absorption model. However, the response of these sensors has been shown to follow the Freundlich absorption model due to the non-linear response of the photo detectors. The sensor can detect concentrations of 2-methyl-2-butanol ranging from 4.36 to 41 ppt. The temperature dependence of the sensor was studied, leading to a calculated enthalpy of absorption with a value of 0.28 eV.

For those who never doubted me

Para quienes nunca dudaron de mí

Acknowledgements

I have so many people to thank who have helped me and made my time rewarding. To Dr. Richardson; without him I would not be where I am today. He was a role model not only as a scientist, but as a person who inspired many people with his passion and good humour. Special gratitude must be expressed to my supervisor, Dr. Alan Dunbar, for his encouragement and guidance throughout my Doctoral Programme.

Dr. Stuart Brittle for coaching me in the Langmuir art and for sharing all those coffees we had.

I owe my sincere thanks to Dr. Jose María Pedrosa Poyato from Universidad Pablo Olavide and Dr. María Teresa Martín Romero from University of Cordoba for allowing me to stay a short period in their laboratories. Dr. Teresa showed me the fascinating formation of monolayers using Brewster Angle Microscopy and Dr. Poyato introduced me to the use of TiO_2 substrates. They all made my stay in Cordoba and Seville a very enjoyable experience and I am truly grateful.

To the Government of Mexico and CONACYT, I thank you with the utmost of appreciation for sponsoring me during my PhD years here.

Special gratitude to my partner, Emily, for keeping me sane during all this time and for always being by my side.

To my father for his support, my sister for her understanding and my mother for her loving support; they have supported me in all that I do and love me without fail. To them I dedicate this thesis.

List of publications and presentations

Gutiérrez, A. F., S. Brittle, et al. (2014). "A proto-type sensor for volatile organic compounds based on magnesium porphyrin molecular films." Sensors and Actuators B: Chemical 202(0): 854-860.

Gutiérrez, A. F., (2014, July) "Prototyping vapour sensor systems." Presentation delivered at the 15th International Conference on Organized Molecular Films. Jeju, Korea.

Gutiérrez, A. F., et al. (2013, August) "Characterization and evaluation of porphyrins". Poster presented at Asia Sense conference. Malacca, Malaysia.

Brittle, S.A. et al., (2012) "Macroscopic expansion of tetraphenylporphyrin Langmuir layers stimulated by protonation." Soft Matter, 8(10): 2807-2811.

Gutiérrez, A. F., et al. (2011, July) "Sensing using porphyrin molecular films". Poster presented at the 12th European Conference on Organized Films. Sheffield, UK.

Contents

Chapter 1

1.1 Introduction

The necessity to detect toxic gases such as NO_2, Cl_2, HCl, SO_2, CO and NH_3 has increased in the last decades, mainly due to the increase in the production of these gases in the general industry. Last year, the UK Department of Energy and Climate Change reported an increase of 1.6 % in the global nitrogen dioxide emissions, 61 % above the levels in 1990 [1].
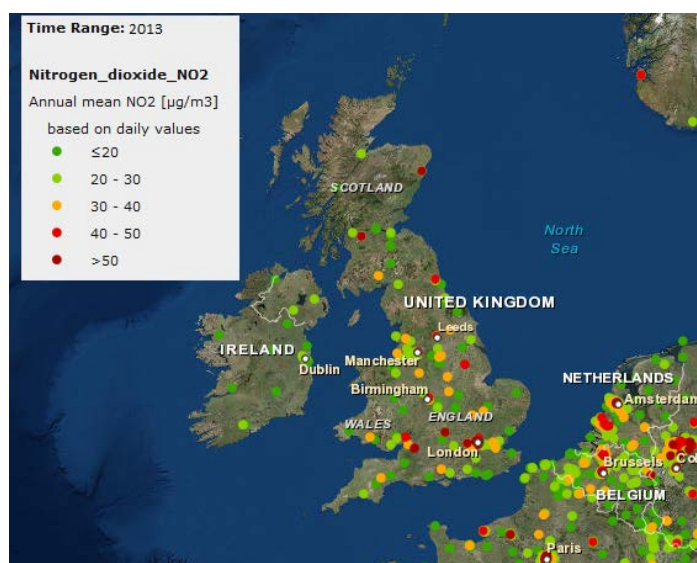
Figure 1.1: Annual mean emission of nitrogen dioxide on 2013 [2].

Meanwhile, there has been a tightening of environmental legislation, increase in the standards for air quality and new policy for the prevention of health risks imposed by National Environmental Agencies, all with the goal of reducing the harmful effect of toxic substances in the environment and on human health [3-6]. However, to achieve this goal, it is necessary to know what the toxic gas levels are which necessitates the development of toxic gas detectors capable of monitoring even lower concentration levels [7]. This, along with the economic need to produce lower cost sensors is a solid justification to motivate this research in the development of toxic gas sensors.

1.2 Gas sensor: definition and desired characteristics.

The following definition of a sensor suggested by Edmonds [8] is appropriate for all the sensors used in this thesis:

"A chemical sensor may be defined as a simple to use robust device that is capable of reliable quantitative and qualitative recognition of atomic, molecular or ionic species"

The purpose of a gas sensor is to provide information about the biological, chemical or physical environment. The basic principles of operation are divided in three stages of the sensing process: recognition, physical change and conversion. The first stage refers to the specific interaction between the analyte and the sensor (selective chemistry). As a consequence of the molecular recognition, a change in the physical properties of the sensor takes place. During the last stage, a conversion from that change is converted into a measurable signal [9].

A gas sensor requires certain basic properties in order for it to be effective. Other properties may also be needed in extreme cases. Generally, an ideal sensor would possess the following characteristics: high sensitivity, reversibility, fast response and recovery, non-contaminating, non-poisoning, cheap to fabricate, temperature independence, chemical selectivity, low noise, ease of construction, ease of operation, portability and durability.

Unfortunately, ideal sensors with all the mentioned characteristics cannot be fabricated at present. In reality, a compromise must be sought between these qualities; then it may well be possible to produce a sensor which is suitable for the environment and the application for which it will be used.

1.3 Cross sensitivity of toxic sensors:

Ideally, a toxic gas sensor only reacts to the gas it is targeted to monitor; which means that other toxic gases should not cause an inaccurate response. An ammonia sensor only detects ammonia and a chlorine sensor only detects chlorine. Unfortunately, while most sensors are quite specific, cross sensitivity does occur.

Cross sensitivity is a sensor's reaction to other gases which can interfere with how the sensor reacts. Exposing a sensor to a gas that is not the target gas can cause an undesirable response, either negative or positive. A positive response means that sensors not only respond to the target gas but also to another untargeted gas. The untargeted gas works to give an impression that there is more of a target gas present than there actually is.

A negative response is when sensors produce a reduced response to the target gas if also exposed to an untargeted gas. Most gas detection fabricants publish toxic gas sensor cross sensitivity charts and often express the cross sensitivity in percentages. These charts anticipate cross-sensitive conditions with their gas monitors and empower them to react accordingly. Table 1.1 reflects the percentage response provided by the sensor listed across the top of the chart when exposed to a known concentration of the target gas listed in the left hand column.

		SENSOR											
		Carbon Monoxide	Hydrogen Sulfide	Sulfur Dioxide	Nitrogen Dioxide			Hydrogen Cyanide	Hydrogen Chloride	Phosphine	Nitric Oxide	Hydrogen	Ammonia
GAS	Carbon Monoxide	100	1	1	0	0	0	0	0	0	0	20	0
	Hydrogen Sulfide	5	100	1	-40	-3	-25	10	300	25	10	20	25
	Sulfur Dioxide	0	5	100	0	0	0	—	40	—	0	0	-40
	Nitrogen Dioxide	-5	-25	-165	100	45	—	-70	—	—	30	0	-10
	Chlorine	-10	-20	-25	10	100	60	-20	6	-20	0	0	-50
	Chlorine Dioxide	—	—	—	—	20	100	—	—	—	—	—	—
	Hydrogen Cyanide	15	10	50	1	0	0	100	35	1	0	30	5
	Hydrogen Chloride	3	0	5	0	2	0	0	100	0	15	0	0
	Phosphine	—	—	—	—	—	-100	425	300	100	—	—	—
	Nitric Oxide	25	1	1	5	—	—	-5	—	—	100	30	0
	Hydrogen	22	0.08	0.5	0	0	0	0	0	0	0	100	0
	Ammonia	0	0	0	0	0	0	0	0	0	0	0	100

Table 1.1: Sensor crossed interference table. The symbol "-"means that no data is available [10].

1.4 Applications of gas sensors.

Gas sensor development has been driven by two primary needs. The first is human protection from health and safety hazards caused by gases and the second, as a means to acquire information about the processes in which gases are consumed or created. Some of the typical applications for gas sensors are mentioned in table 1.

Automobiles

- Filter control
- Gasoline vapour detection
- Alcohol breath tests

Safety

- Fire detection
- Leak detection
- Toxic/flammable/explosive gas detectors
- Boiler control
- Personal gas monitor

Indoor air quality

- Air purifiers
- Ventilation control
- Pollution monitoring

Environmental control

- Weather stations
- Pollution monitoring

Food

- Food quality control
- Process control
- Packing quality control (off-odours)

Industrial production

- Fermentation control
- Process control

Medicine

- Breath analysis
- Disease detection

Figure 1.2: Example applications for gas sensors [11].

1.5 Objectives of this project.

The chapters in this work describe the research conducted towards four major objectives:

i) Explore the molecular characteristics of porphyrins with different functional groups and metal ions and compare their physicochemical features.

ii) Evaluate the sensing capabilities of the porphyrins for a variety of analytes.

iii) Optimize the fabrication of solid state sensors using porphyrin films.

iv) Design an electronic sensing system capable of generating suitable electrical signals in response to the molecular adsorption events caused by exposure to the analyte.

1.6 Thesis overview.

Chapter 2

The theory behind the processes occurring in porphyrin vapour sensors is discussed. Topics include the origin of the porphyrin absorption spectrum, the adsorption of vapours onto surfaces and an overview of the types of vapour sensors that are commonly used in an industrial setting. In the last part of chapter two a review of recent research regarding the detection of toxic gases is presented.

Chapter 3

The experimental techniques used for this research are described. These include techniques to investigate the characteristics of molecules whiles on a Langmuir trough and in solution, methods used to transfer these materials onto solid substrates and those used to characterise these films, including their response to toxic vapours.

Chapter 4

Chapter four consists of four sections each with a different set of metalated or non-metalated porphyrin molecules and their corresponding sensor evaluation.

i) The first section is about zinc porphyrins and their response to amines. The analysis is divided in different studies, such as the porphyrin response in solution, formation of a monolayer of porphyrin molecules at different target pressures, the porphyrin response to analytes in a solid state LB film deposited on glass, and AFM studies. A discussion of the influence of the different functional groups is conferred.

ii) Section two describes the response of free base porphyrins when they are exposed to carboxylic acids. The study is divided in different studies, similar to the ones

presented in the first section. The effect of modifying the side groups and their different reactions is also discussed.

iii) Section three addresses the detection of nitrogen dioxide using a free base porphyrin (EHO). It focuses on controlling the nanostructure of the porphyrin films by either using a host material (TiO_2) or mixing calixarene with porphyrin whilst in solution to enhance the quality of the sensing films. The section presents the benefits of improving the porphyrin film structure with the mentioned agents.

iv) Section four describes the interaction of various vapour alcohol vapours with a magnesium porphyrin. These are generally very weak responses which are presented here because they are significant for the results presented in Chapter 5, section 3.

Chapter 5

This chapter focuses on the fabrication of a portable gas chamber and the development of a sensor prototype able to detect vapour analytes. The chapter is divided in three sections, which describe the chronological development of the instruments used in the study.

i) Section one introduces the concept of an electronic sensing pair consisting of a light transmitter and a receiver with a porphyrin film employed as a sensitizer. Different photo receivers are evaluated as a possible match for the sensing pair. The development of a vapour chamber is described, along with their previous predecessors.

ii) Section two describes the technical details of the sensing pair, such as the characteristics of the receiver, filtering of the sensor signal and control experiments previous to a vapour exposure. The sensing mechanism of the proto-type is described in detail.

iii) A phototransistor coated with magnesium porphyrin and an LED are matched in the purpose built chamber to detect alcohols. Despite their weak response in the conventional sensor tests presented in Section 4.4 the results show that a functional sensor is developed. The sensing pair followed the Freundlich adsorption model in which the response of the sensor depends on the concentration of the vapour. The

temperature dependence of the sensor is correspondingly analysed. The results of this section were published in the journal Sensors and Actuators B: Chemical [12].

Chapter 6

The monolayer formation of a free base porphyrin and the reaction upon the exposure to trifluoroacetic acid is studied in this chapter. The interaction with the acid causes a molecular expansion of the floating porphyrin layer. In this study the correlation between two sets of experimental data: the π-A isotherms and the quartz crystal microbalance (QCM) measurements is described. The isotherms were performed by Dr. Stuart Brittle, whilst the author of this thesis developed the quartz crystal microbalance oscillator circuit, calibrated of the QCM system, the deposited the porphyrin into the quartz crystal and made the measurements related to the quartz crystal system. The results of this work was written up by Dr. T. H. Richardson and it was published in the journal Soft Matter [13].

References:

1. Department of Energy and Climate Change. *Global carbon emissions set to reach record 36 billion tonnes in 2013*. 2013 15/08/2014]; Available from: https://www.gov.uk/government/organisations/department-of-energy-climate-change.
2. Department for Environment Food and Rural Affairs. *Interactive monitoring networks map: Pollution* 2014 [cited 16/08/2014; Available from: http://uk-air.defra.gov.uk/interactive-map.
3. European Commission. *The Clean Air Policy Package*. 2014 18/08/2014]; Available from: http://ec.europa.eu/environment/air/clean_air_policy.htm.
4. Enviromental Protection UK. *Air pollution and health*. 2014 [cited 2014 18/08/2014]; Available from: http://www.environmental-protection.org.uk/committees/air-quality/about-air-pollution/air-pollution-and-health/.
5. Department for Environment Food and Rural Affairs. *Pollution Levels* 2014 [cited 2013 18/08/2014]; Available from: http://uk-air.defra.gov.uk/latest/european-pollution-levels.
6. Charles, K.E., et al., *Indoor air quality guidelines and standards*. 2005: Institute for Research in Construction, National Research Council Canada.
7. Department for Environment Food and Rural Affairs. *Air Pollution in the UK 2012*. 2013 18/08/2014]; Available from: http://uk-air.defra.gov.uk/library/annualreport/viewonline?year=2012_issue_1.
8. Edmonds, T., *Chemical sensors*. 1988: Blackie. Chapman and Hall.
9. Barnes, G. and I. Gentle, *Interfacial science: an introduction*. 2011: Oxford University Press.
10. Industrial Scientific. *Sensor Cross Interference table* 2014 07/02/2015]; Available from: http://www.indsci.com/services/training/general-gas-education/sensor-cross-interference/.
11. Capone, S., et al., *Solid state gas sensors: state of the art and future activities.* Journal of Optoelectronics and Advanced Materials, 2003. **5**(5): p. 1335-1348.
12. Gutiérrez, A.F., et al., *A proto-type sensor for volatile organic compounds based on magnesium porphyrin molecular films.* Sensors and Actuators B: Chemical, 2014. **202**(0): p. 854-860.
13. Brittle, S.A., et al., *Macroscopic expansion of tetraphenylporphyrin Langmuir layers stimulated by protonation.* Soft Matter, 2012. **8**(10): p. 2807-2811.

Chapter 2: Background

2.1 Type of gas sensors

At present, the number of different type of gas sensors in industry is very large. The basic principles and background science of the vapour sensors are similar in all devices, however, a wide variety of technologies have been developed. In this section, many methods used to convert physical parameters to electrical signal are discussed.

The modern gas sensing devices are governed by interdisciplinary sciences ranging from biology, electronics, solid state physics and chemistry. Due to the large variety of sensors, an incomplete list of gas sensors is presented in table 1. The table relates the most common types of sensors (along with some examples) to the physical change produced when the device is interacting with the analysed gas.

Type of devices	Physical change
Conductivity sensors: Metal oxide semiconductors and chemiresistors	Electrical conductivity
Field-effect gas sensors: Metal oxide and metal oxide hybrid devices (polymer and carbon based)	Surface potential
Piezoelectric sensors: SAW or QMB	Mass
Optical sensors: Thin films, fibre optic	Ellipsometry, spectroscopy, interferometry, SPR: Absorption, reflection, and fluorescence properties.
Colorimetric sensors: Glass slides, cellulose-based paper and porous polymer membranes / bubbler	RGB images (colour) / spectrometer
Catalytic gas sensors: Pellistors	Heat or temperature
Electrochemical gas sensors: Potentiometric or amperometric	Electrical current or potential in a solid state electrochemical cell

Table 2.1: Some of the most common type of gas sensors with the corresponding physical change used as gas detection principle [1-4].

The following subsections explain briefly the principles behind the different kind of gas sensors.

2.1.1 Electrical conductivity sensors:

A semiconducting material is exposed to a target gas and as a result of the exposure the conductivity of the semiconductor changes [5]. The main semiconductor used for vapour sensing purposes is indium-tin oxide. The conductivity of a semiconductor is temperature dependent. The main disadvantage of this kind of sensor is their high operating temperatures which are typically above 300°C. If there are oxygen vacancies present in the films the oxygen within the metal oxide films can move and conduct current at these high temperatures. The

metal then acts as an electrolyte and the oxygen ions become charge carriers [6, 7]. Interaction of the oxygen ions with various analytes results in a change in the conductivity which is an indication of the presence of gas. The sensor is not selective, so it changes its conductivity in response to numerous gases.
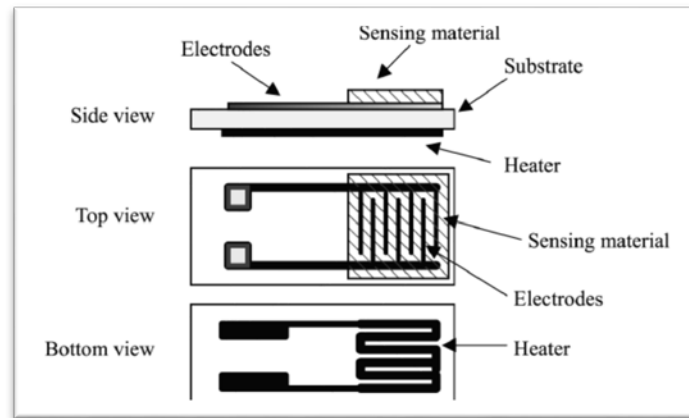
Figure 2.1: Schematic of a typical conductivity sensor. The sensing material is deposited in the space between the electrodes, points at which the resistance change is measured [3].

Similarly, chemi-resistors undergo a change in resistance when exposed to analytes. In these devices the analyte interacts with the sensing material, causing a change in its electronic structure and therefore makes either more or fewer electrons available for conduction of current. Common group of materials used as chemiresistors are phthalocyanines and polymers with semiconducting properties.

2.1.2 FET-based gas sensors

The most common field effect transistor (FET) is metal-oxide-semiconductor (MOSFET). The MOSFET is a device in which the conduction between the source and drain is modified by a charge or potential applied to the gate electrode. The device may be likened to a capacitor, with one electrode as the gate and the other at the channel. Charge on the gate has a reflected charge induced in the channel and this modifies the conduction of the channel. Hence altering the potential of the gate or the charge on the gate will alter the conduction of the channel and this change can be detected as an electrical signal (i.e. A current-voltage characteristic plot).
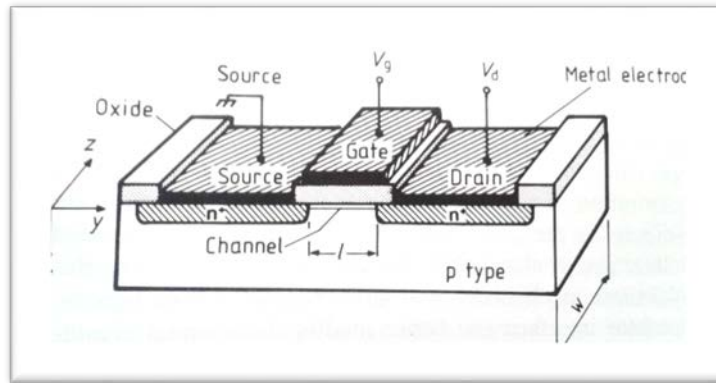
Figure 2.2: MOSFET device. Vd is the applied junction bias, Vg is the gate voltage, l is the length and w is the width of the channel [8].

Gases adsorbed or absorbed (a formal definition of these terms can be found on section 2.2.1) on the gate may have such an effect. The mechanism for changing the gate potential may be via either chemical interaction of the gas with the gate material thereby changing the carrier concentration of the gate or the gas inducing diploes in the gate which alter the potential gradients at the gate-oxide interface. Both mechanisms alter the potential or barrier height at the gate-insulator interface and hence modify the channel conduction.

2.1.3 Piezoelectric sensors

There are two types of gas sensors based on the piezoelectric effect: the quartz crystal microbalance (QCM) and the surface acoustic wave (SAW). The QCM produces a wave that travels through the bulk of the sensor while the SAW device produces an acoustic wave that travels along the surface of the sensor.

Figure 2.3 shows a schematic diagram of a SAW sensor. When a mechanical wave propagates through the surface, the changes in velocity or amplitude of the wave can be tracked by measuring the frequency characteristics of the sensor. The SAW has a receptor agent that is sensitive to the analysed gas [9].
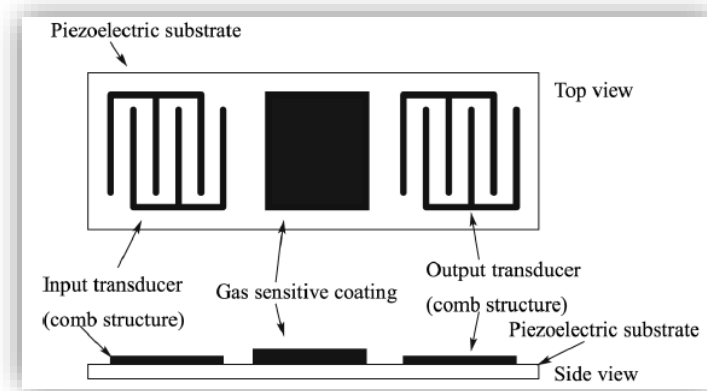
Figure 2.3: The surface acoustic wave sensor is composed of a piezoelectric substrate. The sensing material is deposited between the transmitting and receiving transducer [3].

Similarly, the QCM works on a similar principle. A change in mass due to the gas adsorption causes a shift in the resonant frequency of the piezoelectric sensor. A detailed description of the QCM and its sensing mechanism can be found in section 3.5.3.

2.1.4 Optical sensors

In a sensor based on visible optical spectroscopy, light is directed through a coloured gas. The adsorption or emission spectrum of this gas is recorded by an optical spectrometer. The spectrum recorded is a fingerprint of the gas present. The absorbance can be calculated with the Beer-Lambert equation, which is described in section 3.5.1b. Fluorescence, phosphorescence and luminescence can also be measured using a spectroscopy and used to detect the presence of certain gases.

If more than one gas is present the spectrum will be a superposition of the fingerprints of the two gases. This method of gas detection provides a fast and reliable measurement of gas species. However it relies on the gas emitting or absorbing radiation within the optical window, which is rarely the case. Most gases emit in the infrared region due to the vibration of bonds within the gas molecule.

Other optical methods are based on interferometry (principle described in section 3.5.4) and surface plasmon resonance (SPR). Interferometry can be used to measure the IR absorbance due to the presence of many gases but is hindered by the complexity and expense of the equipment required. SPR is the oscillation of conducting electrons at the interface between

two media (for example, organic films and a metal substrate). The oscillation may be stimulated by illuminating the surface with light with a photon frequency that matches the resonant frequency. This generates electron charge density waves called plasmons. The presence of an analyte adsorbed on the surface will change the nature of the interface and therefore the resonance conditions which any variation in the position of the SPR gives an indication of analytes present.

2.1.5 Colorimetric sensors

Colorimetric sensors rely on a reaction between the sensing medium and the gas so that the sensing medium changes colour. An early example of method of colorimetric sensing was the use of a bubbler [8]. When gas from the atmosphere was bubbled through the sensing solution, a colour change of the solution would occur if the toxic gas was present. Other examples of these sensors are detector tubes which operate by drawing a sample of air into a tube which contains the sensing chemicals and provides an on the spot measurement, and paper tape monitors which are coated in the sensing material and are usually used for personal continuous monitoring.

2.1.6 Catalytic gas sensors

Combustible gases will not burn until they reach an ignition temperature, unless certain chemical media offer a more favourable route to ignition at a lower temperature. Catalytic gas sensors are composed of a catalytic and a compensator (inert) heating elements. The non-catalytic element is a reference and compensates for changes in ambient temperature, humidity and pressure variations.

The combustible gases will burn in the catalytic element, changing its resistance and temperature; however, no effect is observed for the compensator as shown in figure 2.4. Typically, a Wheatstone bridge circuit (figure 2.4b) is formed between the catalytic and compensator.
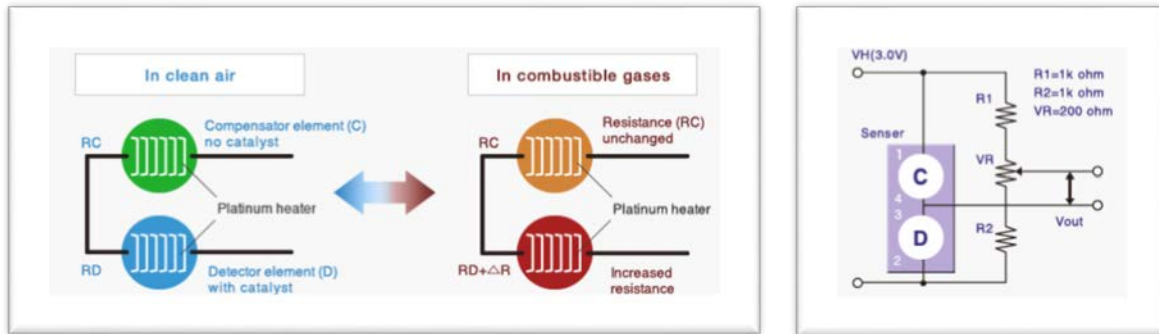
Figure 2.4: Left: measuring circuit, right: Wheatstone bridge circuit [10].

In a catalytic sensor the heat liberated in a controlled chemical reaction is a function of the toxic gas concentration. The catalyst may be platinum, palladium, rhodium or iridium.

The sensor compromises of a surface consisting of the catalyst eg. Pt, PD, Rh, Ir which is coupled to a temperature sensor and a heater to maintain the catalyst at the operating temperature. Heat is supplied to the catalyst and the exothermic oxidation reactions occurring at the catalyst surface are measured as the temperature of the catalyst rises. This is usually performed by resistance thermometry.

In the case of a pellistor, a platinum coil is used as a temperature sensing device and heating element. This is encapsulated in a spherical bead of palladium catalyst that is supported on an inactive oxide core of thoria (ThO_2). The palladium readily oxidised methane (CH_4) at temperatures of 500°C to liberate heat.

$$CH_4 + 2O_2 \rightarrow CO_2 + 2H_2O \quad \text{(800 kJ liberated)} \qquad \text{Eq. 2.1}$$

Equation 2.1 describes the catalytic oxidation of methane. This type of sensor is used to detect flammable gases in air. They provide a useful measure of explosiveness irrespective of gas mixture composition.

As catalytic sensors are sensitive to the ambient temperature and pressure; the resistance of the device is a function of the oxygen partial pressure and the temperature. However, the internal thermistor can be used to constantly monitor the temperature and compensate the output.

2.1.7 Electrochemical gas sensors

This kind of sensor operates by reacting with the gas, producing an electrical signal which is proportional to the concentration of the gas. The typical sensor consists of three electrodes: counter, reference and sensing electrodes; they are enclosed in a sensor housing medium which contains a liquid electrolyte that is responsible for carrying the ionic charges between the electrodes. The sensing electrode is on the inner face of a hydrophobic membrane which is porous to the gas but impermeable to the electrolyte. Figure 2.5 shows a schematic of the typical electrochemical sensor.
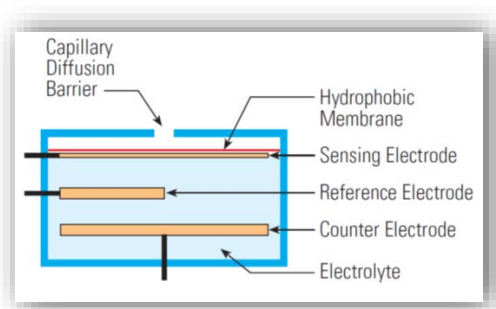
Figure 2.5 Electrochemical sensor setup [11].

When the gas is in contact with the sensor, it passes through the hydrophobic membrane, so the gas begins to react at the sensing electrode. The electrochemical reaction can be either a reduction or an oxidation, depending on the analysed gas. In the case of CO it may be oxidized to CO_2 (or oxygen may be reduced to water). The oxidation takes place in the sensing electrode, CO_2 diffuses into the air and the charge ions (+) migrate to the electrolyte medium.

$$CO_2 + H_2O \rightarrow CO_2 + 2H^+ + 2e^- \hspace{3cm} \text{Eq. 2.2}$$

Conversely, a reduction reaction results in flow of electrons from the counter electrode to the sensing electrode.

$$O_2 + 4H^+ + 4e^- \rightarrow 2H_2O \hspace{3cm} \text{Eq. 2.3}$$

By measuring the current between the counter electrode and the sensing electrode, the electrochemical instrument can be utilized to sense gases.

16

2.2 Adsorption

2.2.1 Adsorption and absorption definitions

Absorption is a chemical or physical phenomenon in which atoms, molecules or ions enter some bulk phase material (the absorbent). Matter that is absorbed can be gaseous, liquid, or solid. Strictly speaking, the absorption process is the dynamic result of three different processes occurring at the same time:

i) Adsorption: The formation of a layer of adsorbed molecules (in solid, liquid or gaseous phase) on the surface of a solid, or less frequently, a liquid.

ii) Desorption: The removal of adsorbed molecules from the active sites/surface. Desorption occurs in thermal equilibrium with adsorption. The rate of adsorption and desorption is dependent on the temperature of the system, so the thermic conditions of the system determines the direction of the equilibrium.

iii) Diffusion: The passage of gas through the bulk of a material enabling it to reach active sites on which to adsorb. The nature of this process is dependent of the temperature of the gas and the porosity of the material.

Normally, the processes are characterized by time constants which are associated with parameters such as the pressure, temperature of the gas, concentration of the adsorbate and the porosity of the adsorbent.

2.2.2 Basic principles

When a molecule impinges upon a surface there are a number of different outcomes of the collision. The molecule can be reflected with no energy loss, an elastic collision. The molecule could lose a small amount of energy to the surface, exciting the surface either electronically or vibrationally, an inelastic collision. If the molecule does not lose too much energy due to the collision, it will be reflected. However if the molecule loses sufficient energy to the surface, it may become bound (adsorbed) to the surface. An adsorbed molecule is called admolecule, a collection of admolecules across a surface is called an adlayer (or adsorbed layer) and the average length of time an admolecule stays on a surface is called the mean stay time and is given by the symbol τ [12].

2.2.3 Adsorption processes

The adsorption of a gas admolecule onto an adsorbing molecule is a consequence of the attractive forces present at that surface, which can be categorized as chemical or physical, resulting in physisorption and chemisorption processes respectively.

Physisorption is driven by weak Van der Waals forces such as dipole-dipole interactions. Although the admolecule may experience a displacement of electrons no actual sharing of electrons takes place and the attraction is governed by forces between two permanent dipoles, a permanent dipole and a corresponding induced dipole or between two instantaneously induced dipoles whose strength decreases with distance. As Van der Waals forces exist between all atomic/molecular species, physisorption always occurs and is not limited to the formation of a single adlayer.
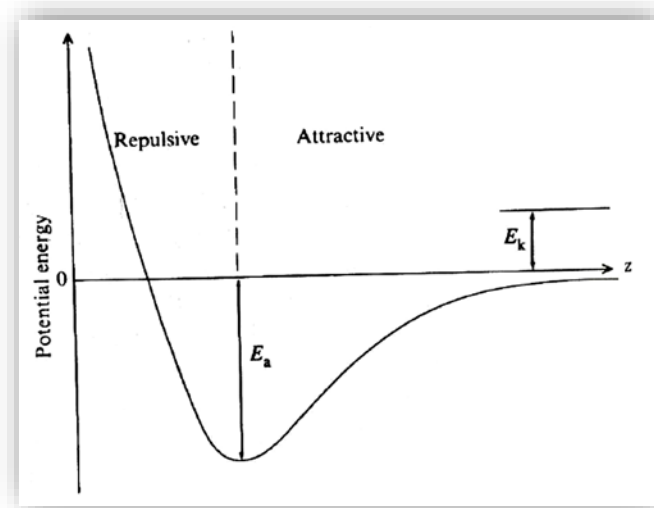
Figure 2.6: Potential energy function for a physisorbed molecule [13].

Chemisorption involves sharing of electrons between the admolecule and the adsorbing surface. This sharing of electrons signifies the formation of a chemical, or valence bond, such as an ionic, covalent or hydrogen bond. The forces present in forming a chemical bond are much stronger than van der Waals and depend on the adspecies and surfaces species valency and geometric requirements. Chemisorption, unlike physisorption, is usually limited to certain combination of adspecies and surface species, and to a maximum thickness of one admolecule.

2.2.4 The fundamental adsorption equations

In order to comprehend the adsorption behaviour of a gaseous analyte into a thin film, the fundamental adsorption equations must be considered. The equations provide a description of the comportment of the porphyrin toxic vapour sensing devices using the adsorbate and adsorbent parameters.

2.2.4.a Surface lifetime of gas molecules

Once a gas admolecule is adsorbed onto an adsorbing surface there is a probability that this admolecule can escape (desorb), providing an associated mean stay time for adsorption (τ_a), which can be described with the following equation:

$$\tau_a = \tau_0 \exp\left(\frac{\Delta H_{des}}{kT}\right) \qquad \text{Eq. 2.4}$$

Where τ_0 is the standard mean surface lifetime of gas molecules at absorbent at that temperature, ΔH_{des} is the enthalpy of desorption, k is the Boltzamnn constant, T is temperature in Kelvin. Importantly it is observed that the likelihood of this process depends on the temperature, thus the strength of bonds is weakened when high temperatures in the system are reached [13].

2.2.4.b Impingement rate

The impingement rate (I) of gas onto a surface is obtained from the kinetic theory of gases, and is given by:

$$I = \frac{p}{(2\pi mkT)^{1/2}} \qquad \text{Eq. 2.5}$$

Where p is the pressure, m is the mass of the adsorbate, T is the temperature and k is the Boltzmann's constant [13].

2.2.4.c Dynamic equilibrium

An adsorbing surface will adsorb gas molecules continuously even during an equilibrium state. At a given pressure and temperature, once equilibrium has been established, the net rate of

accumulation of gas molecules on the surface is zero, thus the rate of adsorption of molecules at this point is equal to the rate of desorption of molecules. In other words, the equilibrium occurs when the number molecules escaping from the surface (desorbing molecules) matches the impingement rate. The rate of desorption (E) can be described as:

$$E = \frac{n_a}{\tau_a}$$

Eq. 2.6

Where n_a is the surface population of adsorbed molecules/cm^2 and τ_a is the mean stay time for an adsorbed molecule (described in equation 2.4). At equilibrium, equations 2.5 and 2.6 are numerically equal:

$$I = E = \frac{n_a}{\tau_a} = \frac{p}{(2\pi mkT)^{1/2}}$$

Eq. 2.7

Nonetheless, τ_a is a function of the enthalpy of desorption and the temperature, as observed in equation 2.4. When the dynamic equilibrium equation (equation 2.7) is combined with the equation 2.4 using the standard lifetime of gas molecules at room temperature (τ_o), the fundamental kinetic equation for adsorptive equilibrium is obtained [13]:

$$n_a = I\tau_a = \left[\frac{p}{(2\pi mkT)^{1/2}}\right] \tau_o exp\left(\frac{\Delta H_{des}}{kT}\right)$$

Eq. 2.8

2.2.5 Adsorption models

There are various adsorption models that characterize the adsorption/desorption dynamic equilibrium of the system at a constant temperature. The models describe the relation between the available sites to bond in the material with the number of adsorbed molecules. Chemical adsorption models describe a molecular adsorption process using theoretical predictions and correlate to the experimental data. On the other hand, empirical isotherms are based on observation, rather than being described on theoretical assumptions.

2.2.5.1 The Langmuir Model

The Langmuir Adsorption Isotherm relates the fundamental kinetic adsorption equation (eq. 2.8) to the behaviour of a real system. The model is useful to describe the adsorption of gas onto monolayers. The Langmuir isotherm is based on certain assumptions regarding the effect that each admolecule has on its subsequent admolecules [14]:

- Adatoms/molecules are held at specific sites on the surface, i.e. they do not move laterally over the surface.
- Each site can only absorb one molecule/atom, therefore the total coverage is limited to a single layer; i.e. n_a is equal to the number of surface sites.
- There is no interaction between admolecules/atoms on different sites.
- The enthalpy of desorption (ΔH_{des}) is independent of the number of sites and is the same for all the sites.

To start deriving an equation for the model, the impingement factor which respects for any striking molecule that impinges an occupied site and does not absorb is added to the fundamental kinetic equation (eq. 2.8), resulting in the following equation:

$$n_a = I\left(1 - \frac{n_a}{n_o}\right)\tau_a \qquad \text{Eq. 2.9}$$

where n_o is the total number of sites available for adsorption. So as the number of occupied sites increases, n_o decreases because there are less available sites in the monolayer. Multiplying out the right hand side of equation 2.9 gives:

$$n_a = I\tau_a - I\tau_a\left(\frac{n_a}{n_o}\right) \qquad \text{Eq. 2.10}$$

Solving for n_a:

$$n_a\left(1 + \frac{I\tau_a}{n_o}\right) = I\tau_a \qquad \text{Eq. 2.11}$$

and dividing by n_o:

$$\frac{n_a}{n_o}\left(1 + \frac{I\tau_a}{n_o}\right) = \frac{I\tau_a}{n_o} \qquad \text{Eq. 2.12}$$

An expression that estimates the number of occupied sites as a fraction of total sites or the fractional coverage of the surface by the monolayer must be represented:

$$\Theta = \frac{n_a}{n_o} = \frac{\dfrac{I\tau_a}{n_o}}{1 + \dfrac{I\tau_a}{n_o}} \qquad \text{Eq. 2.13}$$

Defining χ as:

$$\chi = \left(\frac{\tau_a}{n_o}\right)\left(\frac{1}{(2\pi mkT)^{1/2}}\right) = \left(\frac{\tau_a}{n_o}\right) I/p \qquad \text{Eq. 2.14}$$

And substitution of equation 2.13, with equation 2.7 and 2.14 yields the Langmuir adsorption isotherm equation, which is expressed in terms of the fractional surface coverage (Θ):

$$\Theta = \frac{\chi p}{1 + \chi p} \qquad \text{Eq. 2.15}$$

The Langmuir equation can be applied to experimental data by rearranging eq. 2.15:

$$\frac{p}{\Theta} = \frac{1}{\chi} + p \qquad \text{Eq. 2.16}$$

If at constant temperature a plot of p/Θ versus p yields a linear plot it can be assumed that the absorption process fits the Langmuir model.

Figure 2.7 shows that at high pressures, Θ tends to unity and $\chi p \gg 1$, state which describes that all surface sites in the monolayer are filled.
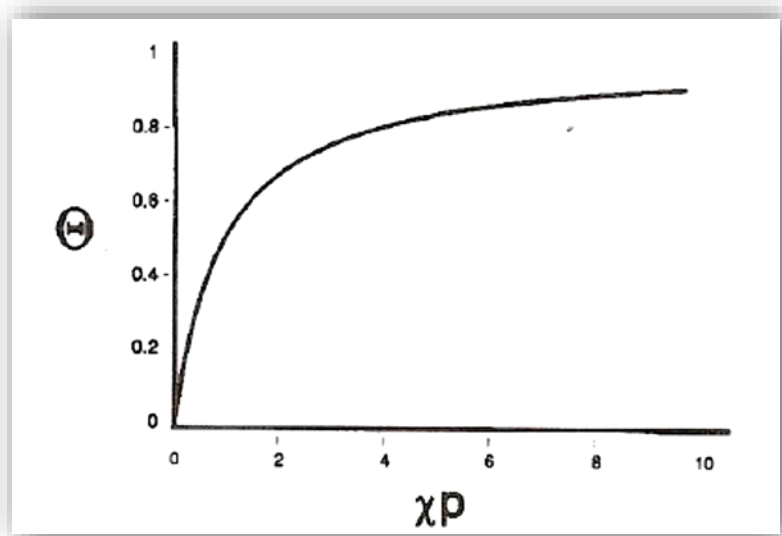
Figure 2.7 The Langmuir isotherm function [13].

At low pressures and moderate temperatures, $\chi p \ll 1$, resulting in the Langmuir adsorption isotherm equation 2.15 approximating to:

$$\frac{n_a}{n_o} = \Theta \approx \left(\frac{\tau_0}{n_0}\right)\left(\frac{p}{(2\pi mkT)^{1/2}}\right) exp\left(\frac{\Delta H_{des}}{kT}\right) \qquad \text{Eq. 2.17}$$

It is possible to use equation 2.17 in the form of Arrhenius equation where taking the natural logarithm of each side:

$$ln(n_a) \approx ln\left(\frac{\tau_0 p}{(2\pi mkT)^{\frac{1}{2}}}\right) + \left(\frac{\Delta H_{des}}{kT}\right) \qquad \text{Eq. 2.18}$$

Over small temperature ranges plots of $ln(n_a)$ versus $1/T$ will be linear, allowing the determination of the binding energy, ΔH_{des}, from the gradient.

Alternatively, the Langmuir adsorption model can be expressed in terms of the concentration of the vapour starting from equation 2.15. Since the pressure is directly proportional to the concentration (c), we can write:

$$\Theta = \frac{\chi c}{1 + \chi c} \qquad \text{Eq. 2.19}$$

In the case of optical absorbance measurements, $\Theta \propto \Delta Abs$. So:

$$\Delta Abs = \frac{\chi c}{1 + \chi c} \qquad \text{Eq. 2.20}$$

$$\frac{\chi c}{\Delta Abs} = 1 + \chi c \qquad \text{Eq. 2.21}$$

$$\frac{c}{\Delta Abs} = c + \frac{1}{\chi} \qquad \text{Eq. 2.22}$$

Therefore, a plot of c/ΔAbs versus c should be a straight line if Langmuir adsorption is occurring.

The y-axis intercept of this plot has a non-zero value, which represents $1/\chi$. From 2.14:

$$\frac{1}{\chi} = \frac{1}{(\tau_a/n_o)(2\pi mkT)^{1/2}} \qquad \text{Eq. 2.23}$$

Therefore, the intercept value is wholly dependent on both the temperature and the number of adsorption sites per cm^2.

2.2.5.2 The BET model

The Langmuir adsorption model has formerly provided a satisfactory description for vapour sensing using porphyrin thin films [15], however, the theory breaks down because it does not consider the interaction between adspecies. Consequently, the Langmuir adsorption model

ignores any gradual accumulation of monolayers on a surface. It is expected that when multilayer formation occurs, the heat of adsorption of an adsorbate molecule adsorbing on a bare substrate will differ significantly from the heat of adsorption associated with an adsorbate molecule adsorbing onto another layer of adsorbate (the strength of adsorbate-absorbent bonds will differ from adsorbate-adsorbate bonds).

Brunauer, Emmett and Teller (BET) developed an adsorption model based on experimental observations that considered a multi-layered system [16]. The BET theory maintain the concepts of the Langmuir adsorption model, except allowing molecules to be adsorbed on top of admolecules, each additional adlayer still obeying the Langmuir equations [17]. In the case of toxic vapour sensing using porphyrin materials, additional adsorbed layers on top of the initial adsorbed layer are not thought to contribute to absorbance changes. So, it is expected that the changes in the absorbance spectrum of porphyrin are a function of the vapour concentration on the surface only, and the relationship can be characterized using the Langmuir adsorption theory. However, plotting the mass of an adsorbed surface as a function of vapour concentration may follow the BET adsorption theory.

2.2.5.3 The Freundlich Model

The Freundlich adsorption model is an empirical function that expresses the isothermal relationship between the magnitude of adsorption and the pressure. The isotherm equation is non-linear, and can be mathematically expressed as:

$$\frac{x}{m} = Kp^{1/n} \qquad \text{Eq. 2.24}$$

Where x is mass of the vapour adsorbed on the adsorbent mass, m, at an equilibrium pressure p. n and K represents constants that depend on the adsorbent and vapour intrinsic nature at a particular temperature. Alternatively, eq. 2.24 can also be expressed in terms of the equilibrium concentration of the vapour (c):

$$\frac{x}{m} = Kc^{1/n} \qquad \text{Eq. 2.25}$$

Adding a logarithm on both side of equation 2.25:

$$log\frac{x}{m} = log\,k + \frac{1}{n}logc \qquad \text{Eq. 2.26}$$

Where eq. 2.26 is comparable with linear equation. Plotting a graph of these terms, a straight line with a slope equal to 1/n is obtained, as shown in figure 2.8.
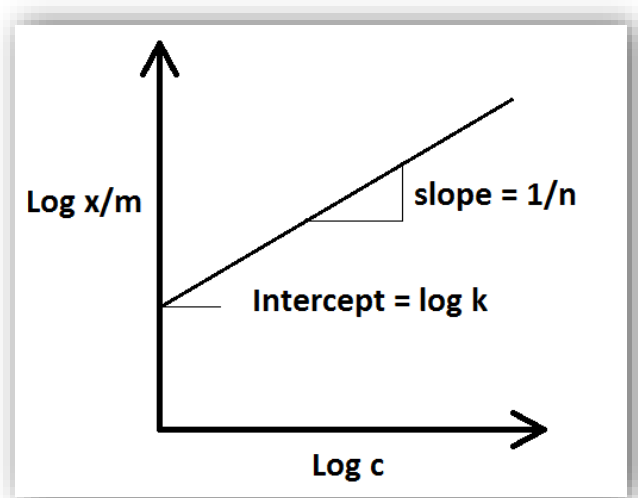
Figure 2.8: Freundlich adsorption isotherm in its linear form.

The model establishes a relationship of adsorption with pressure at lower values; however, the mathematical equation fails to predict the adsorption once the saturation pressure is reached. At that point, the adsorption becomes independent of pressure.

2.3 Electronic Orbitals in atoms and molecules

The energy of a molecule includes components derived from the energy transitions within the atomic nuclei, vibration of atoms within the molecule, rotation of the molecule and motions of the electrons around the nuclei. A molecule has a series of energy levels, and can lose or take on energy in steps corresponding to the differences between various levels. The electronic energy levels are broadly separated and lead to the absorption of visible light and UV; vibrational levels are closer and transitions between them correspond to the absorption in the near IR; rotational levels represent subdivisions of the vibrational levels and their energy differences account for the absorption in the far IR and microwave regions.

In agreement with quantum mechanics principles, even though electrons behave in some respects as particles, they also display the properties of waves. The electron may be assigned a wave function ψ (a complex function of time and position), defined in simple cases by the solution of Schrödinger's equation. This signifies that the energy of the electron can only have

certain discrete values. It follows that there is a series of fixed energy levels that may be occupied by an electron, and these are known as orbitals. For each orbital there is a region in space where an electron is likely to be, and may be represented as a series of three-dimensional figures showing the distribution of ψ. These figures do not define precise limits to electron movement but for a small volume $ψ^2$ represents the probability that the electron will be found in that volume at any one instant.

A series of orbitals are associated with every atom and the energy of an electron determines which of them it may occupy. The Pauli exclusion principle permits each to be occupied by a maximum of two electrons with opposite spin [18]. A molecular orbital (MO) is formed by the overlapping of outer singly occupied orbitals of two or more atoms, and several types may be distinguished, each having a characteristic energy, size and shape. The out of phase and in phase overlap of atomic orbitals results in the formation of anti-bonding (π^*, σ^*) and bonding (π, σ) MOs, shown in figure 2.9. Atomic orbitals that are incapable of combination, such as those containing inner shell or lone pair electrons, are described as non-bonding (n).
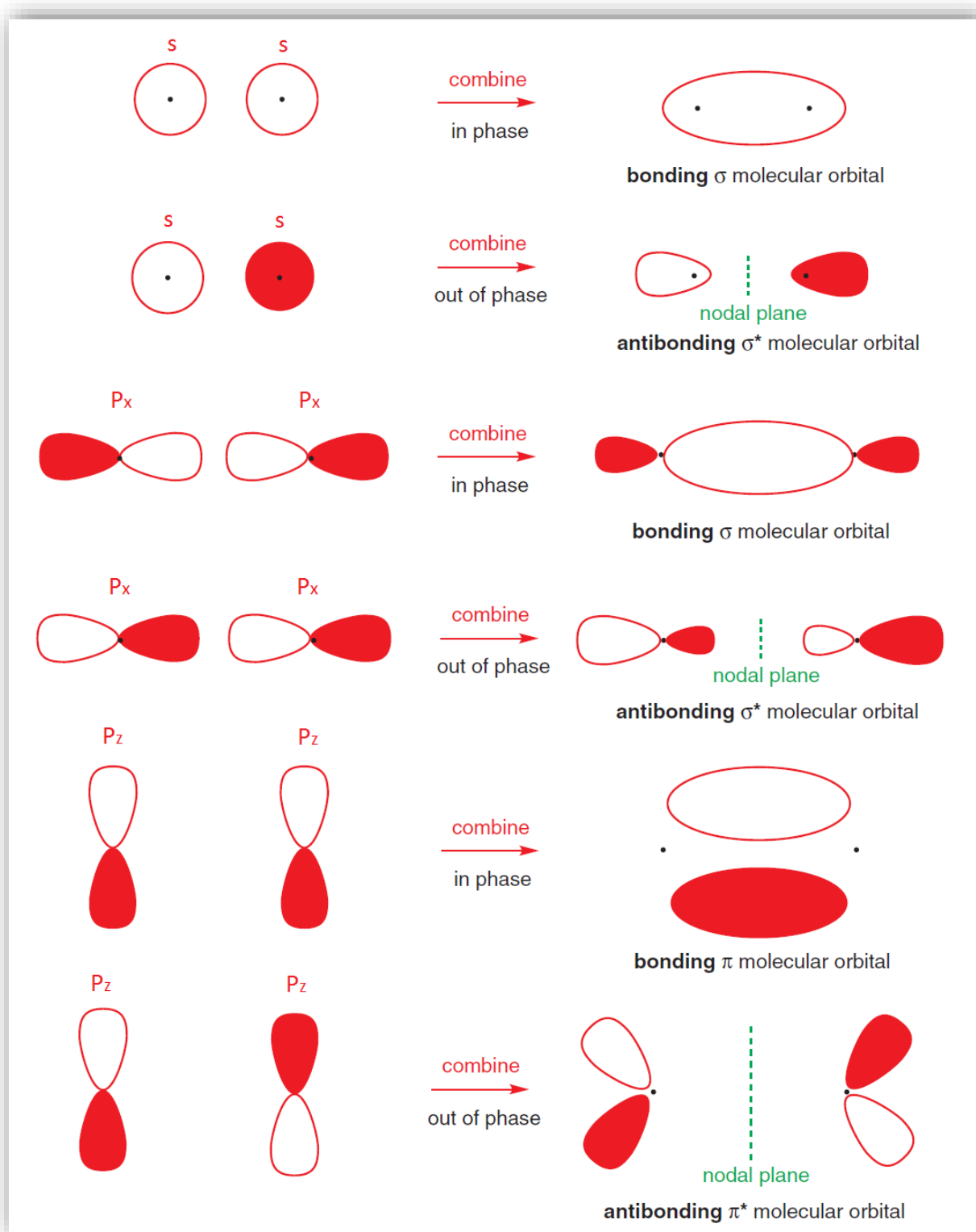
Figure 2.9: The formation of bonding and anti-bonding molecular orbitals by overlap of atomic orbitals [19].

The energy (E_n) of the MOs (ψ_n) is related to the degree of overlap of the atomic orbitals and thus to the position of the constituent electrons. In simple molecules the electronic energy

levels may be represented as shown in figure 2.10. In the lowest or ground electronic state of most organic molecules, all the bonding and non-bonding orbitals are fully occupied and the anti-bonding orbitals are empty. Absorption of a photon with a quantum of energy at wavelength within the visible spectrum will cause a σ or π bonding electron to be promoted to an empty anti-bonding level, thus bringing about an electronically excited state.
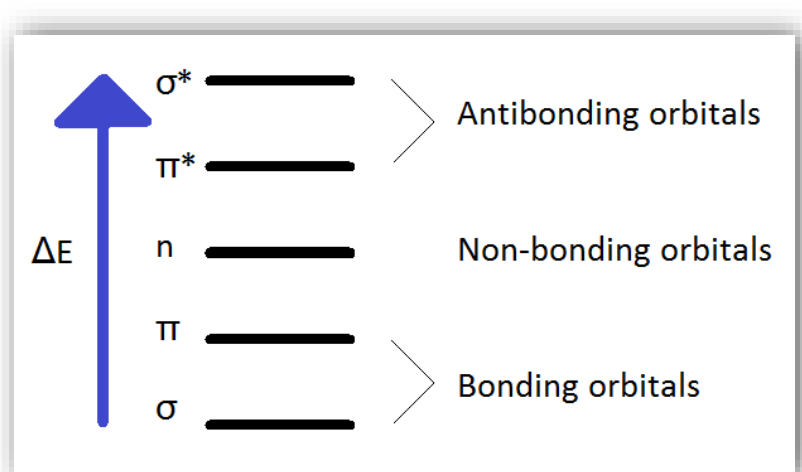
Figure 2.10: Electronic energy levels in a molecule.

The energy gain (ΔE) is to the first approximation equal to the energy difference between the two molecular orbitals concerned in the transition and is related to the wavelength of the light absorbed by the following equation:

$$\Delta E = E_{\psi 2} - E_{\psi 1} = \frac{hc}{\lambda}$$

Eq. 2.27

Where ΔE is the energy of transition, $\psi 2$ is the acceptor orbital, $\psi 1$ is the donor orbital, h is the Planck's constant, c is the speed of light and λ is the wavelength of the light absorbed.

So, each transition gives rise to a sharp absorption line. The absorption spectrum shows broad band envelopes due to vibrational states (j=0, 1, 2, …n) associated with each electronic energy state; the potential energy curves for ground and excited states are shown in figure 2.11.
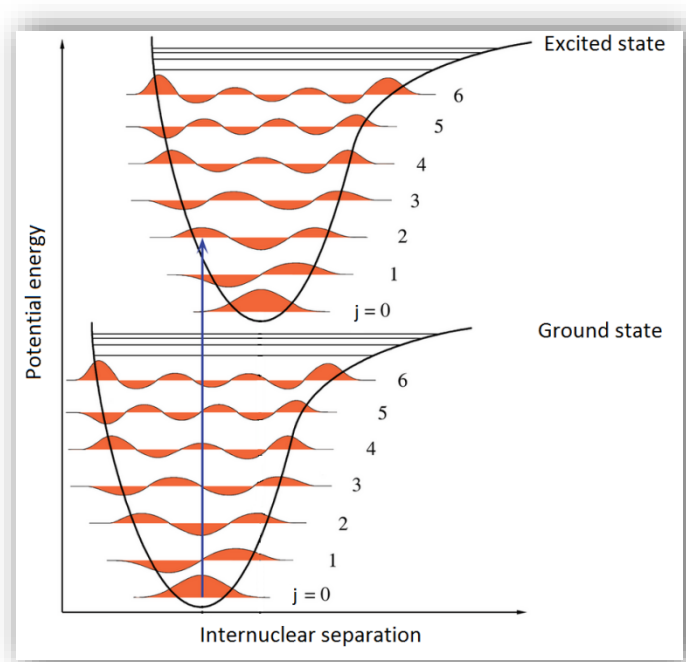
Figure 2.11: Potential energy curves of the ground and excited states of an absorbing molecule [20].

The excited state is displaced relative to the ground state as a consequence of the greater bond lengths in the excited molecule. Electronic transitions between given vibrational levels in upper and lower states have a given probability. The Franck-Condon Principle states that an electronic transition occurs so rapidly in comparison to a molecular movement that no change in inter nuclear separation occurs during the course of the transition [21]. Thus a vertical line may be drawn from ground to excited state on the potential energy diagram to predict the relative intensity of the transitions. In optical absorption, the most probable transition originates from the j=0 level in the ground state to higher levels in the excited state, but other transitions with lower probability on either side of this transition are possible and these give rise to the characteristic distribution of an absorption spectrum.

2.4 Hybridisation

Molecular orbitals can be characterized using Linear Combination of Atomic Orbitals, which by definition is a quantum superposition of atomic orbitals for the whole molecule. Hybridisation is defined as the alteration of the atomic orbital structure where each of the new hybrid orbitals possess average characteristics of those orbitals [22].

For instance, methane contains two elements, hydrogen and carbon, and the molecular formula is CH_4. Carbon has six electrons and four of these are in the outer shell, which allows them to form bonds. These are valence electrons and are contained in the 2s and 2p orbitals, as shown in figure 2.12 (ground state). Only unpaired electrons are suitable for bond formation whereby they pair with an electron from another atom. However, it is well known that carbon is able to bond with up to four atoms. This requires one of the 2s electrons to be promoted to the vacant $2p_z$ orbital (excided state). Even when the system changes its overall energy, shifting to a higher one, it will eventually conduct to a lowering of energy through extra bond formation. The electrons can now hybridise to four identical sp3 orbitals (hybridised state).
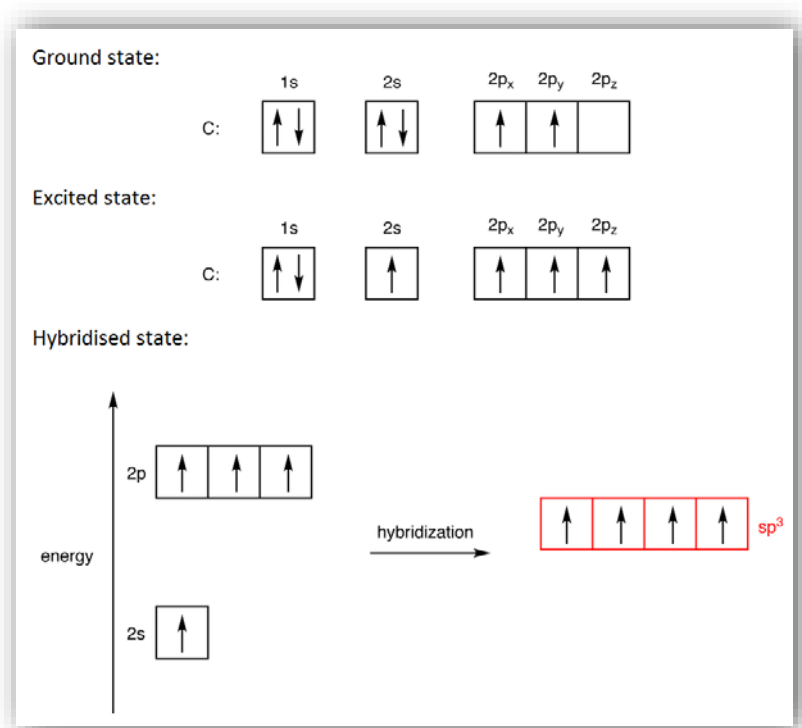
Figure 2.12: Hybridisation of carbon.

The shape of the sp^3 hybrid orbital is a mathematical combination of its 25 percent s-character and 75 percent p-character character, and is represented in figure 2.13. Since there are four sp^3 orbitals they conform into a tetrahedral structure, each orbital repelling the other to align themselves as far away from each other as possible due to Valence Shell Electron Repulsion Theory (VSERT) [19]. Bonds between sp^3 orbitals and hydrogen orbitals are the σ bonds.
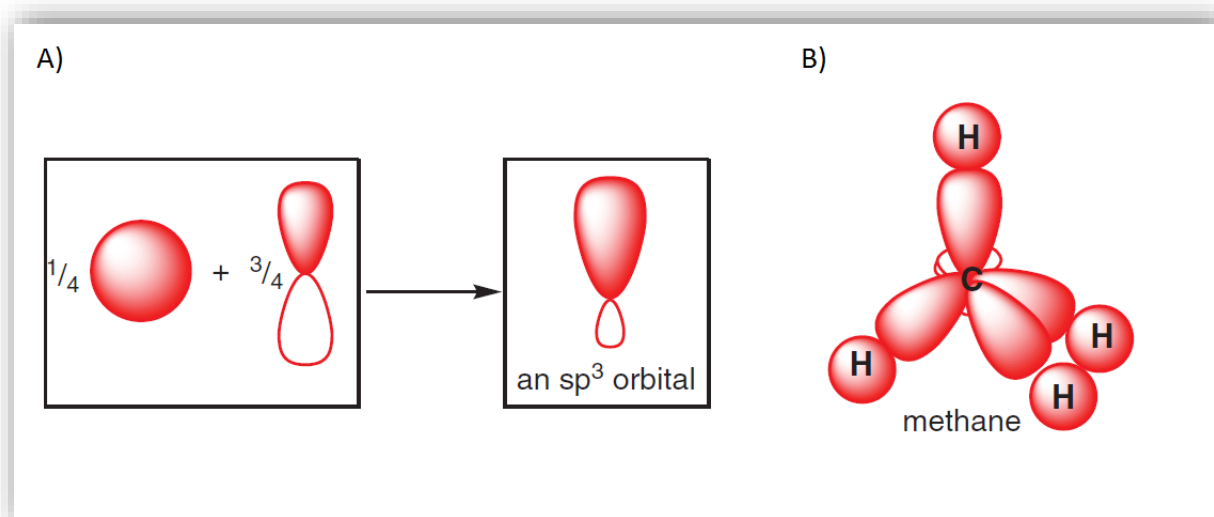
Figure 2.13: A) Formation of a single sp3 orbital, b) hybridisation in carbon producing four equivalent sp3 orbitals [19].

2.5 Conjugation

A conjugated molecule consists of alternating single and multiple bonds with overlapping p orbitals, so π bonds are present in molecules where conjugation occurs. When the right sequence of single-double bonds take place in the structure, the collection of π bonds act as one bond over the entire molecule. The π electrons of these bonds are delocalised over the molecule.

Benzene is a cyclic conjugated molecule formed by six sp^2 hybrids (made by two p orbitals and one s orbital reorganising themselves) and has molecular formula of C_6H_6. The hexagonal structure with alternative single and double bonds was proposed with Kekulé, suggesting that the double bonds might oscillate rapidly around its two possible configurations (as shown in figure 2.14A). Figure 2.14B shows the orbital view of benzene and stresses the cyclic conjugation of the molecules and the equivalence of the six carbon-carbon bonds. The fact that all six p orbitals and six carbon atoms are equivalent, makes it impossible to define three localised π bonds where one p orbital overlaps with just one of its neighbours. Instead, each p orbital overlaps equally well with both of its neighbours and the six π electrons are completely delocalised around the ring. The molecule then, has a doughnut shaped cloud of electrons both below and above the ring.
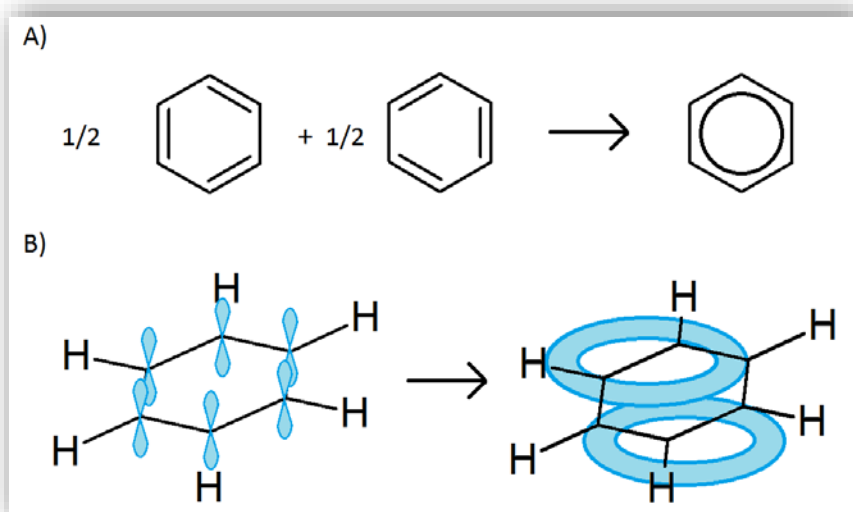
Figure 2.14: A) Representation of the possible benzene ring configuration, b) an orbital picture of benzene showing the 2pz orbitals and the doughnut electron distribution.

There are six new molecular orbitals created within the benzene ring structure due to the conjugation of π-bonds, which are shown in figure 2.15. The lowest energy of these six orbitals, ψ_1, is highly stable and its configuration involves the combination of all 2p orbitals in phase. On the other hand, the molecular orbital with the highest energy, ψ_4, is created when all 2p atomic orbitals combine out of phase. There are two pairs of orbitals created that are degenerate: ψ_2 and ψ_3. ψ_2 has one nodal plane (where square of the wave function is zero) that can be arranged in two ways depending on whether or not the nodal plane passes through an atom or a bond. Correspondingly, there are two ways of arranging two nodal planes for the generate states of the ψ_3 atomic orbitals.
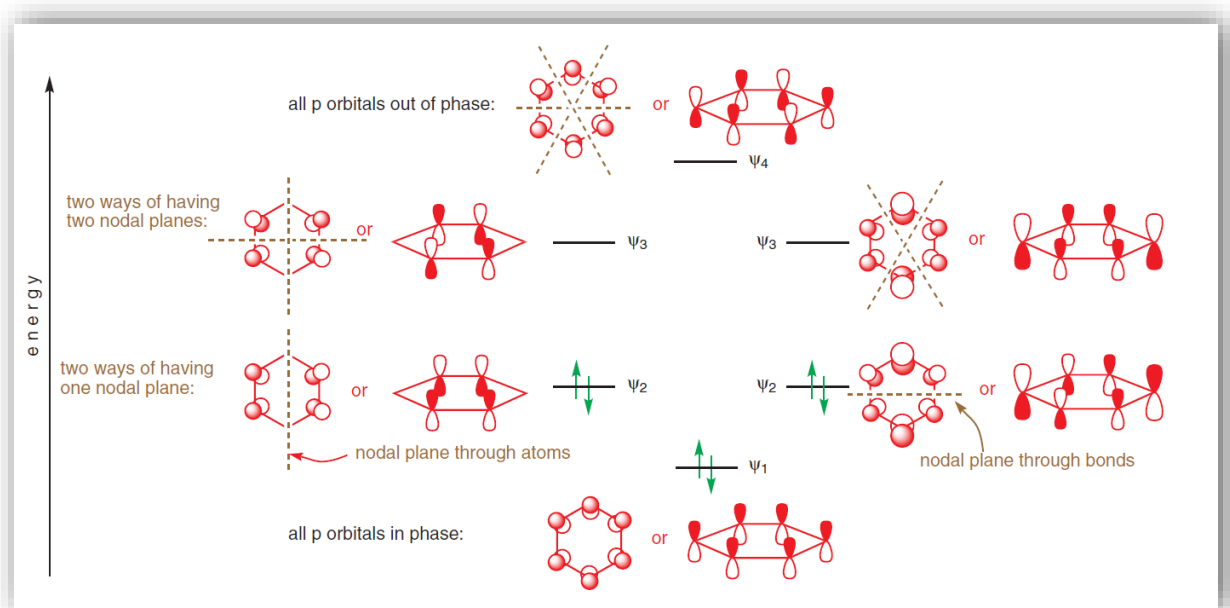
Figure 2.15: The relative energies of molecular orbitals within benzene [19].

2.6 Hückel's rule

An aromatic molecule is a planar ring with a circular cloud of delocalized π electrons. It can be considered as an unsaturated cyclic molecule stabilized by resonance. Hückel introduced a rule for determining whether a cyclic compound with alternate single and double bonds would be aromatic. The rule states that a monocyclic system will be aromatic if there are (4n+2) π-electrons contained within the perimetric ring system, where n is an integer. Although not specifically mentioned in the rule, but implicitly part of aromaticity, is the requirement that the ring is planar. This is simply because delocalisation results from significant overlap of the p orbitals and considerable deviation from planarity will diminish the p orbital overlap.

Hückel also predicted that anti-aromatic molecules having 4n π-electrons around the macrocycle will be destabilised. Figure 2.16, shows the molecular orbitals for a molecule with 4n π-electrons (cyclooctatetraene) and one with (4n + 2) π-electrons (benzene), demonstrating where the rule comes from. If cyclooctatetraene adopted a planar structure, its 8 p orbitals would overlap to give 8 π-electron molecular orbitals. This would result in two unpaired electrons (i.e. free radicals). The presence of two free radicals would result in a highly reactive molecule. To prevent this reduced stability cyclooctatetraene supports a non-

planar structure with isolated double and single bonds. Conversely all the electrons in benzene are paired allowing this planar structure to exist.
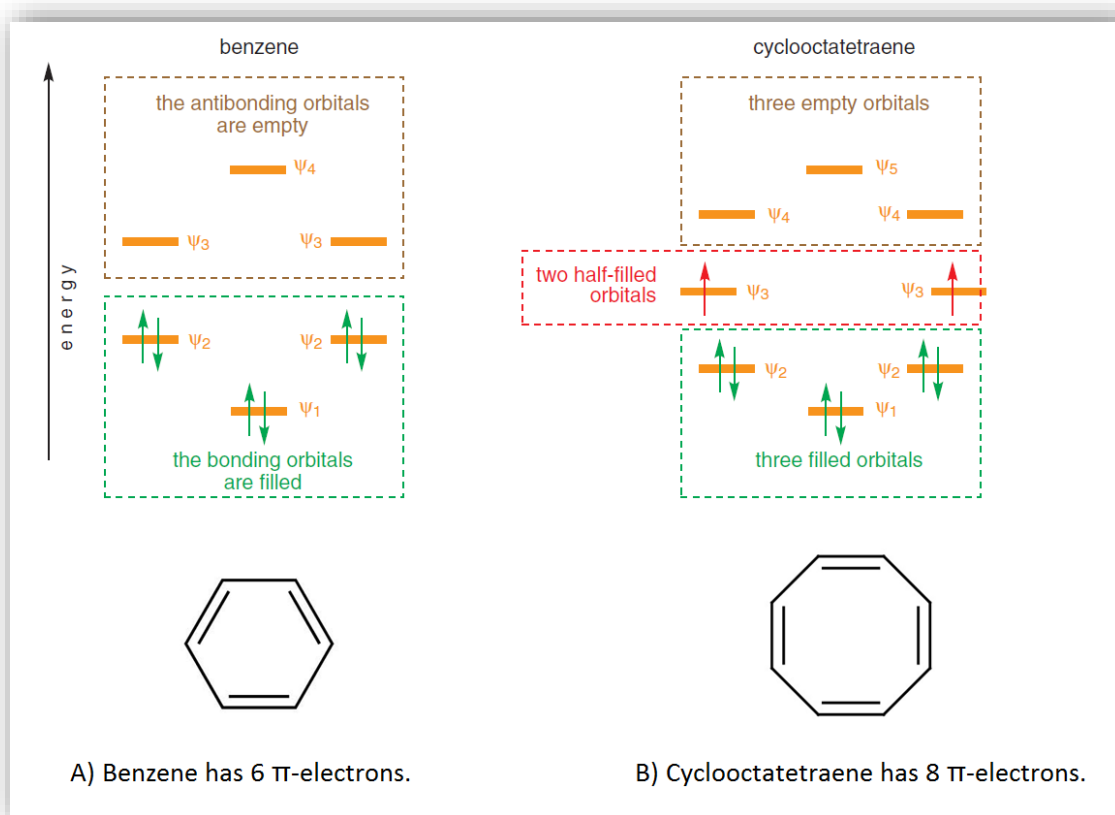
Figure 2.16: The relative energy levels created by the aromaticity in an eight carbon ring compared with the energy levels of a benzene ring [19].

Applying Hückel's rule to porphyrins (where n=4), which contain 22 π-electrons of which 18 are used in its conjugated macrocycle at any one time, it is predicted that they will exhibit aromatic nature.

2.7 Porphyrins

Porphyrins are a ubiquitous aromatic organic molecules that commonly occur in nature. The compounds are involved in biological processes such as the oxygen transport in blood (heme) and photosynthesis (chlorophyll). Porphyrin molecules have a highly conjugated system which exhibits a very intense absorption in the visible region of the electromagnetic spectrum; in fact its name originates from the ancient Greek word for the colour purple, "porphura".

2.7.1 Porphyrins in nature

Porphyrins play an important role in natural biological systems, without the molecule and their relative compounds it is difficult to predict the evolution of life. By substituting or adding a central metal in the porphine, it is possible to change the porphyrin functionality. As an example, an iron porphyrin forms a compound found in blood called heme which is able to reversibly bind with oxygen and transport blood around the body or store the oxygen in the muscle tissues; magnesium porphyrin is an active part of chlorophyll which is implicated in the metabolic phenomena of photosynthesis; cobalt porphyrin found in vitamin B-12 that is responsible of the normal performance on the nervous system and brain in animals; and a free base porphyrin (pheophytin) which is found in photosynthetic apparatus of bacteria and animals [23].

2.7.2 Structure of porphyrin

Porphyrins have the same molecular nucleus, which is the main building block for all porphyrins, this core is also known as porphine. Porphine consists of four pyrrole molecules joined together by four methine bridges. The conjugation of a porphyrin is continued through joining the pyrrole molecules with the methine bridges. Figure 2.17 shows the structure of a phyrrole unit and a methine bridge, that together build up a fourth of a porphine molecule as shown in figure 2.18.
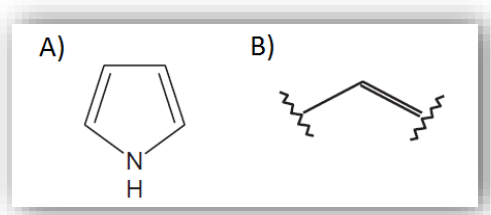
Figure 2.17: A) a pyrrole molecule, b) a methine bridge.

To refer consistently to the position of the porphyrin molecules, Hans Fischer introduce the first porphyrin nomenclature [24], that clearly labels the places in which the side groups could be attached given a number or a Greek letter. Figure 2.18A shows the Fischer nomenclature, note that some of the carbons adjacent to the nitrogen are not labelled. Due to the ambiguity of this nomenclature and the complexity of the synthesis of some porphyrins, the

nomenclature was replaced in 1979 by the International Union of Pure and Applied Chemistry (IUPAC). The mesopositions (5,10,15 and 20 in IUPAC nomenclature) allow the electrophyilic substitution reaction typical of aromatic compounds such as sulphonation, nitration and halogenation [25]. The substitution of side groups in the β-pyrrole positions (2,3,6,7,12,13,17 and 18 in IUPAC nomenclature) does not exist typically in nature.
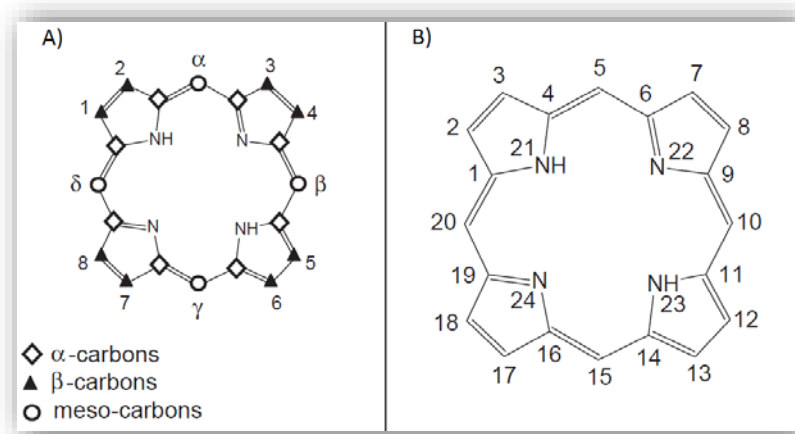
Figure 2.18: Macrocycle nomenclatures of a) Fischer and b) IUPAC [15].

2.7.3 The porphyrin spectrum

The free electron theory (FET) places each π-electron into an orbital the size of the conjugated porphyrin system. The 18 π electrons are only allowed to have certain energy states due to quantisation of orbital angular moment. The allowed angular moment quantum numbers (L) mean that these 18 electrons occupy pairs of degenerate electronic orbitals from L=0, ±1 until ±4. The π electrons occupying any L= ±4 state are in the HOMOs and the available L= ±5 states are the LUMOs. The transitions of electrons between HOMO and LUMO upon excitation occur with ΔL= ±1 and ΔL= ±9, as shown in figure 2.19.
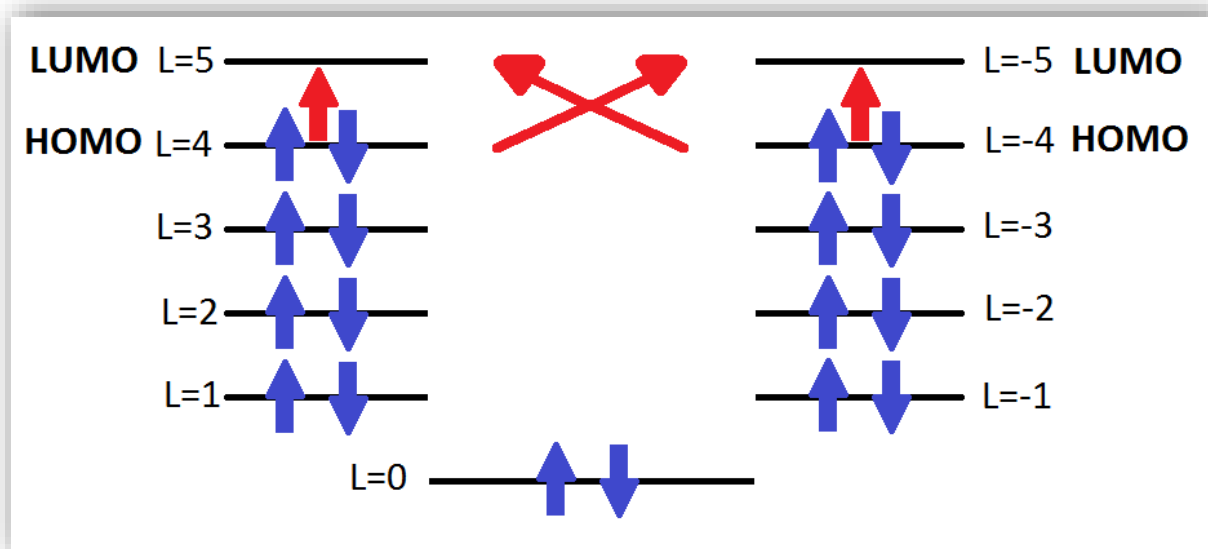
Figure 2.19: The transitions between HOMO and LUMO states due to quantised orbital angular momentum in an 18 membered π-electron system.

Quantum selection rules dictate that ΔL can only be 0 and ±1. Therefore, transitions from HOMO to LUMO with ΔL= ±1 result in a high intensity absorbance peak, whereas the ΔL= ±9 transitions are forbidden and result in weaker intensity absorbance peaks.

Experimentally it can be verified that the allowed transitions (ΔL=±1) are at a higher energy, or shorter optical wavelength, than the forbidden (ΔL=±9) transitions. The shorter wavelength allowed transitions create the strong Soret peak at approximately 420 nm; while the higher energy, lower intensity forbidden transition create the Q bands peaks ranging from 480 to 700 nm.

FET theory provides a reasonable explanation for the relative intensities and positions of the Soret peak and Q bands. However, it does not provide adequate reasoning of their numbers; the observed spectrum of a free base porphyrin consistently has 4 Q bands. The complex theory related to the number, intensity and position of Soret peaks and Q bands in porphyrin molecules is provided by the Gouterman's model [26].

2.7.3.1 Gounterman's model

This model describes the low-lying π–π* excited states of porphyrins in terms of the electronic transitions between the two highest occupied molecular orbitals a_{1u} and a_{2u} (HOMO and HOMO-1) to the two degenerate lowest energy unoccupied molecular orbitals e_g (LUMOs).

For a porphyrin system with D_{4h} symmetry, the e_g orbitals are strictly degenerate whereas the a_{1u} and a_{2u} orbitals are non-degenerate. The electronic configuration of a ground state porphyrin is $^1A_{1g}$ ($a_{1u}^2 a_{2u}^2$). Accordingly, the lowest singlet excited configurations are $a_{2u}^1 e_g^1$ and $a_{1u}^1 e_g^1$. One might envision that this would lead to two absorption bands of very similar energy due to the $a_{1u} \rightarrow e_g$ and $a_{2u} \rightarrow e_g$ transitions however the near degenerate nature of these singlet states causes a strong configuration interaction. The resulting resonance yields the relatively weak visible Q(0,0) band, in which the transition dipoles of the two configurations are deconstructive, and the intense Soret B(0,0) band, in which the transition dipoles of the two configurations are constructive (the Q band is actually forbidden in nature however it can "borrow" intensity by vibronic coupling from the intense Soret band).

2.7.4 Aggregation

Aggregation is referred as the process of large molecular cluster formation. Particle aggregation is commonly observed in nature, for instance the chlorophyll self-association is a pathway to the charge transfer in photosynthetic complexes. As a matter of fact, the charge separation and the light harvesting in photosynthesis are aided by the aggregated chlorophyll species. The molecular conglomeration of porphyrins produces a change in the properties such as its energetic characteristics and its spectral absorbance. It has been observed that deviations from the Beer-Lambert law are perceived when analysing aggregated compounds in solution. Importantly, in most of the cases the effectiveness of the reaction is greatly altered by its grade of aggregation.

Generally, the self-assembly of porphyrins occurs through non-covalent interactions (hydrophobic, electrostatic and hydrogen-bonding) and the event is affected by the physico-chemical parameters, such as the concentration, pH, ionic strength and presence of surfactants [27].

The properties of porphyrins cause a strong π-π interaction between molecules which facilitates the formation of two families of aggregates, H and J type. The H type is characterized by its face to face stacking, this aggregation type cause a blue shift of the Soret band with respect to those of monomer. Conversely, the J type absorbance spectrum is red shifted and forms side to side or edge by edge conglomerates, illustrated in figure 2.20.
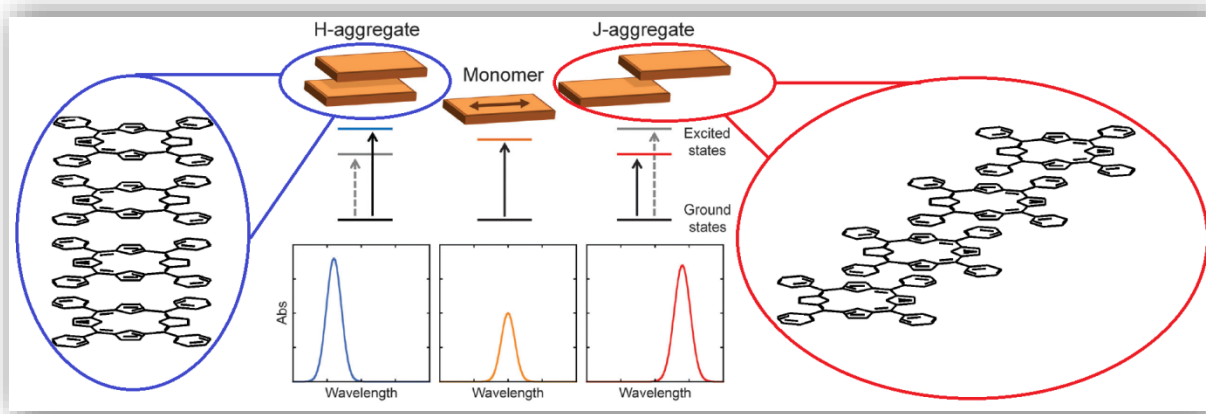
Figure 2.20: Representation of the H and J aggregates in porphyrin [28].

The aggregation of porphyrin can lead to the formation of structural molecular forms, such as ribbons, fibres and tubules. These porphyrin aggregates can be exploited for the development of a chemical gas sensing system [29, 30].

2.7.5 Gas sensing applications

Porphyrins are extremely appealing as gas and chemical sensors due to the ability to bind and release gases. The molecule is able to interact and form ligands with vapour molecules. If the adsorbed molecule is able to alter the π electron system, then this can be monitored through a change in the optical spectrum of the porphyrin. These spectral changes are the main sensing mechanism in this vapour sensing research.

2.8 Recent research into gas sensors

2.8.1 The electronic nose

The human smell and taste senses are still the primary instruments used in various industries to determine the quality of a smell or taste of a product. For example, perfume, food and beverage industries employ professionals to smell and taste their products to ensure the consumers are sold the best possible quality product. The negative side of this is the cost associated with this process for these industries. Only trained experts can smell and taste products and give accurate critical and constructive feedback to their employers. They demand a large salary and due to the nature of the human olfactory system they can only work for short periods of time. The consequence is a high demand, ranging over a number of

industries, for an electronic substitute for the human nose. The concept of an electronic nose refers to the capability of reproducing human senses, taste and smell, using sensor arrays and a pattern recognition system [31].

Strike and Meijerink described the electronic nose as "mimicking the human nose to recognise odours" [32]. However the concept of an electronic nose is easily applied to the area of gas sensing, in which, the gas desired for detection is often odourless. When an electronic nose device is used as a gas sensor a number of gases within a mixture are able to be detected, rather than just one in a classical gas sensor. The sensing materials of an electronic nose should behave unlike any ideal gas sensor: they respond to various gases rather than just one specific gas. A number of sensing materials are placed in an array and this array is exposed to the gas. Each sensor responds in a particular way to each gas and the responses are collected and monitored by a computer. The patterns of response to particular known gases are used as a reference, and when an unknown gas (or mixture) is present the computer uses a pattern recognition system to determine the molecules present.

The ability of porphyrins to be adapted to respond to a number of different gases simply by changing the metal complex within the porphine and the functional groups (discussed in chapter 4) along with their strong optical absorbance spectrum makes porphyrins ideal candidates for elements within an electronic nose sensor array.

Suslick et al used changes in the optical absorbance spectra of an array of sensing materials including porphyrins to detect liquid analytes and vapours [33-39]. The RGB value pattern recognition system, used by Suslick is an example of how the electronic nose device concept can be adapted to suit sensing materials with different characteristics.

Nowadays a wide diversity of electronic noses had been developed to discriminate volatile organic compounds [40-42], analyse the quality of wine and other alcoholic beverages [43-46], and recognition of food freshness [47, 48] and drinking water for human consumption [49, 50].

2.8.2 Porphyrin ChemFETs

Early work on porphyrin LB films began 30 years ago [51]. At that time, researches were attracted to these compounds because they possessed certain desirable properties:

anisotropy, metal complex formation, photoactivity, crystallinity, high dielectric constant, gas adsorption and the possibility of polymerisation between reactive side groups.

Some research groups have reported success in using porphyrin as the organic semiconductor in organic field transistors, due in no small part to the high degree of conjugation within their structure. The use of porphyrins on the gate of an OFET was proposed by Gu et al, thus fabricating the first LB-chemFET device [52]. Since then, diverse research had exploited the molecular recognition events occurring in the porphyrin sensing layers for the fabrication of chemFETs[53, 54]. Different transducers have been developed using porphyrin as a sensory layer, demonstrating exceptional properties in terms of reproducibility, stability and chemical sensitivity [55, 56].

2.8.3 Porphyrin composites and hybrid devices

2.8.3.a Polymer/porphyrin and calixarene/porphyrin composites

The molecular interaction of the porphyrin with gases can be affected by the by proximity of neighbouring porphyrin molecules. In particular the potential aggregation of the porphyrin molecules when they are deposited on a solid substrate, causing a close molecular packing. This aggregation (as described in section 2.7.4 above) can cause poor long-term reproducibility and a loss of sensitivity for porphyrin based sensors. Several porphyrin composites have been examined by several research groups with the interest of dispersing the molecules and reduce the porphyrin areal density to reduce aggregation.

Some authors have used optically transparent polymers (such as dioctylphthalate) matrices in order to disperse the porphyrin molecules. The polymers are generally non-reactive to the gases. The composite films remarkably enhanced the sensor sensitivity. Itagaki and Dini have used optically transparent polymers matrices in order to disperse the porphyrin molecules [57, 58]. The properties of the polymer determine the permeability and consequently it determines the amount of compound entering into the polymer/porphyrin matrix, enhancing the tuning of sensitivity.

Similarly, calixarenes had been used as matrix material to help separate out the porphyrin molecules to reduce the porphyrin aggregation through the formation of a more balanced hydrophobic/hydrophilic environment at the air-water interface. The incorporation of

calixarenes has resulted in sensors with higher sensitivity, higher reproducibility and faster response times [59, 60]. The aggregation diminished by addition of calixarene is discussed in chapter 4, section 3.

2.8.3.b Phtalocyanine/porphyrin composites

Phthalocyanine is a coloured aromatic macrocyclic compound that has a similar molecular structure to porphyrin. The most basic phthalocyanine has four more nitrogen atoms than a porphine and it has a benzene ring bonded to each of pyrrole rings at the side opposite to the nitrogen atom. Like porphyrins, they can be modified by attaching different side groups and their central ring position can form coordination complexes with metals.

When porphyrin and phthalocyanine are co-deposited as thin films, they interact with some reducing and oxidising gases and VOCs by absorption onto the sensing layers, and as a result a physical change in the film is produced. The mixture of a metal porphyrin and metal phtalocyanine in a layer for sensory application is appealing because the compound exhibit alterations of optical properties due to their intense colours. The union of macrocycles is attractive because it offers the possibility of obtaining unique variations of the hybrid material by variations of the porphyrin/phtalocyanine molar ratio [61, 62].

The interaction between the two different kinds of molecules produces a variation of the co-ordination ability in the central metal ions towards analytes, and also a different molecular packing in the deposited samples. Consequently, the selectivity of the porphyrin/phtalocyanine composite films is changed to the ones observed with porphyrin or phtalocyanine by themselves [63]. Kladsomboon have tailored the sensitivity of phtalocyanine/porphyrin composites to create an optical electronic nose [64].

2.8.3.c Carbon/porphyrin composites

One of the main problems for the fabrication of chemiresistor and chemFETs using porphyrin as a sensitizer is due to the fact that porphyrins are poor conductors [65]. On the other hand, carbon nanostructures such as nanotubes had been exploited on chemiresistor/chemFET devices because of their excellent conductivity, however the adsorption of gases onto carbon structures is barely selective. On this basis, hybrids of porphyrin and carbon nanostructures had been investigated as a potential sensitizer in the interest of detecting VOCs [66, 67].

The hybrid devices are able to transduce the absorption events occurring in the porphyrin sensory layers into the conductive carbon nanostructures. In other words, the absorption of gases is limited by porphyrin and those events are transduced into resistance changes on the carbon structure layers.

Various authors have fabricated different devices based on hybrid nanostructures/porphyrin materials to demonstrate their potential application towards gas sensing, [68-71]

8.4 Sensing using LEDs as a light source

The necessity of monitoring the environment on-site for health and security has generated new fabrication parameters for the next generation of sensing devices. Reliability, miniaturization, reduction of cost and low power consumption are the main considerations for the design of a portable sensing system. Generally, the core of most optical system consists of a photo emitter and a photo receiver (or detector) which are matched to detect the colorimetric chemistry occurring between the emitter and receiver by absorbance/transmittance measurements. Flaschka built a photometric cell using a light emitting diode as a source of light with the interest of designing a colorimetric sensor [72]. Since then, light emitting diodes (LEDs) have been commonly used as a source of light in similar systems due to their high brightness, lifetime, flexible configuration and extensive spectral range (from 247 to 1550 nm) [73]. Numerous photo receivers can be matched with the LEDs such as photodiodes, photoresistors and phototransistors; leading to an abundant number of optical sensing systems. Chapter 5, section 1 describes different emitter/receiver configurations.

The design flexibility of the optical sensing system consisting of an LED and a photo receiver along with the reduction of cost and size compared to a typical UV-vis spectroscopy system has resulted in many researches to developing many applications ranging from alcohol breath testing machines to the evaluation of freshness of sea food products [74].

The detection of analytes in an optical emitter/receiver device has been studied in conjunction with pH sensitive films [75, 76] or other sensing systems based chromogenic probes [77, 78]. Recently, porphyrins have been used as a sensitizer in a LED/photo-receiver

portable sensing system in order to detect ammonia [79], carbon dioxide[80, 81] and oxygen[82, 83].

References:

1. Liu, X., et al., *A survey on gas sensing technology.* Sensors, 2012. **12**(7): p. 9635-9665.
2. Capone, S., et al., *Solid state gas sensors: state of the art and future activities.* Journal of Optoelectronics and Advanced Materials, 2003. **5**(5): p. 1335-1348.
3. Arshak, K., et al., *A review of gas sensors employed in electronic nose applications.* Sensor Review, 2004. **24**(2): p. 181-198.
4. Awang, Z., *Gas Sensors: A Review.* 2014.
5. Yamazoe, N., *New approaches for improving semiconductor gas sensors.* Sensors and Actuators B: Chemical, 1991. **5**(1): p. 7-19.
6. Fine, G.F., et al., *Metal oxide semi-conductor gas sensors in environmental monitoring.* Sensors, 2010. **10**(6): p. 5469-5502.
7. Derek, R.M., A.A. Sheikh, and A.M. Patricia, *Nanoscale Metal Oxide-Based Heterojunctions for Gas Sensing: A Review.* Sensors and Actuators B: Chemical, 2014.
8. Moseley, P.T., J.O. Norris, and D.E. Williams, *Techniques and mechanisms in gas sensing.* 1991: Adam Hilger.
9. Afzal, A., et al., *Advanced vapor recognition materials for selective and fast responsive surface acoustic wave sensors: A review.* Analytica chimica acta, 2013. **787**: p. 36-49.
10. Figaro Engineering Inc. *Catalytic gas sensor.* 2014 [cited 20/08/2014; Available from: http://www.figaro.co.jp/en/technicalinfo/principle/catalytic-type.html.
11. International Sensor Technology. *Electrochemical sensors.* 2009 20/08/2014]; Available from: http://www.intlsensor.com/pdf/electrochemical.pdf.
12. Taylor, R.F. and J.S. Schultz, *Handbook of chemical and biological sensors.* 2010: CRC Press.
13. Hudson, J.B., *Surface science: an introduction.* 1998: John Wiley & Sons.
14. Langmuir, I., *THE ADSORPTION OF GASES ON PLANE SURFACES OF GLASS, MICA AND PLATINUM.* Journal of the American Chemical Society, 1918. **40**(9): p. 1361-1403.
15. Richardson, T., et al., *Development and optimization of porphyrin gas sensing LB films.* Advances in colloid and interface science, 2005. **116**(1): p. 81-96.
16. Brunauer, S., P.H. Emmett, and E. Teller, *Adsorption of Gases in Multimolecular Layers.* Journal of the American Chemical Society, 1938. **60**(2): p. 309-319.
17. Brunauer, S., *The Adsorption of Gases and Vapours.* 1945, Princeton University Press: Princeton, New Jersey.
18. Allinger, N.L., *Organic Chemistry.* 1971: Worth Publishers, Inc. .
19. Clayden, G., et al., *Organic Chemistry* 2001, Oxford University Press.
20. Willock, D.J., *Appendix 7: The Franck–Condon Principle*, in *Molecular Symmetry*. 2009, John Wiley & Sons, Ltd. p. 339-342.
21. Robinson, W.R., J.D. Odom, and H.F. Holtzclaw, *Chemistry: Concepts and Models.* 1992: DC Heath.
22. O'Leary, *Hybridisation.* 2000, Ireland: University Collage Cork.
23. Goldoni, A., *Porphyrins: fascinating molecules with biological significance.* Elettra highlights, 2002. **2001**: p. 64-65.
24. Milgrom, L., *The colors of life.* 1997, Oxford University Press: New York.
25. Giovannetti, R., *The Use of Spectrophotometry UV-Vis for the Study of Porphyrins.* Macro to Nano Spectroscopy, 2012: p. 978-953.
26. Collman, J., et al., *The Porphyrin Handbook.* The Porphyrin Handbook, 2003. **11**: p. 1-49.
27. D'Urso, A., M.E. Fragalà, and R. Purrello, *From self-assembly to noncovalent synthesis of programmable porphyrins' arrays in aqueous solution.* Chemical Communications, 2012. **48**(66): p. 8165-8176.
28. Berova, N., L. Di Bari, and G. Pescitelli, *Application of electronic circular dichroism in configurational and conformational analysis of organic compounds.* Chemical Society Reviews, 2007. **36**(6): p. 914-931.

29. Di Natale, C., D. Monti, and R. Paolesse, *Chemical sensitivity of porphyrin assemblies.* Materials today, 2010. **13**(7): p. 46-52.

30. Elemans, J.A., et al., *Molecular Materials by Self-Assembly of Porphyrins, Phthalocyanines, and Perylenes.* Advanced Materials, 2006. **18**(10): p. 1251-1266.

31. Di Natale, C., et al., *Electronic-nose modelling and data analysis using a self-organizing map.* Measurement Science and Technology, 1997. **8**(11): p. 1236.

32. Strike, D., M. Meijerink, and M. Koudelka-Hep, *Electronic noses–A mini-review.* Fresenius' journal of analytical chemistry, 1999. **364**(6): p. 499-505.

33. LaGasse, M.K., et al., *Colorimetric sensor arrays: Interplay of geometry, substrate and immobilization.* Sensors and Actuators B: Chemical, 2014. **197**: p. 116-122.

34. Askim, J.R., M. Mahmoudi, and K.S. Suslick, *Optical sensor arrays for chemical sensing: the optoelectronic nose.* Chemical Society Reviews, 2013. **42**(22): p. 8649-8682.

35. Janzen, M.C., et al., *Colorimetric sensor arrays for volatile organic compounds.* Analytical chemistry, 2006. **78**(11): p. 3591-3600.

36. Rakow, N.A., et al., *Molecular recognition and discrimination of amines with a colorimetric array.* Angewandte Chemie International Edition, 2005. **44**(29): p. 4528-4532.

37. Suslick, K.S., N.A. Rakow, and A. Sen, *Colorimetric sensor arrays for molecular recognition.* Tetrahedron, 2004. **60**(49): p. 11133-11138.

38. Kosal, M.E., et al., *A functional zeolite analogue assembled from metalloporphyrins.* Nature materials, 2002. **1**(2): p. 118-121.

39. Rakow, N.A. and K.S. Suslick, *A colorimetric sensor array for odour visualization.* Nature, 2000. **406**(6797): p. 710-713.

40. Tang, Z., et al., *A colorimetric sensor for qualitative discrimination and quantitative detection of volatile amines.* Sensors, 2010. **10**(7): p. 6463-6476.

41. Long, J., et al., *A colorimetric array of metalloporphyrin derivatives for the detection of volatile organic compounds.* Materials Science and Engineering: B, 2011. **176**(16): p. 1271-1276.

42. Jing, L., X. Jianhua, and X. Shuang, *Volatile organic compound colorimetric array based on zinc porphyrin and metalloporphyrin derivatives.* Energy Procedia, 2011. **12**: p. 625-631.

43. Lvova, L., et al., *Detection of alcohols in beverages: An application of porphyrin-based Electronic tongue.* Sensors and Actuators B: Chemical, 2006. **118**(1): p. 439-447.

44. Kladsomboon, S., et al. *Alcohol gas sensors based on magnesium tetraphenyl porphyrins.* in *Nanoelectronics Conference, 2008. INEC 2008. 2nd IEEE International.* 2008: IEEE.

45. Di Natale, C., et al., *Application of a combined artificial olfaction and taste system to the quantification of relevant compounds in red wine.* Sensors and Actuators B: Chemical, 2000. **69**(3): p. 342-347.

46. Kladsomboon, S. and T. Kerdcharoen, *A method for the detection of alcohol vapours based on optical sensing of magnesium 5, 10, 15, 20-tetraphenyl porphyrin thin film by an optical spectrometer and principal component analysis.* Analytica chimica acta, 2012. **757**: p. 75-82.

47. Di Natale, C., et al., *Electronic nose and sensorial analysis: comparison of performances in selected cases.* Sensors and Actuators B: Chemical, 1998. **50**(3): p. 246-252.

48. Di Natale, C., et al., *An electronic nose for food analysis.* Sensors and Actuators B: Chemical, 1997. **44**(1): p. 521-526.

49. Vlasov, Y.G., et al., *«Electronic tongue»—new analytical tool for liquid analysis on the basis of non-specific sensors and methods of pattern recognition.* Sensors and Actuators B: Chemical, 2000. **65**(1): p. 235-236.

50. Di Natale, C., et al., *Multicomponent analysis on polluted waters by means of an electronic tongue.* Sensors and Actuators B: Chemical, 1997. **44**(1): p. 423-428.

51. Grieve, M.B., et al., *An investigation of the optical properties of tetraphenylporphyrin derivatives in Langmuir and Langmuir-Blodgett films.* Thin Solid Films, 1994. **243**(1–2): p. 581-586.

46

52.   Gu, C., et al., *The design and characteristics of a porphyrin LB film ChemFET gas sensor.* Thin Solid Films, 1996. **284–285**(0): p. 863-865.

53.   Giancane, G. and L. Valli, *State of art in porphyrin Langmuir–Blodgett films as chemical sensors.* Advances in colloid and interface science, 2012. **171**: p. 17-35.

54.   Di Natale, C., et al., *Investigation of quartz microbalance and ChemFET transduction of molecular recognition events in a metalloporphyrin film.* Sensors and Actuators B: Chemical, 2009. **135**(2): p. 560-567.

55.   Seol, M.-L., et al., *Porphyrin–Silicon Hybrid Field-Effect Transistor with Individually Addressable Top-gate Structure.* ACS Nano, 2011. **6**(1): p. 183-189.

56.   Takulapalli, B.R., et al., *Electrical Detection of Amine Ligation to a Metalloporphyrin via a Hybrid SOI-MOSFET.* Journal of the American Chemical Society, 2008. **130**(7): p. 2226-2233.

57.   Dini, F., et al., *Polymer matrices effects on the sensitivity and the selectivity of optical chemical sensors.* Sensors and Actuators B: Chemical, 2011. **154**(2): p. 220-225.

58.   Itagaki, Y., et al., *Toxic gas detection using porphyrin dispersed polymer composites.* Sensors and Actuators B: Chemical, 2005. **108**(1): p. 393-397.

59.   Roales, J., et al., *Optimization of mixed Langmuir–Blodgett films of a water insoluble porphyrin in a calixarene matrix for optical gas sensing.* Thin Solid Films, 2011. **519**(6): p. 2025-2030.

60.   Brittle, S.A., et al., *Amine-sensing properties of a covalently linked calix [4] arene–porphyrin (" calixporph") multilayered film.* Journal of Porphyrins and Phthalocyanines, 2010. **14**(12): p. 1027-1033.

61.   Tonezzer, M., et al., *Optical sensing responses of tetraphenyl porphyrins toward alcohol vapours: A comparison between vacuum evaporated and spin-coated thin films.* Sensors and Actuators B: Chemical, 2007. **122**(2): p. 620-626.

62.   Spadavecchia, J., et al., *Spin-coated thin films of metal porphyrin–phthalocyanine blend for an optochemical sensor of alcohol vapours.* Sensors and Actuators B: Chemical, 2004. **100**(1): p. 88-93.

63.   Mensing, J.P., et al., *Inkjet-printed sol–gel films containing metal phthalocyanines/porphyrins for opto-electronic nose applications.* Sensors and Actuators B: Chemical, 2013. **176**: p. 428-436.

64.   Kladsomboon, S., S. Pratontep, and T. Kerdcharoen. *Optical electronic nose based on porphyrin and phthalocyanine thin films*. in *Electrical Engineering/Electronics Computer Telecommunications and Information Technology (ECTI-CON), 2010 International Conference on*. 2010: IEEE.

65.   Kaya, E.N., et al., *Effect of pyrene substitution on the formation and sensor properties of phthalocyanine-single walled carbon nanotube hybrids.* Sensors and Actuators B: Chemical, 2014. **199**: p. 277-283.

66.   Conoci, S., et al., *Langmuir–Shäfer Transfer of Fullerenes and Porphyrins: Formation, Deposition, and Application of Versatile Films.* Chemistry-A European Journal, 2004. **10**(24): p. 6523-6530.

67.   Andersson, M., et al., *Development of a ChemFET sensor with molecular films of porphyrins as sensitive layer.* Sensors and Actuators B: Chemical, 2001. **77**(1): p. 567-571.

68.   Penza, M., et al., *Carbon nanotube films as a platform to transduce molecular recognition events in metalloporphyrins.* Nanotechnology, 2011. **22**(12): p. 125502.

69.   Sarkar, T., et al., *Single-Walled Carbon Nanotube-Poly (Porphyrin) Hybrid for Volatile Organic Compounds Detection.* The Journal of Physical Chemistry C, 2013.

70.   Shirsat, M.D., et al., *Porphyrin-functionalized single-walled carbon nanotube chemiresistive sensor arrays for VOCs.* The Journal of Physical Chemistry C, 2012. **116**(5): p. 3845-3850.

71.   Llobet, E., *Gas sensors using carbon nanomaterials: A review.* Sensors and Actuators B: Chemical, 2013. **179**: p. 32-45.

72.   Flaschka, H., C. McKeithan, and R. Barnes, *Light emitting diodes and phototransistors in photometric modules.* Analytical Letters, 1973. **6**(7): p. 585-594.

73. O'Toole, M. and D. Diamond, *Absorbance based light emitting diode optical sensors and sensing devices.* Sensors, 2008. **8**(4): p. 2453-2479.

74. Pacquit, A., et al., *Development of a volatile amine sensor for the monitoring of fish spoilage.* Talanta, 2006. **69**(2): p. 515-520.

75. Lau, K.T., et al., *Novel fused-LEDs devices as optical sensors for colorimetric analysis.* Talanta, 2004. **63**(1): p. 167-173.

76. Orpen, D., et al., *The optimisation of a paired emitter–detector diode optical pH sensing device.* Sensors and Actuators B: Chemical, 2011. **153**(1): p. 182-187.

77. Moragues, M.E., et al., *An optoelectronic sensing device for CO detection in air based on a binuclear rhodium complex.* Sensors and Actuators B: Chemical, 2014. **191**: p. 257-263.

78. Capitán-Vallvey, L.F. and A.J. Palma, *Recent developments in handheld and portable optosensing—A review.* Analytica chimica acta, 2011. **696**(1): p. 27-46.

79. Zilberman, Y., Y. Chen, and S.R. Sonkusale, *Dissolved ammonia sensing in complex mixtures using metalloporphyrin-based optoelectronic sensor and spectroscopic detection.* Sensors and Actuators B: Chemical, 2014. **202**: p. 976-983.

80. de Vargas-Sansalvador, I., et al., *A new light emitting diode–light emitting diode portable carbon dioxide gas sensor based on an interchangeable membrane system for industrial applications.* Analytica chimica acta, 2011. **699**(2): p. 216-222.

81. Carvajal, M., et al., *Hand-held optical instrument for CO< sub> 2</sub> in gas phase based on sensing film coating optoelectronic elements.* Sensors and Actuators B: Chemical, 2010. **144**(1): p. 232-238.

82. de Vargas-Sansalvador, I.P., et al., *LED–LED portable oxygen gas sensor.* Analytical and bioanalytical chemistry, 2012. **404**(10): p. 2851-2858.

83. Chu, C.-S. and T.-H. Lin, *A new portable optical sensor for dual sensing of temperature and oxygen.* Sensors and Actuators B: Chemical, 2014.

Chapter 3

Experimental techniques

3.1 Monolayers

3.1.1 Historical background

The study of phenomena related with the formation of floating monolayers in the air-water interface using scientific methods was carried out for the first time by the American politician Benjamin Franklin (1706-1790) [1]. This encouraged other scientists to investigate the field in a deeper way. John Shields (1822-1890) observed how oil spread out on the sea water calms its waves, a convenient fact in the sea when rough weather conditions are present [2].

Lord Rayleigh (1842-1919) observed the reduction in the surface pressure of water when spreading a thin layer of fat or insoluble oil on the water surface, by measuring the surface area of the thin film he estimated a thickness for the films between 10 and 20 Å [3].

Direct measurement of the thickness of the molecular monolayers were performed by Agnes Pockels (1862-1936)., to archive it, she set up a simple device which would be the predecessor of the Langmuir trough [4], subsequently built by I. Langmuir [5]. Using her equipment she obtained the first surface pressure-area isotherms (π-A).

After the experiments made by Rayleigh, the research activity in the field of the monolayers increased significantly, as it happened with the design and construction of devices to measure the thicknesses of various films [6] or in the study of the behaviour of nonpolar oils. Irving Langmuir (1881-1957) stood out for his work in surface chemistry, which led to him winning the Nobel Prize in Chemistry in 1932. His studies [7] along with Rayleigh's hypothesis [8] allowed him to confirm that certain molecules spontaneously orientate themselves at the gas-liquid interface. He concluded that these molecules self-assemble into a monolayer oriented on the surface with the polar group immersed in the water and the long non polar chain vertically positioned (perpendicular to the water surface). His experiments support the hypothesis of the existence of molecular interactions and provided the basis of our understanding of how molecules form homogeneous thin layers.

Katherine Blodgett (1898-1979), under the direction of I. Langmuir, was the first person who transferred fatty acids from an air-water interface to hydrophilic solid substrates [9], forming the first Langmuir-Blodgett (LB) films. In 1938, Vincent Schaefer and Langmuir reported a modification of the traditional LB method, where the sample plate was not deposited into the trough vertically but in an almost perfectly horizontal fashion[10]. From then until now, the LB and LS techniques are considered as very useful tools to build molecular devices with many applications in different areas such as a non-linear optics, sensors and molecular electronics [11, 12].

3.1.2 Amphiphiles

Roughly speaking, molecules can be divided in two categories: those that are soluble in water and those that are not. Polar molecules have uneven distribution of charge within the molecule and are soluble in water. This is because water is a polar molecule: the electron withdrawing tendency of the oxygen atom leads to an overall net negative charge over the oxygen atom and a positive charge on the two hydrogen atoms. As a result there is an asymmetric charge distribution which is quantified by a dipole moment.

δ^+

H

$2\delta^-$ O

H

δ^+

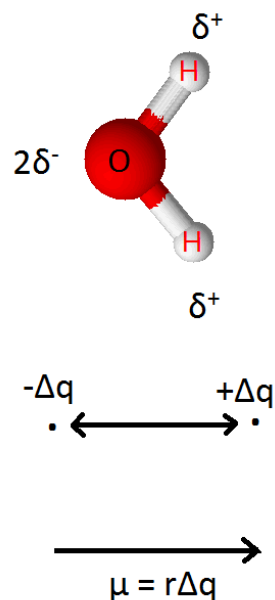$-\Delta q$ $+\Delta q$

$\mu = r\Delta q$

Figure 3.1: The polarity of water: the partial charges on the atoms within the molecule.

The overall neutral water molecule has two regions corresponding to the negative and positive charges, $\pm\Delta q$, separated by a distance r. The dipole moment is given by:

$$\mu = \Delta q \cdot r \qquad\qquad \text{Eq. 3.1}$$

A hydrophilic molecule is defined as a polar molecule with non-zero dipole moments that is attracted to the water and therefore soluble in water. On the other hand, non-polar molecules that do not dissolve in water are hydrophobic molecules. When added to water they are immiscible and assuming they are less dense than water they float on the surface.

A third classification of molecules are those typically used to form a monolayers which have both hydrophilic and hydrophobic characteristics. A typical monolayer molecule will have a tail which is hydrophobic and a head group that possesses a dipole moment which is hydrophilic. These kinds of molecules that have both hydrophobic and hydrophilic properties are called amphiphiles. The balance between the hydrophobicity and hydrophilicity will cause the molecule to orientate itself in a direction on the water surface.
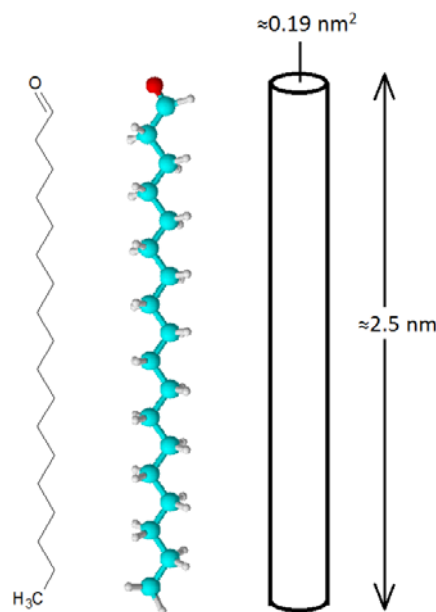

Figure 3.2: The stearic acid molecule (C17H35COOH) and approximate size and shape.

A common amphiphile is stearic acid, represented in figure 3.2. This fatty acid has a polar carboxylic acid group and a long hydrocarbon chain at one end. If the acid group was stronger or the chain shorter, the molecule would dissolve in water.

3.1.3 Formation and study of monolayers in the air-water interface

The formation of monolayers on the air-water interface is based on the insolubility of the molecules that form the layers, and above all, their amphiphilic properties. That is to say, they must possess a hydrophilic part (e.g. an alcohol, acid or amine like functional group) and a hydrophobic part (with one or two aliphatic chains) [13]. Using the Langmuir technique, as depicted in figure 3.3, the preparation of thin films is carried out by adding a certain quantity of amphiphilic molecules dissolved in a volatile solvent which is itself immiscible in water and therefore spreads all over the water surface, occupying the entire available surface. The selection of the solvent or mixture of solvents is important, because it must favour the maximum dispersion of the dissolved molecules on the water [14]. The volatile solvent must have a high volatility, so it could be easily evaporated at room temperatures. Once the solvent has evaporated, the molecules in the monolayer will lie on the surface with their polar groups immersed in the water and the hydrophobic chains outside it. This is the most favourable energetic situation for the system [15]. At this moment, the surface tension (γ) of the area covered by the monolayer is reduced with respect to surface tension of the clean water surface (γ_0). The surface pressure (**π**) is defined as the measure of this reduction.

$$\Pi = \gamma_{0-}\gamma \qquad\qquad \text{Eq. 3.2}$$
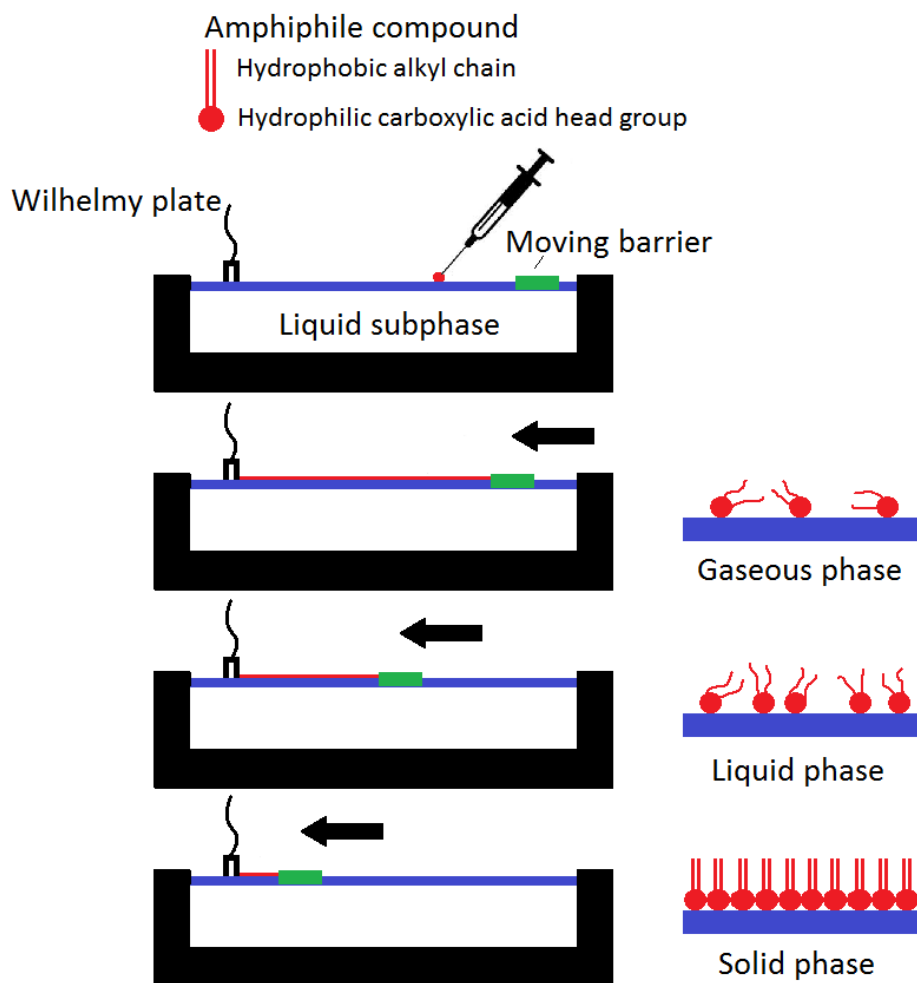
Figure 3.3: Steps for the preparation of a Langmuir monolayer.

In principle, any method that determines the surface tension can be used to measure the surface pressure. In practice, two systems are widely used: the Langmuir [5] and the Wilhemy [16, 17] types. After the evaporation of the solvent, the monolayer is compressed by moving the barrier, reducing the available surface area and increasing the surface density of molecules. This causes a reduction in γ and an increase in π. The representation of the surface pressure versus the area per molecule (A) on the water surface is a two dimensional analogy of a pressure-volume isotherm, and is referred to as the surface pressure – area isotherm or π-A isotherm for short.

3.1.4 π-A Isotherms

A surface pressure-area (π-A) isotherm is a continual measurement of the surface pressure with changing monolayer confinement area. π-A isotherms give information about the stability of the monolayer on the air-water interface, the organization of the molecules and the interaction between them.

Figure 3.4 shows the isotherms of two compounds and the transitions exhibited as the surface pressure rises. Isotherms of fatty acids such as stearic acid, have been studied extensively because the phases are well defined. Other molecules such as phospholipids have a more complicated π-A isotherms with more than three phases and orientational conformations. The phase behaviour of the monolayer is mainly determined by the chemical and physical properties of the amphiphile, the subphase composition and the subphase temperature.

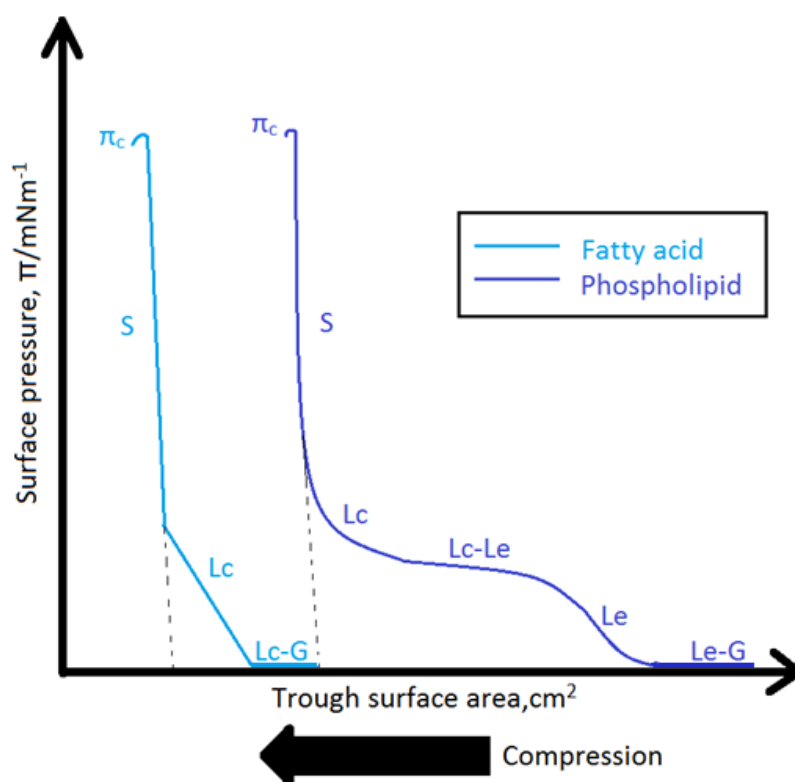**Figure 3.4: Two typical π-A isotherms. The dark blue line is an isotherm of a phospholipid with two hydrocarbon chains and the pale blue line is an isotherm of a fatty acid with a single hydrocarbon chain.**

Two important parameters can be extracted from the π-A isotherms: the value of the lower limit of the area per molecule which is obtained by extrapolating the last stretch of the

isotherm to the x-axis. This corresponds to the minimum occupied area per molecule in a situation of maximum packaging (discontinuous lines in figure 3.4); and the maximum surface pressure in which the monolayer loses its stability and uniformity, also known as collapse surface pressure (π_c in figure 3.4).

The π-A isotherms show different regions that corresponds to different phases and states of organization of the monolayer, as well as the regions in which two phases coexist [15]. In figure 3.4, the different phases are ideally represented. The phases can be described as follows:

Gaseous (G): At very low surface pressures, the molecules are far away from each other's, and its interaction between them are weak. At this point, collisions are rare, just like molecules in a gas, building a two dimensional gas phase.

Liquid: When the surface pressure increases, a compressible fluid phase is reached, in which the molecules experiment attractive forces that makes them adopt a compact structure, forming a liquid expanded (Le) phase.

Between the two described phases a similar process to condensation of a gas takes place, i.e. a region in which both phases coexist: Le-G. In there, the surface pressure is constant, which is consistent with the transaction from the gaseous phase to the liquid expanded phase [18, 19].

Further pressure increase results in a less compressible and more ordered phase, also known as liquid condensed (Lc). Here, the organization of the monolayer is compact and the hydrophobic part of the molecule orient perpendicular to the interface. Once again, a transition is presented between two phases, Le-Lc. First order transitions between phases should appear as constant pressure areas in the π-A isotherms. Transitions between the G phase and the Lc, Le or S phases appear to show constant surface pressure. This last state can only be observed only for the phospholipid due to its more branched structure (it has two hydrophobic tails).

Solid (S): When the monolayer is further compressed and before collapsing, the films enters the solid state (S), in which the film is rigid and the hydrophobic chains forms a compact stacking.

The number and the complexity of the phases observed in an isotherm vary depending of the system. The morphology of the coexistence of two phases in a monolayer can be visualized using Brewster Angle Microscope (BAM) [20].

3.2 Langmuir Blodgett film deposition

3.2.1 LB film deposition

Langmuir and Blodgett developed a technique named after them (Langmuir-Blodgett deposition) with the objective of building and manipulating molecular thin films prepared on the air-water interface [5, 9]. However, the possibility of building a complex self-assembled system in a controlled manner was first conducted in the sixties, mostly due to Kuhn's work [21].

This field has experienced a quick development in the past 40 years. Many papers and international conferences about Langmuir-Blodgett films provide easy access to the most recent literature.

The LB deposition technique is a transfer mechanism in which a solid substrate is passed vertically through a floating monolayer. Figure 3.5 describes the Langmuir-Blodgett deposition process. During the transfer the moving barrier reduces the area so the loss of molecules is compensated and a constant surface pressure is maintained (feed-back mechanism); the thickness, homogeneity and density properties of the monolayers are therefore preserved during the transfer of the Langmuir film from the subphase surface to the substrate.
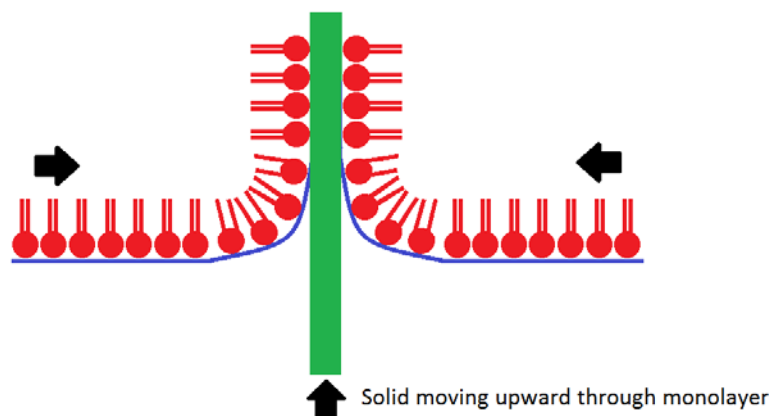

Solid moving upward through monolayer

Figure 3.5: The Langmuir-Blodgett deposition process.

3.2.2 LB deposition forms (X, Y and Z)

Multilayers can be produced by allowing the surface pressure to stabilize and repeating the deposition procedure. There are three types of LB deposition (figure 3.6) depending on a number of factors, namely the nature of the molecule, the type of substrate and the deposition pressure. The most common type is the Y type whereby the transfer from the subphase to the substrate occurs during both downward and upward strokes. Other types of deposition are more difficult to archive, and therefore, less common.
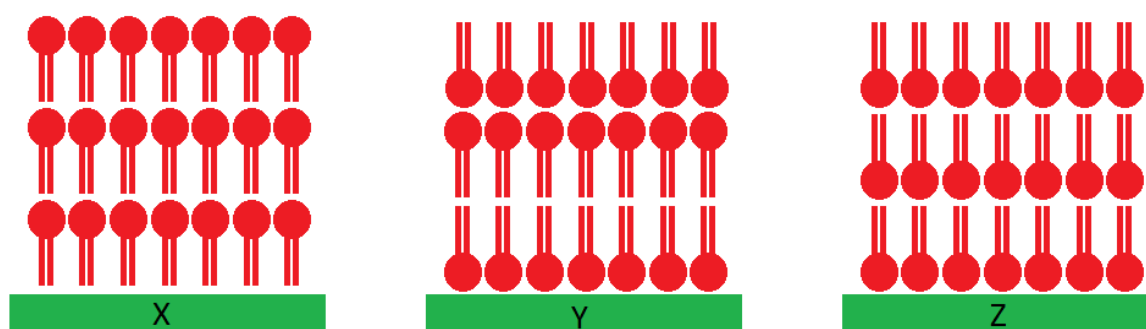
Figure 3.6: Structures of X, Y and Z multilayers.

If a monolayer is only applied to the substrate in the upward motion of the hydrophobic substrate repeatedly this is called Z type deposition. In this case, the layers are applied with tails up. Likewise if the monolayer is only applied during downward motion of the substrate, X type deposition is observed, and layers are applied with tails down [22].

3.2.3 Langmuir-Schaefer (LS) deposition

The LS deposition technique was developed by Vincent Schaefer and Irving Langmuir [10]. During their work on protein monolayers they found out it was advantageous to change the angle of the substrate that makes contact with the monolayer [23]. The LS deposition technique is very similar to LB deposition, but uses a substrate orientated parallel to the subphase surface.

Figure 3.7: Illustration of the Langmuir-Schaefer deposition

The deposition technique can be performed as shown in figure 3.7 the substrate is dipped horizontally and no additional depth is required below the monolayer.

3.2.4 Transfer ratios

The effectiveness of using the LS or LB deposition techniques for a particular substrate and material can be quantified by the calculation of transfer ratio. The transfer ratio measures the reduction in the area of the floating monolayer af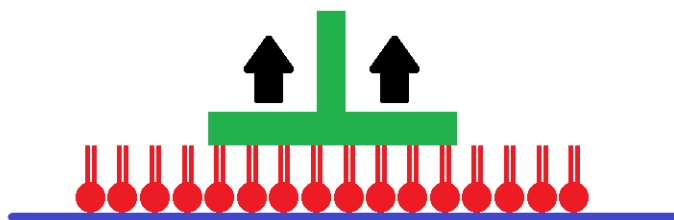ter each deposition cycle. Once again, the surface pressure must be maintained at a constant value during this process via feedback mechanism.

The change in the area of the floating monolayer is compared with the surface area of the part of the substrate exposed to the monolayer and the transfer ration is given by:

$$\pi = \frac{A_L}{A_S}$$
Eq. 3.3

Where π is the transfer ratio, A_L is the change in area of monolayer during deposition and A_S is the area of substrate passed through the air-water interface. A value of 1 for π indicates a perfect uniform transfer with no change in film structure during deposition. In practice transfer ratios of less than one indicate incomplete substrate coverage, whereas ratios greater than one indicate different processes such as dissolution into the subphase, monolayer collapse, molecular reordering or pronounced absorption of the monolayer on barrier surfaces [24].

3.2.5 Deposition Speed

Traditional LB and LS applications require a regular arrangement of the molecules across the substrate and a very high level of homogeneity in the layers. Therefore, conventional slow

deposition speeds must be used; otherwise structural defects in the sample will reduce their effectiveness and sensitivity. A slow deposition speed for porphyrin materials varies from approximately 2 to 20 mm min^{-1}.

In the case of toxic gas sensing applications however a high level of homogeneity resulting in densely packed domains may be unfavourable for the gas sensing capabilities. By definition, a densely packed homogeneous layer will have more active binding sites per layer, but the accessibility to each of these sensing molecules below the outer layer will be limited by diffusion through this dense layer.

The ultra-fast technique has been used to create non homogenous and irregular films, showing benefits in terms of gas sensing properties due to rougher, larger surfaces and their associated large surface areas [25]. In order to maximise binding site accessibility below the outer layer a "bed of nails" rather than a "bed of blankets" is required (as depicted in figure 3.8) [26].

In the top of figure 3.8 a structure made of homogeneous layers is described. The diffusion of the molecules entering into the layers will depend on the amount of layers deposited on the substrate. On the contrary, the bottom of figure 3.8 describes a non-uniform deposition of material, which ease the access to lower binding sites.

Another evident advantage of the ultra-fast LB deposition is the vast reduction in time required for monolayer formation.
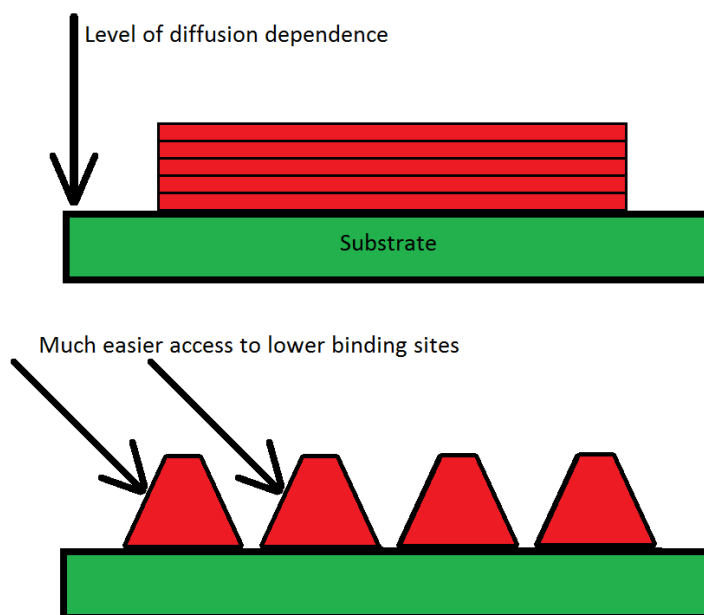
Figure 3.8: The benefit of inhomogeneity to binding site access [26].

3.2.6 Substrates

When choosing a substrate for deposition of an LB film, the application of the film must be considered. Silicon substrates are produced with flatness down to the nanoscale, ideal for deposition of nanoscale monolayers like porphyrins and other organic materials. Glass substrates are rougher than silicon and not used to study the high order of monolayers, however, they have the benefit of transparency and are used when measuring the optical properties of the deposited films.

In this work, two types of substrate treatments have been applied to both silicon and glass. An hydrophobic surface was created when the substrate were treated with 1,1,1-3-3-3 hexamethyldisilazane (HMDS). When the substrate is placed in an oxygen plasma cleaner, the plasma breaks most organic bonds of surface contaminants, removing impurities that were once on the surface. This results in a clean surface which is highly hydrophilic. Note that exposure to air in the lab will reduce this hydrophilicity over a few hours due to the adsorption of airborne volatile organic material.

The substrate treatments do not affect the reflectivity or transparency of the substrates, but permits the monolayer materials to adhere more strongly to them.

60

3.3 Langmuir Trough

The most important element of the equipment in the formation of monolayers is the Langmuir-Blodgett trough, which allows us to hold the subphase. The requirements of a trough material for film deposition or monolayer studies are: it should be hydrophobic to enable easy cleaning, the material must be inert, it must not release impurities into the subphase, and finally, it should withstand inorganic acids and organic solvents [27].

3.3.1 Single barrier compression

A moving barrier is used to compresses the monolayer. When the barrier moves from one end of the trough to the other, the area of the monolayer is reduced. The barrier movement is controlled by an electric motor which in turn is controlled by a feedback system. The feedback systems generally consists of an interface unit and a computer. The interface unit is a transducer that reads the surface pressure and the position of the barrier, and also controls the motor that moves the barrier and the motor that moves the substrate for the deposition. The computer analyse the parameters and evaluates the conditions, so when the iteration is complete, it sends the signals to the interface unit in order to move the barrier to a new position so as to maintain either the surface pressure, barrier speed or barrier position at a constant value depending upon the experiment defined in the software settings .
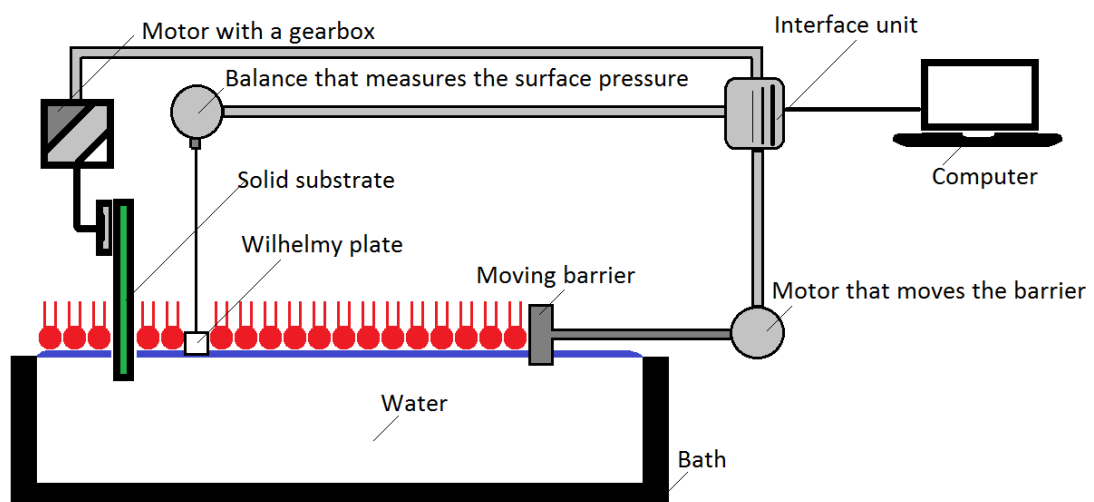

Figure 3.9: Simple LB trough with a single movable barrier.

The computer software allows the user to control parameters such as the target pressure, speed of the barrier and deposition speed. The software also records the position of the barrier and the target pressure, enabling the π-A isotherms to be saved in a digital file.

3.3.2 The surface pressure sensor

A strip of filter paper of fixed width is submerged slightly into the subphase and suspended by a thread which is connected to a micro-balance that measures any change in the force acting on the filter paper enabling the surface tension to be determined. This sensor is called a Wilhelmy plate, and is named after the scientist that who applied the method in a device to measure the surface tension [28].

The Wilhelmy pressure sensor measures the surface tension by determining the changes in the forces it experiences. The forces acting on the plate are: the surface tension of the subphase, the upthrust of the plate due to its buoyancy in water and the weight of the plate due to gravity.
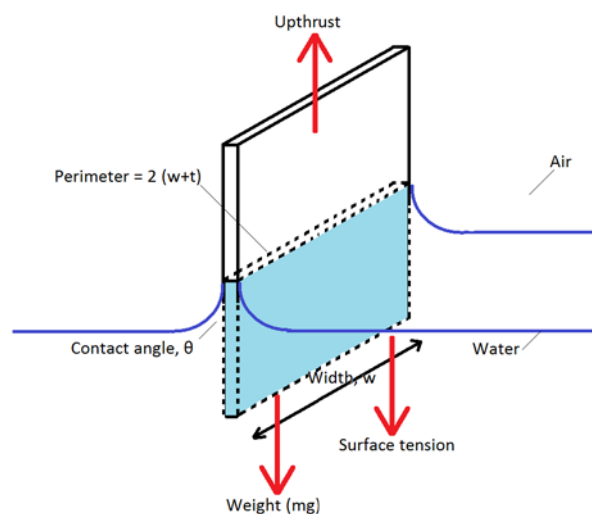
Figure 3.10: Wilhelmy plate for measuring surface tension.

If a plate has dimensions h x t x w then the net force acting on the plate is given by:

$$Force = mg + 2(w + t)\gamma cos\theta - buoyancy \qquad \text{Eq. 3.4}$$

Where m is the mass of filter paper, g is the acceleration of gravity and γ is the surface tension. Because the filter paper is completely wetted by the liquid, a meniscus will form where it passes through the liquid surface, giving a contact angle of zero. Hence, the term

62

including the $cos\theta$ in eq. 3.4 becomes unity. The perimeter of the plate can be given as $2\,w$ because the thickness is very small. Therefore, the equation can be simplified as:

$$Force = mg + 2w\gamma - buoyancy \qquad \text{Eq. 3.5}$$

The changes in these forces are required to measure a change in surface tension.

$$Force = 2w\Delta\gamma \qquad \text{Eq. 3.6}$$

By definition, the reduction in the surface tension (γ) after the material has been deposited onto the surface is the surface pressure (Π). The surface tension observed during the compression of a deposited monolayer is compared to the surface tension of ultra-pure water (approximately 72 mNm^{-1} at 25°C). Therefore:

$$\Pi = \gamma_{Water} - \gamma_{Material} = -\Delta\gamma \qquad \text{Eq. 3.7}$$

Now, arranging to express the surface pressure:

$$\Pi = \Delta\gamma = \frac{\Delta Force}{2w} \qquad \text{Eq. 3.8}$$

The width of the Wilhelmy plate is a known parameter, so the surface pressure can be estimated.

3.4 Clean room protocol

The clean room is a space used in scientific research in order to avoid the problems with unpredictable airflows and pollutant dust particles. When carrying out measurements or preparing Langmuir Blodgett films which are a single molecule thick it is obviously essential to keep the working environment as free from any dirt, microbes, chemical vapours and any dust that may contaminate the sample and create inaccurate results as possible.

3.4.1 General cleaning

All the elaborate samples created with a Langmuir trough were made in a clean room. A two door system and internal air overpressure in the clean room ensures that no dust enters into the cleanroom. To enter the clean room, the user must close the first door before opening the second (in which the equipment is placed). Between the two doors special dust free lab clothing is kept, including hair restrains, coats, soft over boots and glasses.

Samples of porphyrin in this research often arrive from the synthesis labs in powder form, so the glassware must be kept exceptionally clean in order to make porphyrin solutions and reduce the risk of any cross contamination. Three solvents are used to clean the glassware: water, chloroform and isopropyl alcohol (IPA). Each solvent is rinsed in each solvent it collects by dissolving some dirt from the lab utensils. Each solvent is soluble in the preceding solvent, e.g. a small amount of chloroform left in the glassware after cleaning is collected by IPA, and likewise, the IPA leftovers are collected by water. Once the solvents are used in this order, the cleaning process is repeated in reverse: water, then IPA and finally chloroform.

3.4.2 Surface cleanliness

To produce a monolayer with no contaminants the subphase must be extremely clean.

Ultra –pure water is always used during the process. Tap water contains ions from the pipes ($Fe2+$, $Cu+$), soil ($Na+$, $Ca2+$) and other sources. So, ultra-pure water is used during the process. When the ultra-pure water is poured into the trough there are three objects need to be cleaned so the subphase does not collect pollutants as it enters. Firstly, the barrier and the trough must be wiped with a dust free lab towel using chloroform, IPA and water. The Wilhelmy plate is rinsed in chloroform and dried before submerging it. Secondly, the large glass flask used to pour water in the trough must also be cleaned using the three solvents described previously. And finally, once the water is poured, the subphase in the trough must be cleaned by a lab vacuum device in order to ensure that it is completely clean.

In this last procedure, it is convenient to set the barrier to its minimum confinement area (closed barrier position) so the cleaning area is minimum and easier to clean. A pipette is set at the end of the vacuum system to provide a finer water and air suction. The pipette should be carefully moved all over the confinement surface area of the future monolayer.

To verify the cleanliness of the surface, the barrier must move to its open position once the zero reference in the Wilhelmy sensor has been taken. The sensor must measure a surface pressure of no more than ± 0.1 mNm^{-1} whilst the barrier moves from fully open to fully closed, otherwise this indicates that the surface is not clean and the cleaning procedure must be repeated.

3.4.3 Monolayer spreading

The dilute solution of porphyrin (or other molecule to be spread) is applied drop by drop to the water surface using a micro syringe. The tip of the syringe needle must be placed as close to the water surface as possible, so that each drop of the solution does not gather enough momentum to fall straight through the subphase and lie on the bottom of trough [29]. Chloroform (the typical solvent used) is denser than water, but will spread suspended a water surface due to the high surface tension of water, if applied delicately.

Precise measurements are needed to control the amount of material added to the surface. Calculations of area per molecule during monolayer compression can be done if the constituents, amount and concentration of the solution is known.

The number of moles in a monolayer is given by the volume (V) of the solution added to the subphase surface, the concentration (C) of the material in solution (solvent and monolayer material) and the molar mass (M) of the material used.

$$Number\ of\ moles = \frac{C \cdot V}{M}$$
<div align="right">Eq. 3.9</div>

As the solution of organic material is applied to the surface, the solvent evaporates leaving only the solute material. A time of 20 minutes must be allowed to ensure the complete evaporation of the solvent, so the solvent is no longer present in the film during compression.

3.4.4 Porphyrin as monolayers

Porphyrins have an intense colour due to their conjugated π-electron system. The structure and properties of porphyrin is described in section 2.7.2. With the addition of hydrophilic functional groups the porphyrin becomes an amphiphilic molecule which can be transferred in LB films[30].

That characteristic along with the intense colour due to its conjugated π-electron system makes porphyrin LB films a great material for gas sensing applications.

3.5 Analytical techniques

The properties of the thin films must be analysed once they have been deposited into the substrate. The stability and durability of most organic thin films is finite, so the measurements were been carried out shortly after the sample has been produced in order to remain consistent.

3.5.1 Ultraviolet visible spectroscopy (UV-Visible)

Molecular spectroscopy can be defined as the study of the interaction of matter and electromagnetic waves. Spectroscopy is an indispensable field without which characterisation of materials would be very cumbersome. General energy level structure can be determined in the energy range corresponding to UV, Visible and IR light by the usage of a suitable light source and spectral apparatus for radiation analysis.

3.5.1a UV-visible spectroscopy theory

Most organic molecules and functional groups absorb in particular parts of the electromagnetic spectrum. Porphyrins are conjugated systems which have electronic levels which allow transitions involving lone pairs and π orbitals and therefore absorb strongly in the ultraviolet (UV) and visible (VIS) regions, whose wavelengths range from 190 nm to 800 nm. If continuous electromagnetic radiation is passed through a material, some of the radiation might be absorbed. As a result of energy absorption, molecules, atoms or electrons are promoted from a low energy state (ground state) to a higher energy level (excited state). Therefore UV-visible spectroscopy is useful for identifying the energies at which these transitions can occur.

The lowest energy transition occurs between the lowest unoccupied molecular orbital (LUMO) and the highest occupied molecular orbital (HOMO) in the ground state. The difference in energy between the LUMO and HOMO will determines the minimum absorption energy of the system. The relationship between an electronic structure and a molecular absorption can be explained by the energy of the electronic states.

The electronic absorption spectrum of a typical regular porphyrin consists of several $\pi-\pi^*$ absorption bands. Two weak transitions to the first excited singlet state ($S_0 \rightarrow S_1$) occur

66

in the region 500-600 nm corresponding to the Q bands. The lowest-energy transition is attributed to the lowest singlet excited state and is denoted by Q (0,0).

A strong transition to the second excited state ($S_0 \rightarrow S_2$) occurs in the region of ~ 420 nm (corresponding to the Soret band) and is denoted by B(0,0). Internal conversion from S_2 to S_1 is rapid so fluorescence is only detected from the ($S_1 \rightarrow S_0$) relaxation process. Theoretical analysis of the Soret and Q bands has shown that they arise from $\pi-\pi^*$ transitions and can be explained by considering the four frontier orbitals using Gouterman's four orbital model (described in section 2.7.3.1). The model describes the absorbance features in the UV-vis spectrum and explains that whilst higher energy transitions may occur, they are not of interest for gas sensing applications as they are not commonly observed for their high energy.

3.5.1b Beer-Lambert Law

Two laws have been developed about absorption of radiation by a material: Lambert's law shows that the fractional absorbance of light is independent of the total amount of light passing through the sample and Beer's law states that the absorption is proportional to the number of absorbing molecules. These two laws are combined into the Beer-Lambert law which calculates the absorbance of a material.

As light passes through a sample its intensity decreases in a manner described by:

$$\frac{dI}{dx} = -\alpha I$$

Eq. 3.10

Where I is the intensity and $\frac{dI}{dx}$ is the decrease in the light that passes through a sample of thickness dx, and α is the absorption coefficient of the material. Experimental measurements usually involve the amount of transmitted radiation, which estimate the fractional amount of light remaining after the original light source has passed through the sample. The transmittance (T) is defined as:

$$T = \frac{I}{I_0}$$

Eq. 3.11

Where I is the intensity of the light after it passes through the sample medium and I_0 is the intensity of the light before it passes through the reference medium.

The integration of equation 3.9 gives the transmittance in terms of the absorbance coefficient:

$$T = \frac{I}{I_0} = e^{-\alpha x}$$

Eq. 3.12

To get the Beer-Lambert equation, the equation must be naturally logged to obtain:

$$ln\left(\frac{I}{I_0}\right) = -\alpha cl$$

Eq. 3.13

Where c is the concentration of the adsorbing species and l is the path length of light passing through the sample.

Notice that the relationship between the transmittance and the absorbance (A) is logarithmic:

$$A = -log_{10}(T) = -log_{10}\left(\frac{I}{I_0}\right)$$

Eq. 3.14

Equation 3.13 and equation 3.14 can be directly compared, so that two logarithmic equations are equal to sets of constants:

$$A = -log_{10}\left(\frac{I}{I_0}\right); \quad -ln\left(\frac{I}{I_0}\right) = \epsilon cl$$

Eq. 3.15

To convert between natural log base and log base 10 the factor 2.303 is used, and the Beer-Lambert can now be expressed as:

$$A = \epsilon cl$$

Eq. 3.16

Where ϵ is the molar extinction coefficient, an intrinsic property that describes how strongly the material absorbs radiation at a given wavelength. The Beer-Lambert equation is relevant because it relates in a proportional way the absorbance of a material with the concentration of the absorbed molecule and the path length.

Figure 3.11 shows the processes that affect light as it passes through an optical filter and includes transmittance reducing processes such as absorption, scattering and surface reflectance.
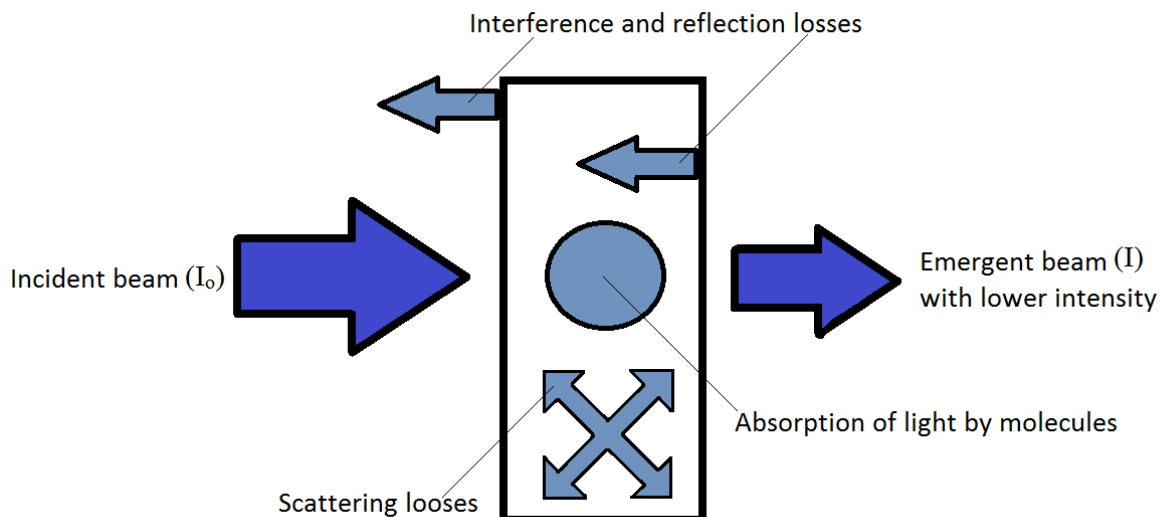
Figure 3.11: As the light passes through the optical filter, the incident light is reduced in intensity due to reflection, absorption, scattering and interference of light.

The other optical processes apart from absorption are removed from experimental analysis by taking a suitable initial reference.

3.5.1c UV-Visible: Experimental

In this research, the optical absorbance measurements of solid samples were made using an ocean optics USB2000 miniature fibre optic spectrophotometer which incorporates a multichannel photodiode detector and a miniature deuterium tungsten halogen source.

Figure 3.12: The spectroscopy apparatus. Left: Light source, right: spectrometer.

The intensity of light is converted to absorbance and the spectra may be observed in real-time through a computer using the Ocean Optics software. One of the features of the system is that it can plot the kinetics of the absorbance at selected wavelengths. Usually, the measurements taken were in film and solution form.

The light source takes time to heat up and provide a stable light source. Figure 3.13 shows the change in output intensity of different wavelengths once the bulb has been turned on. It has been concluded that one hour (marked as a black arrow in figure) is sufficient time to allow the light source to provide a steady signal.
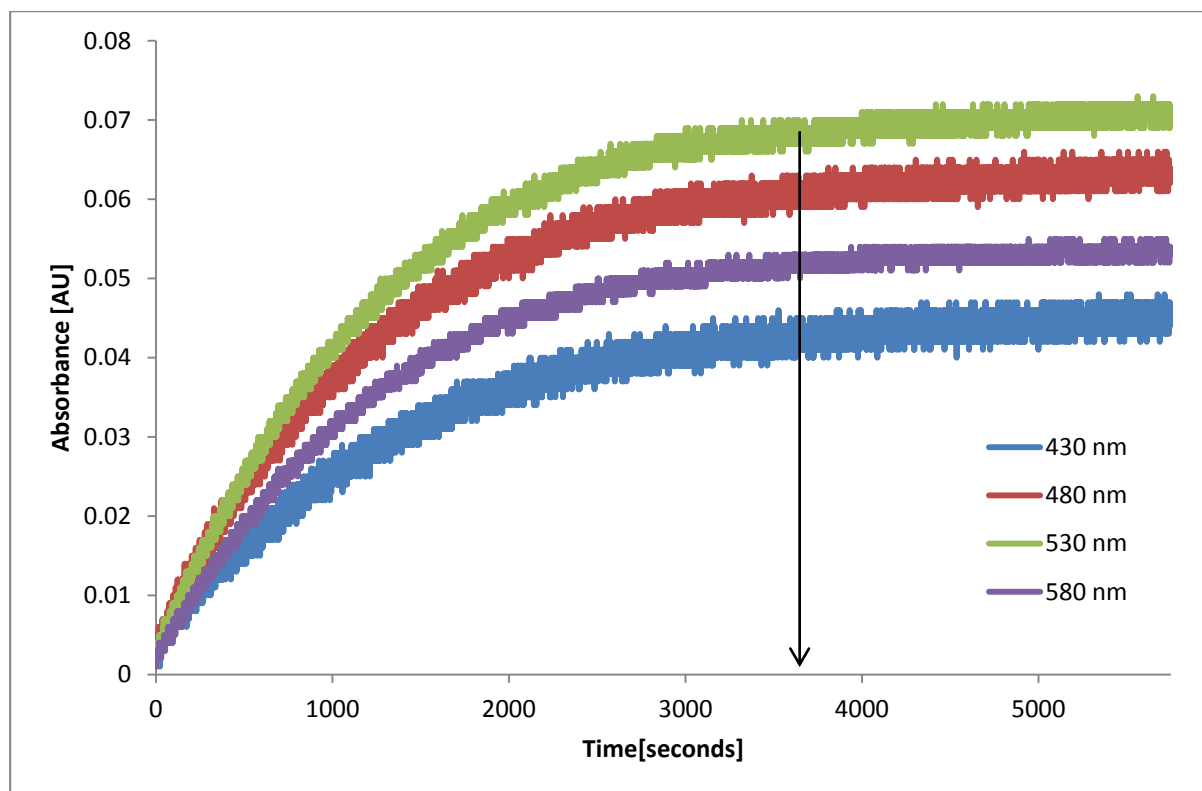

Figure 3.13: The UV-Vis light source stabilising.

3.5.1d Solution spectroscopy

In order to be able to identify the porphyrins as a possible toxic gas sensor, the material needs to be tested for sensitivity to diverse number of analytes. The process of LB films is extremely time consuming and therefore is not time efficient to transfer each material into a substrate and test with all the available analyte vapours.

To overcome this problem, the porphyrin is normally dissolved in a suitable solvent and its sensitivity to various analytes observed in dilute solution form. The solvent used in this work is chloroform ($CHCl_3$), however, other organic solvents can also be used. Porphyrins solutions were prepared to approximately 4 X 10^{-6} M, the concentration varies depending on the material, with the condition that the optical absorbance spectra must not be saturated at any wavelength.

One ml of chloroform is added to a quartz cuvette so that a suitable reference (spectral intensity) is recorded. The spectra are taken using the light source and the spectrometer described in the last section. For this research, the measured wavelength range was set between 350 nm and 850 nm, which corresponds to the range of the porphyrin spectrum. Once the reference spectrum is taken, the sensing material is injected into the cuvette and an absorbance spectrum regarding the porphyrin solution can be observed. After that, the absorbance spectrum is recorded whilst the analyte is added to the cuvette in 20 μl increments until the no further changes were noted in the absorbance spectrum.

3.5.1e Spectroscopy and optical chamber

The study of the detection of toxic gases by solid state LB films on substrates was carried out using a gas testing chamber. The objective is to monitor the changes in the optical spectrum of the solid films during exposure to gases. The changes that are observed in the spectrum of the LB films can be used to identify the amount of gas and also to identify the type of analyte.

Figure 3.14 depicts the purpose-built optical gas testing chamber, in which the samples were placed in order to observe its spectral response to different analyte vapours. The gas testing apparatus can deliver gas to the surface of the sample, heat the sample and record the absorbance spectra of the sample simultaneously.

The chamber is composed of two stainless steel pieces, corresponding to the base and a top lid. To close the chamber, it is necessary to place a rubber O-ring between the base and the lid, and seal the enclosure using a quick clamp. In the base of the chamber, the LB film sits on a Peltier heating device used to assist with recovery. It is important to mention that the heater has a small hole in its middle that allows the pathway for light from the optical fibre to be collected and delivered from the film. The ceramic Peltier heater is capable of heating the sample up to 95°C. The temperature is controlled by a thermocouple mounted in the base of the chamber and a feedback loop provided by software. In normal operation, the LB film was exposed at room temperature (25°C) and the recovery phase (dry nitrogen) occurred at elevated temperatures (<70°C). These conditions were used in all experiments unless otherwise stated.
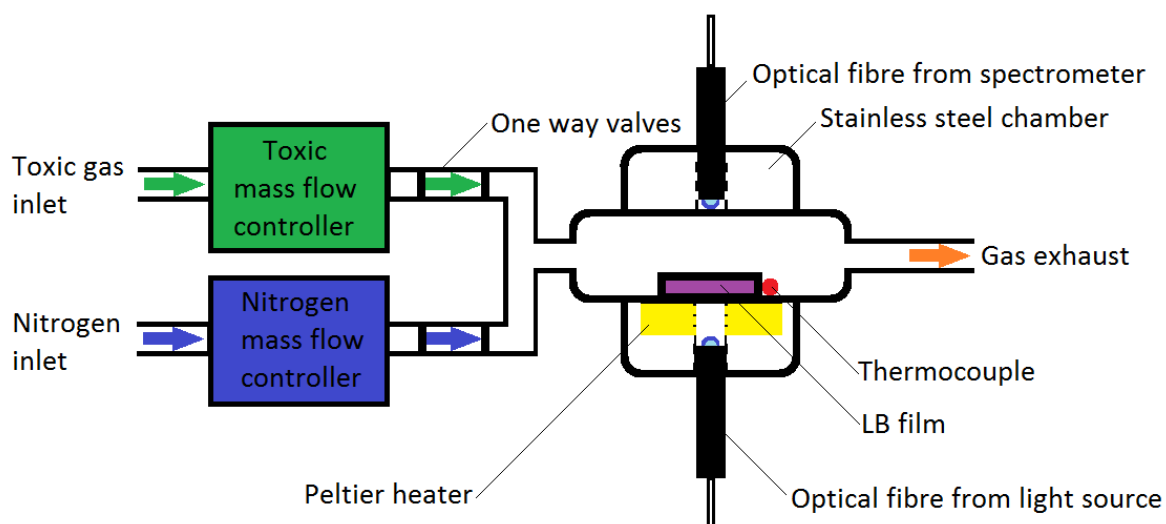
Figure 3.14: Schematic diagram of gas testing apparatus.

The chamber has an inlet port to allow the delivery of either clean nitrogen or the toxic gas to the surface of the LB film and an exhaust port. The control software is written in Labview, and it allows to the user to program cyclic periods of exposure and recovery during which the clean nitrogen or the toxic gas is delivered to the LB film. The rate of gas supply is controlled by using by two mass flow controllers (Model: Tylan FC-260). After the gas passes through the sample, the gas is transported to an exhaust pipe which filters the gas using activated charcoal and then liberating it into the atmosphere.

3.5.1f Equilibrium vapour pressure and concentration calculation

The spectroscopic experiments in solids films were carried out using the system described in figure 3.14. The figure shows simplistically two different gas inlets: one containing the toxic vapour and the other containing clean dry nitrogen. The toxic gas can be provided directly from the analyte tank, as in the case of NO_2; however, most of the times the analyte is found in its liquid form.

Liquid analytes are converted to their gaseous form using a vessel containing the liquid analyte submerged in a water bath and subsequently dry nitrogen is flushed through the headspace of the sealed vessel, producing the analyte vapour.

The process of evaporation in the closed system will proceed until there are as many

molecules returning to the liquid as there are escaping. At this point of equilibrium the vapour is said to be saturated, and the pressure of that vapour is called the saturated vapour pressure. Since the molecular kinetic energy is greater at higher temperature, more molecules can escape the surface and the saturated vapour pressure is correspondingly higher. Thus, the saturated vapour pressure of the analyte can be varied by changing the temperature in the water bath, so the concentration of the vapour analyte flushed into the chamber can be controlled.

In the experimental sections, the concentrations of the delivered vapour were calculated based on the assumption that the gas flow rate through the vessel was sufficiently low so the vapour pressure of analyte gas in the headspace above the liquid analyte remains at equilibrium at the saturated vapour pressure; so the sum of low rates of analyte gas and clean dry nitrogen were constant (maintaining a fixed total flow rate).

To calculate the analyte saturated vapour pressure of each analyte, it is necessary to introduce the Antoine equation. The equation describes the relationship between the temperature and the vapour pressure for pure substances, and can be defined as:

$$log_{10}(P) = A - \frac{B}{T + C}$$
<div align="right">Eq. 3.17</div>

Where A, B and C are Antoine coefficients that vary from substance to substance, P is the vapour pressure in bar and T is the temperature in Kelvin.

Table 3.1 shows the Antoine equation coefficients corresponding to one of the carboxylic acids used in the experimental sections. Figure 3.15 shows the relation between the acetic acid vapour pressure and its corresponding temperature.

Temperature range (K)	A	B	C
289-592.56	7.8152	1800.03	246.894

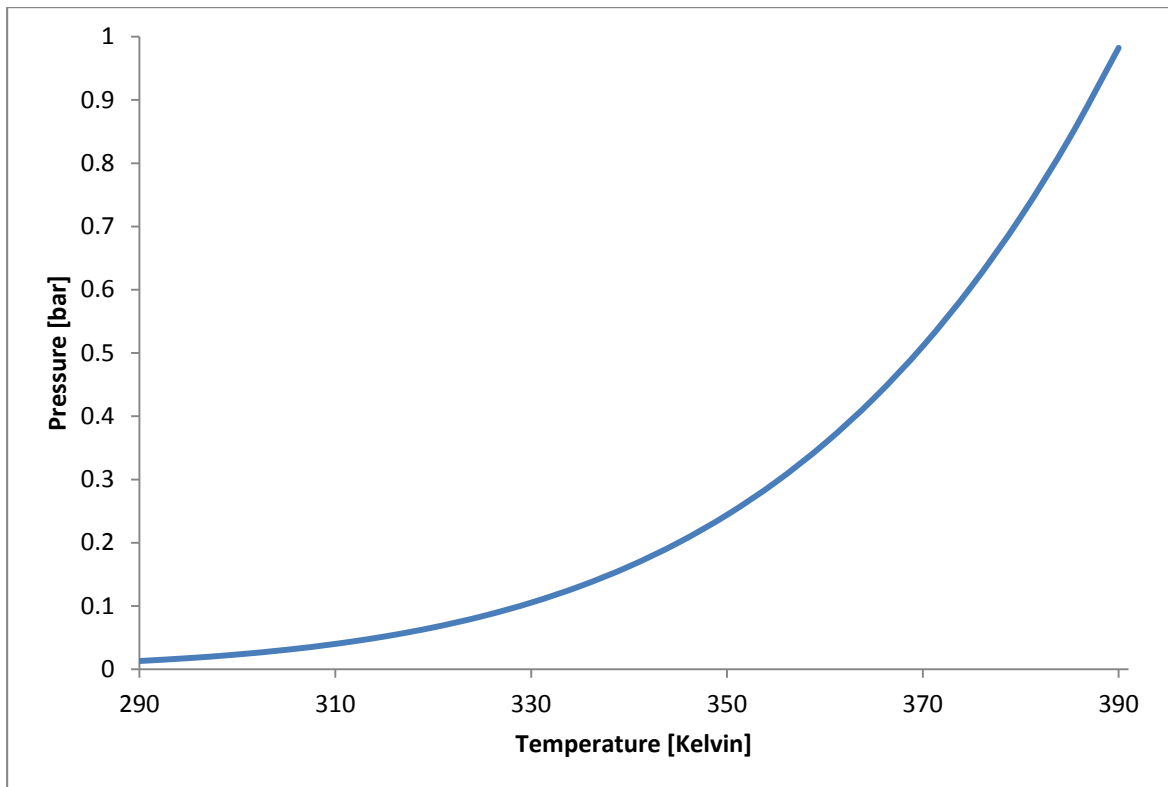**Table 3.1: Antoine equation parameters of acetic acid [31].**

Figure 3.15: Relationship between vapour pressure and temperature in acetic acid.

Generally speaking, the more sensitive the better for toxic gases as this allows an early detection system. In this thesis, parts per thousand are used as a pseudo unit to describe small values of miscellaneous dimensionless quantities, e.g. mass fraction (ratio of vapour analyte to the mass of the total vapour mixture containing the analyte and dry nitrogen). Since the fraction is quantity per quantity measures, it is a pure number with no associated unit of measurement.

To calculate the theoretical concentration of toxic vapour flushed into the chamber through the headspace of the vessel, the next equation must be defined:

$$c = \frac{VP_{c[mmHg]}}{760_{mmHg}} \cdot 10^3 \qquad \text{Eq. 3.18}$$

Where c is the concentration in ppt (parts per thousand), VP_c is the vapour pressure of the analyte in mmHg and 760 mmHg is the pressure exerted by the weight of the atmosphere at sea level, also known as standard atmospheric pressure.

Most authors in the gas sensing field express their concentrations with three digits maximum. For convenience, this trend was followed and parts per thousand (ppt) were selected to be the standard concentration for the analyte vapours.

Alternatively, when the concentration is even lower, parts per million (ppm, one part in 10^6) units are used.

3.5.1g Fabrication parameters in the optical characterisation of samples

Preparation of samples was carried out using different parameters in the fabrication procedure such as concentration of porphyrin, deposited target pressure, barrier speed in trough, dip velocity, type of porphyrin and number of layers deposited.

One important parameter in determining the response to toxic gases is the number of layers of porphyrin deposited. The number of layers is proportional to the number of excursions (submerging and withdrawal of the substrate).

A lot of scientific work has shown the absorbance is directly proportional to the number of layers deposited in the substrate [32-34]. On the other hand, this affects the recuperation time. In other words; more layers mean more absorption but this leads to a long recuperation time.
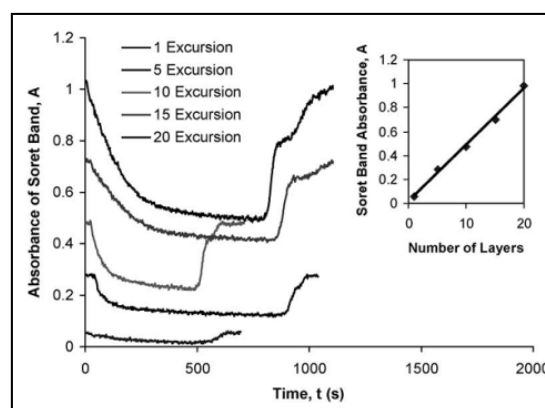

Figure 3.16: Left: Desorption and adsorption kinetics for different number of excursions at 443 nm (Soret band). Up-Right: Absorbance of Soret band vs. number of layers [26].

It is essential to keep in mind that the sensitivity of the sensor depends on the number of layers. Nevertheless, when multilayers exceed a certain number, the material begins to behave as a bulk which is accompanied by a significant loss in response and sensitivity. So the number of layers must

be carefully optimized. The effect of the number of layers in a sensor is discussed in section 5.2.4 and it can be observed in figure 5.23.

3.5.1h Concentration dependence in the optical characterisation of samples

The response of the optical sensors made of porphyrin not only depend on the fabrication parameters of the sample, but also on the concentration of the analyte. A good sensor is able to detect low concentrations of vapour analytes. The response of the sensors as a function of gas concentration is important as it indicates the range of concentration over which the material is sensitive. Normally if the concentration is augmented, the sensors response also increases until the sensors reaches a saturation point in which no more porphyrin sites are available to bind with the analyte and no more reactions take place. In other words, the higher the concentration the higher the response in the sensor.

In order to quantify the response of the sensor in terms of the vapour concentration, it is necessary to define a concentration dependence graph. Figure 3.17 shows the magnitude of optical response (total change in Soret band absorbance induced by gas exposure) as a function of gas concentration. The graph proves that the change in Soret band absorption depends on the concentration, even at low concentrations.

Figure 3.17 (left) suggests that the graph obeys Langmuir Adsorption theory, the displayed curve is commonly observed in cases where Langmuir adsorption occurs. To corroborate that this kind of adsorption is occurring, it is necessary to plot the data using the Langmuir Model equations. According to equation 2.22, a plot of c/ΔAbs versus c should be a straight line if Langmuir adsorption is occurring. Figure 3.17 (right) displays the Langmuir plot showing the Langmuir parameter dependence as a function of concentration.
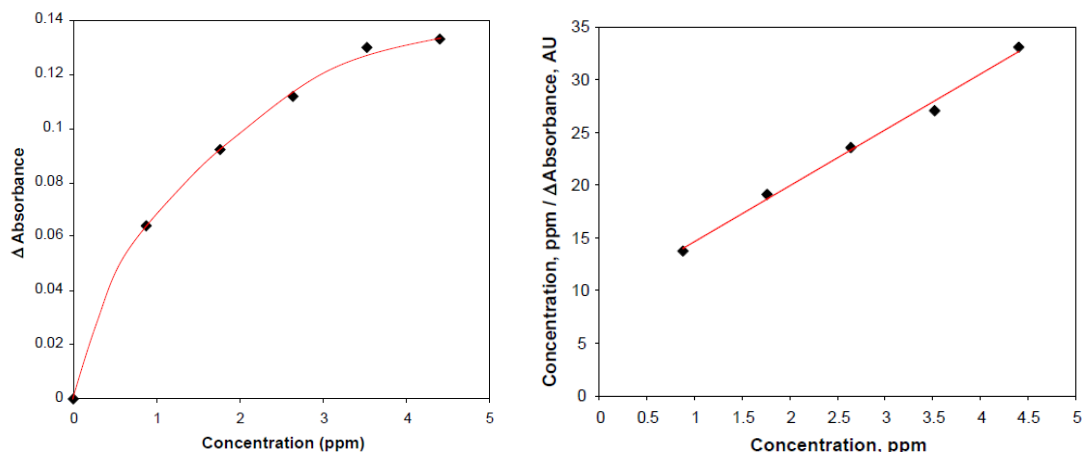
Figure 3.17: Left: Concentration dependence of an EHO LB film assembly from 0 to 5 ppm. Right: Langmuir adsorption plot of an EHO LB film [35].

The Langmuir adsorption model correlates the magnitude of the change in absorbance with the concentration of the toxic gas. Early works of the NMEG have proven that free base porphyrins and metalled porphyrins behave according to the Langmuir adsorption model [26, 33, 35-37].

Even though the Langmuir model ignores the possibility of adlayers thicker than one monolayer, surface heterogeneity, lateral interactions between adsorbed analyte molecules and surface mobility; it nevertheless provides a basic understanding of the adsorption process for the porphyrin/analyte complexes. An example of a concentration dependence graph is discussed in section 5.3.3, figures 5.28 and 5.29.

3.5.2 Atomic Force Microscopy

Atomic force microscopy (AFM) is a very high resolution method of measuring surface topography of a thin film. The name microscope is rather misleading because the sample is not been seen, but scanned using a physical probe (or tip) that and the response of the tip is used to generate an image of the sample. The tip is held above the surface and can controlled using an electronic feedback mechanism that measures the force of interaction between the tip and the surface. Software is used to interpret the interaction and produce the image of the topography of the surface.

3.5.2a Historical Background

The first AFM was made in 1985 by Gerber and Binning. They extremely methodically glued a tiny piece of diamond into one end of a strip made of gold foil to form a cantilever that could examine surfaces. That system was able to detect features as small as 30 nm using the diamond shard to make contact with the surface. They soon realized that the images were distorted when the gold cantilever was bent. This effect was caused by Van der Waals forces interacting between the surface and the tip. Later on, a young scientist called Albrecht introduced the frequency modulation of the cantilever, in which the change in resonant frequency of the sensor is tracked directly. Albrecht fabricated a silicon micro-cantilever, and with it was able to measure the atomic structure of boron nitride. The breakthrough made the surface imaging technique popular and useful to the majority of the scientific world. Since then, AFM technology has evolved extremely rapidly, meeting the needs of those who demand more detailed high resolution images.

3.5.2b The AFM technique: Experimental

A sharp tip, typically made from silicon or silicon nitride, is scanned over a surface with feedback mechanisms that enable the piezoelectric scanners to maintain the tip at a constant height (to obtain force information) or force (to obtain height information). Repulsive interactions between the surface and the tip cause the cantilever to bend away from the surface.

A laser diode light source is focused onto the back of the reflective cantilever, as the tip moves down and up with the surface of the sample, the laser beam is reflected onto a position sensitive photo detector. The photo detector measures the position from the laser diode source and converts it into a voltage. The voltage is fed back to the cantilever controller which permits the tip to maintain a constant height above the sample and allows the piezoelectric transducer to monitor the height deviation in real time.
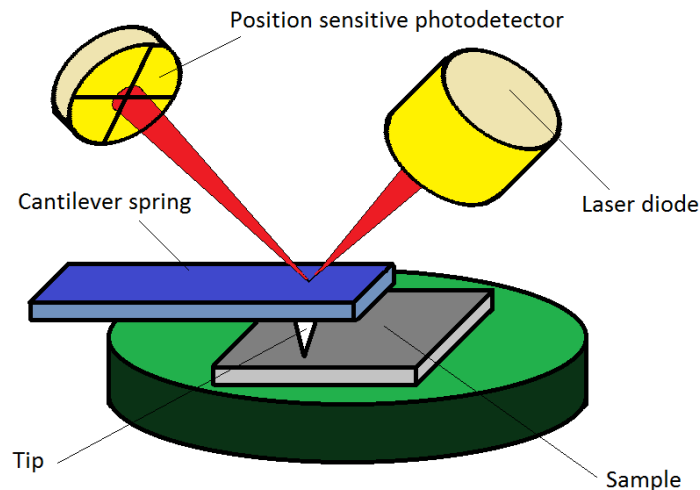
Figure 3.18: Schematic diagram of AFM imaging technique.

There are three possible methods to operate the AFM: tapping, non-contact and contact modes. The AFM images in this work were conducted at room temperature in air by tapping mode using a Nanoscope IIIa microscope with Nanoscope III software. In this mode, the cantilever oscillates vertically during scanning when it alternately taps the surface and then lifts off the sample. The frequency of oscillation of the cantilever is in the range from 50 to 500 KHz (nominally 300 kHz) . As the cantilever begins to occasionally contact the surface, the oscillation is reduced by the loss of energy caused by the tip when it touches the surface. As the tip is rastered across the sample the degree of oscillation reduction is used determine the height for position and therefore generate each pixel to build up an image of the surface characteristics.

3.5.3 Microbalance

Certain crystalline materials, such as quartz, have piezoelectric properties. This means that if a quartz crystal is squeezed it creates a potential difference across some of its crystal faces. If a potential difference is applied across these faces, the crystal responds by changing shape. This is called the piezoelectric effect, shown in figure 3.19, and was first discovered in 1880 [38]. Figure 3.19 depicts the deformation of the quartz crystal when a potential difference is applied to it.

The quartz crystals used in quartz crystal oscillators consist of a thin plate of quartz which has a natural resonant frequency. The resonant frequency depends on elasticity, size, shape and the speed of sound in the material [39].
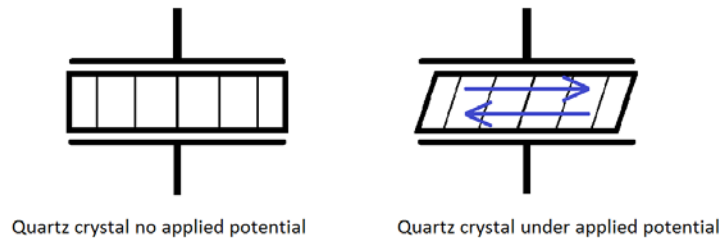

Quartz crystal no applied potential   Quartz crystal under applied potential

Figure 3.19: Graphical illustration of shear mode oscillation.

3.5.3a Quartz Crystal Oscillator

An oscillation is a system that is able to create disturbances or waves in a medium in a periodic way. In electronics, an oscillator circuit is a device that is able to transform the continuous current into alternating current, all of it at a constant frequency. In other words, this circuit converts a constant current into a current that varies periodically with time. Using the properties of a vibrating crystal of a piezoelectric material, it is possible to generate an electrical signal with a very precise oscillating frequency.

Quartz crystals can be represented electrically as a series LCR branch in parallel with a shunt capacitance (C_0), the circuit is illustrated in figure 3.20. C_0 represents the physical capacitance formed by the crystal electrodes plus any holder capacitance, L1 is the equivalent inertial component of the oscillation that is related to the mass displaced during the vibration, C1 is the mechanical resistance and R1 is the dissipation of the oscillation energy from the medium in contact with the crystal. Altogether, the series LCR branch (L1, C1 and R1) represents the pullability of the crystal that denotes the change in frequency of a crystal unit from the natural resonant frequency (f_0) to a load resonant frequency.
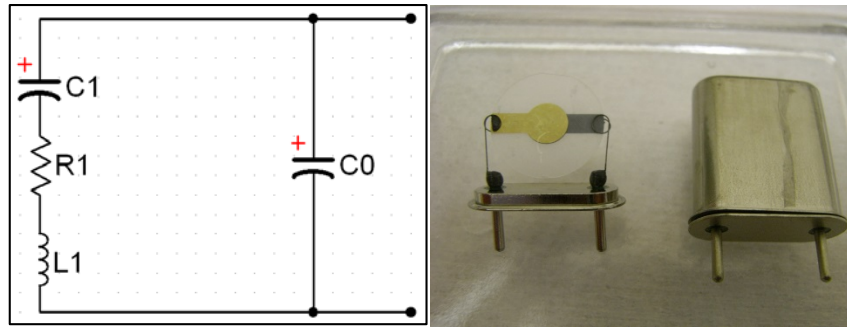
Figure 3.20: Left: Equivalent circuit for a quartz crystal, right: quartz crystal and its protective metal lid.

It can be inferred from the circuit that the crystal presents two resonant frequencies, a series resonant frequency and a parallel resonant frequency (also known as anti-resonant frequency) [40-42]. The series resonant frequency can be described as:

$$f_s = \frac{1}{2\pi\sqrt{L_1 C_1}}$$

Eq. 3.19

Whereas the anti-resonant frequency, can be represented as:

$$f_a = \frac{1}{2\pi\sqrt{L_1\left(\frac{C_1 C_0}{C_1 + C_0}\right)}}$$

Eq. 3.20

The rate of contraction and expansion of the quartz must match the resonant frequency, so the equilibrium in the system can be achieve. When the energy loses matches the energy generated in the frequency, the oscillation is said to be reached.

3.5.3b Quartz crystal microbalance (QCM)

QCM is a highly sensitive mass sensing device that allows the measurement of small mass changes on a crystal resonator. Adding mass to the oscillating crystal by wetting of the crystal resonator surface or depositions of material at the surface causes a frequency shift because the mass being oscillated changes. The resonant frequency of this oscillation is very sensitive to the mass being oscillated and therefore can be used as very sensitive mass sensor. The method of relating the mass deposited on the surface of the crystal with the changes in the oscillation frequency was firstly explored by Sauerbrey in 1959. He reported a linear relationship between the bound elastic mass of deposited metal and the frequency decrease

of an oscillating quartz crystal [43]. The first QCM chemical sensors were used to detect environmental pollutants [44] and volatile organic compounds [45, 46].

The Sauerbrey method is a useful tool in QCM experiments for conversion of frequency to mass in many chemical applications that measure the mass of gas-phase species binding to the quartz surface. The resonant frequency change (Δf) of a QCM for an LB film can be defined as:

$$\Delta f = \frac{2f_0{}^2 \Delta m}{A\sqrt{\mu_q p_q}} N \qquad \text{Eq. 3.21}$$

Where f_0 is the resonant frequency (Hz), Δm is the mass per unit area per layer (g cm^{-2}), A is the area between electrodes (cm^{-2}), μ_q is the shear modulus of quartz (2.947x10^{11})gcm^{-1}s^{-2} , p_q is the density of quartz (2.648 gcm^{-3}), and N is the number of deposited layers [47].

3.5.4 Fourier-transform infrared spectroscopy (FTIR)

FTIR is a chemically-specific analysis technique based on absorption events. The technique is commonly used to identify chemical compounds and substituent groups.

The principle by which FTIR can be used to identify chemical compounds is depicted in figure 3.21 in which a diatomic molecule is vibrating. If a quanta of infrared light interacts with the molecule the oscillation of the bond may absorb the energy provided by the photon, and that will make the molecule to vibrate even faster. Therefore by measuring the IR absorbance the precise vibrational energies of the bonds present within the sample can be determined.
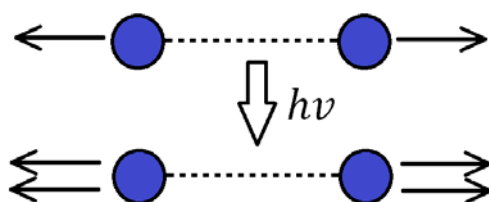

Figure 3.21: Basis of the FTIR spectroscopy.

The infrared radiation does not have enough energy to induce an electronic transition as it happens with the UV-Vis. Two conditions must be carried out in order to allow the infrared absorption to occur: the incoming infrared photon must have enough energy for the

transition to the next allowed vibrational energy state and the molecule must have a change in dipole moment due to vibration.

The FTIR spectrometer is based on the Michelson interferometer. The apparatus is illustrated in figure 3.22.
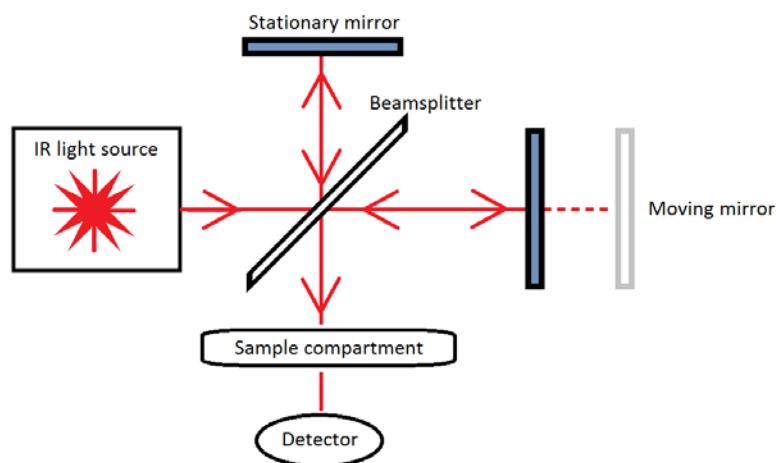

Figure 3.22: Diagram of an FTIR spectrometer.

The IR light emitted from the source is split in two paths by the beamsplitter, which passes half of the light to the moving mirror and the other half to the stationary mirror. The two resulting beams reflect off their respective mirrors and the beam-splitter recombines the two light waves which are then guided on towards the sample compartment, where the light is absorbed by the sample and then passed to the detector. Because the path of one beam is constantly changing as the mirror moves and the other is at a fixed length, the received signal is the result of the two beams interfering with each other. The resulting signal is called interferogram, and contains the information of every infrared frequency which comes from the source as a function of the moving mirror position, in other words, it contains all the frequencies simultaneously. Due to the complicated nature of the interferogram, the signal must be converted back to the frequency domain (a spectrum) using the Fourier transform, this operation is performed by a computer. The result is that the absorbance spectrum of the sample can be simultaneously measured across a wide range of IR wavelengths.

3.6 Materials

3.6.1 Calixarenes

The name calixarene was derived from the Greek word "calix" meaning vase and the word "arene" that refers to the aromatic building block. The molecules have hydrophobic cavities which can hold smaller ions or molecules, i.e. molecular baskets. The cyclic shaped molecules contain phenolic monomers joined cyclically to enclose a cavity [48]. Figure 3.23 shows the similarity between a cyclic tetrameter and a calix crater. The size of the molecular basket depends on the number of monomers in the calix ring, e.g a calix[8]arene has eight repeating units in the ring, whereas a calix[4]arene has only 4. The repeat units are not necessarily carboxylic acid containing.

Figure 3.23: Left: Molecular model of a cyclic tetramer, right: calix crater [49].

Calixarenes are capable not only of binding small molecules within their cavities but also of exhibiting high porosity to other species [50]. The preparation of a mixed film containing porphyrin and calixarene can lead to a more uniform Langmuir layer and therefore less aggregated films when applied to gas sensing [51].

3.6.2. Analytes:

3.6.2.1 Amines:

Amines are a group of chemical compounds that contain a basic nitrogen atom with a lone pair of electrons. The simplest amine is ammonia (NH_3), in which three hydrogen atoms are bonded to the nitrogen atom. Amines are classified depending on how many of the hydrogen

atoms are replaced with larger organic substituents. The replacement of these hydrogen atoms in ammonia produces other organic compounds: primary amines have only one of the hydrogen atoms replaced by an organic substituent, secondary amines have two organic substituents and tertiary amines have all three hydrogens of the original ammonia replaced by organic substituents. Figure 3.24 depicts the classification of amines.

The properties of amines are mostly controlled by the electronic characteristics of the central nitrogen atom and the use of the lone pair of electrons for donation. The ability of the nitrogen atom to donate its lone pair in chemical reactions varies depending on the functional groups bonded to the nitrogen atom, which can decrease or increase the ability to donate the lone pair of electrons [52].
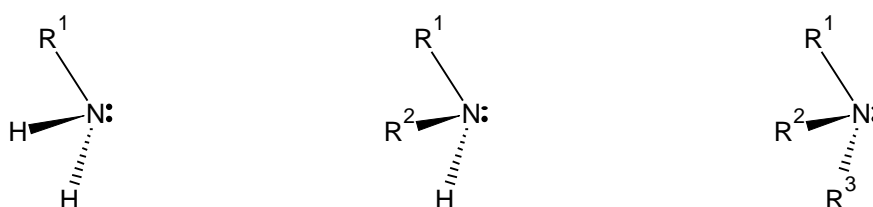

Figure 3.24: From left to right: primary, secondary and tertiary amines.

One main characteristic of these organic compounds is that they possess an identifiable amine smell, often described as being like rotting fish [53].

3.6.2.2 Alcohols:

The alcohols may be considered as derivatives of hydrocarbon in which the hydroxyl functional group (-OH) replaces a hydrogen [54]. The hydroxyl group is attached to a carbon atom in an alcohol molecule by a covalent bond. Alcohols may be classified as primary, secondary or tertiary, depending on whether one, two or three side groups are bound to the carbon atom that is bound to the hydroxyl group.
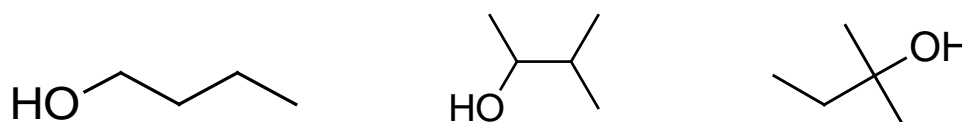

Figure 3.25: From left to right: 1-butanol a primary alcohol, 3-methyl-2-butanol a secondary alcohol and 2-methyl-2-butanol a tertiary alcohol.

Many compounds contain more than one –OH functional group. The general name for this class of compounds is polyhydric alcohols. Alcohols have much higher boiling points than hydrocarbons or most other compounds of similar molecular weight because they associate through hydrogen bonding [55]. For alcohols in general, the boiling point increases as the number of carbon atoms increase.

3.6.2.3 Carboxylic acids:

The carboxylic acids are compounds containing the –COOH side group. The organic acid is a combination of a carboxyl (C=O) and a hydroxyl group (-OH) and is obtained by the oxidation of an aldehyde group. Carboxylic acids are polar because they have two polar groups: carbonyl (hydrogen bond acceptor) and hydroxyl (hydrogen bond donor). As a result, they often form hydrogen bonds with each other [56].

Carboxylic acids are weak acids because they are proton donors (H^+). The water solubility of carboxylic acids is roughly parallel to that of amines, alcohols and other compounds which water can solvate through hydrogen bond formation. Lower carboxylic acids, from one to four carbons, are miscible with water. As the alkyl chain gets longer their solubility decreases because of the increasing hydrophobic nature of the long carbon chain.

3.6.2.4. Nitrogen dioxide (NO_2):

Nitrogen dioxide is an irritant reddish-brown toxic gas. It can be naturally formed in the atmosphere by plants or as a result of lightning strikes; however the oxides of nitrogen are mostly produced during high temperature combustion processes causing the oxidation of nitrogen in the air. The initial product of the gas reaction is nitric oxide (NO) formed under high temperatures (> 2000°C) as the hydrocarbon fuel burns providing heat. The NO can easily react with oxygen in the atmosphere to form NO_2. Together, NO and NO_2 are known as NO_X. Figure 3.26 shows the two-stage process of nitrogen dioxide production in the internal combustion engine.
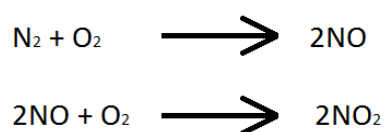
$$N_2 + O_2 \longrightarrow 2NO$$

$$2NO + O_2 \longrightarrow 2NO_2$$

Figure 3.26: NO_X processes.

Most of the NO_2 in cities is produced by motor vehicle exhausts, but other sources such as the electricity generation (from coal-fired stations), petrol refining or other manufacturing industries also contribute to the production of the gas.

References

[1] B. Franklin, Philos. Trans. R. Soc. , 64 (1774) 445.
[2] J. Aitken, Proc. R. Soc., 12 (1882) 56.
[3] L. Rayleigh, Philos. Mag., 30 (1890) 386.
[4] A. Pockels, Nature, 43 (1891) 437.
[5] I. Langmuir, J. Am. Chem. Soc. , 39 (1917) 1848.
[6] H. Devaux, Kolloid. Z., 58 (1932) 260.
[7] I. Langmuir, Am. Chem. Soc., 40 (1918) 1361.
[8] L. Rayleigh, Philos. Mag., 48 (1899) 321.
[9] K. Blodgett, Phys. Rev., 51 (1937) 964.
[10] I. Langmuir, V.J. Schaefer, Journal of the American Chemical Society, 60 (1938) 1351-1360.
[11] G.G. Roberts, Langmuir-blodgett films, Plenum press New York, 1990.
[12] C.W. Tang, Appl. Phys. Lett., 51 (1987) 913.
[13] N.K. Adam, Physics and chemistry of surfaces, 1941.
[14] T. Ishii, Thin Solid Films, 178 (1989) 47.
[15] G.L. Gaines, Insoluble monolayers at liquid-gas interfaces, 1966.
[16] L. Wilhelmy, Ann. Phys., 119 (1863) 177.
[17] H. Kuhn, D. Möbius, H. Bücher, A. Weissberger, B. Rossiter, Vol. 1Wiley, New York, (1972) 577.
[18] M.W. Kim, D.S. Cannell, Physical Review A, 13 (1976) 411.
[19] N.R. Pallas, B.A. Pethica, Journal of the Chemical Society, Faraday Transactions 1: Physical Chemistry in Condensed Phases, 83 (1987) 585-590.
[20] S. Hénon, J. Meunier, Review of Scientific Instruments, 62 (1991) 936-939.
[21] H. Kuhn, D. Möbius, Physical Methods of Chemistry Series, vol. IXB. John Wiley & Sons, UK, (1993) 375.
[22] M.C. Petty, M.R. Bryce, D. Bloor, An introduction to molecular electronics, Oxford University Press, USA, 1995.

[23] I. Langmuir, Science, 88 (1938) 430-432.

[24] N. Hardy, T. Richardson, F. Grunfeld, Colloids and Surfaces A: Physicochemical and Engineering Aspects, 284 (2006) 202-206.

[25] C.M. Dooling, O. Worsfold, T.H. Richardson, R. Tregonning, M. Vysotsky, C.A. Hunter, K. Kato, K. Shinbo, F. Kaneko, Journal of Materials Chemistry, 11 (2001) 392-398.

[26] C. Dooling, T. Richardson, Materials Science and Engineering: C, 22 (2002) 269-274.

[27] M.C. Petty, Langmuir-Blodgett films: an introduction, Cambridge University Press, 1996.

[28] G. Barnes, I. Gentle, Interfacial science: an introduction, Oxford University Press, 2011.

[29] S. Brittle, Selective Vapour Sensing Using Nanoscale Porphyrin Films, in: Department of Physics and Astronomy, The University of Sheffield, 2009.

[30] C.M. Dooling, Fast Optical NO2 Gas Sensing of Porphyrin LB Films, in: Department of Physics and Astronomy, The University of Sheffield, 2002.

[31] R.A. McDonald, S.A. Shrader, D.R. Stull, Journal of Chemical & Engineering Data, 4 (1959) 311-313.

[32] S.O. Korposh, N. Takahara, J.J. Ramsden, S.-W. Lee, T. Kunitake, www. amsi. ge/jbpc, (2006).

[33] T. Richardson, C. Dooling, O. Worsfold, L. Jones, K. Kato, K. Shinbo, F. Kaneko, R. Tregonning, M. Vysotsky, C. Hunter, Colloids and Surfaces A: Physicochemical and Engineering Aspects, 198 (2002) 843-857.

[34] A. Tsuda, A. Osuka, Science, 293 (2001) 79-82.

[35] T. Richardson, C. Dooling, L. Jones, R. Brook, Advances in colloid and interface science, 116 (2005) 81-96.

[36] M.B. Grieve, A.J. Hudson, T. Richardson, R.A.W. Johnstone, A.J.F.N. Sobral, A.M.d.A. Rocha Gonsalves, Thin Solid Films, 243 (1994) 581-586.

[37] V. Smith, T. Richardson, H. Anderson, Supramolecular Science, 4 (1997) 503-508.

[38] J. Curie, P. Curie, Comput. Rend. Acad. Sci. Paris, 91 (1880) 294.

[39] M. Plant, Basic Electronics, Second edition ed., Hodeer & Stoughton, 1990.

[40] H. Ehahoun, C. Gabrielli, M. Keddam, H. Perrot, P. Rousseau, Analytical chemistry, 74 (2002) 1119-1127.

[41] C. Robinson, M. Baker, Journal of Physics E: Scientific Instruments, 11 (1978) 625.

[42] K. Wessendorf, T. Payne, SaRonix/Sandia National Laboratories/Page2, (1998).

[43] G. Sauerbray, Z. Phys., 155 (1959) 206.

[44] G.G. Guilbault, CRC Rev. , 19 (1988) 1.

[45] W.H. King, Anal. Chem, 36 (1964) 1735.

[46] G.G. Guilbault, Anal. Chem, 55 (1983) 1682.

[47] R. Çapan, Z. Özbek, H. Göktaş, S. Şen, F.G. İnce, M.E. Özel, G.A. Stanciu, F. Davis, Sensors and Actuators B: Chemical, 148 (2010) 358-365.

[48] J. Vicens, V. Böhmer, Calixarenes: a versatile class of macrocyclic compounds, Springer, 1990.

[49] C.D. Gutsche, Calixarenes: an introduction, Royal Society of Chemistry, 2008.

[50] T.H. Richardson, R.A. Brook, F. Davis, C.A. Hunter, Colloids and Surfaces A: Physicochemical and Engineering Aspects, 284–285 (2006) 320-325.

[51] G. de Miguel, M.T. Martín-Romero, J.M. Pedrosa, E. Muñoz, M. Pérez-Morales, T.H. Richardson, L. Camacho, J. Mater. Chem., 17 (2007) 2914-2920.

[52] S.A. Lawrence, Amines: synthesis, properties and applications, Cambridge University Press, 2004.

[53] S.A. Brittle, T.H. Richardson, J. Hutchinson, C.A. Hunter, Colloids and Surfaces A: Physicochemical and Engineering Aspects, 321 (2008) 29-33.

[54] C.E. Mortimer, (1967).

[55] W.R. Robinson, J.D. Odom, H.F. Holtzclaw, Chemistry: Concepts and Models, DC Heath, 1992.

[56] N.L. Allinger, Organic Chemistry, Worth Publishers, Inc. , 1971.

Chapter 4

Characterization and evaluation of porphyrins as optical sensing devices

In this chapter, different porphyrins (free base and metalated) will be employed as sensing materials either in solution or deposited on a glass substrate. The samples will be exposed to analytes that are intended to interact with the highly conjugated porphyrin system, altering the energies of the conjugated π-electrons and subsequently changing the absorption spectra. The resulting responses of the materials will be compared.

The objective of the chapter is to determine the suitability of the studied materials for use as optical gas sensors for the various analytes and to evaluate the influence of the functional groups upon the porphyrin sensing behaviour.

There are four sections in this chapter that divide the sensors into groups in which similar porphyrins are exposed to analytes containing the same functional groups. Most of the sections contain the response of the materials in solution and in solid film, providing an overview of the reactions of the materials when exposed to the analytes. In addition, the isotherms and the AFM images are presented to highlight the organization of the molecules at certain surface pressures and the importance of the molecular packing.

The first of the section compares several zinc porphyrins and their response to amines. The second section investigates five different free base porphyrins and their response to carboxylic acids. The third section addresses the detection of nitrogen dioxide using a free base porphyrin (EHO) and a host material, either calixarene or titanium dioxide rods, to enhance the response of the sensors. In the fourth section, a magnesium porphyrin (MgEHO) is used to detect various alcohol vapours.

Section I: Zinc metallo porphyrins and amines

Amines are indispensable organic compounds in nature, e.g. amino acids are used by our bodies to make proteins and to perform roles as neurotransmitter, which are essential processes in the biochemistry of the body.

Industrially, amines are used in different sectors for the production of coatings, pharmaceuticals, emulsifiers, pesticides, dyes, corrosion inhibitors and polishes [1]. For example n-butylamine is used in the production of pesticides and alkyl amines are used to make many pharmaceuticals such as anti-histamine for allergies, tranquilizers and decongestants.

Amines are harmful if they are accidently inhaled or if they come into contact with the eyes or skin, so their detection is of commercial interest because of their health threat to people that work in industries where amines are being used [2].

Some plants and animals produce trimethylamine once they are decaying, so another amine sensing application is the tracking of food spoilage.

In this section various porphyrins with the same zinc porphine but different side groups will be exposed to primary, secondary and tertiary amines. The response of the sensing materials varies depending on the different electron withdrawing or electron donating properties of the substituted side groups attached to the metallo porphyrin. The modification of the structure, leads to a change in the electric properties of the sensing materials which also alters important parameters such as the molecular packing, which in turn changes the reaction rate and the aggregation of porphyrin.

4.1.1. Materials

4.1.1.1 Zinc porphyrins

The sensing materials in this section contain not less than one phenyl group attached to the porphyrin ring at each of the methine bridges and a zinc ion at the centre of the porphine. It is anticipated that a different response to the analytes will be observed according to their different electron donating/withdrawing strength. Table 1 shows the diversity of side groups

attached to the porphyrin ring. The synthesis of the zinc porphyrins used in this study, shown in table 4.1, has been reported elsewhere [2, 3].
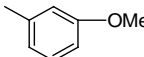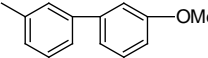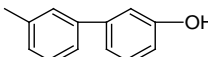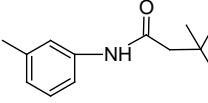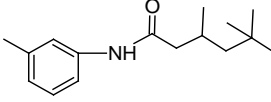
Zinc porphyrin name	Side groups molecular structure
SMT2_028	
SMT5_075	
SMT5_016	
SMT2_040	
SMT2_012	

Table 4.1: Distinctive side groups attached to the methine bridge for the respective materials.

SMT2_012 is characterized as the biggest molecule in the study because of its bulky branched hydrocarbon chain. Similarly, SMT2_040 contains a similarly large side group; however, the length of the alkyl chain within the amine functional group is shorter. Both side groups possess electron donating properties which are attributed to the alkyl chains. Correspondently, SMT2_028 is akin to SMT2_040 and SMT2_012 but the amide group is replaced with OMe, which is much smaller and also electron donating.

A methyl part at the end of the substituents groups can be found in the porphyrins SMT2_028 and SMT5_075. The OMe side group is an electron donating group characterized by lone pairs on the atom adjacent to the π system, for these two materials, the π electrons are pushed toward the porphyrin molecule. The main difference between these materials is that the SMT5_075 has two phenyl rings instead of one. It was theorized that the extra phenyl ring would give a slower and more deactivating reaction because of steric hindrance.

In a similar way, both SMT5_075 and SMT5_016, can be directly compared since they both have a double phenyl ring group attached to the porphyrin ring; the difference being that, SMT5_016 has a hydroxyl group at the end of the side group.

It is important to notice that all the substituents on the side groups have an electron donating nature, i.e. that all side groups increase the activating effect to analytes [4]. The side groups can be categorized depending on how strongly activating the substituent groups are. Table 4.1 shows the effects of side groups on a benzene ring. Note that all the zinc sensing materials contain their side groups located either in the moderately or strongly activating substituents. So, it is fair to say that a direct comparison can be made between the sensing materials and activating strength.
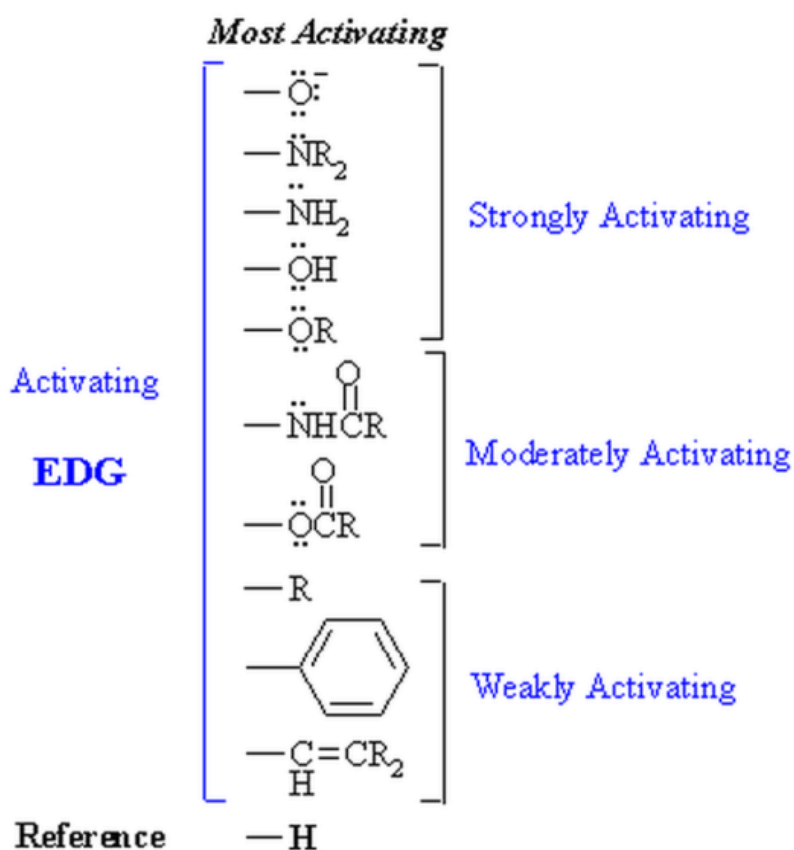

Figure 4.1: Table of substituent effects on a benzene ring [4].

92

4.1.1.2 Amines

Primary, secondary and tertiary amines were used in this study in order to analyse the different responses produced in the zinc porphyrins. Octylamine, n-butylamine and benzylamine are primary amines, dibutylamine is a secondary and tributylamine is a tertiary amine. Table 4.2 shows the chemical structure of the different analytes.
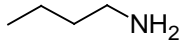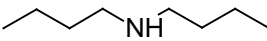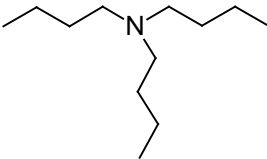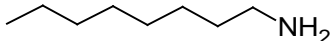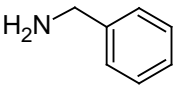
Amine	Molecular structure
N-butylamine	
Dibutylamine	
Tributylamine	
Octylamine	
Benzylamine	

Table 4.2: Structure of the selected amines

It is important to notice that the difference between N-butylamine, dibutylamine and tributylamine is the number of hydrocarbons attached to the central nitrogen. This characteristic will help to determine a correlation between the response of the sensing material and the size of the amine.

For the particular case of benzylamine, the situation is different in comparison with a simple primary amine. Benzylamine contains a lone pair of electrons on the central nitrogen which overlaps with the delocalised electrons in the benzene ring, increasing the electron density around the ring but reducing the availability of the lone pair on the central nitrogen to intervene in other reactions. For this reason, benzylamine is a much weaker base than primary amines such as n-butylamine [1].

4.1.2. Experimental details

Porphyrin solutions using chloroform as a solvent of approximately 0.02 mg/ml were prepared. This stock solution was further diluted by adding it to a cuvette containing 1 ml of chloroform. Afterwards, 100 μl of the selected analyte was added and stirred, so the reference spectrum of the porphyrin could be compared with the mixture of analyte/porphyrin. The objective of the procedure was to investigate the interaction of zinc porphyrins in solution with different amines.

For the rest of the studies (isotherms and LB/LS depositions), solutions of the porphyrins were prepared to 0.2 mg/ml using chloroform as a solvent.

For the substrate depositions, 250 μl of the porphyrin solution was then spread on the air-water interface of the Langmuir trough. Three Langmuir Schaeffer layers were deposited for both, glass and silicon substrates at a target pressure of 15 mNm^{-1}.

For the molar extinction coefficient measurements, a high molar concentration (0.2 mg/ml) of diluted porphyrin is mixed with a further 1 ml of chloroform in an optically transparent cuvette. As further aliquots of 5 μl of concentrated porphyrin solution are added to the 1 ml of chloroform in a cuvette, further spectra are recorded.

4.1.3. Results and discussion

4.1.3.1 Extinction Coefficient

The molar extinction coefficient (ϵ) for SMT2_012 is calculated using its spectrum in chloroform solution. Figure 4.2 shows the absorbance spectra of the SMT2_012 solution at different concentrations.
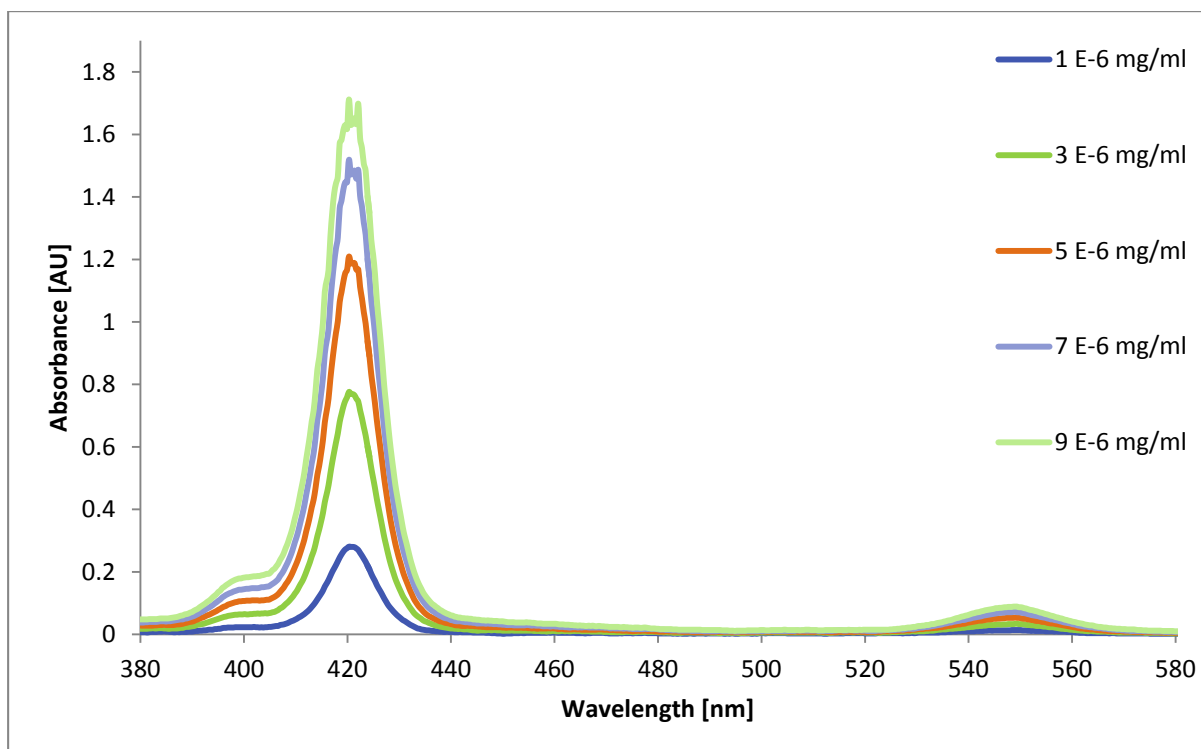
Figure 4.2: The spectra of SMT2_012 in chloroform solution at various concentrations.

The molar extinction coefficient (ϵ) is then calculated using the Beer-Lambert Law:

$$A_\lambda = \epsilon c l$$

Where l is the path length that the light passes through the SMT2_012 solution. A_λ can be plotted against the increasing concentration c, so ϵ is determined experimentally when tracking the changing absorbance at a particular wavelength, as depicted in figure 4.3. The concentration of the porphyrin solution is converted from µl of concentrated SMT2_012 solution into mg/ml. The Soret maximum absorbance is used for A_λ.
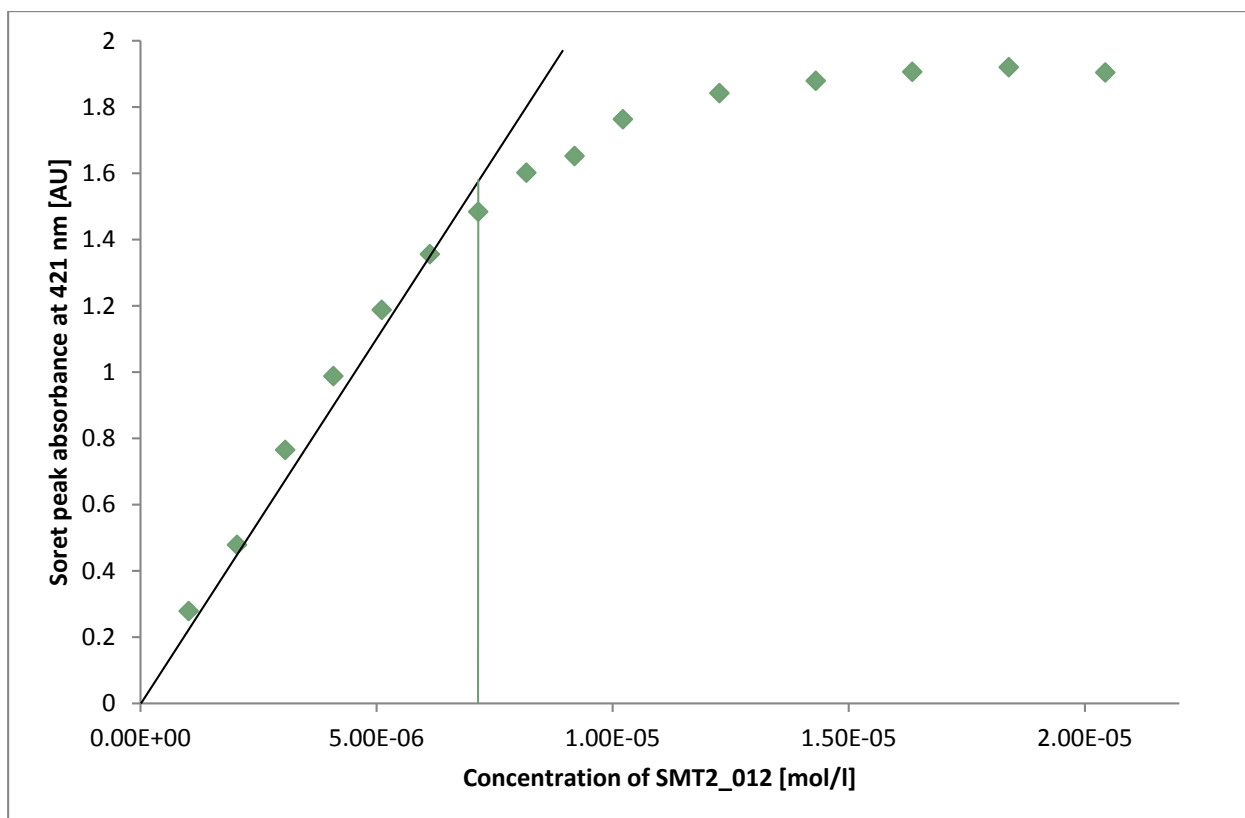
Figure 4.3: The Soret peak absorbance intensity is plotted against the concentration of SMT2_012.

The gradient of the straight line reveals ϵ, since l is a known length (1 cm). The molar extinction coefficient calculated for SMT2_012 is 2.08E5 $mol^{-1}cm^{-1}$. At approximately the point indicated by the vertical line (figure 4.3) the linear relation between the concentration and absorbance predicted by the Beer-Lambert Law begins to fall away. The reason for this is the possible initial aggregation. Higher concentrations of SMT2_012 solution cause the rate of increase of the Soret peak absorbance to decrease with further concentration increases.

The same process was then applied to the rest of the zinc porphyrins. Table 4.3 shows a list of the materials and its corresponding extinction coefficient.

Zinc porphyrin	Extinction Coefficient ($mol^{-1}\ cm^{-1}$)
SMT5_075	2.67 E5
SMT2_028	2.50 E5
SMT2_040	1.84 E5
SMT2_012	2.08 E5
SMT5_016	1.34 E5

Table 4.3: Porphyrins materials and their calculated extinction coefficients.

4.1.3.2 π-A isotherms

Identifying the correct surface pressure to use during film transfer is of absolute importance for vapour sensing applications. A low surface pressure may produce a film with few deposited molecules, and hence just a few available sites where the analyte can bind; on the other hand, a high surface pressure may lead to a higher number of deposited molecules, but due to the high density of film, the sites may not be accessible because the molecules are so close together.

A Langmuir isotherm was taken for all materials to identify suitable surface pressures for LS film transfer. The differences in the functional groups should play a large role in determining how the porphyrins will pack and also the extent of aggregation. The isotherms of the zinc porphyrins have been recorded so that any differences in the packing during monolayer compression can be highlighted.
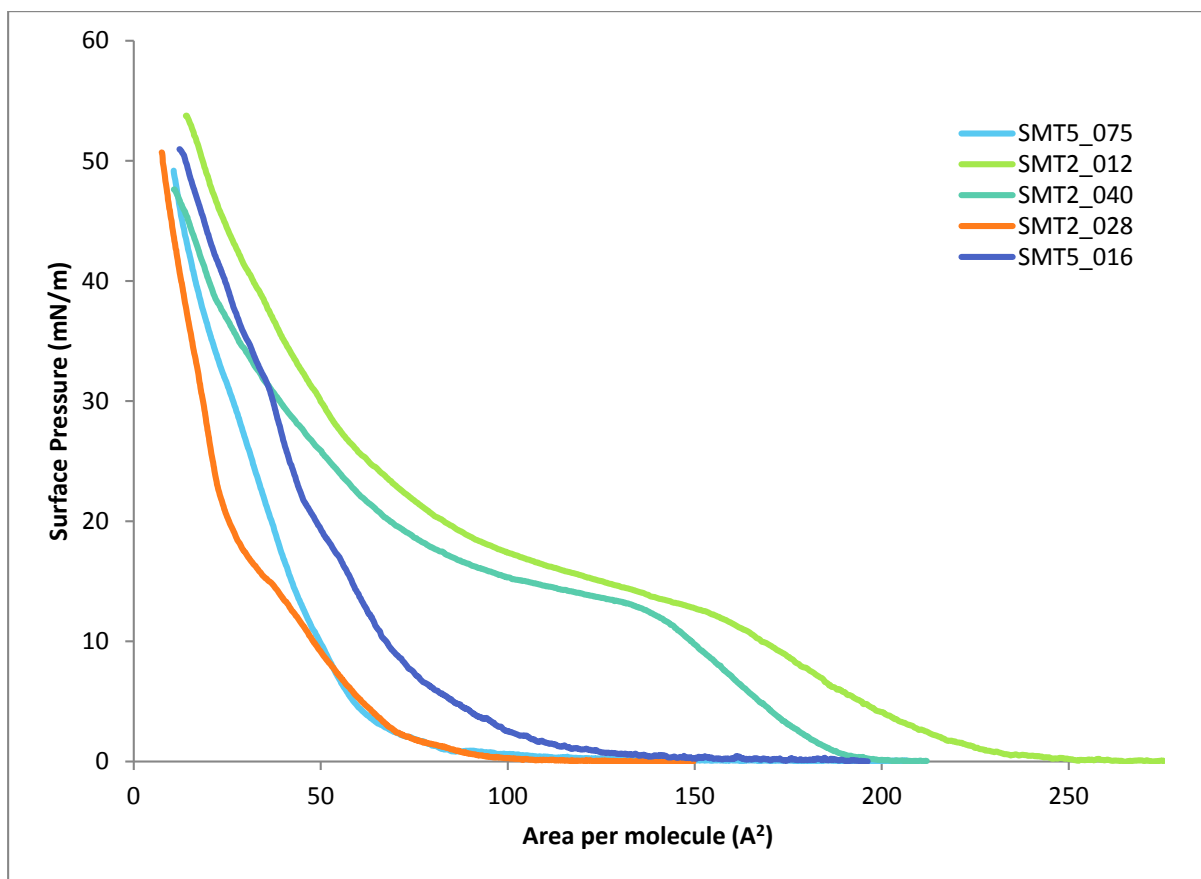
Figure 4.4: Isotherms of the zinc porphyrin series

The porphyrins SMT5_075, SMT2_028 and SMT5_016 show three separate phases during monolayer compression, which is similar to the isotherm formed by a fatty acid. In these cases, the transitions from liquid condensed to solid state are more abrupt because their moieties are relatively short as compared to the porphyrins containing a hydrocarbon chain. The short size of the side groups attached to the zinc porphine produce a quicker transition from one phase to another when the barrier is compressed.

The other two materials, SMT2_012 and SMT2_040, have more complicated phases with a relative flat regions (approximately in the range from 80 to 150 A^2), in which the molecules are being reoriented when the barrier is further compressed between the liquid expanded and liquid condensed phase. During the phase change from liquid expanded to liquid condensed-liquid expanded phase, the molecules are squeezing each other. For the phase transition corresponding from liquid condensed-liquid expanded phase to liquid condensed the molecules of the materials SMT2_012 and SMT2_040 are rotating over and orientating themselves progressively until they reach a completely ordered state (section 3.1.4 describes

the phase transitions occurred during the compression of the trough barrier). Further compressions results in the collapse of the monolayer at approximately 46 mN/m.

The take-off area (the area per molecule at which the surface pressure increases above zero) is significantly larger for SMT2_012 and SMT2_040 than for the rest of the materials. SMT2_012 shows a larger area take off area, attributed to the fact that the length of the SMT2_012 alkyl chain is longer than any other porphyrin in the study. At the same time, a longer chain results in increased steric hindrance for the packing of SMT2_012 compared to SMT2_040. It is evident that the longer the side group attached to the zinc porphyrin, the highest the take-off area. The take-off area for the materials follows the trend SMT2_012 > SMT2_040 > SMT5_016 > SMT5_075 > SMT2_028.

The SMT2_028 and SMT5_075 shows a very similar isotherm at early stages of the barrier compression, however, as the monolayer is compressed the area per molecule occupied by the SMT5_075 is slightly higher due to the extra benzene attached to the porphine.

At pressures above 15 mN/m when compressed into the solid state the isotherms are closer together for the five porphyrins than when in their liquid phases.

4.1.3.3 AFM

Upon fabricating solid state films the porphyrins have less freedom to move, and as a result, the film structure plays an important role in determining the sensitivity of the sensor films. Figure 4.5 shows AFM images of five samples each consisting of four LS layers of their respective zinc porphyrin on a flat silicon substrate. All samples were deposited at a surface pressure of 15 mN/m.

SMT2_012:
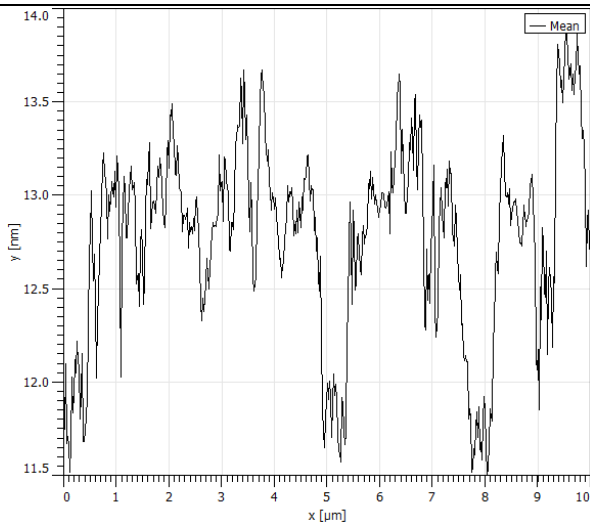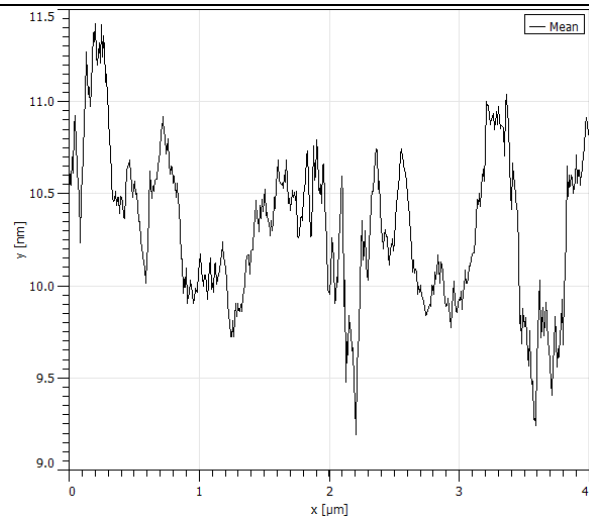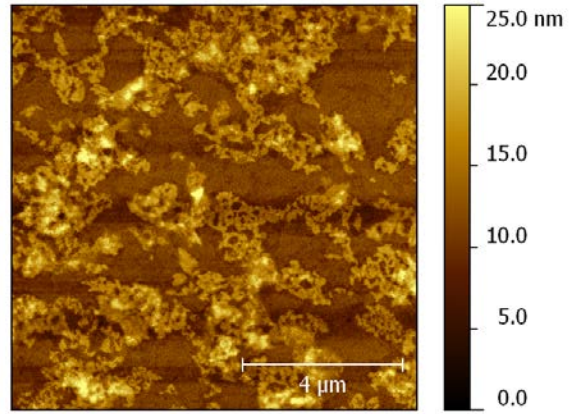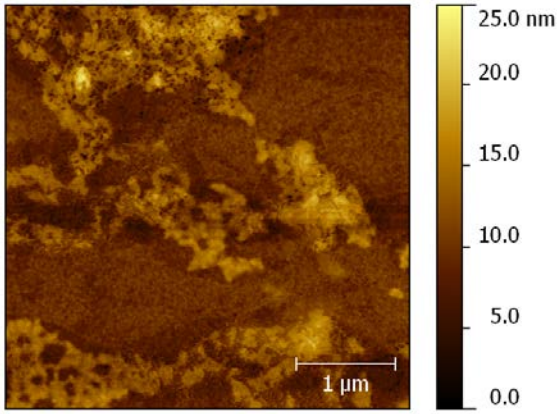
SMT5_016:
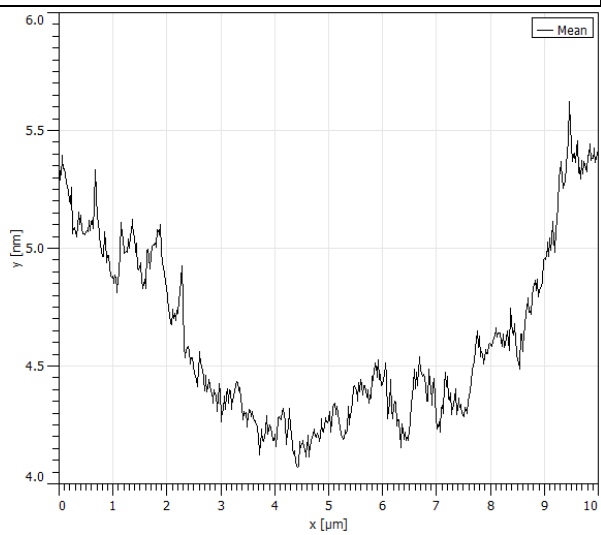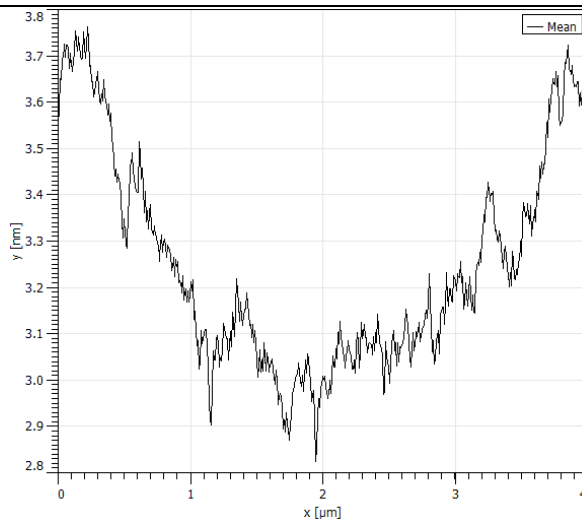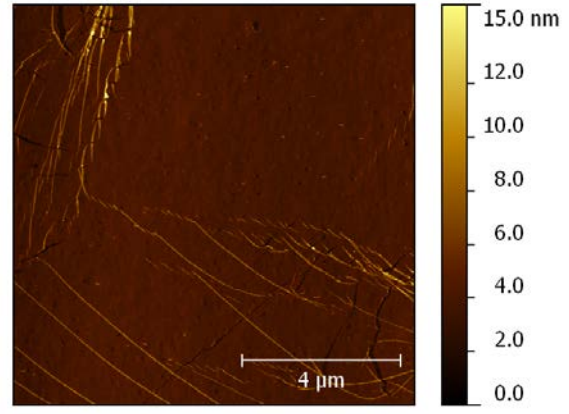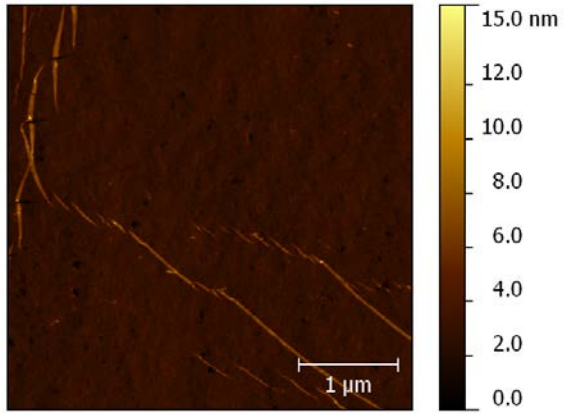
SMT2_028:
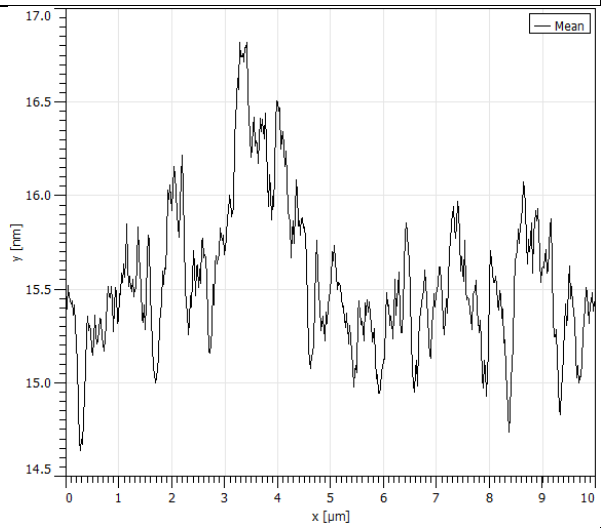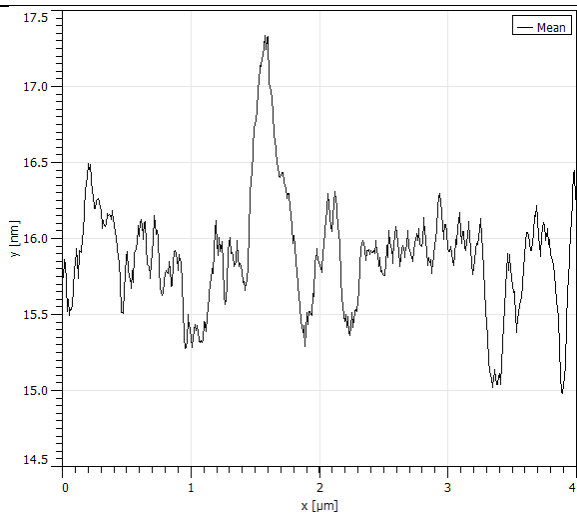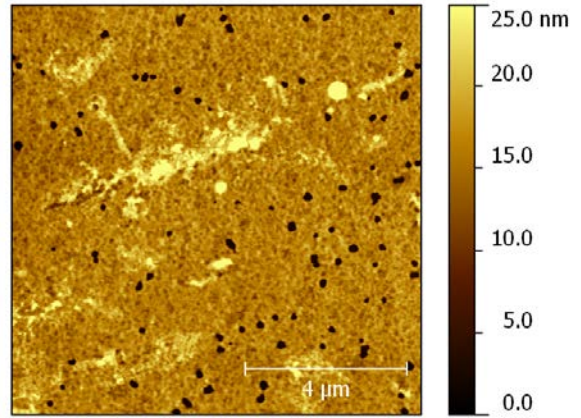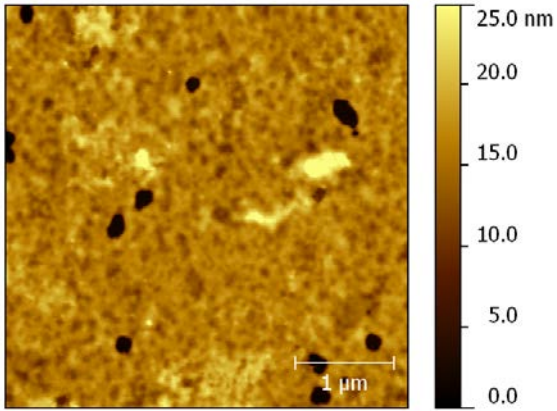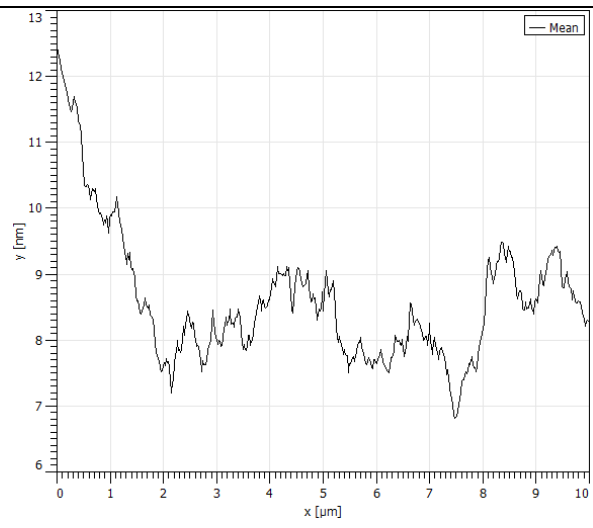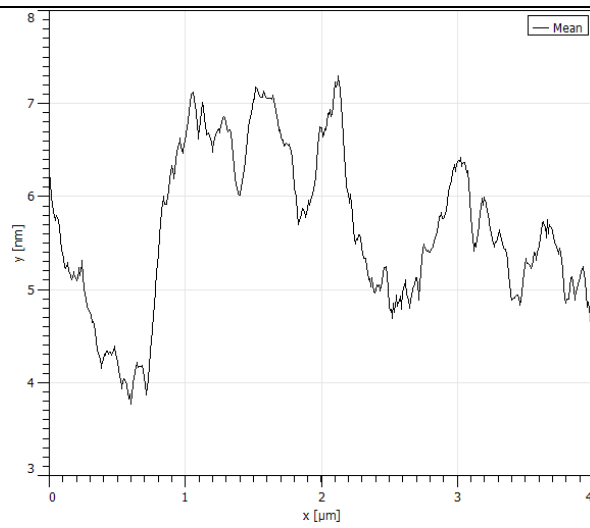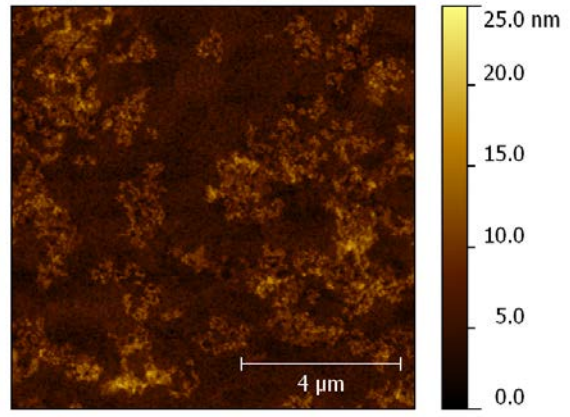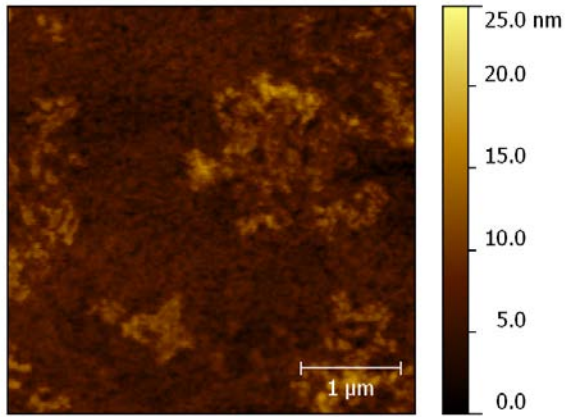
SMT2_040:

SMT5_075:
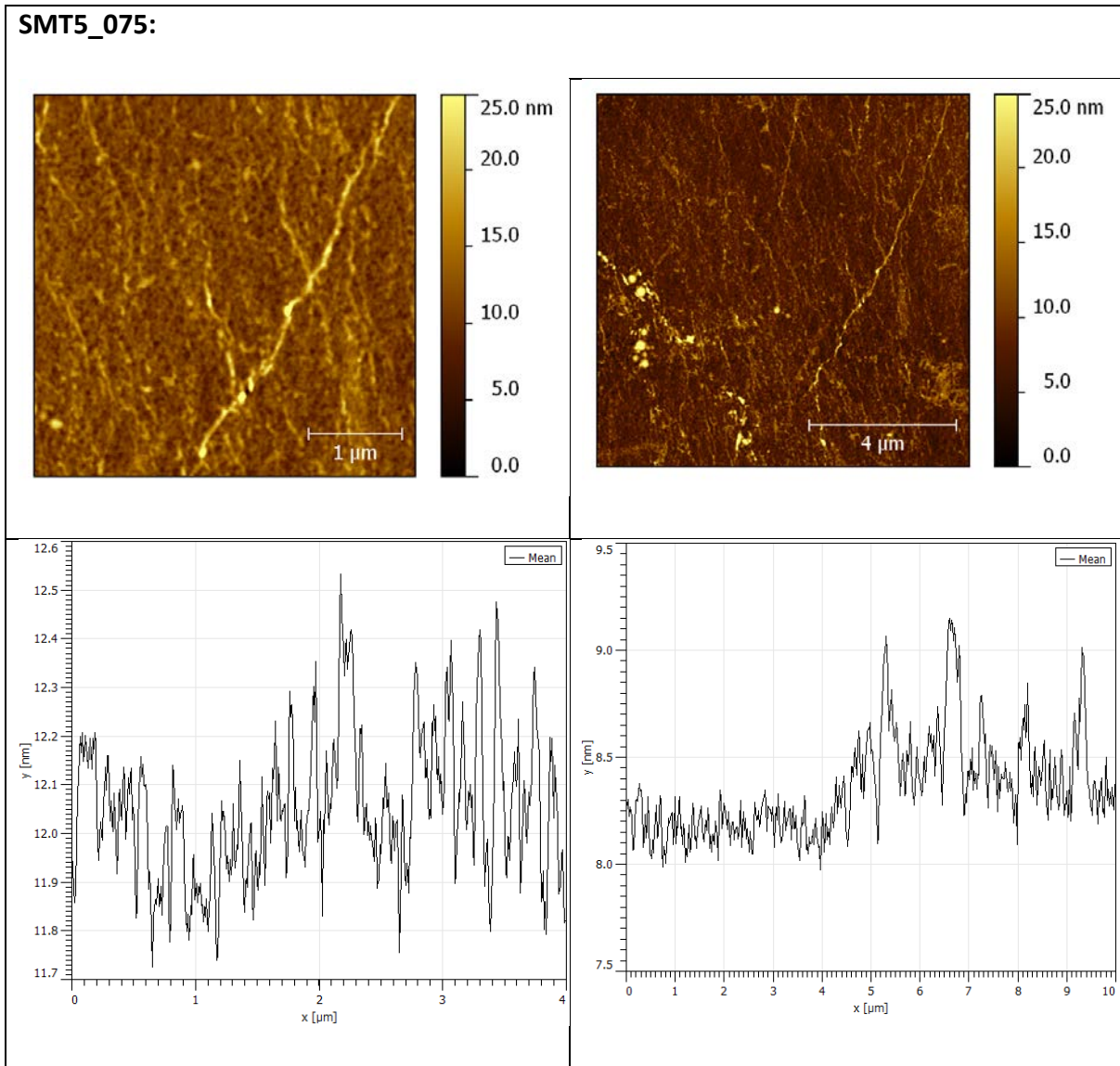
Figure 4.5: AFM images and roughness analysis of five LS films of the zinc porphyrins deposited at 15 mN/m.

The SMT2_040 sample appears to have different patches of thick material, resulting in the formation of different domains with various thicknesses among the sample. In the image which corresponds to the SMT2_012 all the silicon is covered with porphyrin. Both films, SMT2_012 and SMT2_040 appear to have quite open structures with significant area of void between the porphyrin molecules. The lighter areas can be interpreted as the peaks in which the porphyrin is accumulated.

The image of the SMT5_075 suggests a formation of wrinkles aligned in the same direction, which could be the result of the compression of the film. There are some spots over the

surface, which could be identified either as impurities or as an aggregated cluster of molecules.

The SMT2_028 sample shows small circular holes that cover part of the total area. It is very possible that the uncovered spots are a result of a dewetting process, however, it is also possible that no material was deposited there in the first place (the deposition was uneven). The rest of the film is fairly even, presenting a varying height from 15 to 17 nm, as depicted in the surface roughness analysis graph.

In the image of the SMT5_016 it is shown a film containing little holes and what appear as long wires on the top of the film. However, it is more likely to consider them as wrinkles of material caused during the compression of the monolayer. The material also shows cracks on the film. Despite the fact that the sample shows various defects within the film, most of the area is fairly homogenous.

By comparing the structures observed for SMT2_012 and SMT2_040 effects due to the size of the alkyl chain attached to the benzene ring can be determined. It is noticeable that the porphyrin SMT2_040 forms a more homogenous layer because it forms a less pronounced areas form by bulky material. On the other hand, the SMT2_012 seems to have more deposited material over its surface and that can be observed in the heights of the peaks which vary from 9 to 14 nm. As a result, a more inhomogeneous layer is presented in the SMT2_012, which has a longer alkyl chain within the amine functional group.

Similarly, the SMT5_075 and the SMT2_028 films vary only in the presence of an extra benzene in the SMT5_075 which gives the material a different conformation when it was deposited: it is shown that the image of the SMT5_075 lacks holes after the addition of the extra benzene, also the areas of bulky material are greatly decreased. It is possible that the addition one benzene in the material gives a variation in its molecular flexibility, and with that, a completely different film is formed.

In a similar case, the samples of the SMT5_075 and the SMT5_016 can be compared to determine the effects of changing the functional group attached to the two benzene rings (either hydroxyl or OMe). Both films appear to have buckling as a result of compression, but in the case of SMT5_016 the wrinkles are less aligned and also they are not as frequent nor

as thick as in the SMT5_75 sample. Overall, the SMT5_016 has a more homogeneous and continuous surface area despite the occurrence of cracks.

4.1.3.4 Solution Spectroscopy (response to analyte in solution)

The different zinc porphyrins have different absorption strength due to the variety of the side groups found in the materials. In order to standardize the response of the sensing materials, a normalization process was implemented. The normalization involved scaling the peak intensity after the Soret band to unity, in other words, all the responses will be considered as a fractional change in absorption. Figure 4.6 shows the absorbance spectrums of the porphyrin solutions once they have been normalized.
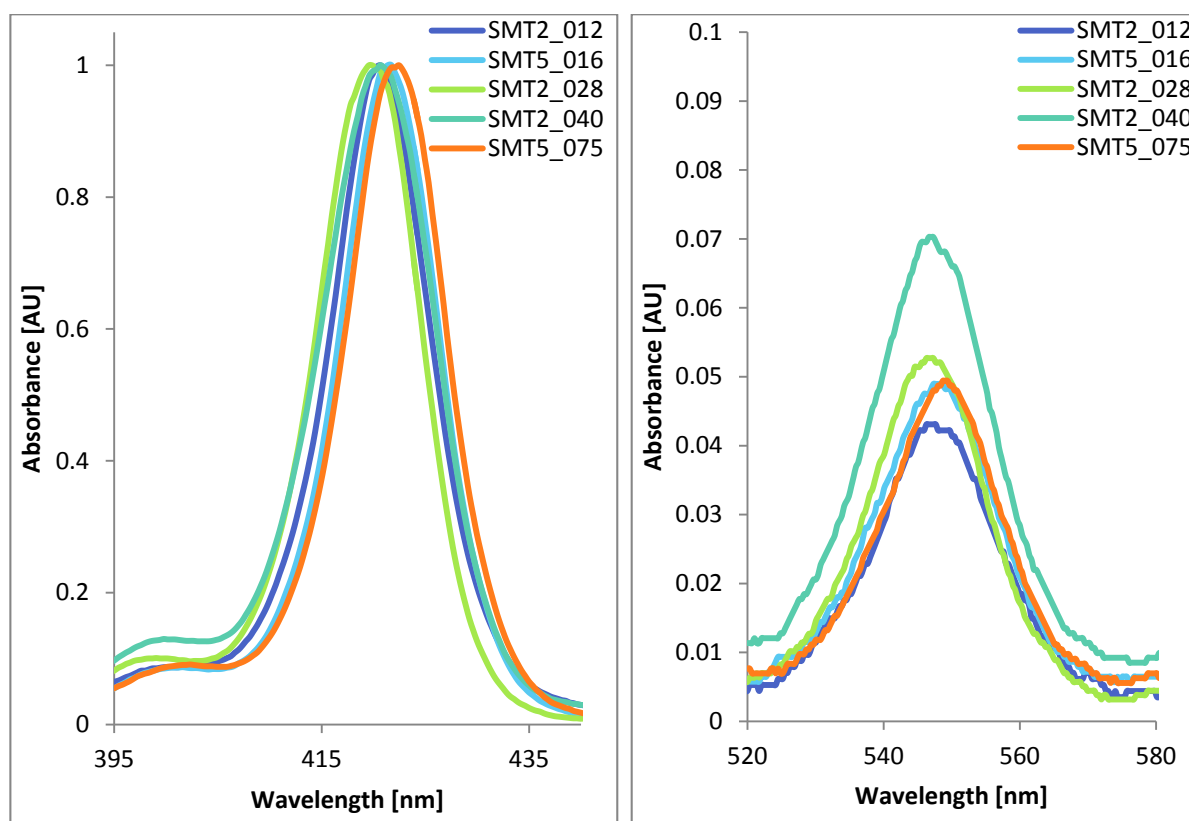
Figure 4.6: Closer look into the absorbance spectrum of the zinc porphyrin solutions. Left: normalized Soret band peak, right: Q band located approximately at 545 nm.

It is important to mention that the side groups not only gives the materials different absorption strengths, but also a different location in the electromagnetic spectrum for its Soret peak and Q bands. Table 4.4 summarizes the position of the Soret band peaks and their

Q bands. Note that the values in the table have an estimated error of 0.48 nm, which is the optical resolution of the Ocean Optics USB2000+ fiber optic spectrometer.

	SMT2_012	SMT5_016	SMT2_028	SMT2_040	SMT3_075
Soret Band	420±0.5nm	421±0.5nm	419±0.5nm	420±0.5nm	422±0.5nm
Q band 1	547±0.5nm	547±0.5nm	547±0.5nm	546±0.5nm	548±0.5nm
Q band 2	589±0.5nm	588±0.5nm	585±0.5nm	588±0.5nm	589±0.5nm

Table 4.4: Absorption spectrum of the zinc porphyrins in solution.

The analysis in solution between the porphyrin molecules and the liquid analyte reveals the interaction of the dissolved and therefore non- aggregated material and the amine species to be bound. In figure 4.7, the absorption spectrum of SMT5_075 before and after exposure to benzylamine is observed. The spectral change of the solution is also illustrated in the figure, in which the corresponding change in absorbance is plotted as a difference spectrum (an exposed spectrum subtracted from an unexposed spectrum).

Throughout this thesis difference spectra are obtained by subtracting the exposed spectrum of the porphyrin (after being exposed to the analyte) from the non-exposed spectrum. A difference spectrum may be used to quantify the amount to which the original porphyrin spectrum is modified by the reaction caused by the analyte. Since both spectrums (exposed and non-exposed) had been normalized, the graph can be interpreted as a percentage change in absorption at a specific wavelength. In this way the largest changes in absorbance can be observed as positive and negative peaks, as depicted in figure 4.7. The green line shows a maximum negative peak located at 421±0.5 nm and a maximum positive peak located at 434±0.5 nm.

It is noticeable that exposure to the amine analyte caused a significant shift in the position of the Soret absorption peak, going from 421 to 432 nm. Their respective Q bands are also altered upon exposure, shifting from 588 to 606 nm and from 548 to 565 nm respectively. It is crucial to mention that the value of the maximum absolute value for each analyte and sample occurs at different wavelengths.

Zinc porphyrins are notoriously good at coordinating nitrogen containing ligands; so it is theorized that this interaction arises with amines too. The shift in the Soret peak band occurs because the zinc metal is marginally pulled out of the plane of the porphyrin in the 5-coordinate complex, formed when the amine interacts [5].
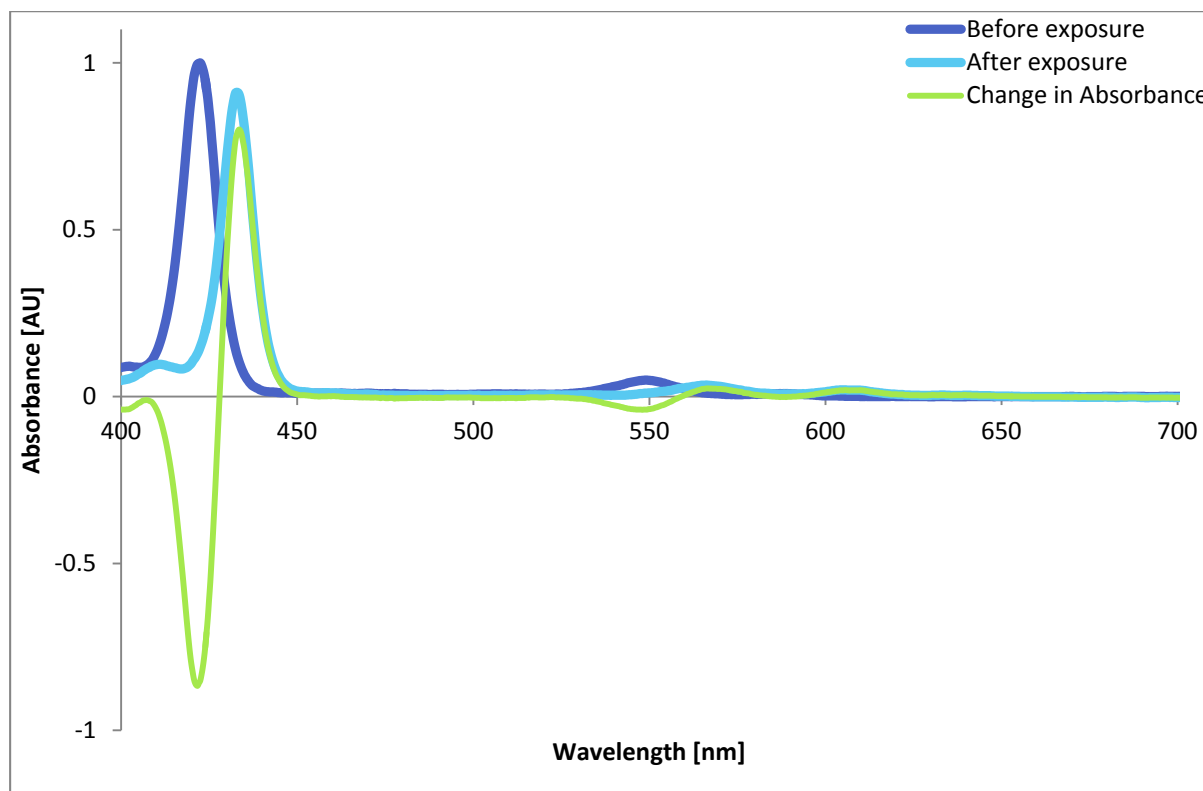
Figure 4.7: Uv-visible absorption spectra of SMT5_075 in solution and its exposure to benzylamine.

The responses of different amines in solution were measured for the five zinc porphyrins in order to better understanding of the analyte-porphyrin reactions. The maximum absorbance wavelength shift and the change in absorbance was plotted for the various analytes. Once again, all the results were normalized, so they could be directly compared with other porphyrin/analyte pairs.

Figures 4.8 and 4.9 show the maximum change in absorbance for the SMT5_075 when exposing to various amines. The same process was carried out with the rest of the materials. The single case of the SMT5_075 is shown in figures 4.8 and 4.9 as an example.

Figure 4.8 shows the difference in the response to three classes of amines: primary (N-butylamine), secondary (dibutylamine) and tertiary (tributylamine). In like manner, secondary

and tertiary amines can also be compared, as in the case of diethylamine and triethylamine, dipropylamine and tripopylamine, and dibutylamine and tributylamine.

It is clear that a primary amine induces a higher change in response, followed by a secondary and finally a tertiary amine. So, the bigger the analyte molecule, the less the change in absorbance. The effect can be explained in terms of the accessibility to the nitrogen lone pair: a "spidery" and bulky molecule will have more difficulty to access to it, whereas a small molecule will pass easily.

It is also noticeable that this also applies to amines that are in the same category: i.e. diethylamine is less bulky than another secondary amine such as dibutylamine, so the response is notably higher. In figure 4.8 diethylamine shows the highest change in response, however, the porphyrin was not exposed to its corresponding primary amine (ethylamine).
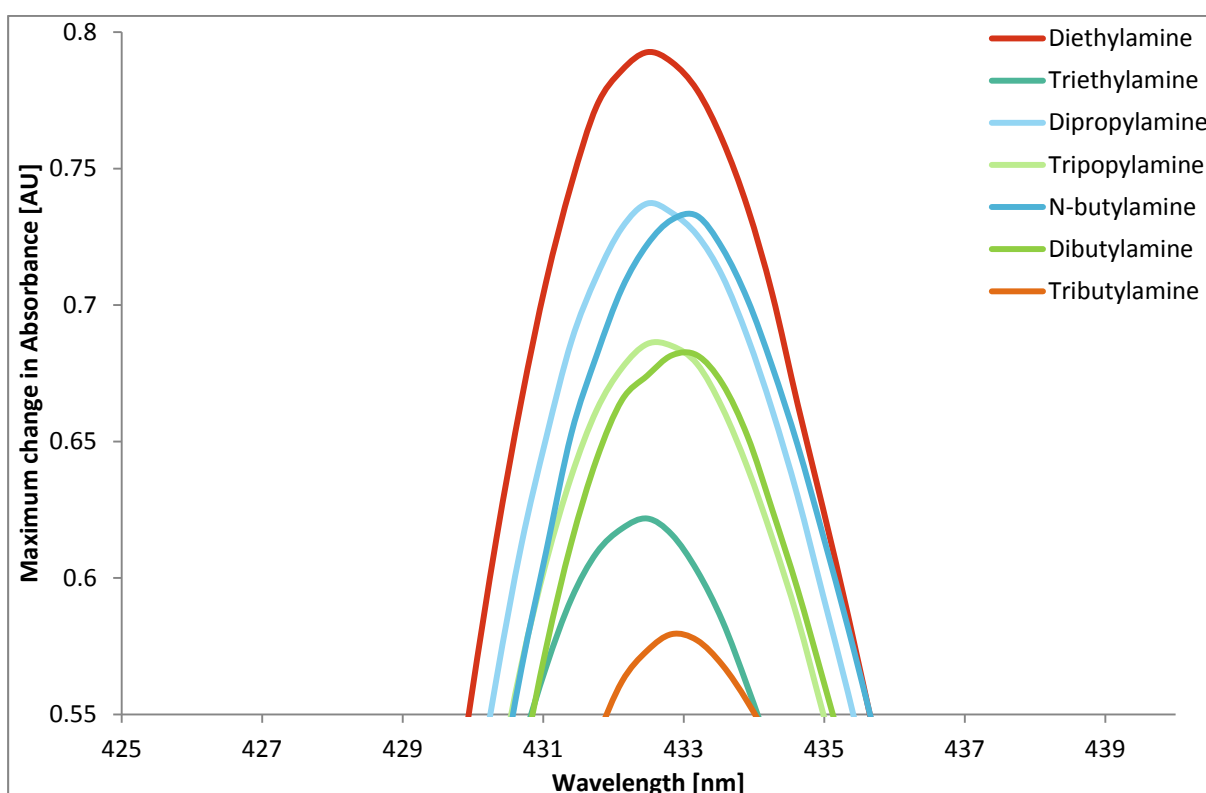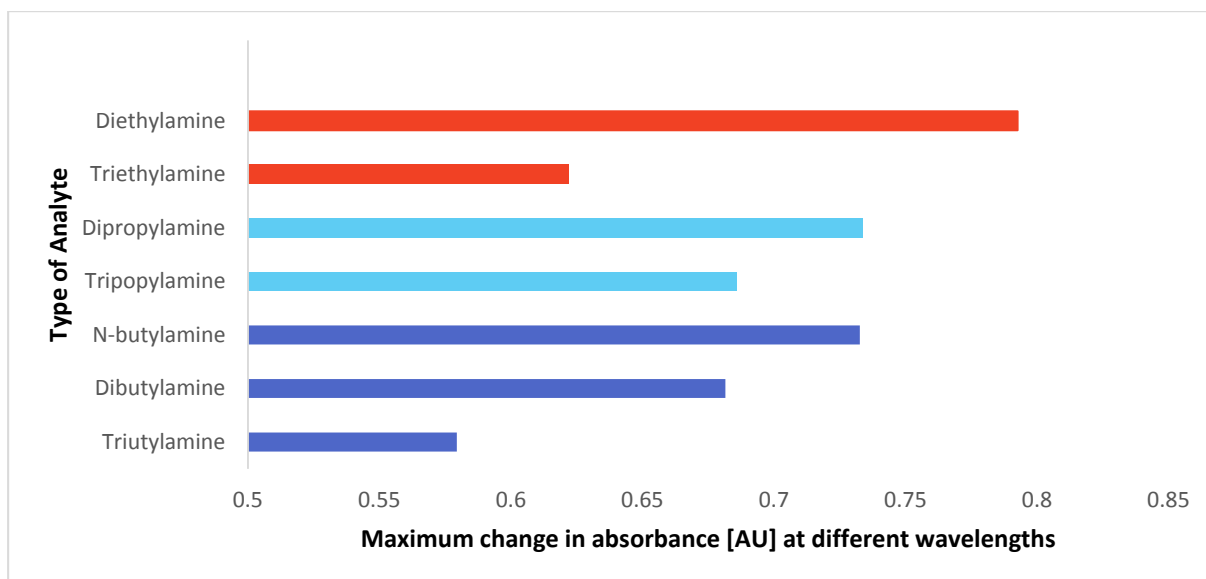
Figure 4.8: Top: Spectrum of the corresponding change in absorbance of SMT5_075 to primary, secondary and tertiary amines in a range from 425 to 440 nm. Bottom: Maximum change in absorbance at different wavelengths.

Figure 4.9 shows the change in absorbance of primary amines with the same functional group but different number of carbon atoms attached to the central nitrogen, i.e.: propylamine (3), n-butylamine (4), pentylamine (5), hexylamine (6), heptylamine (7) and octylamine (8). The

results follow the same trend, in which the higher the number of carbons attached to the functional group, the less the change in absorbance induced by the amine.
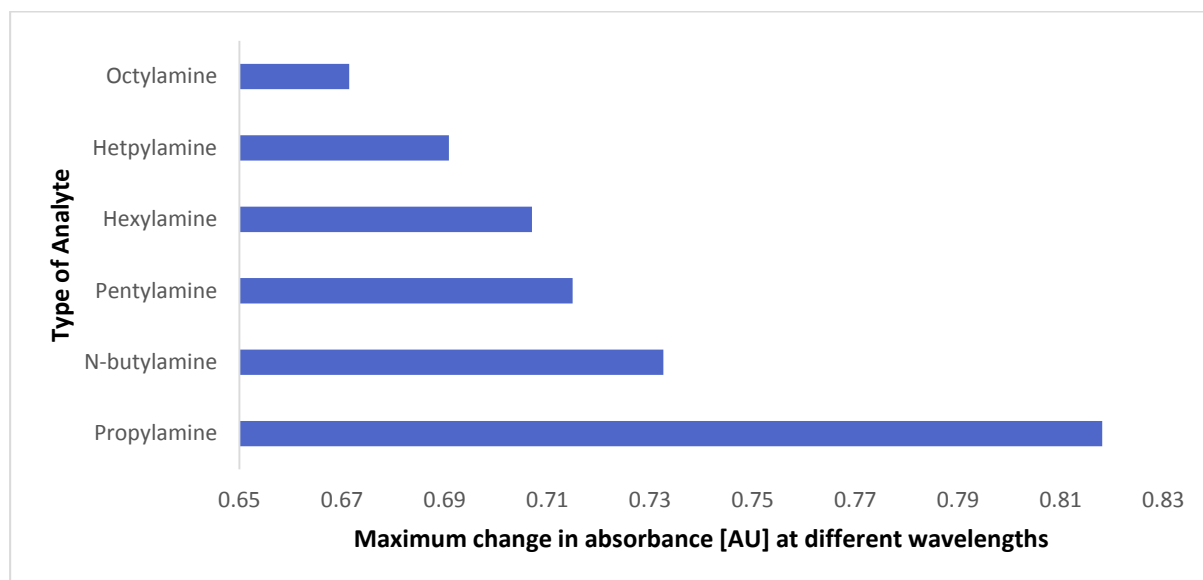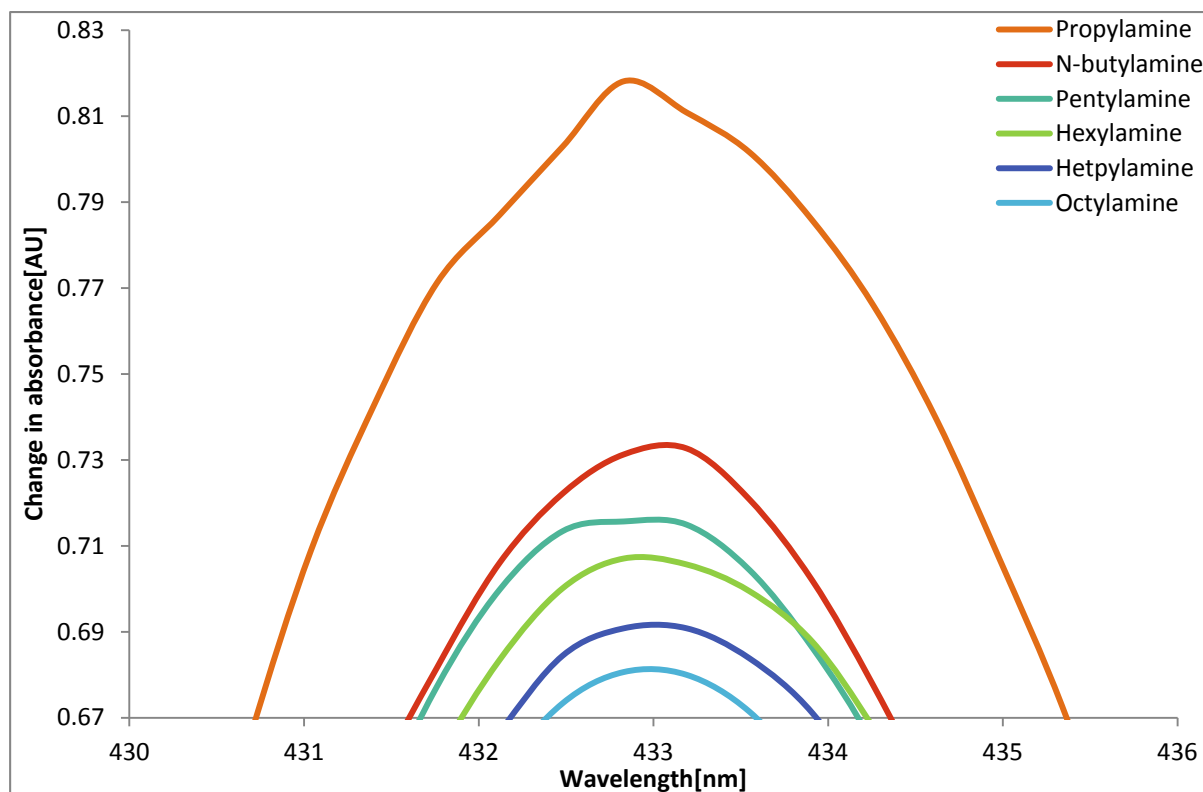

Figure 4.9: Top: Spectrum of the corresponding change in absorbance for the SMT5_075 porphyrin to primary amines with different carbon chain sizes attached to the central nitrogen, in a range from 430 to 436 nm. Bottom: Maximum change in absorbance at different wavelengths.

Figure 4.10 is a table of results of the materials exposed to five different amines. The analytes are arranged by molecular weight, from the lightest (n-benzylamine) to the heaviest (tributylamine).

All zinc porphyrin solutions were made at the same concentration (0.02 mg/ml). To quantify the response induced by the analytes in the porphyrin solutions 100 µl of the pure amine (~99% purity) was added into the cuvette; that volume is enough to saturate the porphyrin (in which no more sites are available to bind with analyte molecules) so no further spectral changes are observed even if the analyte volume is augmented. The injected volume of the different amines was kept constant for all the analyte/porphyrin complexes, and since the volume is enough to saturate the porphyrin solution, the reactions presented in figure 4.10 shows a maximum reaction response in the porphyrin solutions.

Figure 4.10 shows the maximum change in absorbance presented for every amine/zinc porphyrin complexes. The corresponding value of the maximum change in absorbance is a representation of the highest peak presented in the difference spectrum, described in section 4.1.3.4 and depicted in figure 4.7. The value is taken is the highest peak value, either positive or negative, depending of which one is higher. The difference peaks occurs at various wavelengths regions, that is to say that the maximum change in absorbance for an analyte does not necessary happen at the same wavelength for every zinc porphyrin and this effect can be attributed to the different side groups presented in the sensing materials.

In order to simplify the results and directly compare the porphyrin/amine complexes, the reactions in the figure 4.10 were plotted based on the highest numerical value presented at the difference spectra, i.e. the maximum change in absorption.
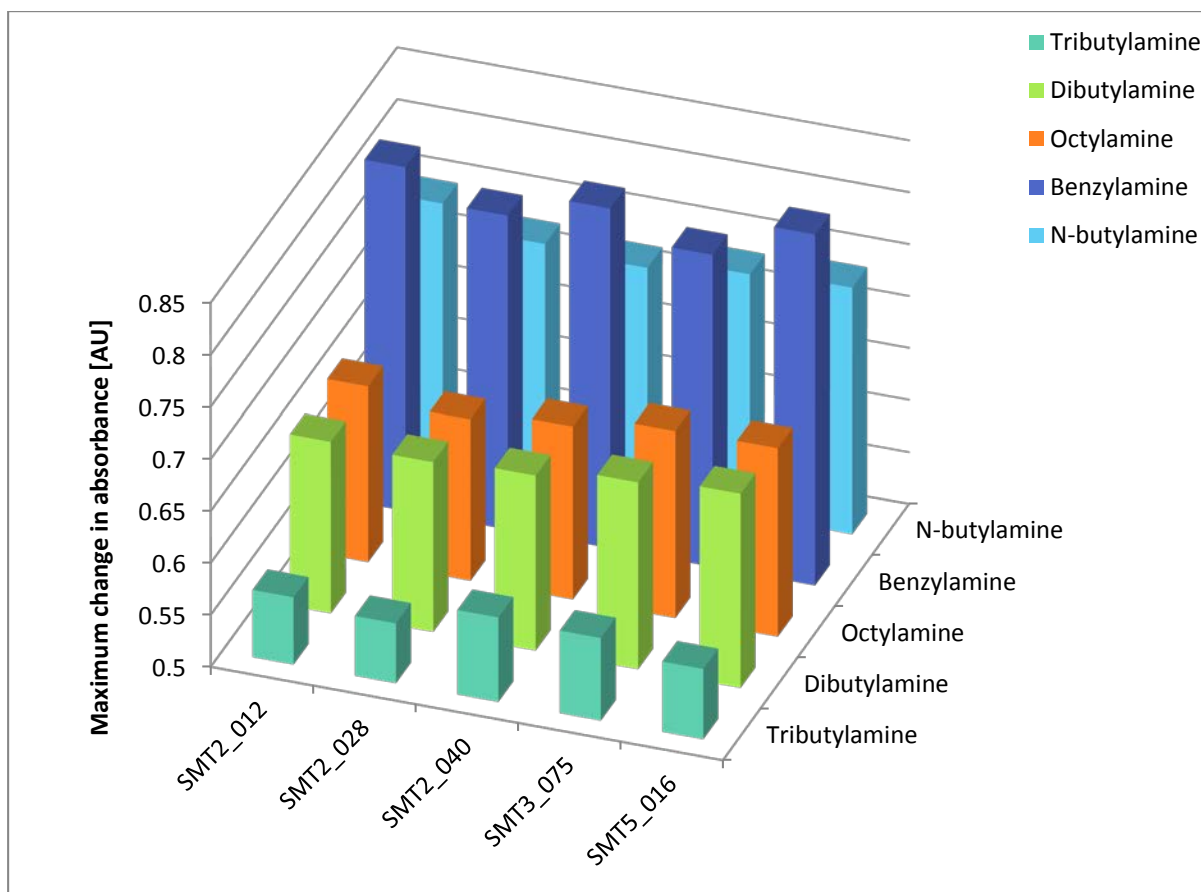
Figure 4.10: Histogram of the maximum absorbance changes of the five zinc porphyrin solutions when exposed to each of the five amines.

It is noticeable that all analytes show a similar strong response, except for tributylamine. When the porphyrins are in solution, they are free to interact with the analyte because they are continually moving through the available space, which facilitates interactions because steric effects may limit access to the active sites. However, for tributylamine the process is hindered since the nitrogen cannot easily interact directly with the porphyrin because of the three carbon chains attached to it preclude a direct reaction, so the analyte itself is a source of steric hindrance. As a result, a smaller absorbance change is observed for all the zinc porphyrins upon exposure to tributylamine.

4.1.3.5 LS film properties of porphyrin (response to analyte in films)

Solid films have some advantages over liquid systems; firstly, they do not have the inconvenience of a possible leaking or evaporation of the sensing solution. Another advantage of the LB solid films gas sensors is the reversible interaction of the gas with the surface of the

solid state materials [6]. To enhance those characteristics, solid films of the porphyrins were produced.

All the porphyrins deposited on a glass substrate contain the same number of deposited monolayers and were made at the same target pressure of 15 mN/m. Table 4.5 depicts the Soret bands in the materials along with the firsts Q band. The second Q bands (with a longer wavelength) were no longer perceived by the UV-vis spectrometer.

	SMT2_012	SMT5_016	SMT2_028	SMT2_040	SMT3_075
Soret Bands	439±0.5nm	444±0.5nm	441±0.5nm	436±0.5nm	441±0.5nm
Q bands	559±0.5nm	557±0.5nm	558±0.5nm	558±0.5nm	557±0.5nm

Table 4.5: Absorption spectrum of the zinc porphyrins deposited on a glass substrate.

The Soret and Q bands are significantly different from the ones presented in solution due to the absence of solvent effects and the immobilization and possible aggregation of porphyrin molecules. The structure of the solid films plays an important role in determining sensor activity. The electrophilic nature of the side groups along with the physical dimensions of the molecule results in a different interaction between the porphyrin molecules. That is to say that the deposition rate and the way the molecules lie down on the water-air interface at a specific target pressure before being deposited will result in a different molecular packing of the molecules.

Figure 4.11 demonstrates a typical exposure/recovery graph of a 3 LB layers sample of SMT5_075 deposited at 15 mN/m when exposed to 1.05 ppt of benzylamine; the figure shows the absorbance kinetics over time of a 452 nm wavelength in which the absorbance difference is maximum (see figure 4.13). Each cycle is composed of two different stages: the exposure, in which the sensor is exposed to the vapour amine for duration of 300 seconds; and the recovery, in which the sensor is flushed with pure nitrogen and gently heated to outgas the porphyrin film returning it back to its initial state, for a total duration of 600 seconds. The application of heat during the recovery stage by the Peltier heater helps to overcome the binding energy of the charge-transfer bond between the amines and the zinc porphyrin which is relatively weak, so full recovery of the sensor is realized during this stage of the cycle [7].

During the exposure the sensor is at 25 °C, and during recovery the temperature is raised to 65° C.

Porphyrins are sensitive to abrupt changes of temperature [8]. In order to corroborate that the porphyrins were reacting to the analyte and not the change of temperate from 25 °C to 65°C, a control experiment was carried out by flushing pure N_2 during the exposure and recovery times. In all cases, it was shown that the absorbance spectrum of the porphyrin samples deposited on glass did not present a spectral change during the heating process. This fact corroborates that the absorbance difference presented in the samples was produced by the analyte and not by the temperature. For more details, refer to the experimental techniques chapter (section 3.5.1e).

In a similar manner, to confirm that the analytes vapours are transparent in the spectral range of interest for porphyrins (from 350 to 850 nm), a second control experiment was performed in which no sample was placed in the chamber. The absorbance remained null for all analytes during the exposure to the analytes and the recovery (clean nitrogen), which means that the shift of absorbance was produced by the porphyrin/analyte reaction and not by the vapour itself.
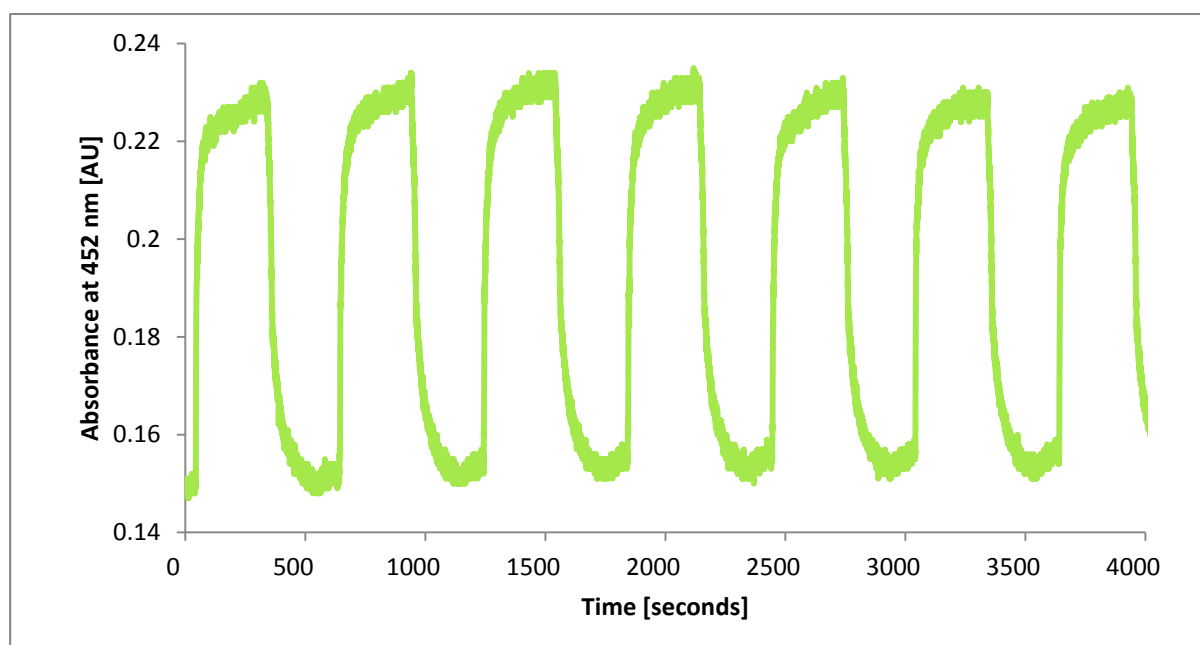

Figure 4.11: The absorbance change observed at 452 nm for the SMT5_075 sample during exposure and recovery cycles to benzylamine.

Figure 4.12 shows the spectrum of a 3 LB layers sample of SMT5_075 before and after being exposed to 1.052 ppt of benzylamine vapour. As mentioned in section 4.1.3.4, the materials used in this study have different absorption strengths due to the various side groups attached to the porphine. With the objective of standardizing the responses induced by the analytes, a normalization process was carried out. The process involved scaling the Soret band of the non-exposed porphyrin to unity; likewise, the same scaling factor is used for the exposed spectrum. As a result the normalization process consider all the responses as a fraction change in unexposed and is useful to compare the various porphyrins/analyte interactions directly.

The normalized spectral change of the 3 LB sample of SMT5_075 when exposed to 1.052 ppt of benzylamine vapour is depicted in the figure 4.13, in which the corresponding change in absorbance is plotted as a difference spectrum, i.e. an exposed spectrum subtracted from an unexposed spectrum. The difference spectrum or spectral change graph is a useful tool to visualize the wavelengths at which a change in absorption is taking place. Interestingly, the maximum change of absorption occurs at 452.5±0.5 nm and not in the Soret band peak. This is because for this particular porphyrin-analyte interaction the maximum absorbance peak position only shifts very slightly upon exposure and the maximum change (and therefore optimum sensitivity) actually occurs at a wavelength on the upper side of the Soret band.

It must be noted that all the liquid amines being vaporised to produce the analytes are held at 25 °C prior to delivery into the sample chamber. Since their vapour pressures are different, the concentrations delivered to the test chamber will not be the same. So, they are different across the range of amines but will be consistent for each amine. The vapour pressures for the primary series follows the trend n-butylamine (molecular weight, MW=73) > benzylamine (MW=107) > octylamine (MW=129), and that for the butylamine series follows the trend n-butylamine (MW=73) > dibutylamine (MW=129) > tributylamine (MW=185) [9].

The calculated concentration corresponding to the vapour pressure induced at 25° C by the water bath in the analyte was 122.230 ppt of n-butylamine, 2.763 ppt of dibutylamine and 0.135 of tributylamine. For the rest of the analytes, the produced vapour concentration was 0.920 ppt of benzylamine and 1.184 ppt of octylamine.
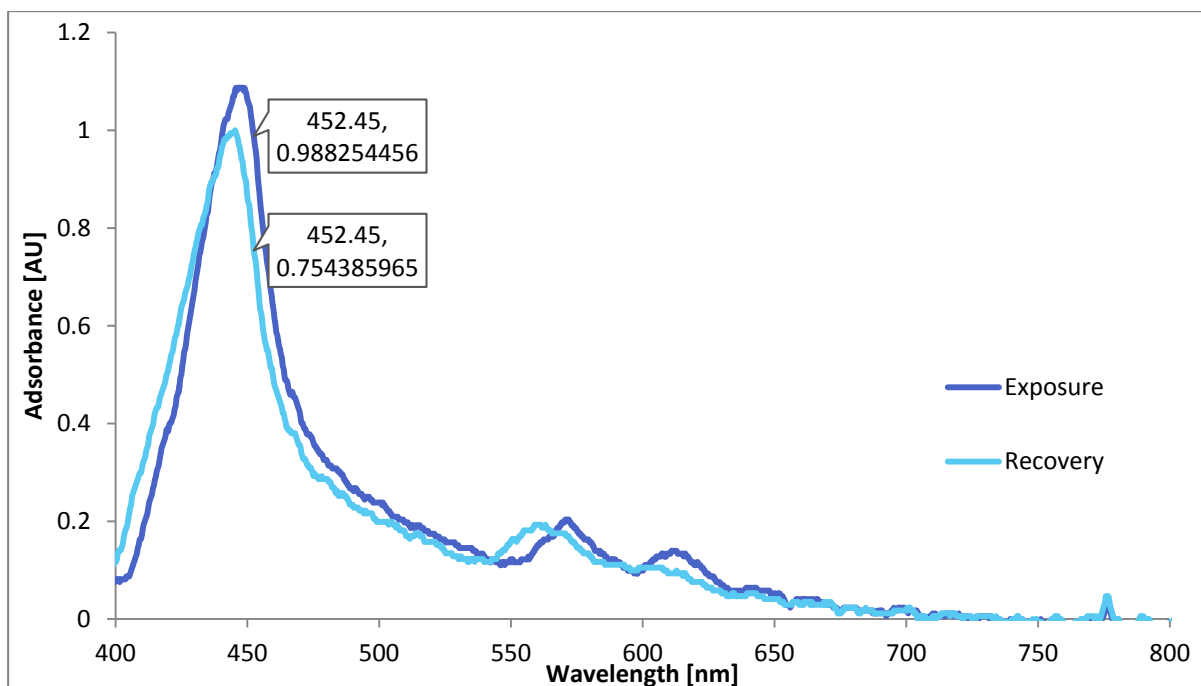
Figure 4.12: Exposure/recovery graph of SMT3_075 when exposed to benzylamine vapour at 25°C (1.052 ppt).
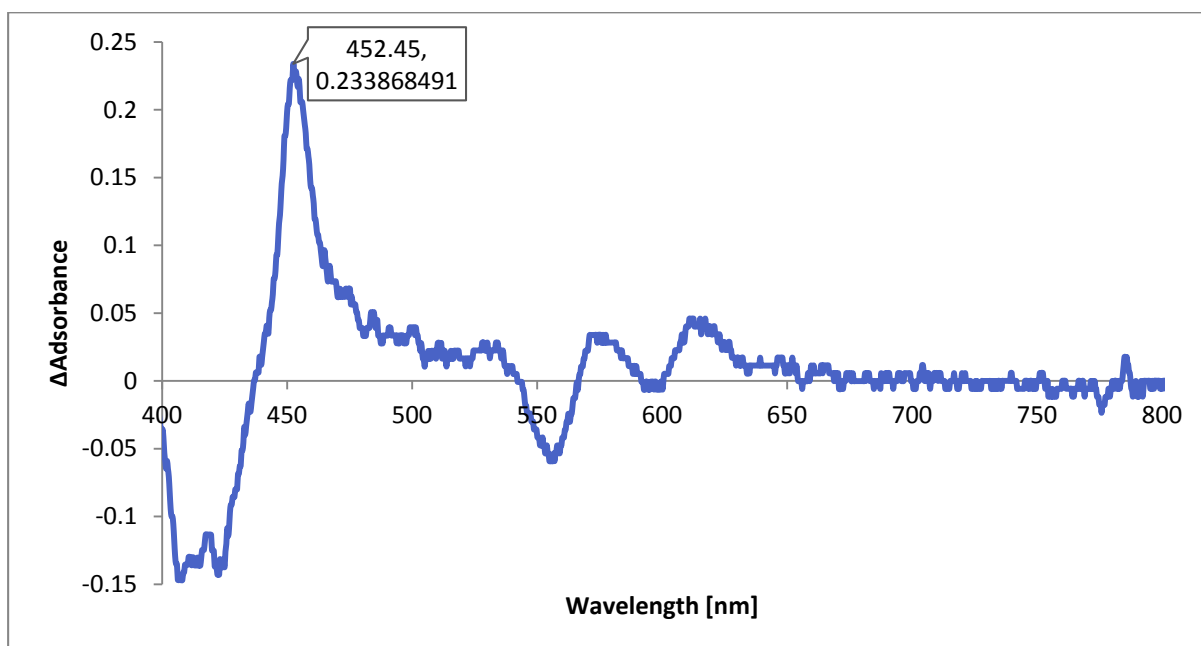
Figure 4.13: Difference in absorbance glass sample when exposing SMT3_ 075 and to benzylamine (1.052 ppt).

Figure 4.14 shows a table of results for the glass samples when exposed to the various amines. For primary amines, the trend in the response follows the logical arguments that as the size

of the molecule increases, reactions decreases due to slower diffusion. So, due to the small size of the n-butylamine, the molecules can easily go through the films without any problem; whereas for octylamine, it is observed that the response is significantly decreased.

Generally as the amines increase in size and molecular weight, the absorbance shift induced in the zinc porphyrins decreases i.e. primary amines invoked the greatest sensing response. Larger amines experience an increased difficulty travelling to active sites and penetrating into bulk layers of films and also induce the smallest spectral shifts in the zinc porphyrins compared to those induced by secondary amines.
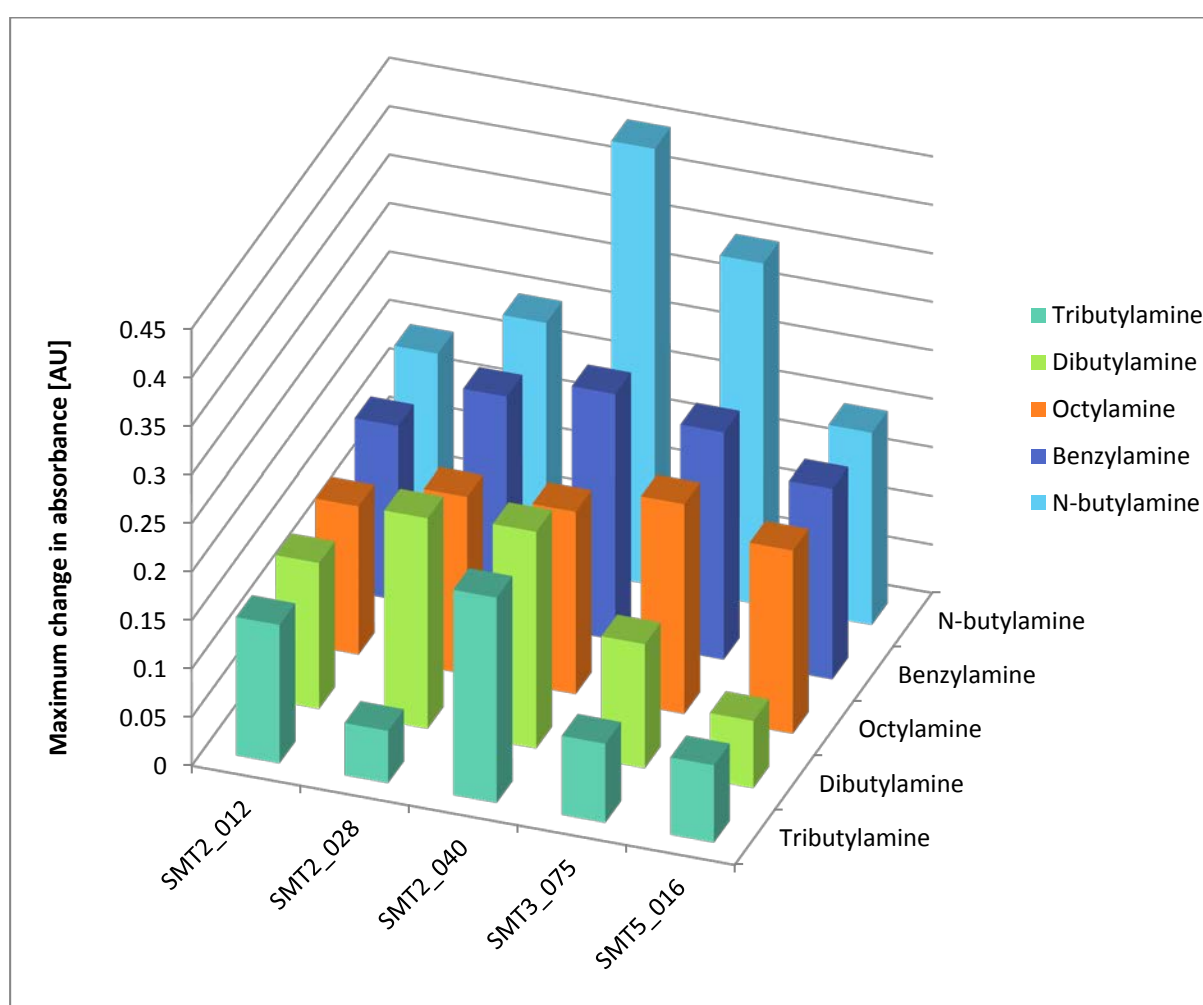
Figure 4.14: The average absorbance shifts of zinc porphyrins during exposure and recovery cycles of amine vapours.

The samples corresponding to SMT5_075 and SMT5_016 showed a good response variation between the primary and secondary amines. The comparison can be made with two analytes,

dibutylamine and octylamine, in which both share the same molecular formula and average mass.

For the tertiary amines, the longer carbon chains protrude from three points on the nitrogen atom effectively shielding the nitrogen atom and reducing its likelihood of binding, whereas for the primary amines, the nitrogen atom is at the end of the carbon chain and remains equally exposed for all the primary amines. It is believed that tertiary amines are restricted to surface interactions only [10]. Also, it is been hypothesized that the binding of secondary amines by zinc porphyrins results in a strongly asymmetric porphyrin ring distortion compared to the resulting from the binding of tertiary amines [2]. For all the zinc porphyrins films, the secondary amines always showed a higher response than the tertiary ones.

According to the electron donating substituent effects in the side groups (shown in figure 4.1), a strong electron donating interaction is expected for the –OH group, followed by the –OR group and finally the –NHCOR group. Despite the fact that the side groups play an important role in the activation of the porphyrin ring, it is also important to consider other variables in the system such as the porphyrin-porphyrin interactions that can lead to aggregation of molecules in the thin films. That aggregation parameter can be roughly examined using the isotherms and the AFM images. The porphyrins SMT2_012 and SMT2_040 have a better response overall because they show a more open structure, which allows the amine vapour to interact with the porphyrin ring.

A very uniform deposited layer, as in the case of SMT5_016, can be a drawback when considering gas sensing applications. Making the porphyrin films more porous increases the accessibility of the analyte to the central ring and allows an increase in the number of available porphyrin binding sites and thus leads to a larger spectral response and sensor signal [11]. A good example of this is SMT2_028, containing only electron donating side groups, is highly responsive to liquid analytes but after transferring it to the solid film, the material exhibits a much supressed level of response compared to the solution. This imbalance is attributed to the short side groups substituted onto the phenyl groups. The small side groups do not lead to sufficient separation of adjacent porphyrin molecules to prevent porphyrin/porphyrin aggregation. This prevents analyte vapours easy access to the central core binding sites within the LS films.

The response of the LS film of SMT2_040 is greater than that of film SMT2_012 for each corresponding amine. This is because the LS film of SMT2_040 possesses a higher molecular density and therefore a greater density of available sites for interaction with amine molecules [2]. In other words, the SMT2_040 is porous enough, whereas SMT2_012 is so openly structured that the response begins to become diluted. This implies that there will be an optimal porosity for the solid state film structure.

An alternative way to present the spectral changes of the sensing materials induced by the analytes is by plotting the non-normalized results (raw data) divided by the analyte concentration for each analyte molecule.

In other words, it represents a measure of the spectral change of absorbance induced by a single analyte molecule, and is a simple way to describe the magnitude of the reaction for each analyte.

However, the graph does not allow direct comparison between the porphyrins because they have different absorption strengths.

Figure 4.15 depicts the maximum change in absorbance for the different porphyrin/analyte complexes.
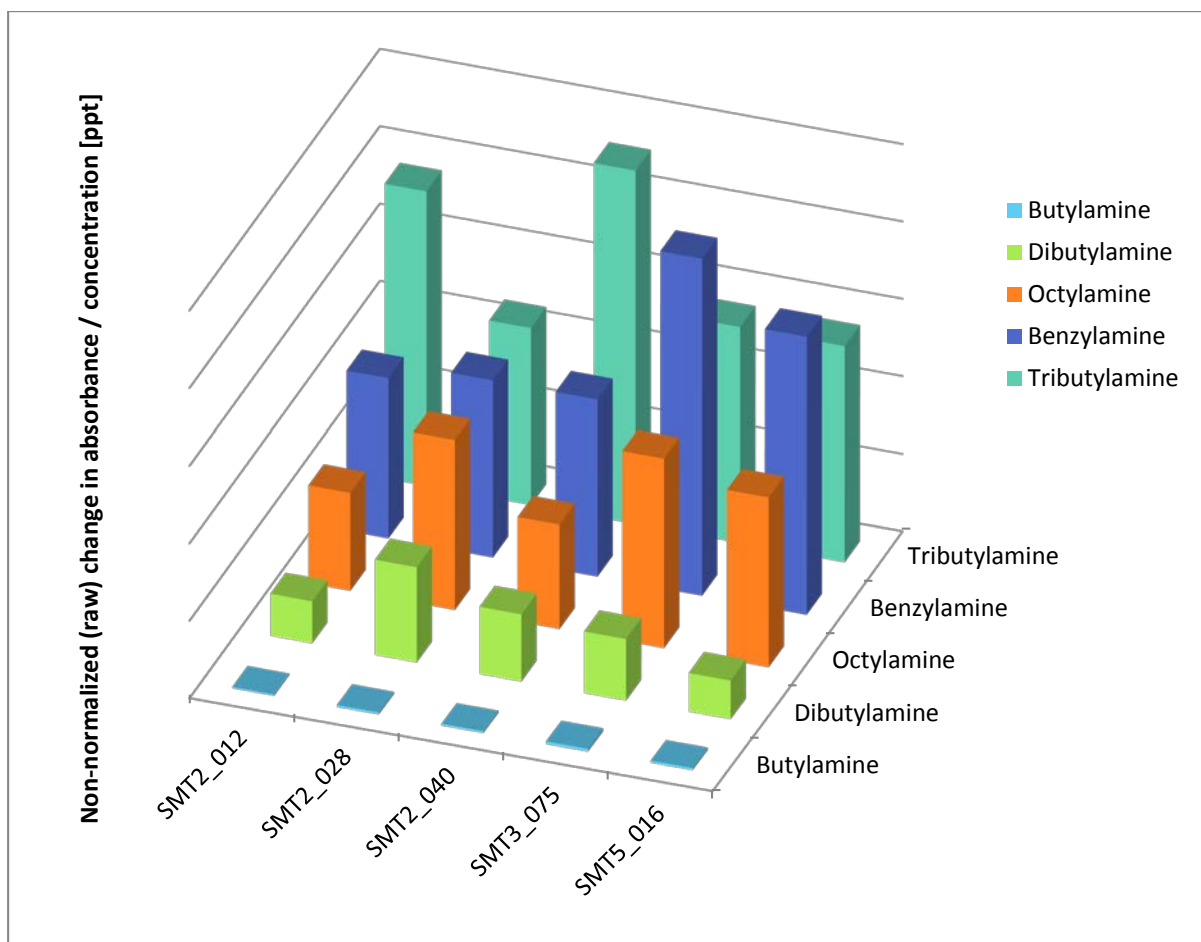
Figure 4.15: Response in film of the zinc porphyrins when exposed to amine vapours: 122.230 ppt of n-butylamine, 0.920 ppt of benzylamine, 1.184 ppt of octylamine, 2.763 ppt of dibutylamine and 0.135 of tributylamine. The response of the sensors are expressed as the magnitude of reaction of the porphyrins at a fixed concentration (single analyte molecule).

The dominating factor in the sensors response to primary, secondary and tertiary amines of the butyl amine series was the concentration of the gaseous analyte. However, it was expected that a higher magnitude of reaction in n-butylamine would be observed because there is just one long hydrocarbon chain attached to the nitrogen with the lone pair of electrons, so the interaction with the available porphyrin sites was supposed to be eased by the small size of the analyte molecule as compared to the secondary and tertiary amine. However, tributylamine shown the highest response in all the materials and n-butylamine shown the lowest change in absorption.

It is very possible that the bulky size of tributylamine facilitates photons to interact with a bigger porphyrin-analyte complex, or alternatively the response may be larger because the

larger analytes cause a larger spectral change due to a stronger complexing interaction. The trend is followed by dibutylamine (two hydrocarbon chains) and finally n-butylamine (a single hydrocarbon attached to the nitrogen), which shows the lowest response.

For the rest of the primary amines, benzylamine and octylamine, they both shown a higher response than n-butylamine. The reason that the absorbance difference of octylamine is higher than n-butylamine could be explained in a similar manner.

Note that octylamine and dibutylamine have the same molecular formula ($C_8H_{19}N$), and since the measured parameter in f figure 4.15 is essentially concentration independent, it means that for this case the only difference between the magnitudes of reactions depends on the molecular structure. It is believed that the magnitude of reaction in octyalmine is higher because its long hydrocarbon chain and the lone pair of electrons in the nitrogen produces an asymmetric charge distribution which facilitates the interaction with the porphyrin.

Benzylamine is different from the rest of the primary amines because the lone pair on the nitrogen touches the delocalising electrons and becomes delocalised with them. That is to say that benzylamine is more delocalized than the other primary amines, and that gives it the ability to interact easier with the porphyrin molecules and produce a higher magnitude of response.

4.1.3.6 Time parameters: t^{50} and t^{90}

The diffusion of the amine vapour through the monolayers depends of the porosity and molecular arrangement of the material in the sample. The t^{90} is a parameter used in the sensor community to quantify the response rate, and is defined as the time taken for 90 percent of the total change in absorbance (saturation) to occur. It was expected that a higher time of response could be observed for formation of amine-porphyrin binding pairs as the molecular weight of the amine increases. Figure 4.17 shows the average t^{90} values of zinc porphyrin samples during exposure to amine vapours. In general, the average t^{90} value of the porphyrin LB films is increased as the molecular weight of the diffusing amine type increases. In other words, the primary amines experience a relatively easy diffusion through a dense LB film, whereas a bulkier amine will have a lower diffusion rate due to the steric hindrance caused by the larger molecular weight of the amine.
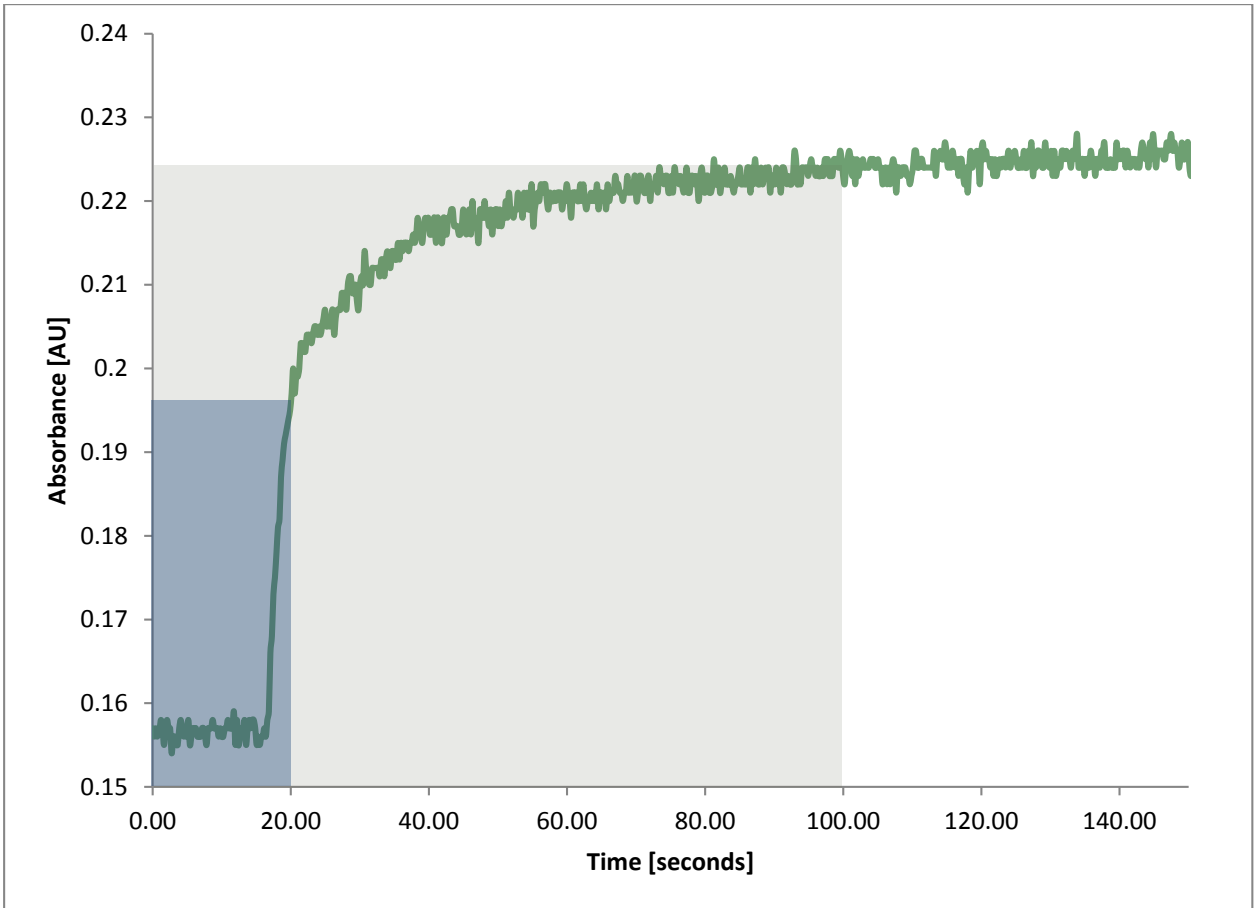
Figure 4.16: t_{50} and t_{90} representation of the SMT3_075 glass sample when exposed to at 25°C (1.052 ppt).
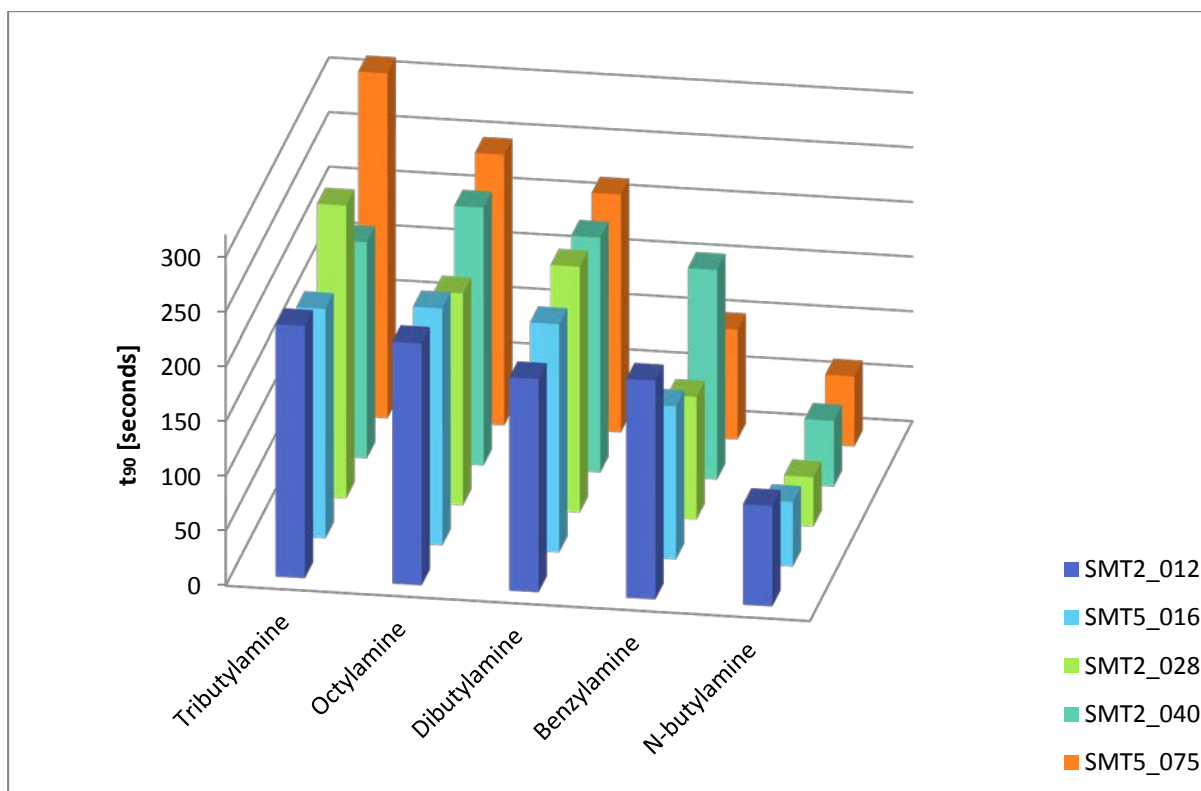
Figure 4.17: The average t90 values of zinc porphyrin spectra during exposure to and recovery for amine vapours.

Section 2: Free base porphyrins and carboxylic acids

In this section, five different free base tetraphenyl porphyrins with different functional groups attached to the phenyl rings are studied. A comparison of the reaction of the porphyrins with different carboxylic acid vapours is made. The objective of this work is to determine the suitability of the porphyrins for use as optical based gas sensor for the carboxylic acids and to determine the influence of the functional groups upon the porphyrin sensing behavior.

In order to investigate the surface morphology of the films after deposition onto a solid substrate LS films were deposited on both silicon and glass substrates. The transparent glass substrate films were used to observe changes in the optical absorption spectra of the porphyrins during exposure to carboxylic acids, and the silicon substrate films were used for AFM analysis.

This section presents a strong correlation between the optical response that the materials display when exposed to the analytes and the morphological properties of free base tetraphenyl porphyrin side groups.

4.2.1. Materials

4.2.1.1. Porphyrins

The molecular structures of the porphyrins are shown in table 4.6. The synthesis of the materials used in this study, has been reported elsewhere [3, 12, 13].

All the porphyrins used in this study are similar, that is to say the molecules contain the same free base porphine ring and contain at least one phenyl group attached to the molecule. However, they differ in that they contain different side groups. Every side group is different in size and also in its electrical structures. This results in variations in the electron density distribution within the porphine ring. The side group properties not only affect the electrical distribution along the whole molecule, but also the way they interact with other molecules, leading to different packing arrangements at the air-water interface.

The SMT2_011 is the biggest molecule, containing a relatively long carbon chain. Similarly, the SMT2_076 also has a big carbon chain; however, this is much smaller than the other. It is also noticeable that due to the two oxygen atoms presented in the SMT2_076 side group, the molecule may have a higher electronegativity.

The SMT5_054 and the SMT2_029 molecules can be directly compared because both have an OH group at the end of the side group. Nevertheless, the first one contains two phenyl rings instead of one. This extra phenyl group will lead to differences in response due to the steric hindrance effect.

Another interesting comparison occurs between SMT5_054 and SMT5_053; since they have a double phenyl rings in the side group, they share some of the properties of the molecule; however, in the case of the SMT5_053, it has a methoxy functional group at the end of the molecule.
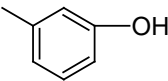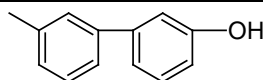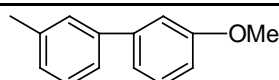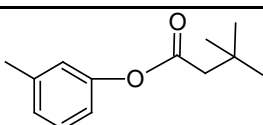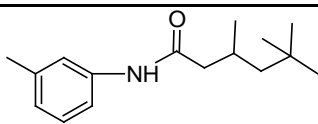
Free base porphyrin	Molecular structure
SMT2_029	
SMT5_054	
SMT5_053	
SMT2_076	
SMT2_011	

Table 4.6: Molecular structure of the free base porphyrins.

4.2.1.2 Carboxylic acids

A selection of five analytes corresponding to the carboxylic acids (–RCOOH) was selected to carry out this study. The R determines the size of the hydrocarbon chain attached to the

functional group. I.e. acetic acid has 2 carbons whereas the hexanoic acid contains 6 carbons. Table 4.7 shows the molecular structure of the various carboxylic acids.
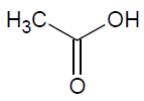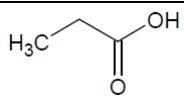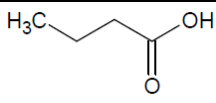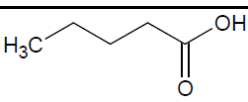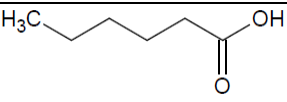
Analyte	Molecular structure
Acetic acid	H_3C ... OH, O
Propionic acid	H_3C ... OH, O
Butyric acid	H_3C ... OH, O
Valeric acid	H_3C ... OH, O
Hexanoic acid	H_3C ... OH, O

Table 4.7: Molecular structure of carboxylic acids.

Carboxylic acids have much higher melting and boiling points than other compounds of similar molecular weight because they experience strong intermolecular association through hydrogen bonds (it can bond two COOH groups, doubling its size) as well as dipole-dipole interactions and van der Waals dispersion forces [14]. The high boiling point is significant when analysing the vapour concentrations of the analytes.

4.2.2. Experimental details:

To investigate the response of the porphyrins in solution when exposed to the carboxylic acids, various solutions of each of the porphyrins were prepared to approximately 0.0025 g/l using chloroform as the solvent. An initial absorption spectrum of 1 ml of each solution in a quartz cuvette was recorded; subsequently 20 µl aliquots of the analytes to be investigated were added by stirring to each of the solutions until saturation occurred.

Subsequently, solutions of the five porphyrins were prepared using chloroform as the solvent at concentrations as follows: SMT2_011 at 0.25 g/l, SMT2_076 at 0.25 g/l, SMT5_053 at 0.25 g/l, SMT5_054 at 0.3 g/l and SMT2_029 at 0.3 g/l. These were used to make the Langmuir

layers of the porphyrins. Three porphyrin layers were deposited into the glass and silicon substrates using the Langmuir-Schaefer technique (dipped horizontally) while the barrier was compressed at a speed of 50 cm^2/min to a fixed surface pressure of 15 mN/m.

Images of the porphyrin films were taken using an Extended Multimode AFM (Veeco Ltd) with a Nanoscope IIIa controller operated in tapping mode.

4.2.3. Results and discussion

4.2.3.1 π-A isotherms
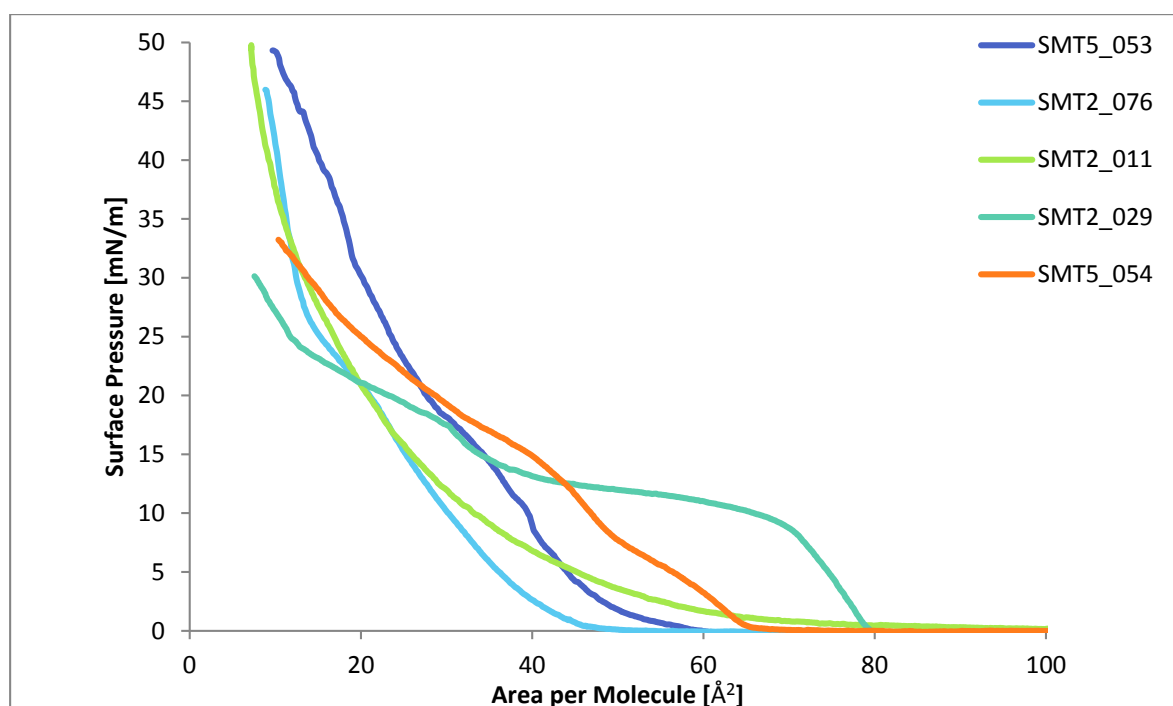
Figure 4.18: Surface pressure – area isotherms of the free base porphyrins.

The isotherm of the SMT2_11 and SMT2_076 in figure 4.18 shows three separate phases, as discussed in section 3.1.4. The shapes of the curves along with the rapid change of phases suggest that with increasing gradient of the isotherm the molecules are more densely packed.

The take-off area (the area per molecule at which the surface pressure π higher than 0 mN/m) of the SMT2_011 is the largest compared to the rest of the materials (90 ± 10 Å^2), and is attributed to the length of the alkyl chain within the amide group. A longer chain results in increased steric hindrance, that could be the case for the packing of SMT2_011 molecules compared to SMT2_076.

128

The isotherms presented for the porphyrin SMT5_053, SMT5_054 and SMT2_029 in figure 4.18 are fairly similar to each other. The isotherm for SMT2_029 is interpreted such that after the take-off area the molecules are oriented in a flat way (that is, the porphyrin ring could be oriented parallel to the plane of the water surface). In this phase, the molecules are just lying on the water surface squeezing each other. After that, a flattish plateau area is presented, in which little change in the surface pressure is observed. During this state, the porphyrins are tipping up, rotating over and ordering themselves progressively until they reach the last state, in which they have completely changed their orientation. The step like feature in the isotherms is indicative of a change in the packing order of the molecules. When the barrier is further compressed, the monolayer finally collapses. The SMT5_053 and SMT5_054 isotherms have similar features but the plateaus are less distinct.

Surprisingly, the take-off area of the SMT5_054 (64 ± 10 Å^2) is smaller than the SMT2_029 (78 ± 10 Å^2). Both have a phenyl group attached to the porphine, but the SMT2_029 has an extra one, which may induce not only a different polarity, but also a different flexibility property to the molecule and hence, a changed molecular packing nature.

It is important to mention that the glass samples made for the optical experiments and the silicon samples for the AFM studies were deposited at the same target pressure. The selected target pressure was 15 mN/m, which is a pressure at which the films are already in a solid phase. At that target pressure, three of the free base porphyrins (SMT2_076, SMT2_029 and SMT5_054) have approximately the same area per molecule at 33 ± 5 Å^2. For the rest of the materials, SMT5_053 and SMT2_011 the area per molecule at 15 mN/m is 25 ± 5 Å^2.

The fact that the surface area and the area per molecule of the materials are approximately at the same converging point it is useful because the materials and their structure formed once they have deposited can be compared directly in the AFM studies.

4.2.3.2 AFM

In order to understand the morphology of the deposited thin films on a solid substrate it is important to consider the dissimilarities between one material and the other, which can be done by comparing the substituent groups side by side. Figure 4.19 shows the AFM images of the porphyrins samples deposited on silicon.

The SMT2_011 is the biggest molecule, containing a long hydro carbon chain. The AFM image in the SMT2_011 sample shows evidence that a dewetting process has occurred. It is possible that the long chain in the group sides makes the molecule more hydrophobic. The image shows accumulations of droplet like material that have dewetted from the surface in certain areas, leaving large areas of void where the porphyrin molecules have receded from.

Similar to SMT2_011, SMT2_076 also has a relatively long carbon chain; however, this it is smaller than SMT2_011. It should also be noted that due to the two oxygen atoms presented in the SMT2_076 side group, the molecule may be more electronegative. In the SMT2_076 image, a partial dewetting is observed due to the smaller carbon chain presented in the side groups. The irregular film observed could be an indication of possible aggregation. In the illustration, the lumpy regions of material have a minimum height of at least a layer of material of approximately 5 nm.

SMT2_011
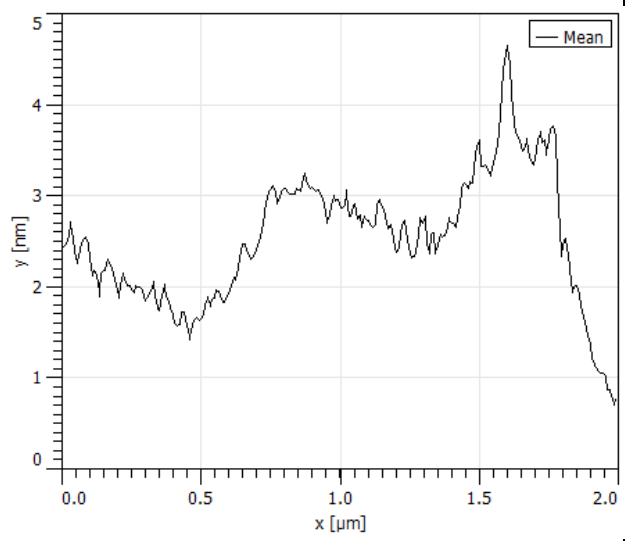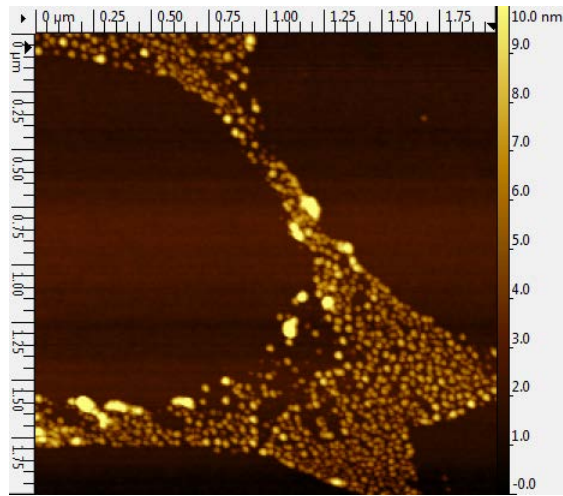
SMT2_029
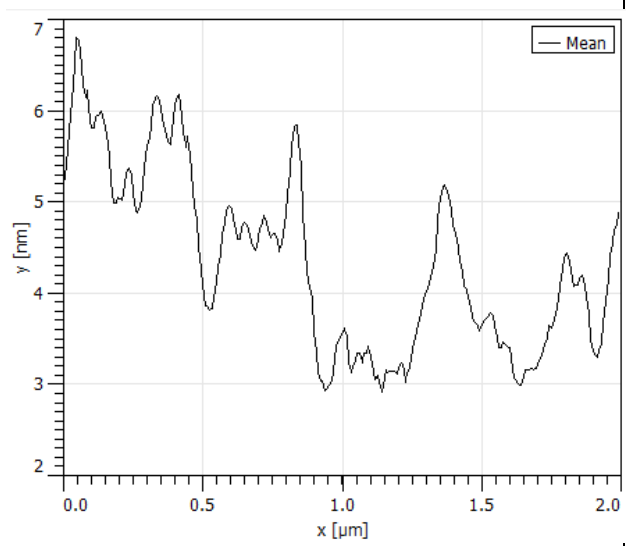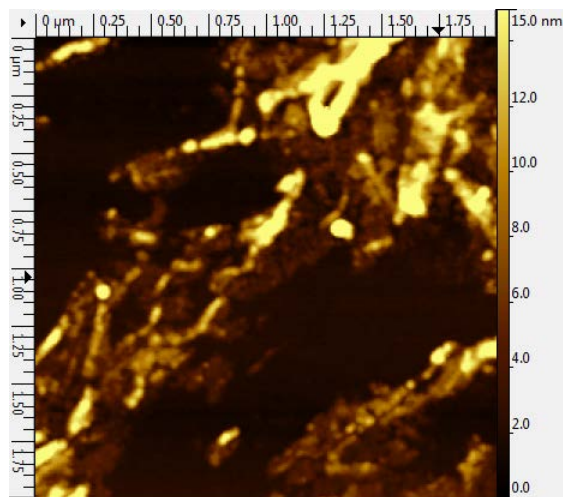
SMT2_053
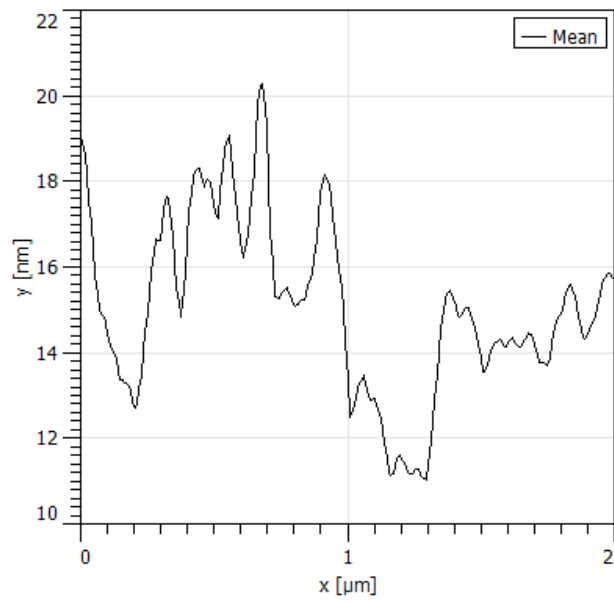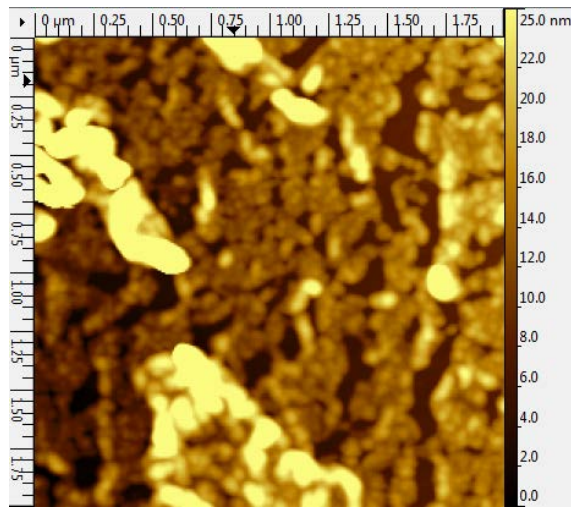
SMT2_054
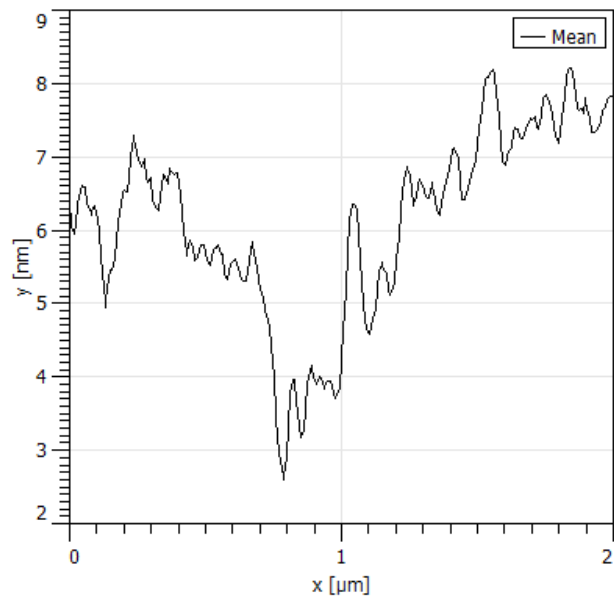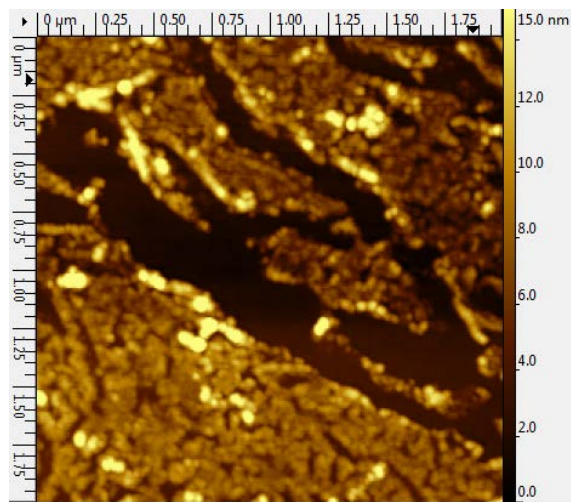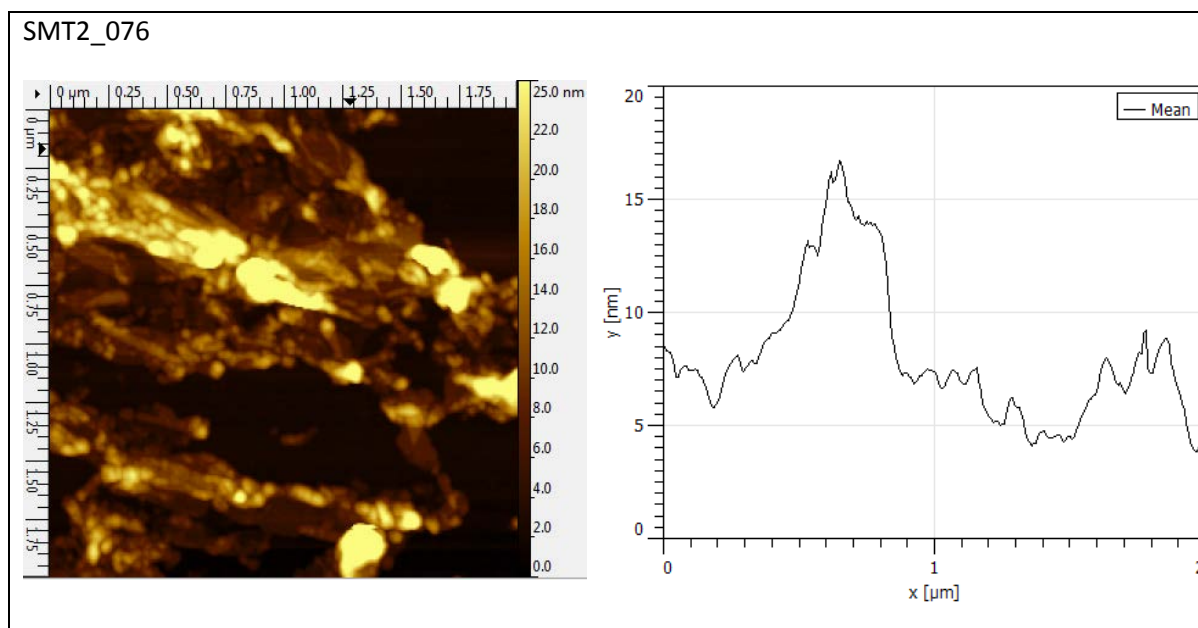
Figure 4.19: AFM images and roughness analysis of the silicon samples containing three deposited layers of the various materials using the LS technique.

The SMT5_054 and the SMT2_029 molecules are quite similar in that they both have an OH group at the end of the side group. Nevertheless, the SMT5_054 contains two phenyl rings instead of one. The deposition of the SMT2_029 has produced a fairly continuous thin film decorated with structured aggregates of porphyrin which are elongated and therefore may suggest fibril formation. On the other hand, the extra phenyl ring in the SMT2_054 should give less elasticity to the molecule and that helps with the conformation within the film, leading to a close-packed film structure.

SMT5_054 and SMT5_053 are also similar in many ways since they have a double phenyl ring in the side group, they share some of the properties of the molecule; however, in the case of the SMT5_053, it has a methoxy (OMe) functional group at the end of the molecule, rather than a hydroxyl (OH) group for SMT5_54.

For the SMT2_054 sample, the film is uniform but cracked. Similarly, the SMT2_053 sample had shown a cracked film but with different patches of chunky material giving different thicknesses among the area. The divergence between those side groups lead to a dissimilar molecular packing conformation in the films which can be explained by the different formation of porphyrin domains in the air water interphase and/or their different amphiphilic properties.

4.2.3.3 Spectral shifts during film exposure to acetic acid

To investigate the response of the free base porphyrins as solid films upon exposure to acetic acid vapour, a vessel containing the acetic acid was submerged in a water bath held at 25°C in order to produce analyte vapour with theoretical concentration corresponding to 20.68 ppt.

Figure 4.20 shows the dynamic changes in absorbance at the wavelength (462 nm) with the highest change in absorbance plotted as a function of time. During the exposure, the sample is exposed to the carboxylic acid vapour for 300 seconds at 25 °C, and during the recovery the sensor is flushed with pure nitrogen and gently heated to 65 °C for another 300 seconds. It is clear that the exposure-recovery cycle is reproducible and that, over the seven cycles shown, little or no degradation in response is observed, allowing for reliable industrial application of such a molecular device.
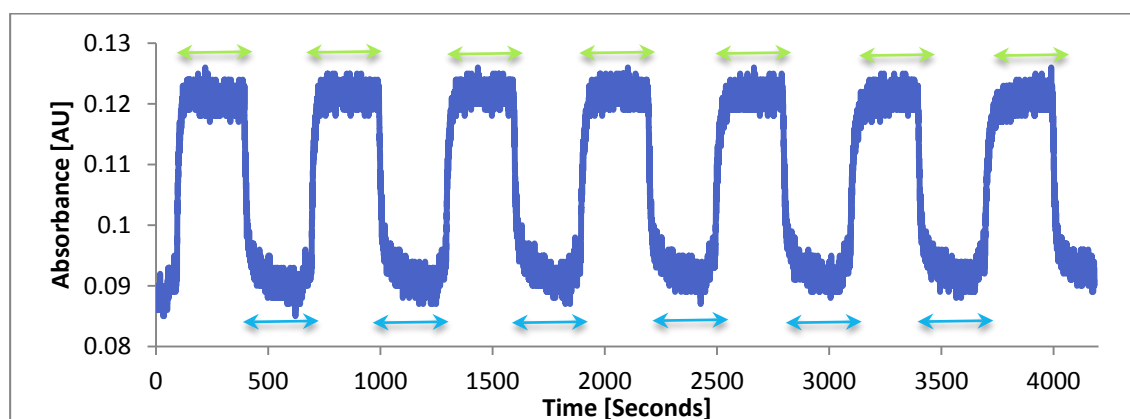
Figure 4.20: Absorbance dynamics at 462 nm for a 3 layer LS film of SMT2_029 upon exposure to acetic acid with a concentration of 20.68 ppt.

Figure 4.21 show the absorbance spectra of the free base porphyrins investigated in the section before the exposure to acetic acid. As in the last section, the responses of the porphyrins were normalized in order to standardize the absorption strength of the materials. In other words, the responses will be taken as a percentage change in absorption.

Similarly, figure 4.22 shows the absorbance spectra of porphyrins after the exposure to 20.68 ppt of acetic acid. It is noticeable that the change in absorbance in the samples is minimal (excluding the SMT2_029) and almost imperceptible to the naked eye. In fact, the only

134

substantial difference is for SMT2_011, in which there is a double peak appearance once the free base porphyrins has been exposed to the acetic acid vapour.

However, the data can be easily analysed when the recovery absorbance is subtracted from the exposure absorbance to calculate the 'change in absorbance'. To exemplify the case, figure 4.23 shows the absorbance differences of the normalized responses of the free base porphyrins when exposed to 20.68 ppt of acetic acid.
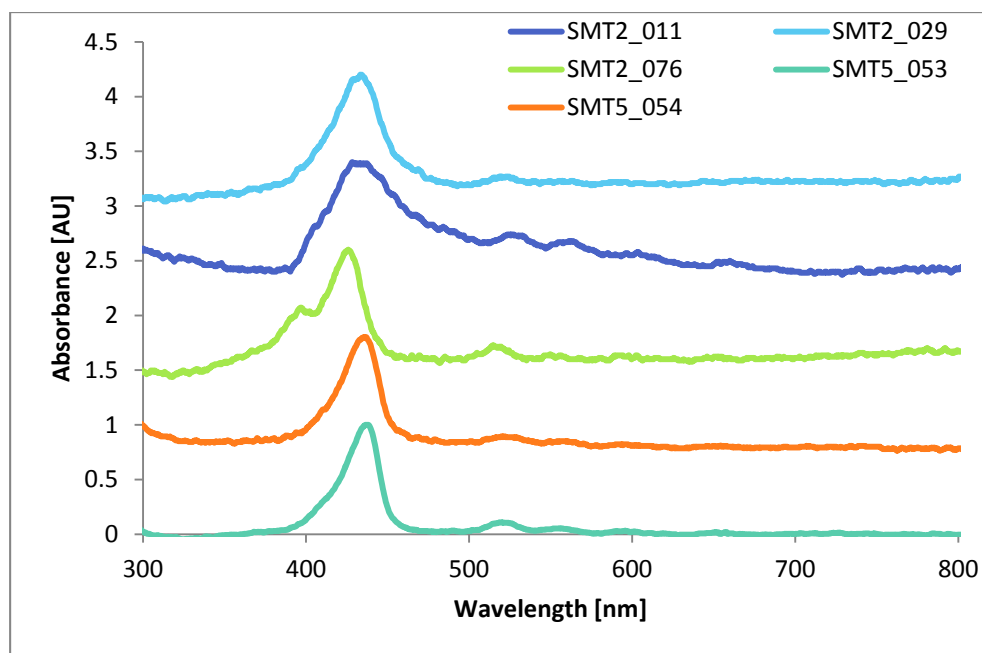
Figure 4.21: The absorbance spectra for LS films of the free base porphyrins before exposure to 20.68 ppt of acetic acid.
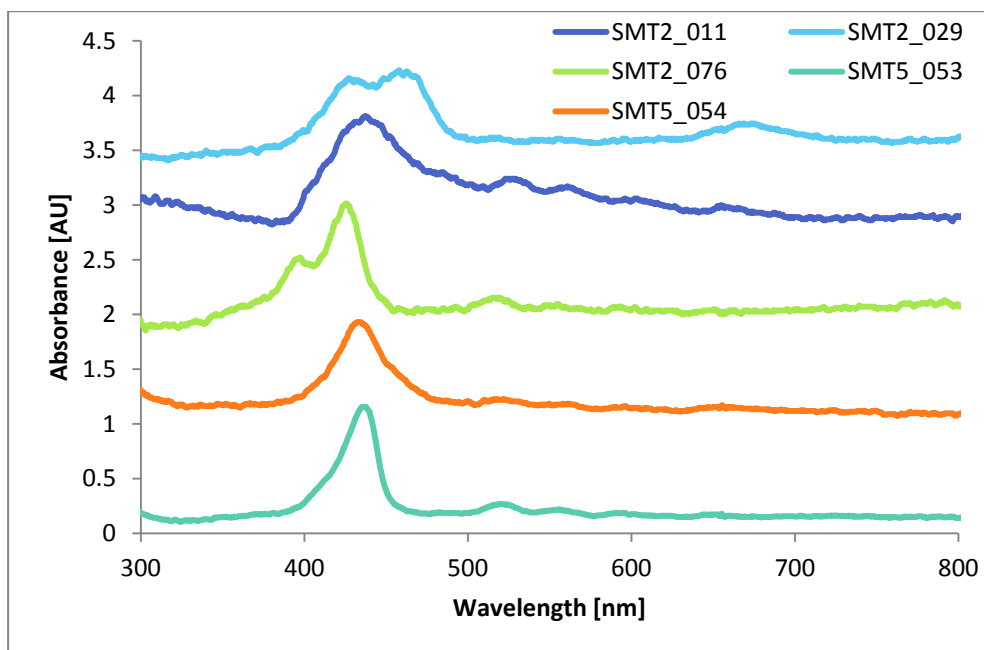
Figure 4.22: The absorbance spectra for LS films of the free base porphyrins after exposure to 20.68 ppt of acetic acid.
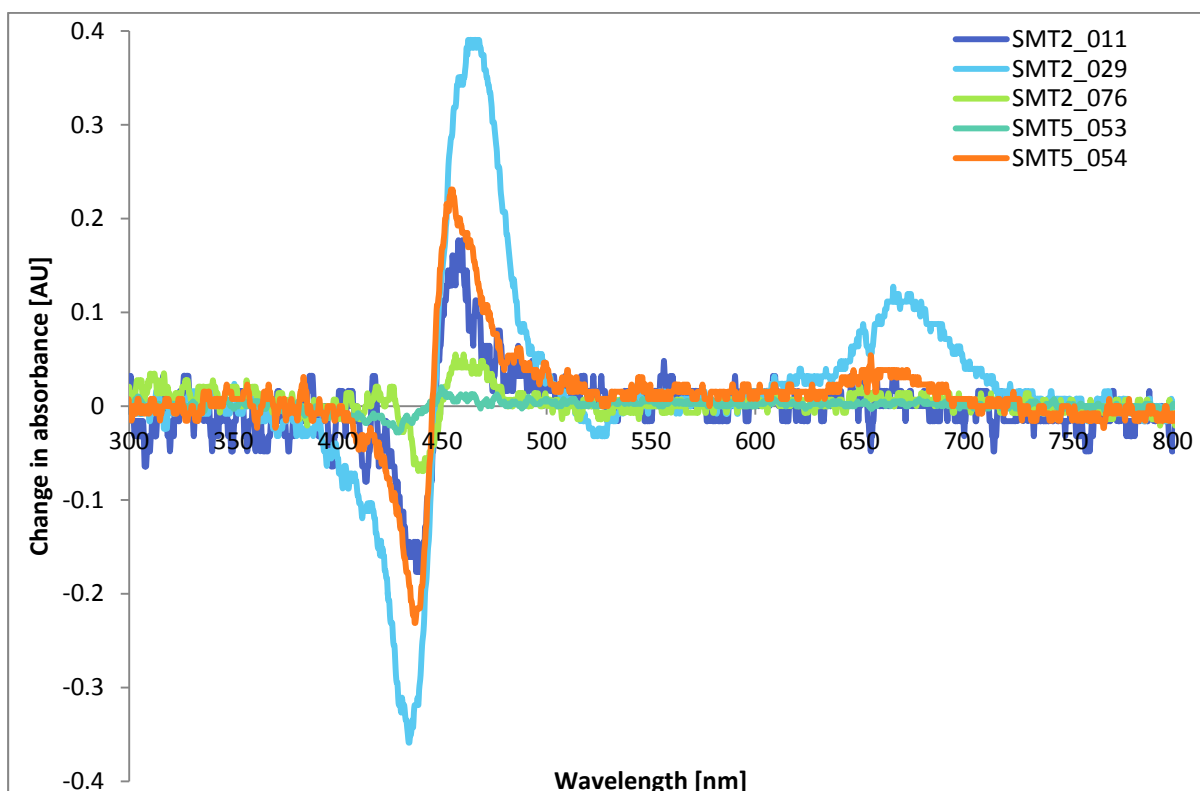
Figure 4.23: Change in absorbance of the free base porphyrins upon exposure to 20.68 ppt of acetic acid.

4.2.3.4 Comparison between solution spectra and solid film spectra

The addition of analytes (in liquid form) to porphyrins in solution offers an insight into the interaction between the non-aggregated, discrete porphyrin molecule and the analyte species to be bound [2]. The divergence in the responses of the porphyrins deposited in a substrate and in solution can be explained in terms of the spacing between one molecule and another. Figure 4.24 shows the comparison of the difference between the spectra before and after exposure to acetic acid for the free base porphyrins in LS films and chloroform solutions.

Evidently, the response of the porphyrins in solutions is higher than the ones presented in LB films. When the molecules are dissolved at low concentration in chloroform they do not interact with each other, whereas in a solid state the molecules can aggregate in order to minimize energy in the system. The response is greater in solutions just because the porphyrins in a liquid medium do not interfere with each other, giving a maximum rate of absorbance change.
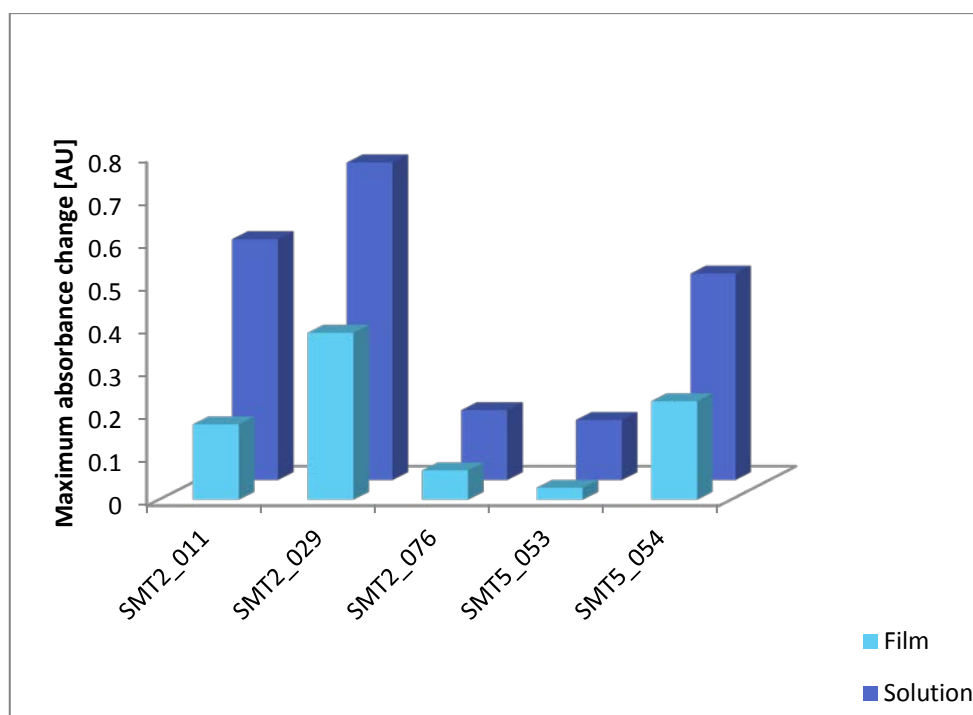
Figure 4.24: Histogram of the absorbance changes of the free base porphyrins when exposed to acetic acid. The porphyrin solutions of 0.0025 mg/ml were exposed to 100 µl of acetic acid and the 3 LS porphyrin layers deposited on glass substrates were exposed to a vapour concentration of 20.68 ppt of acetic acid.

When the molecules are deposited in the glass, the Soret Peak is slightly shifted and also becomes broader because the variety of deposited porphyrins is increased (i.e. stretched, expanded or overlapped).

The pattern of response in figure 4.24 is similar, just the values are different. In most of the cases, the responses to carboxylic acid in solution and in films remain highly responsive, except in the case of SMT5_053 and SMT2_076, where the response in solid state is severely decreased. It is very possible that the porphyrin molecules interacts with neighbouring molecules when they are being transferred onto the glass substrate during deposition, in such a way that they aggregate, leading to a different molecular packing and possibly blocking the available sites to bind with the analyte. Other authors have reported such effects [15].

4.2.3.5 LS film properties of porphyrin (response to analytes in films)

In the interest of investigating the response of the solid porphyrin films to the other carboxylic acids, the same exposure/recovery process was executed with the five porphyrin samples on glass with the other carboxylic acid vapours. However, since all analytes have a different boiling point, it is expected the exposures will be to different vapour concentrations at the fixed water bath temperature of 25°C. The concentrations of the analyte were calculated using established Antoine equation parameters for the carboxylic acids investigated [9] . The calculation of the concentration of vapours is described in section 3.5.1f.

Since the vapour pressures of the carboxylic acids are not the same, the concentrations delivered to the gas chamber will be different. The resulting concentrations of the carboxylic acids at 25°C were as follows: acetic acid, 20.68 ppt; propanoic acid, 5.52 ppt; butanoic acid, 1.46 ppt; pentanoic acid, 657 ppm; hexanoic acid, 263 ppm.

Figure 4.25 shows a table containing the maximum absorbance differences upon exposure to carboxylic acids. The normalization process was applied when analysing the responses of the films deposited in glass, as described in the first section of this chapter (4.I.3.4). The analytes are ordered according to their molecular weight.
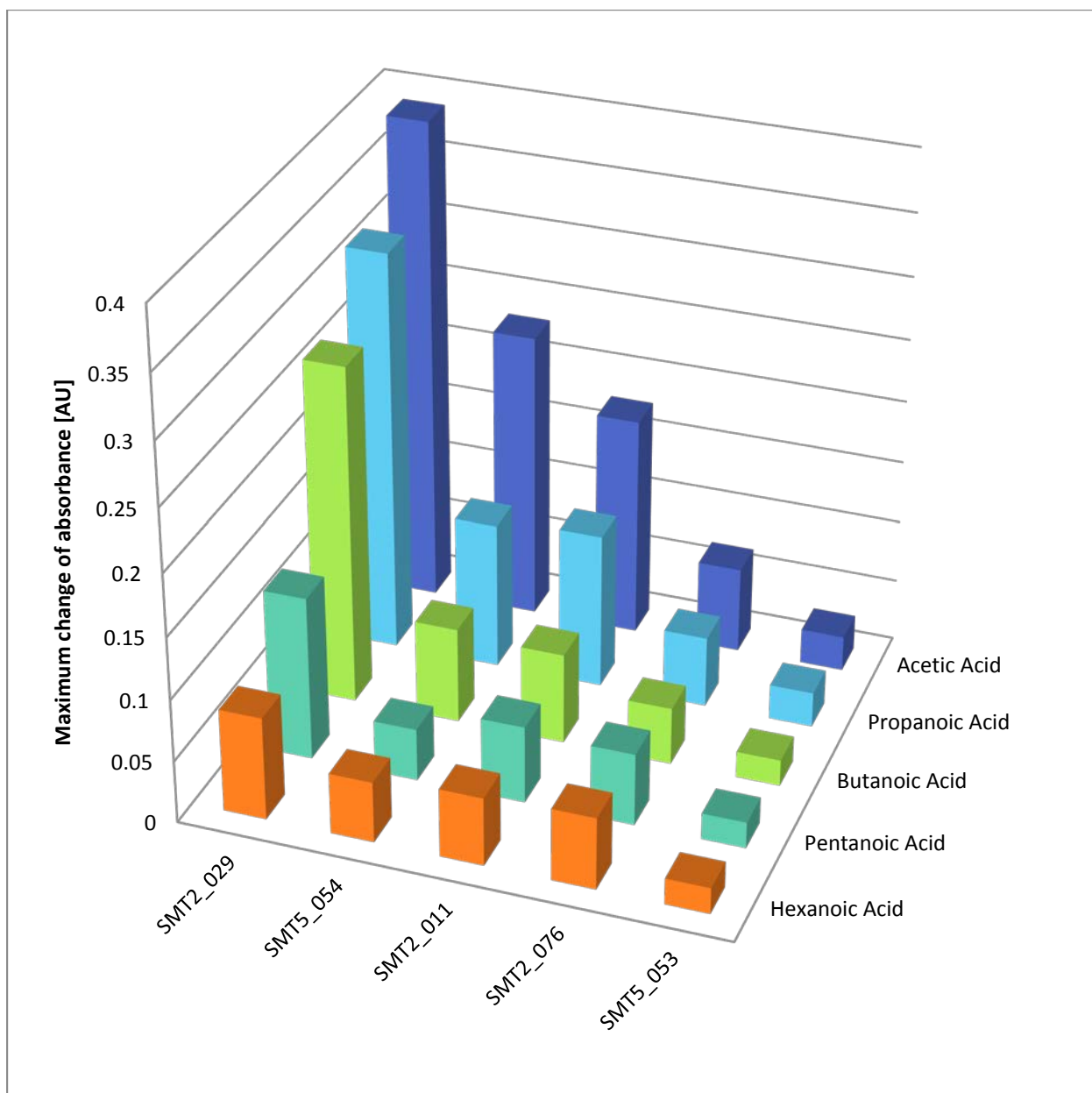
Figure 4.25: Response in film of the porphyrins when exposed to the carboxylic acids vapours. The concentrations of the analytes are: acetic acid, 20.68 ppt; propanoic acid, 5.52 ppt; butanoic acid, 1.46 ppt; pentanoic acid, 657 ppm; hexanoic acid, 263 ppm. The absorbance results have been normalized.

The concentration of the gaseous carboxylic acids was the dominating factor in determining the sensor response: the shorter analyte (acetic acid) exhibited the greatest response due to its higher concentration. In the same way, the longer the hydrocarbons chain in the acid, the slowest the response.

Previous research from the Nano Material Engineering Group in Sheffield shows the response of various free base and metalled porphyrins sensors in terms of the concentration of volatile

organic compounds and toxic gases [8, 16-19]. The response was mathematically modelled using the Langmuir Adsorption Model (descried in section 2.2.5.1).

To analyse a specific carboxylic acid/free base porphyrin complex it is necessary to express the data in different terms. Figure 4.26 shows a representation of the change of absorbance of the free base porphyrins upon exposure to a single analyte molecule. The results presented in the figure are a mere description of the magnitude of reaction, where the concentration is "normalized". In this manner, the absorbance change term in the sensor response (ΔAbs/concentration) in figure 4.26 cannot be normalized because it would alter the scale of the result; the response would not reflect a rate of change absorbance/single analyte molecule.
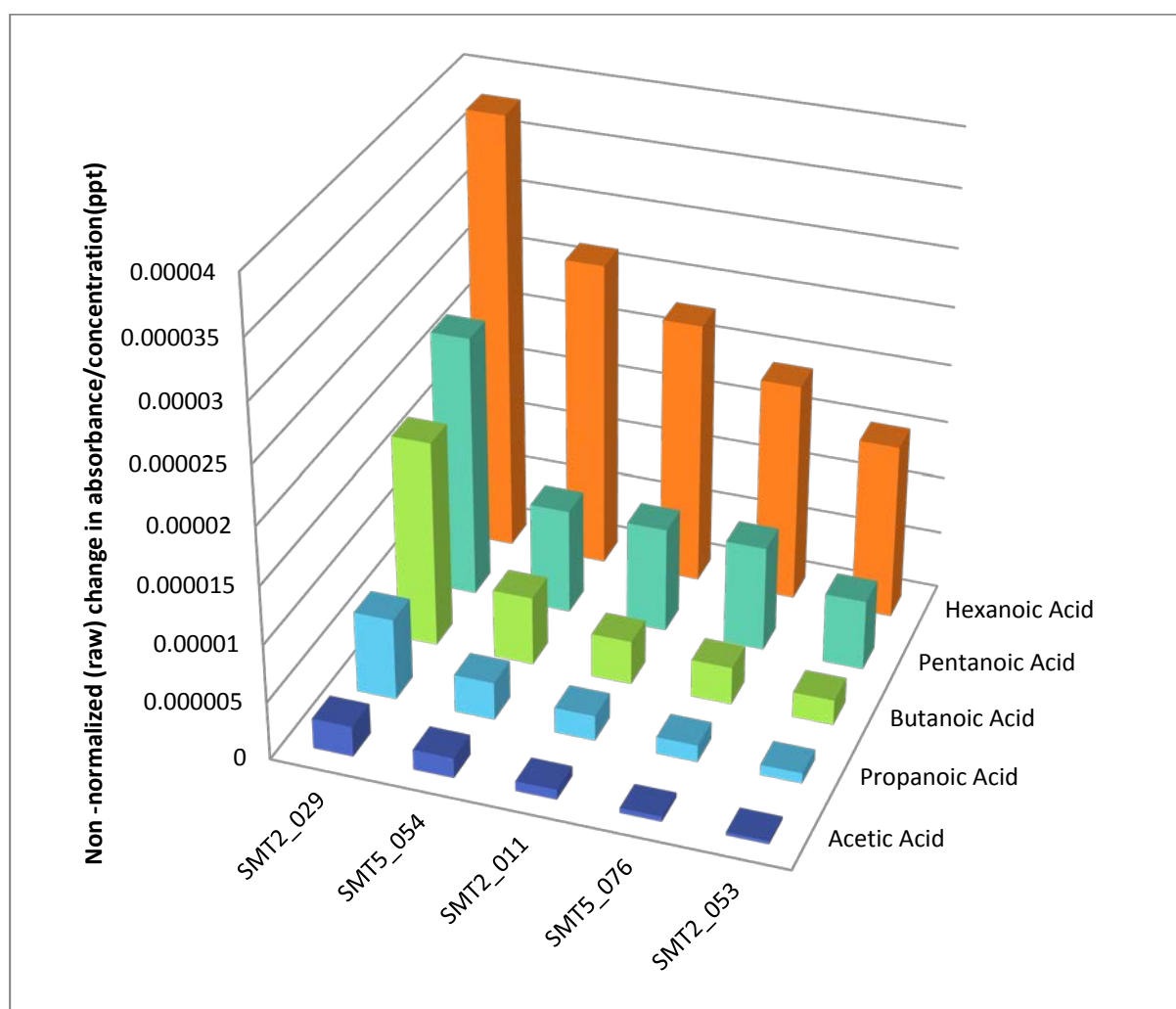
Figure 4.26: Response in film of the porphyrins when exposed to carboxylic acids vapours. The response of the sensor is expressed as the magnitude of reaction of the porphyrins at a fixed concentration.

It was expected to observe a higher magnitude of reaction in smaller hydrocarbon chains, because a higher number of carbons atoms in the branch decrease the acidity of the molecule. A higher acidity in the molecule would result in a stronger interaction between the acid and the free base porphyrin. However, the results presented in figure 4.26 shows an opposite behaviour.

A possible explanation could be described in terms of the band gap structure of the porphyrin. When an analyte molecule is bound to the porphyrin ring, which has a π-electron system above and below, asymmetry is introduced in the system because an electron rich molecule is being injected and pushed on the surface of the film. So, the distribution of the electrons within the complex is changed. The result is a distortion of the band structure and this distortion is bigger for the bigger acid molecule (hexanoic acid).

An alternative explanation could be that is more likely for a photon to interact with a bigger acid molecule and therefore being absorbed. The absorbance may be increasing that way by increasing the size of the acid.

Regardless of how the results are presented, it is palpable that some materials are more responsive than others when exposed to the gaseous acids. The response differences are attributed to their corresponding side groups. The porphyrins containing hydroxyl groups (-OH), SMT2_029 and SMT5_054, showed a bigger response than the rest of the materials; this effect can be explained in term of the molecular compression of the monolayer observed in the isotherms and in terms of the electron donating nature of the side groups.

The SMT2_029 porphyrin is a better sensor material, this may be because the electrons of the side groups are pushed towards the centre of the porphyrin, and that increases is tendency to protonate. The addition of the extra benzene in the SMT5_054 makes the film structure better, but the dilution of the electron donating effect from the side groups makes the sensor significantly less sensitive. Also, the larger side group results in increased steric hindrance for the packing of molecules of SMT5_054 compared to SMT2_029, so the absorbance difference is reduced because the individual porphyrins are spaced further apart.

Both side groups in the porphyrins STM2_011 (-NHCOR) and SMT2_076 (-OCOR) are categorized as moderately electron donator groups, however, the response of the SMT2_011

shows a higher response, even when the film dewets after it is deposited on a solid substrate. Nonetheless, the morphology of the deposited material may be more porous for the SMT2_11 than the one SMT2_076. A higher porosity film enhances the response of a gas sensor because the area per volume ratio is maximized and the accessibility of the analyte to the central ring and that allows an increase in the number of available binding sites.

It was expected that the porphyrins containing strong electron donating properties would show a higher response to amines, as in the case of SMT2_053. However, the interaction of porphyrin-analyte is not only limited to the electron donating nature of the side groups but also depends on the porphyrin-porphyrin interactions. It is possible that stronger porphyrin-porphyrin interactions led to densely packed aggregated films, limiting the access to the porphyrin binding sites. Thus, an open structure along with strong electron donating properties within the side groups would be the best scenario.

Side groups give different properties to the porphyrin molecule: not only in terms of electron density distribution along the molecule, but also the structure of the films produced through giving the ability to bend/twist the side groups and promote/demote the aggregation interaction between the porphyrin molecules.

4.2.3.6 Time parameters: t^{90}

The t^{90} value is a useful measurement when considering the absorption of vapour molecules on the porphyrin films. A large t^{90} value shows that vapour molecules are slower to absorb into the LB film, whereas a lower t^{90} values indicate that the molecules are infiltrating the films very quickly. Figure 4.27 shows how a small carboxylic acid (acetic acid) has small t^{90} values. Larger carboxylic acids struggle to diffuse into deeper layers and longer t^{90} are observed as a result.
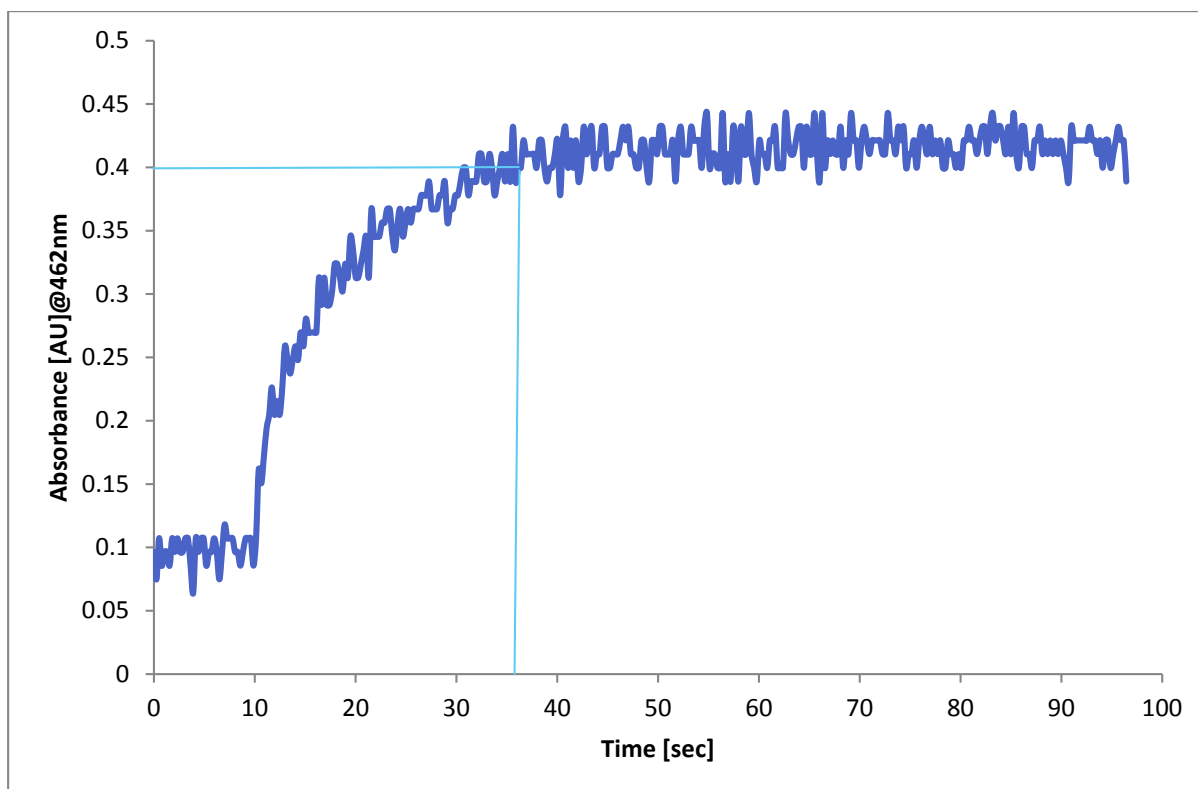
Figure 4.27: Absorbance dynamics at 462 nm for a 3 layer LS film of SMT2_029 upon exposure to acetic acid with a concentration of 20.68 ppt. The t90, marked by the blue lines, was 38 seconds.

Figure 4.28 shows the average t^{90} value of the free base LB films upon exposure to a different concentration of carboxylic acids (acetic acid, 20.68 ppt; propanoic acid, 5.52 ppt; butanoic acid, 1.46 ppt; pentanoic acid, 657 ppm; hexanoic acid, 263 ppm). With a few exceptions (such as SMT5_054 exposed to pentanoic and butanoic acid) it is noticeable that a higher time of response is observed for the analytes that have a higher volume. In other words, despite the fact that the response in films of the materials is higher for a bigger carboxylic acid molecule, as shown in figure 4.26, the molecular diffusion of the analyte molecules trough the LS porphyrin films is dependent of the hydrocarbon chain of the carboxylic acid.
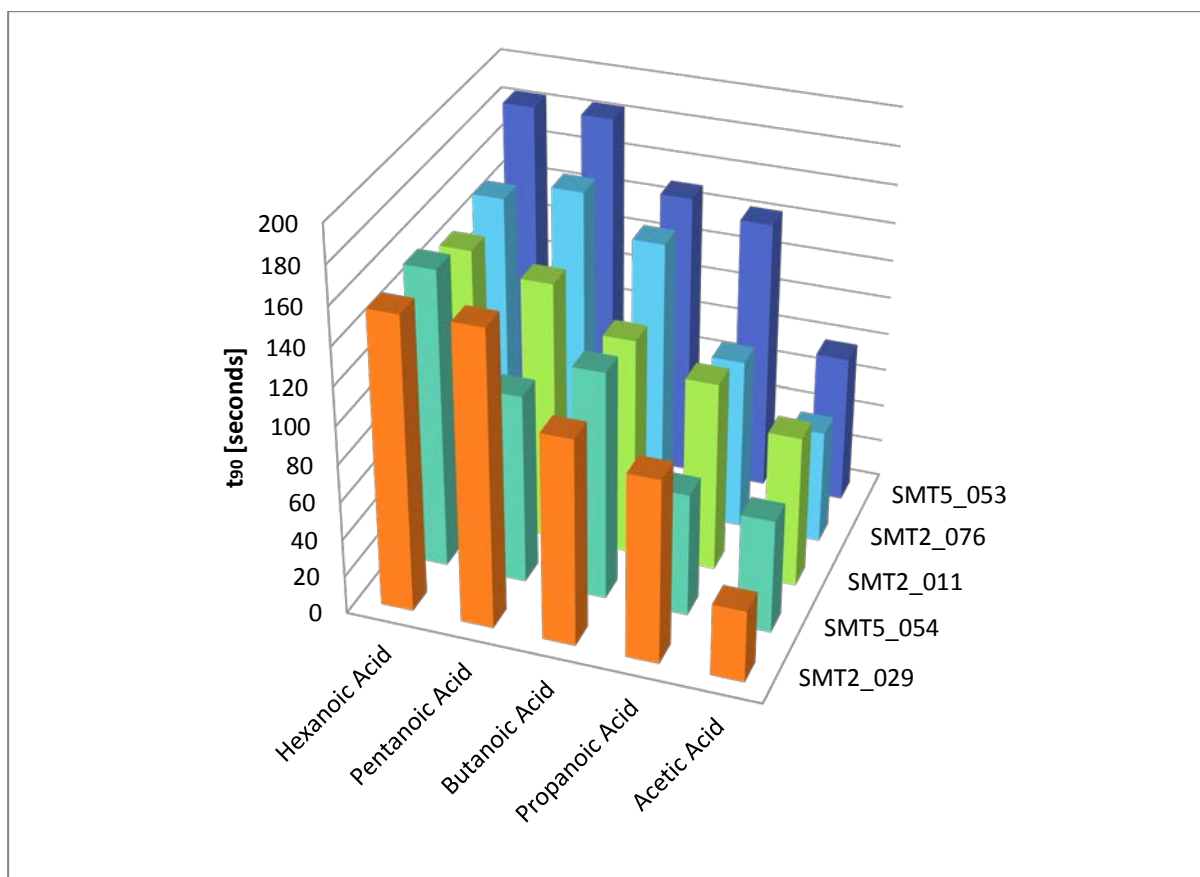
Figure 4.28: The average t90 values of free base porphyrin spectra during exposure to and recovery for carboxylic acid vapours.

Ergo, the molecular diffusion of the carboxylic acid depends on the porosity of the LS porphyrin monolayers regardless of the binding strength of the carboxylic acid/free base porphyrin complex.

Section 3: Nitrogen dioxide (NO$_2$) detection

This section focuses on the detection of nitrogen dioxide, and is divided in three subsections: The first section will extend the study of the free base and zinc porphyrins used in the previous sections (section 4.1 and 4.2) for the detection of NO$_2$. The second one will talk about EHO, its physical properties and sensitivity to NO$_2$ gas; it also introduces the concept of mixing calixarenes with porphyrin to decrease aggregation in the sensing material in order to make the surface more accessible to the NO$_2$ molecules. And finally, the third subsection will be focused on the preparation and gas-sensing properties of an optically transparent free base porphyrin/TiO$_2$ composite; the advantages and disadvantages of using the composite will also be discussed.

4.3.1. Materials

4.3.1.1 Host materials

4.3.1.1.a Optically transparent titanium dioxide (TiO$_2$) thin films:

When porphyrin molecules are deposited on solid substrates, the mere presence of π-π interactions between the molecules may lead to aggregation in the sample. As a consequence, a shifting, broadening or splitting of the bands in the spectrum with respect to the porphyrin solution will occur [20]. The excitonic Davydov splitting predicts the splitting of bands in the electronic or vibrational spectra due to the presence of more than one (interacting) equivalent molecular entity [21].

In the interest of minimizing the aggregation many methods had been successfully applied, such as the pre-bubbling with NO$_2$ [22], adding acid [23] and adding calixarene to the porphyrin solution [20]. Section 2.8.3.a describes some of those methods.

Here, a solid substrate made of micro structured columnar TiO$_2$, prepared by a glancing angle physical vapour deposition technique, has been used in order to reduce the aggregation of porphyrin. The TiO$_2$ solid substrate and the porphyrins used in this study were provided by Dr. J. Pedrosa-Poyato, from the Pablo de Olavide University (Seville, Spain).

For the fabrication of the solid substrate, pellets of titanium oxide in solid state were used for evaporation, which were turned into vapour by bombardment from a high energy electron beam. As the vapour condensed on glass substrates it formed a thin layer of TiO_2. Using this method, films with a thickness from 150 to 400 nm were prepared. The TiO2 films are non-dispersive and thin, allowing optical transmission measurements for UV-visible spectroscopy.

In the interest of analysing the molecular arrangement of the TiO_2 structure deposited on substrate, a silicon wafer was prepared following the same evaporation process. The TiO2 structures on silicon sample were imaged using a field emission scanning electron microscope(Model Hitachi S5200). A columnar microstructure with open and large pores was observed as shown in in figure 4.29.
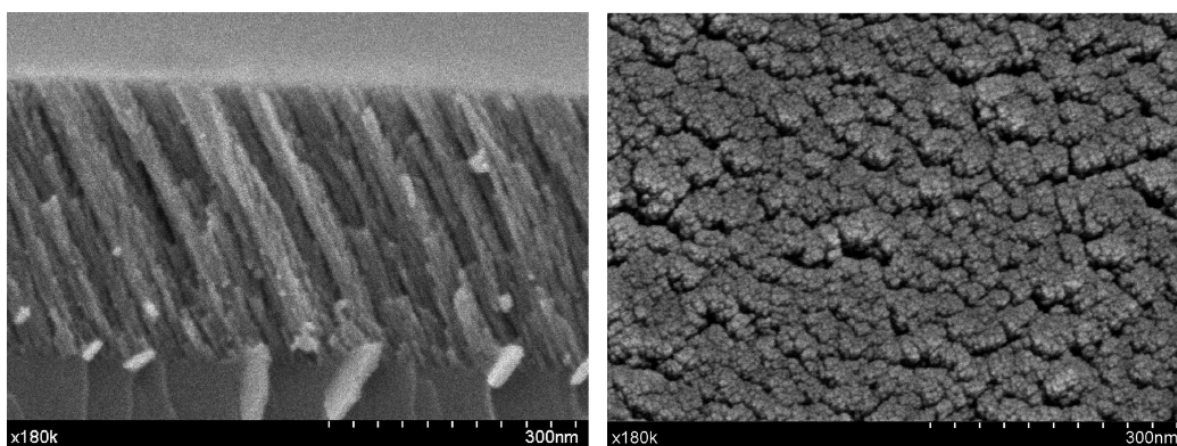
Figure 4.29: Cross-section (left) and planar (right) views of the TiO2 thin films used as host of porphyrin molecules [24].

The cross-section image [24] shows a thickness of the film of approximately 350 nm. For the fabrication of the TiO_2 films, the substrates were placed at an angle of 70° with respect to the evaporator source. The planar view shows pores with an average diameter between 2 and 7 nm; however, larger pores of 14 nm were also observed. The TiO_2 structures are excellent for porphyrins because they can be deposited on the rods, and that offers an open access to analyte molecules coming from outside the film [25].

4.3.1.1.b Calix[8]arene as a molecular disperser (host material)

The calix[8]arene (eight carboxylic acid monomers in the ring) used in this study is described in figure 4.30. Using calixarene in a calixarene-porphyrin matrix when producing films has continually proven to increase EHO film quality and stability [26]. The basket shaped molecule allows a faster diffusion of vapour or gas molecules into deeper layers within the multi-layered film. Furthermore, the molecule has many side groups containing hydrophilic properties, which helps to anchor itself to the water surface. This characteristic provides a 2D matrix of calixarene in which the porphyrin guest can be incorporated.

This characteristic provides a 2D matrix in which porphyrin molecules distributed within.
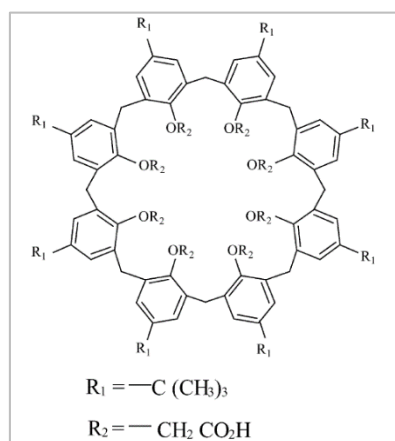
Figure 4.30: Molecular structure of calix[8]arene.

4.3.1.2 Porphyrins deposited on glass, calixarene matrix and TiO$_2$ substrate.

For the first set of experiments the same materials as those used in sections 4.1.1.1 and 4.2.1.1 corresponding to free base porphyrins (SMT2_029, SMT5_54, SMT5_53, SMT2_076 and SMT2_011) and zinc metalloporphyrins (SMT2_012, SMT2_040, SMT5_016, SMT3_075 and SMT2_028) will be deposited on glass substrates.

In the second subsection, EHO is incorporated into a calixarene host in the form of a mixed film. For the third subsection, porphyrins MCMPP, MCTPP, T4CPP(p-TCPP) and T3CPP(m-TCPP) will be deposited within the TiO$_2$ matrix material.

The materials for second and third subsections are described in table 4.8. Notice that all the materials are free base porphyrins containing different number of side groups and not

necessary the same one within the molecule. The side groups are located in the methine bridges of the porphyrin ring (position 5, 10, 15 or 20 according to the numbering system nomenclature declared by the International Union of Pure and Applied Chemistry).
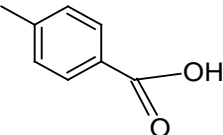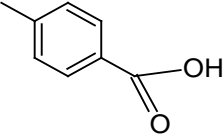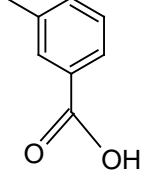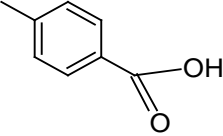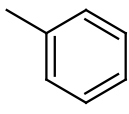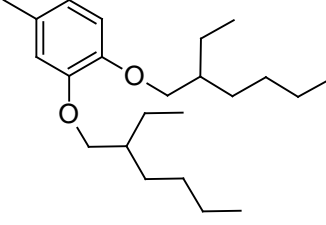
Name	Number of group side attached to the porphine	Side group structure
MCMPP	1	
T4CPP (p-TCPP)	4	
T3CPP (m-TCPP)	4	
MCTPP	1	
	3	
EHO	4	

Table 4.8: Free base porphyrin with various side groups located at the methine bridge position of the porphyrin ring.

4.3.1.3 Analyte

A mixture of clean dry nitrogen and nitrogen dioxide will be mixed to modulate the concentration rates of the toxic gas and thereafter flushed into the gas ring. The concentration of the NO_2 will be measured in parts per million. Sections 3.5.1e and 3.5.1f describe the details of this process.

4.3.2. Experimental details

4.3.2.1 Free base and zinc porphyrin LS samples deposited on glass substrates

The LS glass samples of the free base and zinc porphyrin materials were produced following the same methods described earlier in this chapter, including the concentration of the solutions and the deposition parameters (as detailed in sections 4.1.2 and 4.2.2).

4.3.2.2 EHO and EHO/calixarene solutions deposited on glass substrates

A 0.25 mg/ml of EHO solution was prepared using chloroform as a solvent. For the mixed solution, a 0.1 mg/ml solution of calix[8]arene was mixed with a 0.1 mg/ml solution of EHO to form a EHO (38%)/calixarene[8]arene(62%) (molar ratio) solution.

The barrier speed of the trough was set at 50 cm^2/min for sample depositions. Three Langmuir Schaeffer layers for both samples, EHO and EHO/calixarene, were deposited at a target pressure of 15 mN/m.

4.3.2.3 Preparation of the porphyrin/TiO₂ composite

The addition of the dye into the TiO_2 sample was made by immersing the films in a 10^{-4} M ethanol solution at room temperature for 1 hour. The chemical binding between the TiO_2 and the porphyrin molecules have been found to be compatible with chelating and/or bidenate in which the carboxylate groups binds to the TiO_2 surface. In chelating one functional group binds to the central metal atom of TiO_2 whereas bidenate binds two functional groups [27]. To remove the physisorbed porphyrin molecules, the films were rinsed in ethanol and then dried by flushing with dry nitrogen using a N_2 gun. All samples were then dried by heating to 110 °C for 30 minutes and allowed to cool to room temperature before taking the exposure to analytes measurements.

4.3.3. Results of the exposure to NO$_2$

4.3.3.1 Free base and zinc porphyrins deposited on glass substrates:

LS films of both free base and zinc porphyrins are now used in order to test NO$_2$ gas sensing capabilities. The films were exposed to 5.39 ppm. It has been observed that there is a colour change associated with the binding between the porphyrin ring and NO$_2$; the effect is observed in the free base and zinc porphyrins. It is theorized that the adsorption of the analyte into the porphyrin ring causes a change in the electronic energy levels within the delocalized π system. The change in energy levels influences the absorption spectrum of the materials because the absorption features are a result of photons exciting electrons inside the porphyrin from a lower to a higher state of energy. The results of the exposure to the toxic gas are represented in figure 4.31.

Nitrogen dioxide molecules are normally found in a doublet state, because its nitrogen atom has one unpaired electron. When the molecule is on its single state, the lone electron interacts with the porphyrin rings π-electron system. The sensing mechanism for the free base porphyrin/NO$_2$ reaction could be explained in terms of protonation, in which the porphine protonates in order to oxidize to form a π-radical cation or to form a porphyrin dication [28].
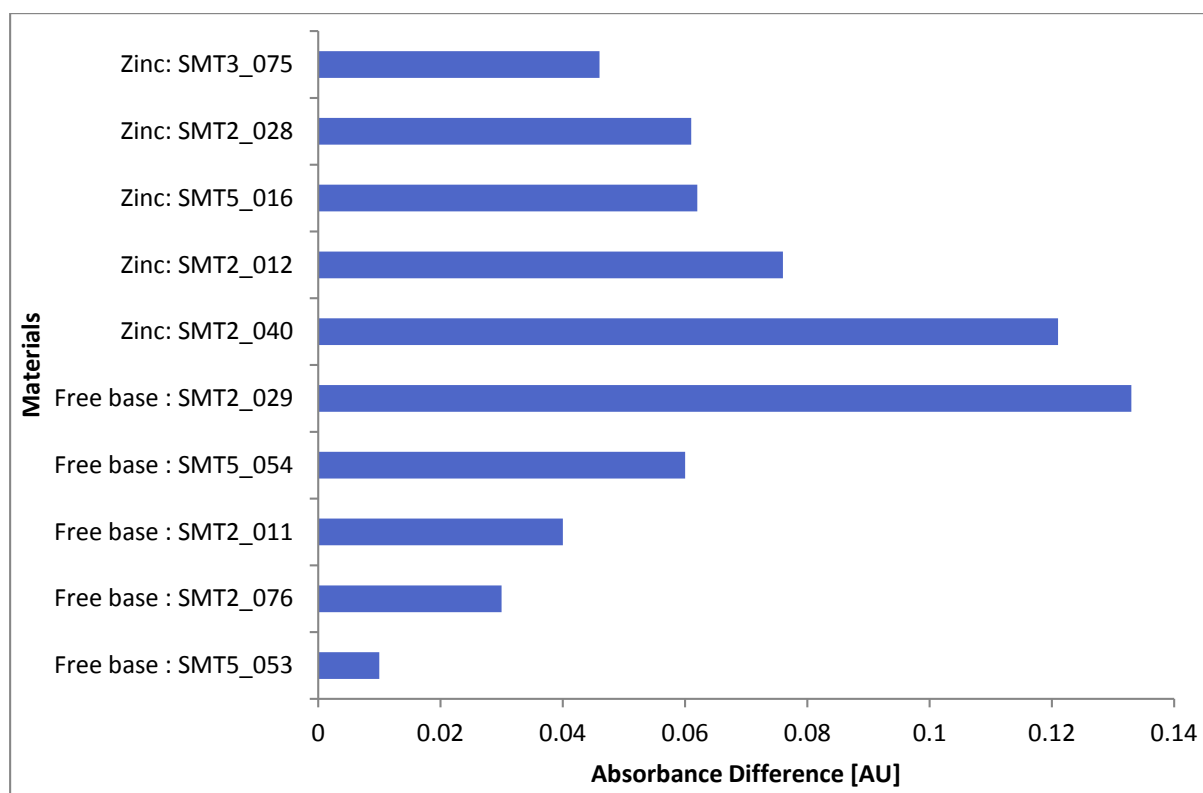
Figure 4.31: Response of the free base and zinc metallo porphyrins to 5.39 ppm of NO$_2$.

Exposing a metal-free porphyrin to an electrophilic gas results in a spectral change. The mechanism of interaction between the free base porphyrin and NO$_2$ is similar to the protonation of the porphine to form a dication [29]. For porphyrin protonation to occur, the NO$_2$ gas would need to be dissolved in water to produce HNO$_3$ (nitric acid) and HNO$_2$ (nitrous acid). In this work, dry gases are used which means that the presence of water could be a consequence of the LS film formation [16]. However, this would likely be driven off during the gentle heating of the recovery cycles. Therefore it is likely that the NO$_2$ directly interacts with the porphine centre and withdraws electrons from it in the same way H$^+$ can.

Figure 4.31 shows that most of the free base porphyrins are responsive to small amounts of NO$_2$, allowing them to be considered as a tentative candidate for future gas sensing applications. However, SMT5_053 and SMT2_076 have shown a relatively low absorbance difference as compared with SMT2_029. It is very possible that SMT5_053 and SMT2_076 are in an aggregated state (at the deposited target pressure) and that may prevent the gas penetrating the bulk and reactive active sites. So, the molecular interaction between those low responsive sensing materials and NO$_2$ molecules may be hindered sterically physically and/or chemically. Therefore the reaction is lower than in the other free base porphyrins.

151

The response of the free base porphyrins when exposed to nitrogen dioxide are similar to the ones presented in carboxylic acids, where in both cases SMT2_012 shows the highest response and SMT5_053 the lowest. The similarity of the results can be easily observed when comparing figure 2.30 with figure 4.25.

The comparison can be done directly with these two different kinds of analytes (NO_2 and carboxylic acids) because both have the same electron withdrawing nature. It is believed that the kinship of the responses can be due to the fact that both analytes produce a similar interaction, in other words, both withdraw electrons from the central ring of the porphyrin.

In the case of the metalloporphyrins, the exposure to amine results do not present a correlation with the results observed upon exposure to NO_2. It is evident that both analytes have a different electron donating/electron withdrawing nature. Some literature sources propose that the mechanism for the metalloporphyrin/NO_2 reaction can only occur through oxidation, resulting in only π-radical cation formation [28]. That effect effectively quenches the protonation in the central metal atom of the porphyrin. Furthermore, it is difficult to understand how the metallo porphyrin binds to reducing species [8].

4.3.3.2 Pure porphyrin and Porphyrin/Calixarene compound deposited on glass substrates:

One of the main disadvantages of porphyrin molecules is that some of the materials have the tendency to aggregate into three dimensional clusters, impeding access for an analyte to bind to the porphyrin molecule. A further consequence of this aggregation is that frequently the porphyrin films are not very homogeneous, so a poor reproducibility from sample to sample is often observed. In order to improve the uniformity in the LB films, a method to enhance the porosity, reduce aggregation and improve uniformity is required.

Some researchers had reported that mixing functional groups with passive matrix materials, such as fatty acids, improves the film homogeneity as a result of the amphiphilicity of the carrier material [30]. In this subsection, calixarene was used as a host Langmuir film matrix material due to its outstanding film forming capability. Calix[8]arenes contain eight polar carboxylic acid groups which anchor the molecule to the air-water interface . They are also well known for exhibiting high porosity to other small molecule species.

Figure 4.32 shows the absorbance spectra of two samples on glass substrates: one made of pure EHO and the other made of a mixture of calixarene and EHO. Both samples have the same number of deposited layers and the spectra have been normalized, so the peak intensity of the Soret band was scaled to unity and hence the responses are considered as a fractional change in absorption.

Noticeably, the EHO spectrum is less noisy than the one presented in the EHO/Calixarene, this is because originally the absorbance spectra of the pure substance has a much higher absorbance due to the greater amount of the optically absorbing material deposited in the sample. Technically speaking, the EHO/Calixarene composite is a dilution of the pure EHO; however, the distribution of porphyrin molecules are more uniform, and that will help to reduce the EHO aggregation. On top of that, the EHO/Calixarene composite has an undoubtedly narrower absorption peak in its spectra, which implies that the local environment of the molecules within the film is more homogenous than the one presented in the pure form of EHO. This is an indication that the EHO within the EHO/Calixarene composite does not aggregate to the same extent as that in the pure EHO film.
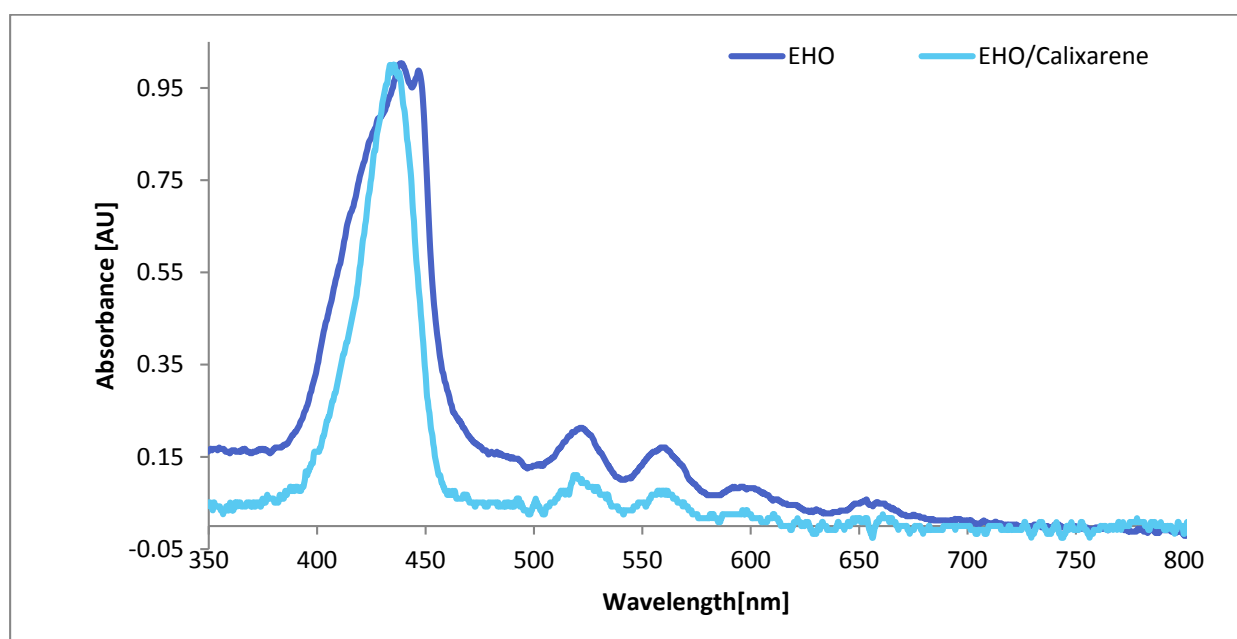
Figure 4.32: Normalized absorbance spectra of pure EHO and EHO/Calixarene.

In EHO, the exposure to NO_2 causes spectral changes, i.e. a Soret band intensity reduction (434 nm) and the appearance of a new strong band at approximately 470 nm. The change in

absorbance induced by 5.39 ppm of NO_2 for the EHO and EHO/calixarene samples are illustrated in figures 4.33 and 4.34.
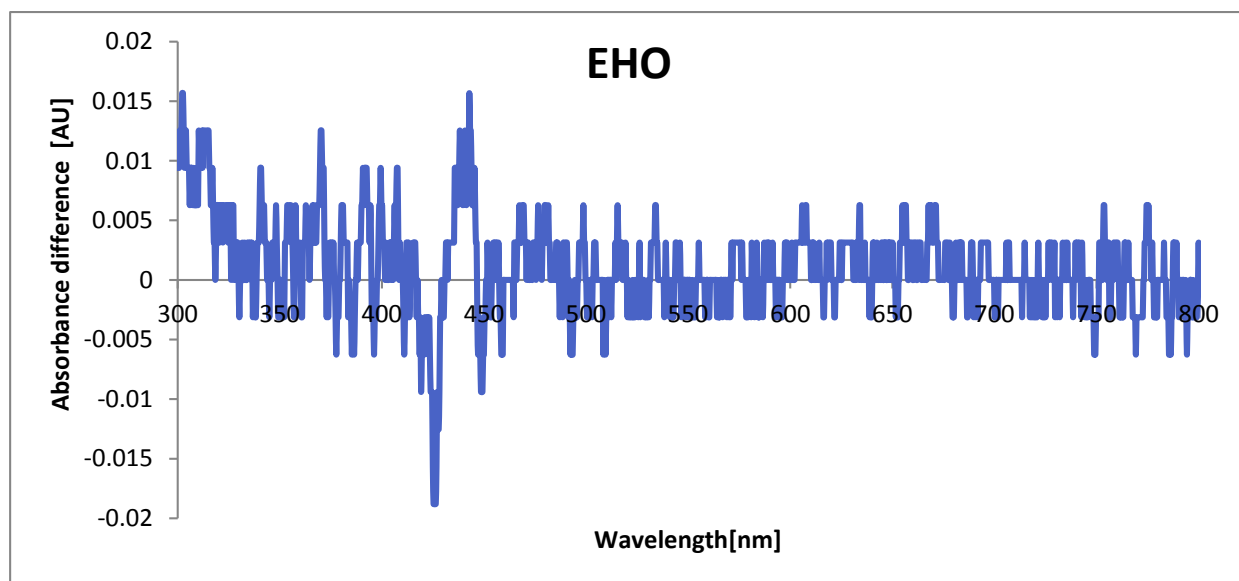
Figure 4.33: Spectrum difference of the EHO LS sample when exposed to 5.39 ppm of NO_2.
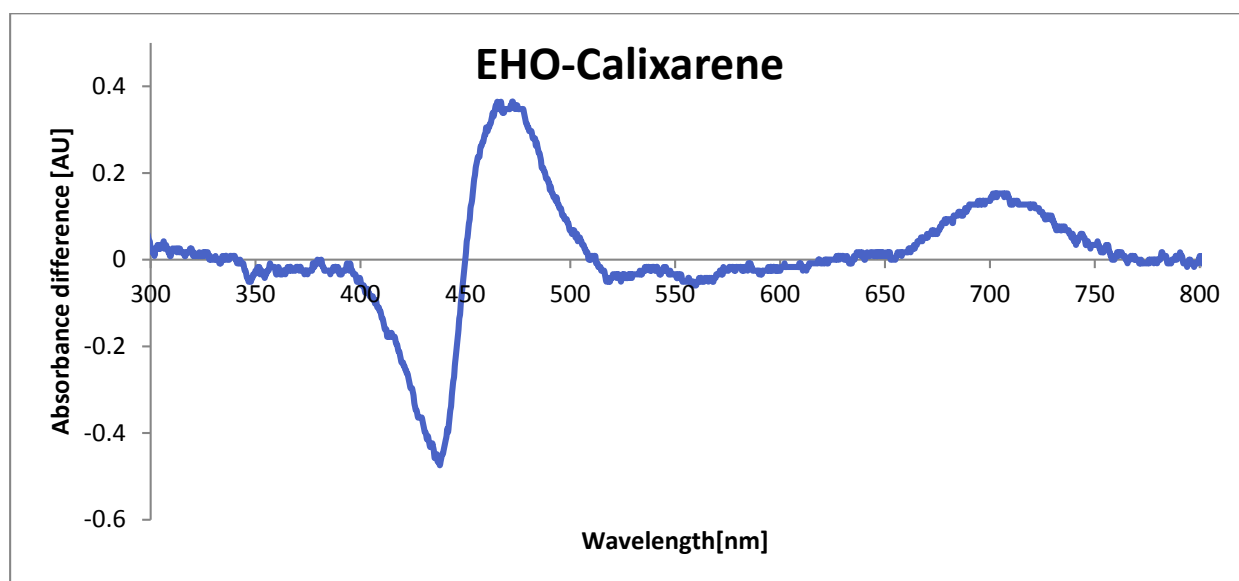
Figure 4.34: Spectrum difference of the EHO LS sample when exposed to 5.39 ppm of NO_2.

Clearly, a higher absorbance difference is perceived in the EHO/Calixarene sample, and two clear peaks located at 436 and 470 nm are presented in figure 4.34. On the other hand, figure 4.33 shows the absorbance difference of a sample made of pure EHO; note that there is a low spectral change in the Soret peak, shifting from 434 to 442 nm.

154

It is evident that the preparation of a mixed film containing calixarene and EHO reduces the aggregation of the porphyrin molecules. The calix[8]arene molecules act as matrix for the porphyrin, leading to a less rigid and very stable films. The organization of the porphyrin molecules is altered by the calix[8]arene matrix, which lessen the EHO aggregation through the formation of a more equitable hydrophobic/hydrophilic situation at the air-water interface. The result of the more uniformly ordered porphyrin molecules in mixed films with calix[8]arene has been visibly demonstrated by the enhancement of a higher spectral response during exposure to NO_2.

4.3.3.3 Porphyrin/TiO_2 composite:

In this subsection, TiO_2 samples were immersed in four porphyrin solutions in order to anchoring the sensing molecules on the aligned TiO_2 rods present upon the glass substrate. It is important to remark that not all materials are able to anchor with the TiO_2 rods, by way of explanation, it is necessary to have side groups such as chlorosilanes, alkoxysilanes, isocyanates and carboxylic acids [31]. So, the highly polar side groups of the carboxylic acid presented within the side groups of the porphyins allowed the molecules to be anchored onto the TiO_2 rods by chelating and/or bidenate binding.

Figures 4.35, 4.37, 4.39 and 4.41 show the absorption spectra of the MCMPP, MCTPP, T3CPP and T4CPP porphyrins deposited onto the TiO_2 solid substrate before and after exposure to 500 ppm of NO_2. Figure 4.36, 4.38, 4.40 and 4.42 shows the spectral change of the samples induced by the gas, in which the corresponding change in absorbance is plotted as a difference spectrum (the exposed spectrum is subtracted from the unexposed spectrum). The absorbance spectrums were normalized, i.e. the maximum peak in the non-exposed reference spectrum of the porphyrin was adjusted to unity, and the exposure was modified by the same ratio. Hence, the results should be interpreted as a fractional change in absorption.

As shown in figure 4.35, noticeably the MCMPP spectrum is different from the rests of the materials; not only in its shape, but also in its higher signal-to-noise ratio. The porphyrin sample shown a Soret band localized at 477 nm and two shoulders at 380 and 685 nm. Before being normalized the Soret shown to be at least 10 times smaller in absorbance than the rest of the deposited porphyrins. So, it is very possible that the number of porphyrins deposited

on the film is lower than the rest of the materials. Also, due to the fact that there is only one side group attached to the porphine by the methine bridges, the response is not only smaller, but also less reactive to the toxic gas. The delocalization of the π-electrons around the phenyl helps to disperse the charge in the porphyrin molecule, so the absence of three additional phenyl rings in MCMPP causes a lower magnitude of reaction. In figure 4.35, a small shift in absorbance is perceived at 424 nm, lowering its absorbance at that particular wavelength approximately 15 percent.

Figure 4.35: Absorbance spectra of MCMPP before and after being exposed to 500 ppm.
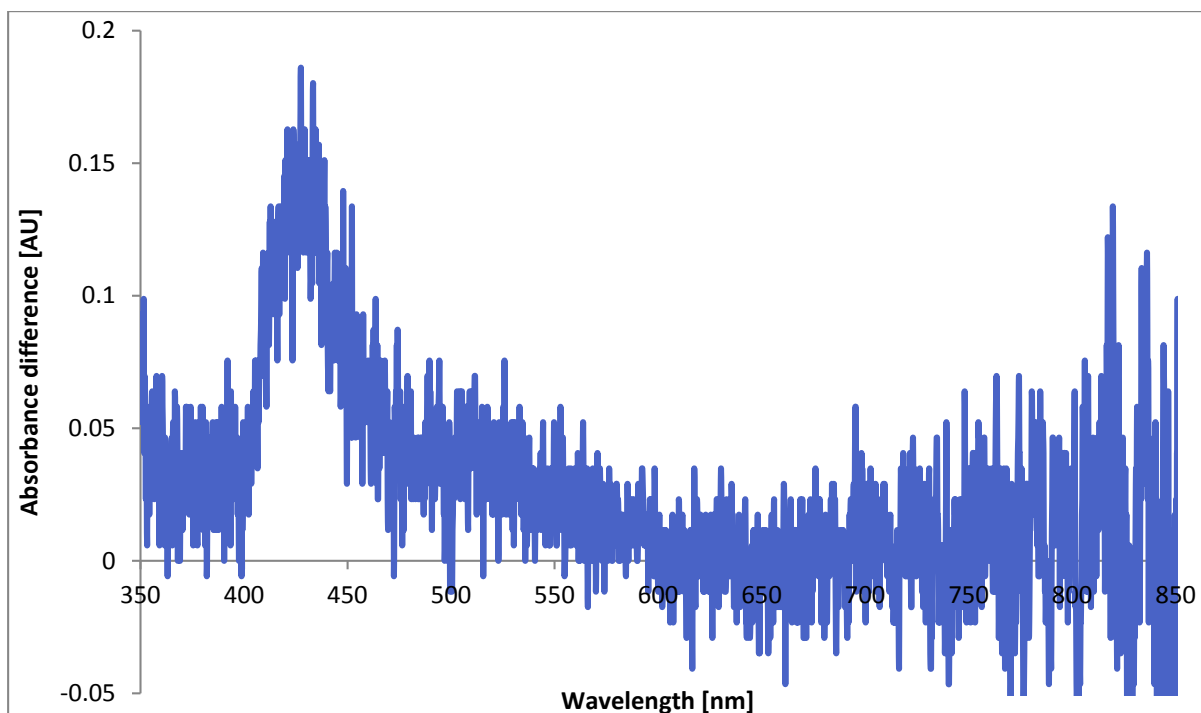
Figure 4.36: Change in absorbance for the MCMPP after being exposed to 500 ppm of NO$_2$.

Figure 4.37 shows the absorbance spectrum of the MCTPP/TiO$_2$ composite, the Soret and Q bands can be seeing clearly before the exposure to the analyte and they are located at 409, 519, 554, 592 and 650 nm respectively. The difference in absorbance between the two states (exposed and unexposed) is shown in figure 4.38. Upon exposure to NO$_2$ the Soret band shifts from 409 to 430 nm, whereas the Q bands are slightly red shifted. Nevertheless, due to the limitations of the UV-VIS apparatus, it is hard to point out the precise new location of the Q bands.
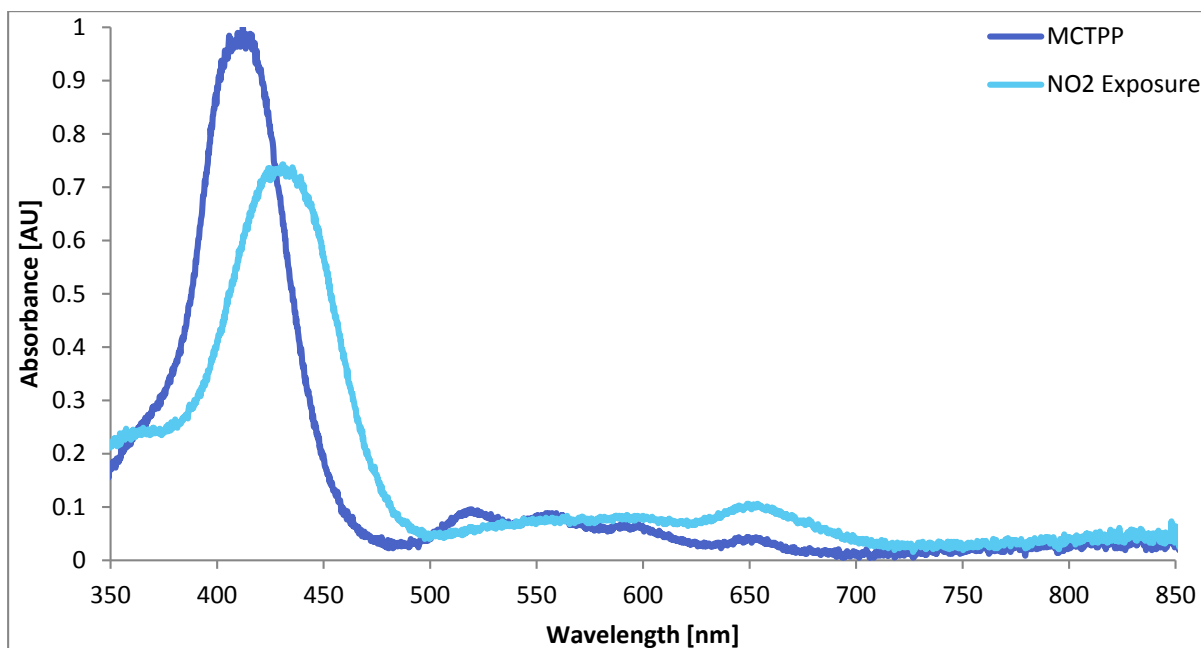
Figure 4.37: Absorbance spectra of MCTPP before and after being exposed to 500 ppm.
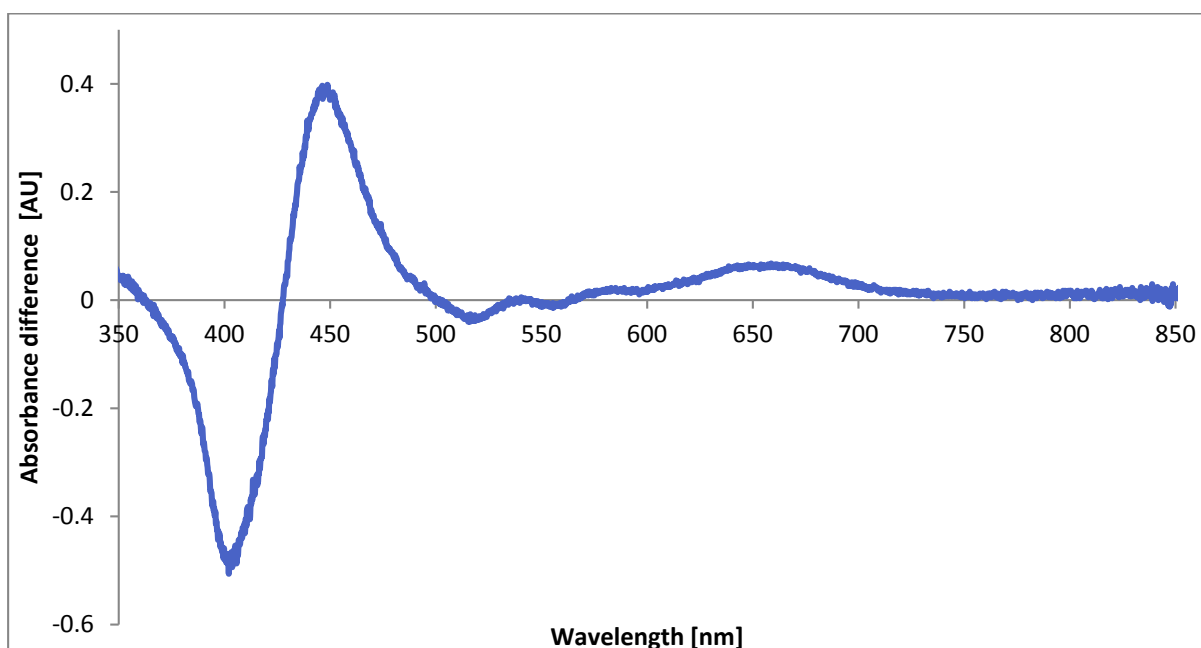
Figure 4.38: Change in absorbance for the MCTPP after being exposed to 500 ppm of NO₂.

Similarly, figure 4.39 depicts the T3CPP sample. The figure shows a Soret peak at 415 nm and four Q bands positioned at 517, 554, 593 and 650 nm approximately. The repositioning of the Soret band is a red shift to a new position 433 nm. This material can be directly compared to T4CPP because both porphyrins have the same number of side groups with the same carboxylic acid substituent; however, the end of the functional group is located in the para

position for the T4CPP and in the meta position for the T3CPP. The difference in absorbance due to the exposure is noticeably higher for the T4CPP than the T3CPP. It is possible that the binding mechanism to the substrate may be the same for both materials because they both have four phenyl groups with a carboxylic acid on their side groups. So the difference between T4CPP and T3CPP samples lies in the overall delocalization of π-electrons, which favours the T3CPP material by resonant effects because the carboxyl group its attached on the meta position. Yet, the stability given by the side groups located in the para position (for the T4CPP) may overcome the resonant effects and as a result, the sample exhibits a higher absorbance change, illustrated in figure 4.41.
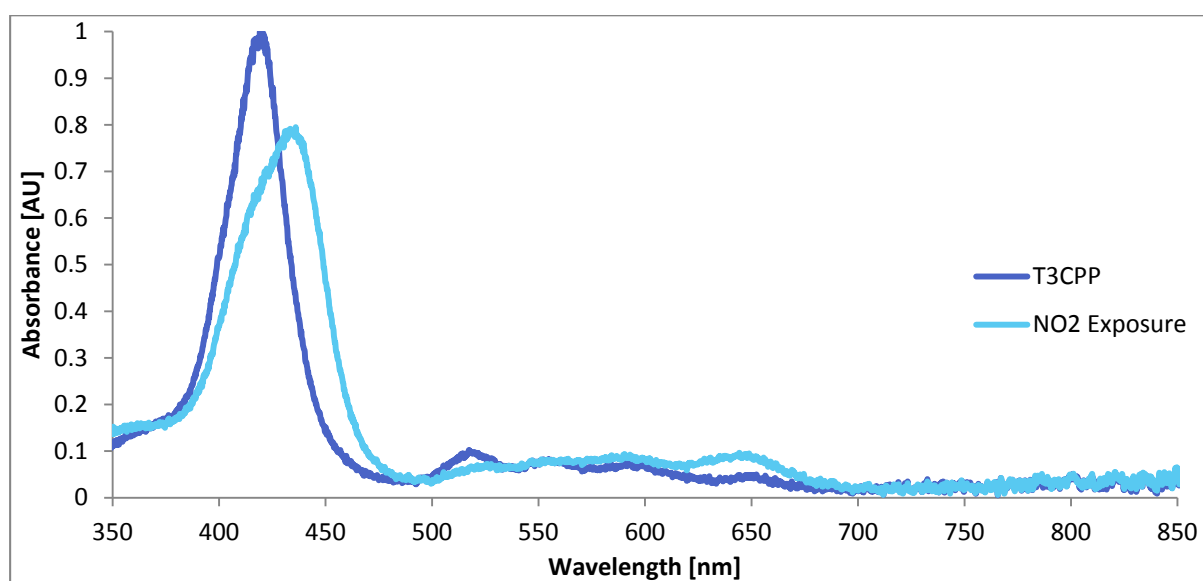
Figure 4.39: Absorbance spectra of T3CPP before and after being exposed to 500 ppm.
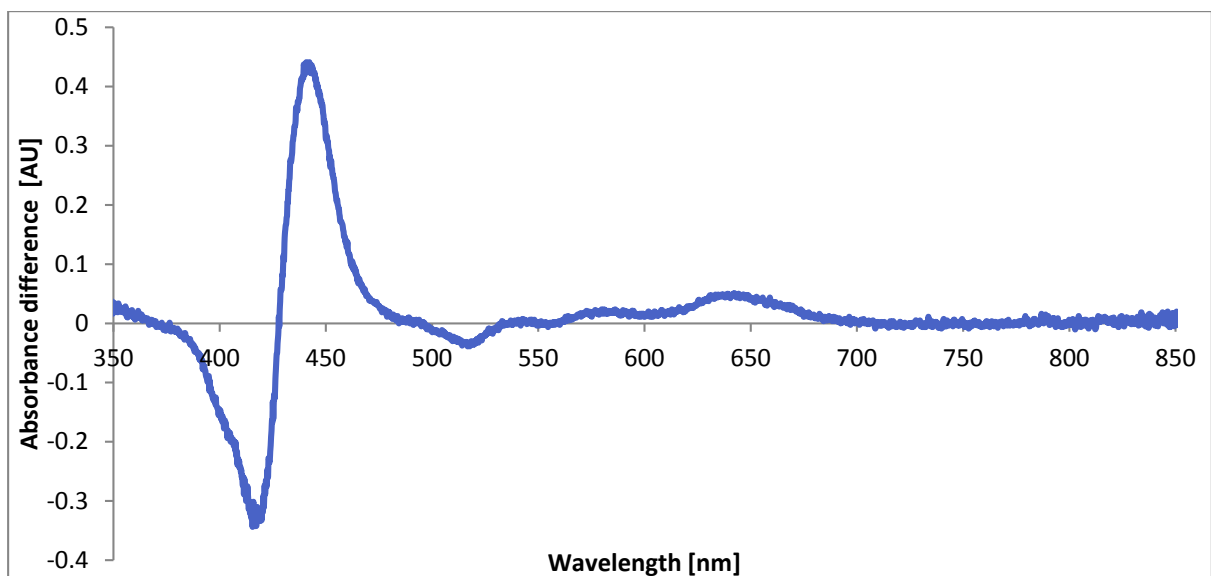
Figure 4.40: Change in absorbance for the T3CPP after being exposed to 500 ppm of NO$_2$.
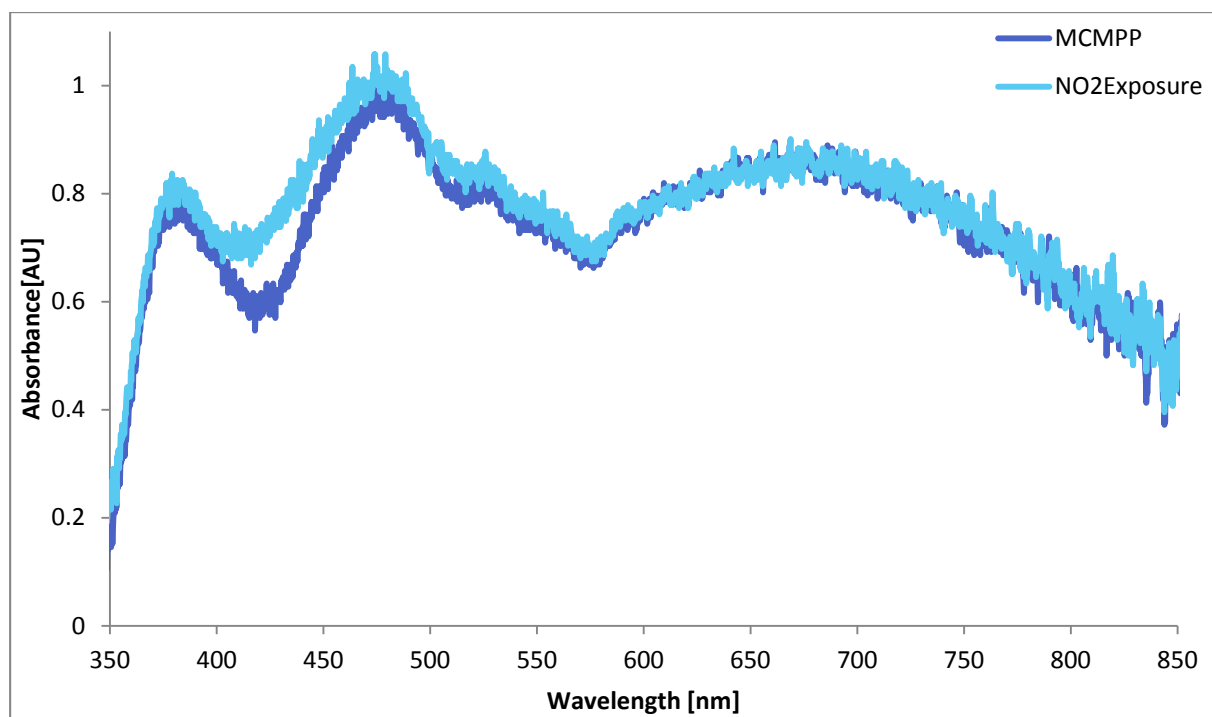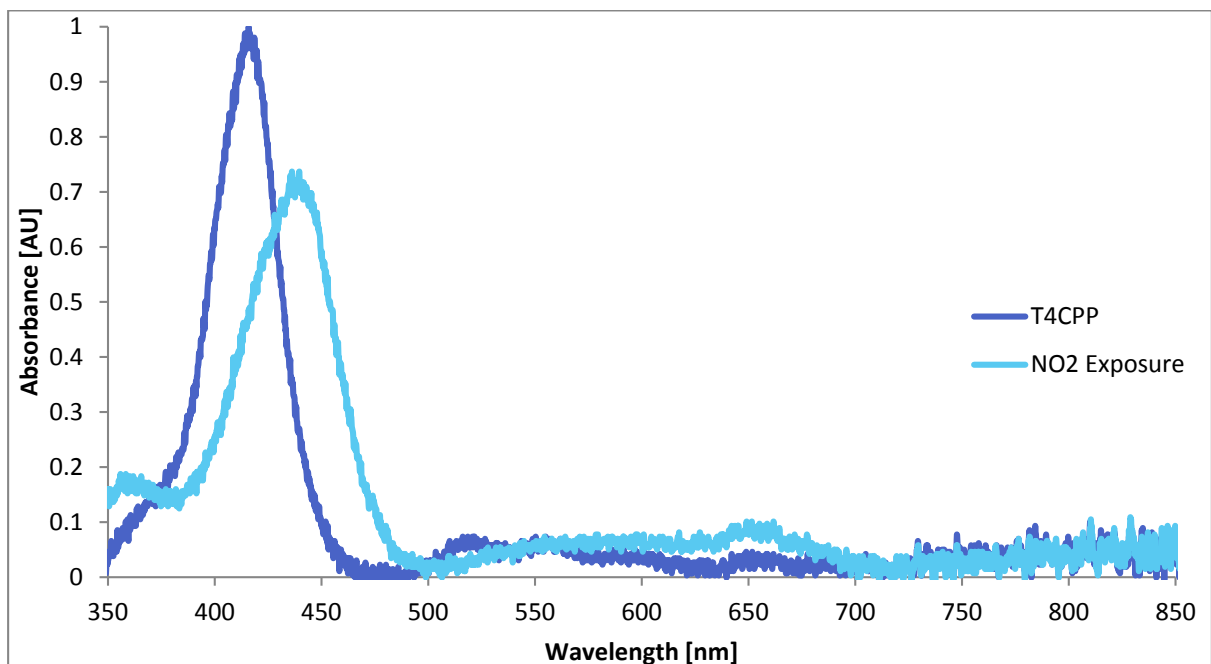

Figure 4.41: Absorbance spectra of T4CPP before and after being exposed to 500 ppm.
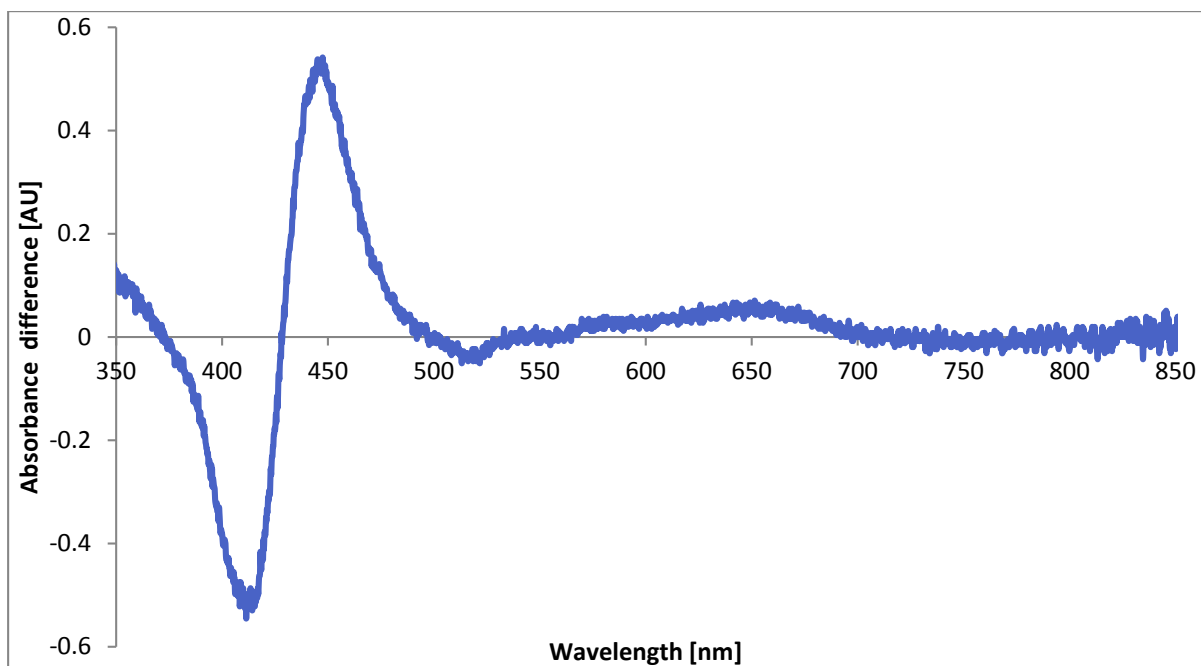
Figure 4.42: Change in absorbance for the T4CPP after being exposed to 500 ppm of NO$_2$.

Apart from MCMPP, all the absorbance spectrums shown to have a similar shape in their Soret peaks and Q bands. The spectrum of MCMPP may be different from the other porphyrins because it only contains one single side group, and this causes a lack of symmetry within the molecule. The rest of the materials have four phenyl rings, however the position and the number of their carboxyl groups differs for each porphyrin, as shown in table 4.8. The highest responses were presented with the materials that have four phenyl groups with a carboxyl end in their side groups. In this manner, T4CPP was the most responsive material presumably due to the position at which its four side carboxyl groups attach to the porphyrin ring i.e. at the para position.

Using composites of TiO$_2$ as host material infused with porphyrin presents two advantages to the simple films of porphyrin deposited on glass substrate: an extremely low concentration of dye is needed to create the sensing film and very little aggregation of the porphyrin molecules within the composite solid film is observed. On top of that, the TiO$_2$/porphyrin composites also help to facilitate the diffusion of analytes e.g. nitrogen dioxide into the composite matrix due to its high porosity. These optical based sensor show good stability with temperature and allows a fast recovery with temperature [32].

Section 4: Alcohol detection

This last section is focused on the detection of alcohols using metalloporphyrin as a sensing material. In particular, the detection of the various alcohol vapours based on the optical sensing response of magnesium EHO porphyrin LS thin films. The characterization of the magnesium porphyrin and responses to alcohols results were used for the elaboration of the proto-type sensor described in section 5.3.

4.4.1. Materials

4.4.1.1 Porphyrins

Magnesium EHO porphyrin (MgEHO) is a derivate of the free base porphyrin EHO; differing from it by the magnesium ion placed on the centre of the porphine ring. The chemical structure of the metalloporphyrin is illustrated in figure 4.43.
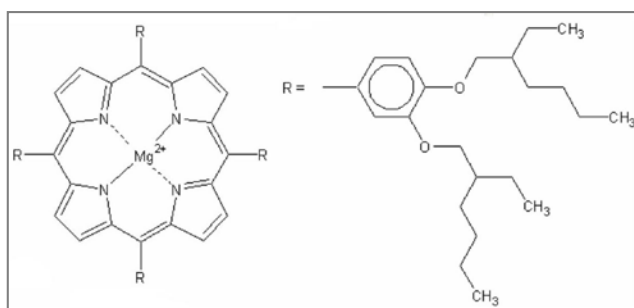
Figure 4.43: Chemical structure of MgEHO.

4.4.1.2 Analytes

In this study alcohols are used as the analyte to be detected; the functional group characteristic of this organic compound is the hydroxyl group (-OH) bound to a carbon atom. Three kind of alcohols are presented in this work: primary, secondary and tertiary. The primary alcohols are methanol, ethanol and octanol, and differ one from the other by its hydrocarbon chain size. 2-propanol falls into another category, a secondary alcohol; and finally, 2-methyl-2-butanol is a tertiary alcohol.

162
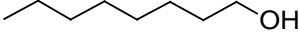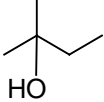
Analyte	Chemical structure
Methanol	—OH
Ethanol	⌒OH
Octanol	⌒⌒⌒OH
2-Propanol	(structure) OH
2-methyl-2-butanol	(structure) HO

Table 4.9: List of alcohols used in this study

4.4.2. Experimental Details

A solution of 1.75 mg/ml of MgEHO was prepared using chloroform as a solvent. Five MgEHO LS layers were deposited on a hydrophobic glass substrate while the barrier compressed the film to a surface of 8 mNm^{-1}. The deposition of the metalloporphyrin was carried out at a rate of 1000 mm min^{-1} according to the procedure described in section 3.2. It is well-known that the thin film structure made by the ultra-fast deposition rate produces a high porosity morphology within the film, which facilitates the diffusion of analyte trough the sample [33].

The liquid analytes were placed in a vessel and submerged in a heated water bath to a constant temperature of 40°C. Since all materials have a different molecular weight and boiling points, it is expected there will be a different vapour concentration for every alcohol. The concentrations of the alcohols were calculated by the Antoine equations on the assumption that the sum of flow gas rates of toxic and pure nitrogen were constant at all-time. The calculated concentrations of the alcohols were: 26 ppt of octanol; 50 ppt of 2-methyl-2-butanol; 68 ppt of 2-propanol; 176 ppt of ethanol and 350 ppt of methanol.

4.4.3. Results

4.4.3.1 Response of the magnesium porphyrin to alcohol vapours

Figure 4.44 shows the absorbance spectrum of a five MgEHO LS layers sample deposited on a glass substrate. The characteristic Soret peak, two Q bands and a shoulder can be find at 435, 571, 613 and 657 nm respectively.
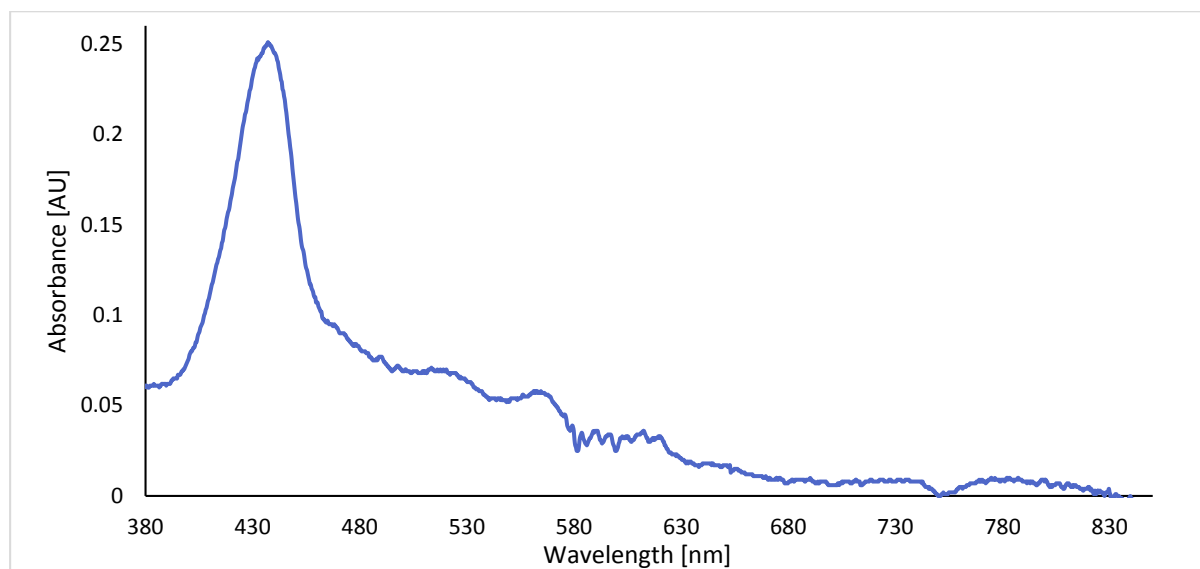
Figure 4.44: Absorbance spectrum of five MgEHO LS layers deposited on a glass substrate.

The MgEHO sample was then exposed to the alcohol vapours. Sections 3.5.1e describes the gas delivery process. In all cases, it has been observed that there is a small colour change associated with the binding between the magnesium porphyrin and the alcohols.

Figure 4.45 shows the absorbance change that occurs as a result of analyte binding and any forces formed by the interaction between the metalloporphyrin and the vaporised analytes. The change in absorbance between the porphyrin and the alcohol can be explained in terms of molecular interactions. The subtle change is due to the magnesium porphyrin axially binding an alcohol ligand to the central Mg^{2+} ion, causing a spectral change [34]. However the alcohol-MgEHO porphyrin reaction is not limited to the formation of the ligand, other weaker interactions such as hydrogen bonding and van der Waals are also involved [35].

Notice that for this particular experiment the results have not been normalized because there is only one material, so no comparison with other porphyrins is necessary. A point to be noticed is that the change in absorbance in figure 4.45 is noisy for all analytes, indication that

164

the UV-Vis is good enough for detecting the change in absorbance but the instrument is near its limit of detection. The magnitude of response between the alcohols and the magnesium porphyrin is particularly weak compared to other analyte-porphyrin complexes [36]. This case was studied comparatively to demonstrate the advantages of incorporating an optical amplifying device, as described in section 5.3.
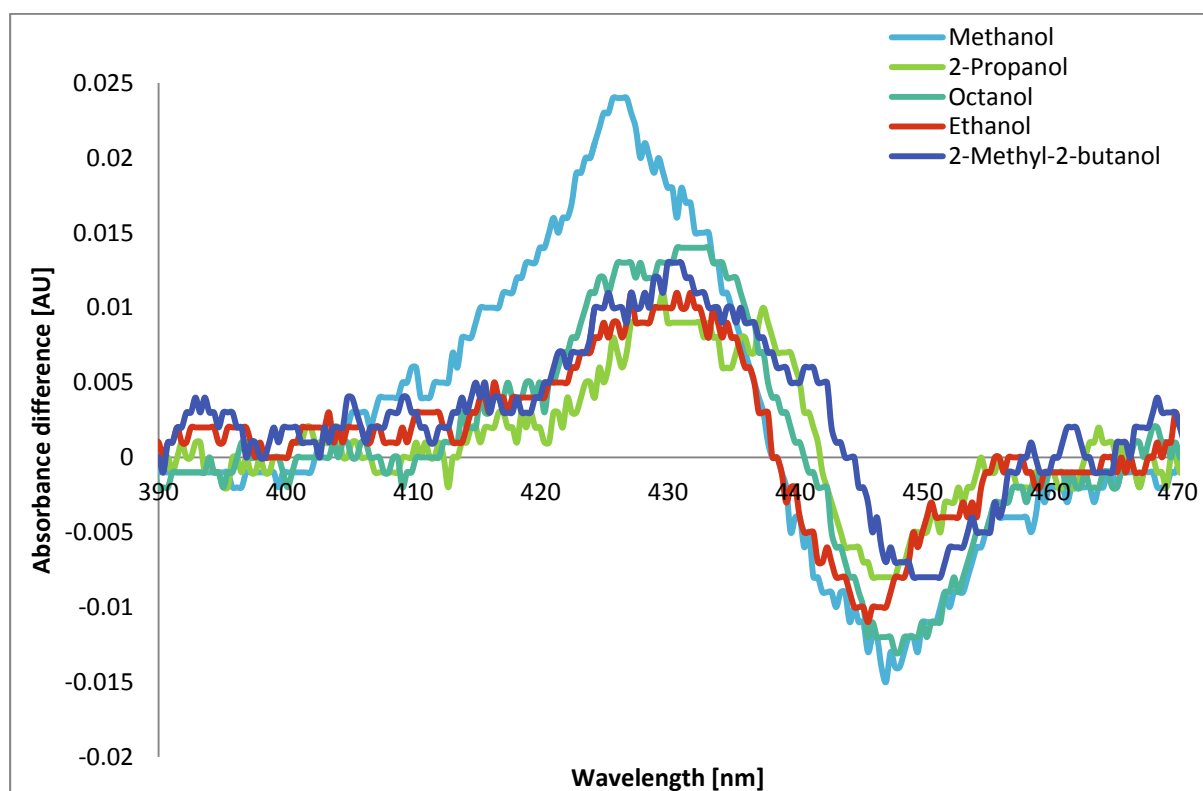
Figure 4.45: Spectral difference of the MgEHO sample when the sample is exposed to vapour analytes.

The analysis also shows that the absorbance difference graph is fairly similar to all the different alcohols studied; the main change between different analytes is that the strongest absorbance peaks seems to occur at different wavelengths for different alcohols. As an example, the upper peak is located at 425±0.5 nm for methanol and 433±0.5 nm for octanol. This effect may play an important role in the next chapter and it will be explained in more detail later.

Figure 4.46 shows a numerical representation of the maximum absorbance difference obtained in the MgEHO sample. Clearly, methanol shows the highest response, followed by ethanol. This result was not surprising, because it was expected to have a higher response with a smaller molecules due to their high vapour concentration in comparison with the other

alcohols. 2-propanol shown an intermediate behaviour, as well as 2-methyl-2-butanol. It is important to remark that the high vapour concentration of methanol (in the order of hundreds of ppt) may saturate the magnesium porphyrin sample, in such a way that no more sites are available and there is no longer places to bind with.

2-Propanol and 2-methyl-2-butanol have a similar vapour concentration of 68 and 50 ppt respectively. However, even when the concentration of 2-propanol is higher, 2-methyl-2-butanol exhibits a higher absorbance difference. It is possible that the difference in their chemical structure induces a different reaction in the magnesium porphyrin, facilitating the reaction of the 2-methyl-2-butanol due to the extra carbon in its structure (see table 2.9).

It is indisputable that the lower response corresponds to the biggest analyte molecule (octanol) due to its low vapour pressure at the water bath fixed temperature. However, the response has a similar numerical value to the response induced by 2-propanol. Despite the fact that octanol showed the lowest absorbance difference in the graph it is possible that in proportion it is the analyte that induces a higher spectral difference.
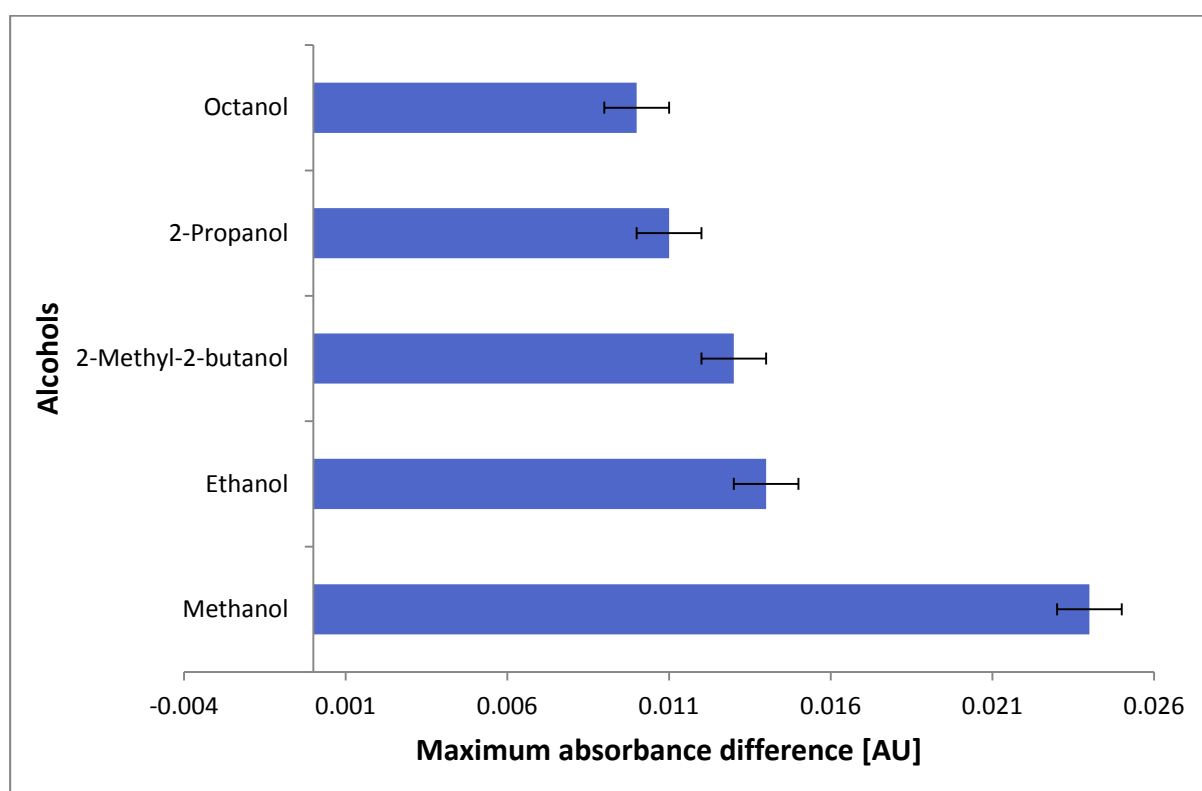
Figure 4.46: Optical response of the MgEHO glass sample to the various analytes.

4.4.3.2 Kinetics of the magnesium porphyrin and 2-methyl-2-butanol complex

The following section contains data that was obtained after the exposure of alcohols to the proto-type vapour sensor described in section 5.3. So, the results presented here are complementary to the ones presented in chapter 5. In this manner 2-methyl-2-butanol was studied because it induced a maximum spectral shift at 430 nm (as depicted in figure 4.45), the selection of the wavelength range for the proto-type is particularly important in order to obtain a decent optical response.

Figure 4.47 shows the absorbance change of the metalloporphyrin glass sample before and after exposure to 2-methyl-2-butanol vapour with a concentration of 50 ppt. After the exposure, a very small spectral change in the absorbance is observed: the Soret peak is slightly blue shifted by only a few nanometres (approximately 3) and also absorbs slightly more strongly. The difference spectrum for the 2-methyl-2-butanol-MgEHO complex can be observed in figure 4.45.
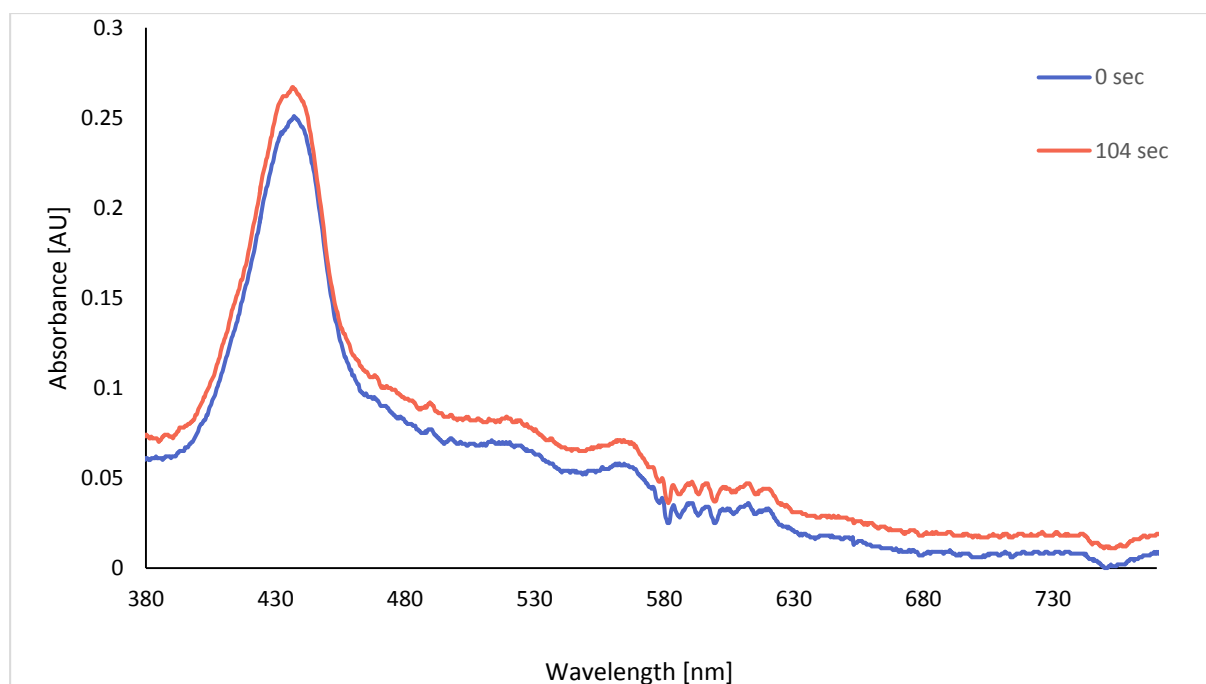
Figure 4.47: Absorbance spectrum of the glass MgEHO spectrum before and after exposure to 50 ppt of 2-methyl-2-butanol vapour. The Soret peak changes its position upon exposure, blue shifthing from 435 to 432 nm approximately.

Additionally, figure 4.48 depicts the kinetics of the absorbance spectrum at the peak located at 430 nm, wavelength at which the largest change in absorbance for the MgEHO-2M2B

complex is registered (as shown in figure 4.45). The measurements were reported at times corresponding to 0, 8, 31, 56, 80 and 104 seconds after the exposure of 2-methl-2-butanol. It is important to mention that after 104 seconds, no more spectral changes were observed, so the glass sample was considered to be saturated after that point.
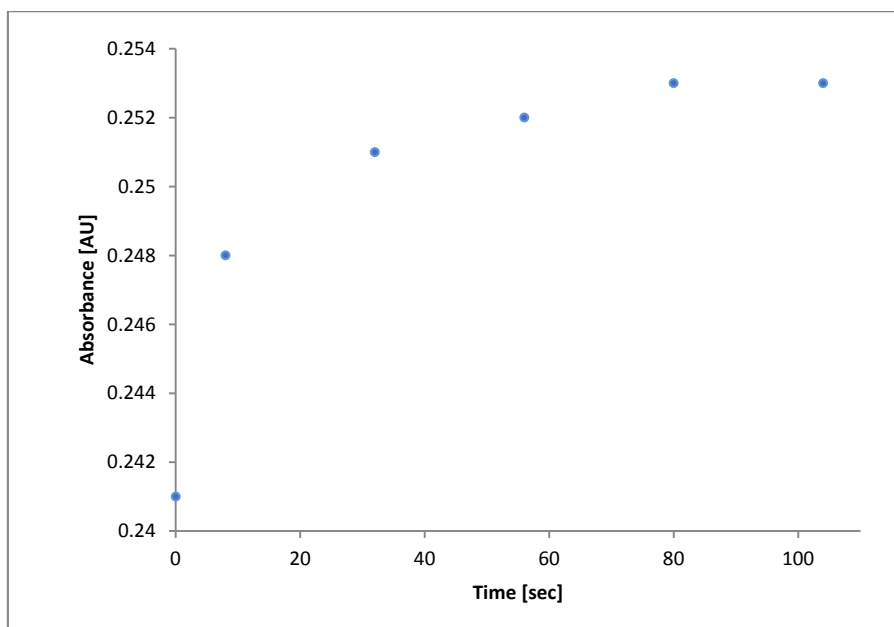
Figure 4.48: Kinetics of the adsorption peak located at 430 nm corresponding to the spectral change in the glass MgEHO sample after the exposure to 50 ppt of 2-methyl-2-butanol.

The magnesium porphyrin-alcohol interactions are clearly weak, as observed in figure 4.46. This porphyrin analyte pair which demonstrate weak but measurable optical features were deliberately selected for further study in a prototype sensor device to demonstrate the advantages of using a system that amplifies a the sensor signal using an LED and phototransistor as an electrical transducer. This further study of MgEHO continues in the next chapter, where the material is used to develop the proto-type sensor system presented in section 5.3.

Conclusions, implications and future work

Both metalled and free base porphyrins have shown a response to a variety of analytes. Zinc porphyrins were responsive to a series of amines, including primary, secondary and tertiary; free base porphyrins reacted to carboxylic acids and nitrogen dioxide; and a magnesium porphyrin was responsive to a series of alcohols.

In the case of the free base porphyrins (STM, MC and TxCPP series) and zinc porphyrins the responses induced by the analytes varied depending on the sensing material, which differ one from each other in their moieties. Their side groups played an important role not only in their activating strength between the material and the analyte, but also determines the porphyrin/porphyrin interaction which in turn is related to the degree of aggregation.

The isotherms in the free base porphyrins (SMT series) show that the longer the side group attached to the porphine, the higher the take-off area. Most materials show three separated phases, however materials containing long hydrocarbon chains in their group sides (SMT2_040 and SMT2_012) show more complicated changes of phase.

For the zinc porphyrins the isotherms shows that the take-off area does not correspond to the length of the moieties. In fact, the isotherm shows that most of the porphyrins may be aggregated, so the characteristic curves are attributed to porphyrin/porphyrin interactions.

In solution the interaction between the analyte and the non-aggregated porphyrin are simple because the molecules can move freely. Once the material is deposited on a substrate, aggregation of material may occur resulting in steric hindrance.

The zinc porphyrins deposited on glass substrate proved that an open structure is more important than the electronic donating properties of the materials in the vapour sensing of analytes. On the other hand in materials with a lower degree of aggregation (such as zinc porphyrins) electrophilic properties of the moieties determined the response of the sensor. For that case, the more electron donating, the higher the spectral response because the density of electrons is pushed toward the centre of the porphyrin, easing the interactions with

the analytes. Furthermore a strong electron donating properties along with an open structure that allows the analyte molecules to flow through the layers would be optimal properties for the fabrication of a vapour sensor.

It is important to say that in all cases, the typical time responses (t_{90} and t_{50}) increased as the size of the diffusing analyte type increases. In the case of carboxylic acids, the longer the hydrocarbon chain, the slower the response. Similarly, primary amines shown the quickest response whereas tertiary amines shown the slowest.

Future experiments will be focused on the variation of the concentration of analytes in order to obtain saturations points and the possible variation of the kinetics involved in the system.

Hosting porphyrin molecules either with calixarenes or TiO_2 composites helps to reduce the aggregation of molecules and improves the spectral response of the sensing materials. Porphyrins/TiO_2 composites were highly reactive to NO_2. It was found that symmetrical porphyrins (containing the same number of side groups in their para and/or meta positions) were more responsive due to their resonance properties. Also, it was found that the higher the number of side groups containing carboxylic acid the higher the response of the sensor because more side groups were able to anchor to the TiO_2 substrate. Pure EHO tends to aggregate, so in order to avoid that a solution of EHO/calixarene was made. Both, the pure and the EHO/calixarene solutions were deposited on a glass substrate and then the results to the exposure of NO_2 were compared. It was proven that the response of the mixture improved the spectral response of the pure EHO. Further experiments will contemplate the reduction of aggregation of other sensing materials using either calixarenes or TiO_2 substrates. However, the main limitation of the latter one is that it requires specific side groups such as carboxylic acids, chlorosilanes, alkoxysilanes and isocyanates in order to anchor to the TiO_2 rods.

Magnesium porphyrins were responsive to different alcohols. The subtle change is due to the porphyrin axially binding an alcohol ligand to the central magnesium ion, causing a spectral change. However, the interaction between the analytes and the sensing material is so weak that it is near to the limit of the UV-Vis spectrometer. The characterisation of the responses to alcohols was an ideal candidate to show the potential of the amplification achieved in the proto-type vapour sensor system developed in chapter 3.

References:

1. Lawrence, S.A., *Amines: synthesis, properties and applications*. 2004: Cambridge University Press.
2. Brittle, S., et al., *Alkylamine Sensing Using Langmuir–Blodgett Films of n-Alkyl-N-phenylamide-Substituted Zinc Porphyrins.* The Journal of Physical Chemistry B, 2008. **112**(36): p. 11278-11283.
3. Hunter, C.A., M.C. Misuraca, and S.M. Turega, *Dissection of Complex Molecular Recognition Interfaces.* Journal of the American Chemical Society, 2010. **133**(3): p. 582-594.
4. Carey, F.A. and R.J. Sundberg, *Advanced Organic Chemistry: Part A: Structure and Mechanisms*. 2007: Springer.
5. Hunter, C.A., et al., *Optical changes induced in Zn porphyrin solutions and LB films by exposure to amines.* Journal of Porphyrins and Phthalocyanines, 2006. **10**(07): p. 978-985.
6. Capone, S., et al., *Solid state gas sensors: state of the art and future activities.* Journal of Optoelectronics and Advanced Materials, 2003. **5**(5): p. 1335-1348.
7. Pedrosa, J.M., et al., *Characterization and fast optical response to NO2 of porphyrin LB films.* Materials Science and Engineering: C, 2002. **22**(2): p. 433-438.
8. Richardson, T., et al., *Gas sensing properties of porphyrin assemblies prepared using ultra-fast LB deposition.* Colloids and Surfaces A: Physicochemical and Engineering Aspects, 2002. **198**: p. 843-857.
9. Haynes, W.M., *CRC handbook of chemistry and physics*. 2012: CRC press.
10. Brittle, S.A., et al., *Comparing zinc and manganese porphyrin LB films as amine vapour sensing materials.* Colloids and Surfaces A: Physicochemical and Engineering Aspects, 2008. **321**(1–3): p. 29-33.
11. Kosal, M.E., et al., *A functional zeolite analogue assembled from metalloporphyrins.* Nature materials, 2002. **1**(2): p. 118-121.
12. Banfi, S., et al., *Photodynamic effects of porphyrin and chlorin photosensitizers in human colon adenocarcinoma cells.* Bioorganic & Medicinal Chemistry, 2004. **12**(18): p. 4853-4860.
13. Chekmeneva, E., et al., *Evidence for Partially Bound States in Cooperative Molecular Recognition Interfaces.* Journal of the American Chemical Society, 2008. **130**(52): p. 17718-17725.
14. Clayden, G., et al., „*Organic Chemistry* ", 2001, Oxford University Press.
15. Brittle, S.A., et al., *Tuning free base tetraphenylporphyrins as optical sensing elements for volatile organic analytes.* Journal of Materials Chemistry, 2011. **21**(13): p. 4882-4887.
16. Richardson, T., et al., *Development and optimization of porphyrin gas sensing LB films.* Advances in colloid and interface science, 2005. **116**(1): p. 81-96.
17. Dooling, C. and T. Richardson, *Thickness dependence of the toxic gas response in EHO Langmuir–Blodgett films prepared by ultra-fast deposition.* Materials Science and Engineering: C, 2002. **22**(2): p. 269-274.
18. Grieve, M.B., et al., *An investigation of the optical properties of tetraphenylporphyrin derivatives in Langmuir and Langmuir-Blodgett films.* Thin Solid Films, 1994. **243**(1–2): p. 581-586.
19. Smith, V., T. Richardson, and H. Anderson, *Optical detection of chlorine gas using LB films of a zinc porphyrin dimer.* Supramolecular Science, 1997. **4**(3): p. 503-508.
20. de Miguel, G., et al., *Dis-aggregation of an insoluble porphyrin in a calixarene matrix: characterization of aggregate modes by extended dipole model.* Physical Chemistry Chemical Physics, 2008. **10**(11): p. 1569-1576.
21. Collman, J., et al., *The Porphyrin Handbook.* The Porphyrin Handbook, 2003. **11**: p. 1-49.
22. Dunbar, A.D.F., et al., *Langmuir–Schaefer films of five different free base tetraphenylporphyrins for optical-based gas sensing of NO2.* Sensors and Actuators B: Chemical, 2008. **128**(2): p. 468-481.

23.   Worsfold, O., et al., *Nitrogen dioxide sensing characteristics at elevated temperature of sol–gel glass thin films containing substituted porphyrin dyes.* J. Mater. Chem., 2001. **11**(2): p. 399-403.

24.   Castillero, P., et al., *Active and optically transparent tetracationic porphyrin/TiO2 composite thin films.* ACS applied materials & interfaces, 2010. **2**(3): p. 712-721.

25.   Roales, J., et al., *Selective Detection of Volatile Organic Compounds by Spectral Imaging of Porphyrin Derivatives Bound to TiO2 Porous Films.* ACS applied materials & interfaces, 2012. **4**(10): p. 5147-5154.

26.   Dunbar, A., et al., *Understanding the interactions of porphryin LB films with NO2.* Colloids and Surfaces A: Physicochemical and Engineering Aspects, 2006. **284–285**(0): p. 339-344.

27.   Cano, M., et al., *A transparent TMPyP/TiO2 composite thin film as an HCl sensitive optochemical gas sensor.* Sensors and Actuators B: Chemical, 2010. **150**(2): p. 764-769.

28.   Dunbar, A.D., et al., *Langmuir–Schaefer films of five different free base tetraphenylporphyrins for optical-based gas sensing of NO< sub> 2</sub>.* Sensors and Actuators B: Chemical, 2008. **128**(2): p. 468-481.

29.   McNaughton, A., et al., *Characterisation of the reaction of free-base porphyrin to nitrogen dioxide.* Colloids and Surfaces A: Physicochemical and Engineering Aspects, 2006. **284**: p. 345-349.

30.   Richardson, T.H., et al., *The NO2 gas sensing properties of calixarene/porphyrin mixed LB films.* Colloids and Surfaces A: Physicochemical and Engineering Aspects, 2006. **284–285**(0): p. 320-325.

31.   Paz, Y., *Self-assembled monolayers and titanium dioxide: From surface patterning to potential applications.* Beilstein journal of nanotechnology, 2011. **2**(1): p. 845-861.

32.   Cano, M., et al., *A transparent TMPyP/TiO< sub> 2</sub> composite thin film as an HCl sensitive optochemical gas sensor.* Sensors and Actuators B: Chemical, 2010. **150**(2): p. 764-769.

33.   Pedrosa, J.M., et al., *The optical gas-sensing properties of an asymmetrically substituted porphyrin.* Journal of Materials Chemistry, 2002. **12**(9): p. 2659-2664.

34.   Di Natale, C., et al., *Characterization and design of porphyrins-based broad selectivity chemical sensors for electronic nose applications.* Sensors and Actuators B: Chemical, 1998. **52**(1): p. 162-168.

35.   Gutiérrez, A.F., et al., *A proto-type sensor for volatile organic compounds based on magnesium porphyrin molecular films.* Sensors and Actuators B: Chemical, 2014. **202**(0): p. 854-860.

36.   Dunbar, A.D.F., et al., *Detection of Volatile Organic Compounds Using Porphyrin Derivatives.* The Journal of Physical Chemistry B, 2010. **114**(36): p. 11697-11702.

Chapter 5

Proto-type vapour sensing using molecular films

This chapter is focused on the fabrication of a portable, efficient and inexpensive system able to detect vapour analytes. The main components of the proto-type are a light emitter and a photo detector coated with porphyrin which acts as a sensing material.

In the first section of this chapter, various emitter-receiver pairs are analysed and the evolution of the chambers models is shown. The second section covers the sensing principles, variables in the system and a guide to selecting a suitable porphyrin to detect a specific analyte. Finally, the third section explores in detail an investigation conducted using a porphyrin-analyte pair which display a weak interaction in order to show the benefits and capabilities of using a phototransistor in the proto-type sensors system.

Section I: Design of the proto-type

In this section, the development of the proto-type will be described. Different emitter-receiver circuits were proposed, along with descriptions of their sensing characteristics. For development of the gas exposure chamber, a series of considerations were taken into account in order to reach to the final chamber design. Internal variables in the system such as the distance between the emitter-receiver, alignment of devices, and light interference are discussed. Also, the previous versions of the chambers will be described along with its final version.

5.1.1 Emitter-receiver principle:

Traditional UV-vis systems for absorption and emission measurements are composed of a light source and a spectrometer (UV-Vis spectroscopy is described in section 3.5.1). The proposed vapour sensor system is intended to reduce the scale and the cost of a classical UV-Vis system, and in order to do so, the sensor must have a small-scale and minimalistic design.

The proposed sensing system is based on an emitter-receiver circuit, in which one of the devices is coated in porphyrin that is the heart of the sensor. When an analyte interacts with the delocalized π-electron system of the porphyrin, it alters the energy levels within the molecule causing a change in the absorbance observed. That shift in energy can also be interpreted as a change in colour. The spectral change can be detected with an optoelectronic receiver. For more details refer to the following sections: 2.2, the adsorption process; 2.3, the molecular orbital model (explains the shift in energy produced by the analyte); and 2.7.3, the characteristic porphyrin spectrum.

A light emitting diode (LED) serves as an emitter that provides light to the system. For the detection of light, different optoelectronic devices can play the role as a receptor, e.g. photodiode, photoresistor or phototransistor.

The sensor system is also intended to be as small as possible for two reasons. The first is regarding the portability of the sensing system: the smaller the design, the easier will be to fabricate a portable version of it. The second reason is regarding the size of the gas ring: the chamber must be designed with a minimal internal volume, so the filling and emptying times could be reduced in comparison with big chambers, and therefore more cycles (exposed-recovery) can be performed.

For convenience, the sensor material (porphyrin) is deposited directly on the casing of either the emitter or the receiver; this characteristic is ideal because it reduces the sensing area, so no more additional elements are needed. At the same time, a disposable sensing element (such a Langmuir film deposited on a transparent substrate) was not considered in the design for space minimization reasons.

The circuitry of the system must include a filtering process to supress the electronic noise levels superimposed on the signal, in which the electrical interference and the oscillations are smoothed over and after that the signal is amplified. After the signal has been processed, a data acquisition system connected to a computer reads the voltage output from the sensor as a function of time and storage the data into a digital file that can be further analysed at a later time.
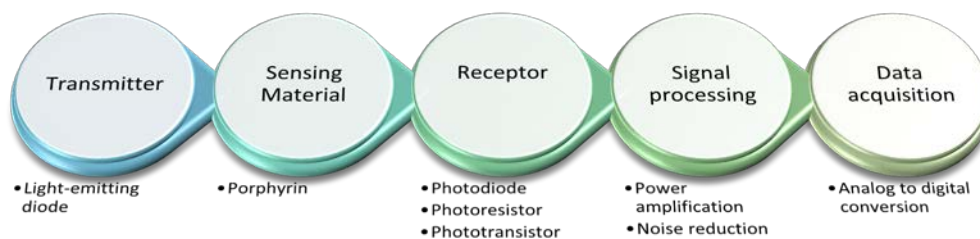
Figure 5.1: Diagram of the sensing system. The porphyrin can be deposited on either, the emitter or the receiver.

It is important to note that in order to pair the emitter and receiver successfully as a sensing device, there must be a convergence of the wavelength ranges in which both devices operate. The sensing pair must also be matched in a way that the wavelength range covers not only the emitter and receiver operational range, but also the range at which the absorption shift in porphyrin induced by analytes takes place.

By way of explanation, suppose that it is necessary to develop a sensing system to detect nitrogen dioxide using a generic photo receiver, which is responsive to the wavelength range from 250 to 1050 nm. Section 4.3.3.2 has shown that EHO/calixarene LS films are highly responsive to the toxic gas, exhibiting a strong change in absorbance corresponding to a wavelength range of 400-500 nm (as depicted in figure 2.34). Using EHO/calixarene as a sensitizer, it is necessary to pair the photo detector with an appropriate light source. Figure 5.2 shows the response of the photo receiver (black line) as well as the wavelength range at which the sensing material is responsive to NO_2 (range between the purple lines). Neither a red nor green LED would cover the range at which the porphyrin exhibits the absorbance change, so the sensor will not be able to detect the gas. Hence, for this application a blue LED would be the best candidate to match the photo receiver. The next section of this chapter describes in detail the design considerations for a specific porphyrin/analyte complex.
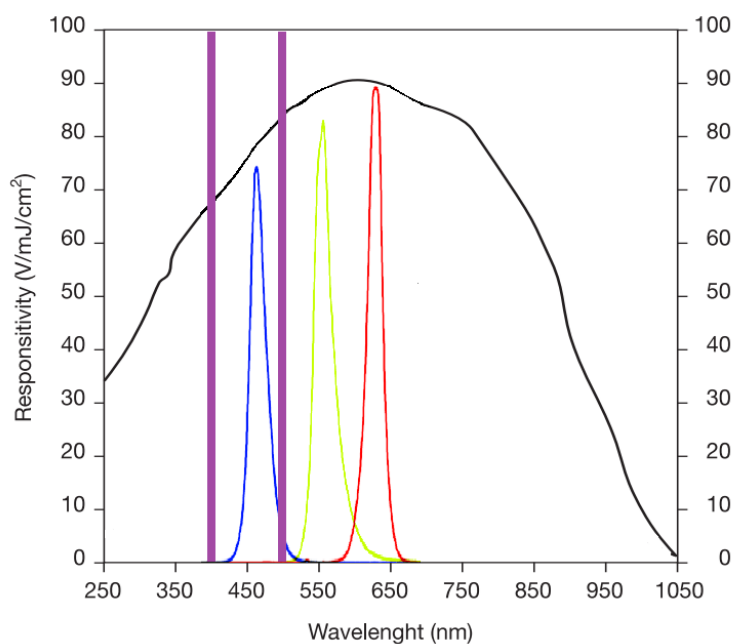
Figure 5.2: Pairing of a generic photo receiver and several light emitting diodes (blue, green, red) using EHO/calixarene LS layers as a sensitizer. The blue LED turned out to be the best option for the sensing system, because its transmittance is in the range at which the sensing material is responsive to NO2 (delimited area between the purple lines).

5.1.2. Types of prototypes

Various electronic devices such as photoresistors, phototransistors and photodiodes were paired with different coloured LEDs in order to optimise the sensor response. Either the emitter or the receiver was coated with a porphyrin sensing material in order to detect certain analytes. To develop a sensing system that is able to detect a specific analyte, it is necessary to select not only a porphyrin responsive to the analyte, but also a suitable sensing pair capable of detecting the wavelength range where the spectral shifts of porphyrins are conducted.

The following subsection discusses in general the circuitry for each of the sensing pairs (photoresistor-LED, photodiode-LED and phototransistor-LED). The application of these different circuits is not limited to a specific porphyrin-analyte complex.

The author's previously published work offers a detailed description of the electronics of the different types of prototypes [1]. The design considerations for a specific analyte-porphyrin

complex along with the pairing of the electronic devices is described in section 5.2. The circuit diagrams were drawn using the simulation and circuit design software Multisim [2].

5.1.2.1 Light dependent resistor

A photoresistor, also known as light dependent resistor, is a photo device in which its internal electrical resistance varies depending on the light intensity. Generally speaking, the internal resistance of the device increases with decreasing incident light intensity; i.e. the material of the photoresistor becomes more conductive because it absorbs electromagnetic radiation (in the case of these sensors this would be emitted by the LED). When light is absorbed by the photoresistor material, the number of electron holes and free electrons increases; in other words, the LEDs photons give enough energy to electrons in the semiconductor to jump into the conduction band and that improves the electric conductivity.

Ordinarily, light dependent resistors are used in light sensitive detector circuits; in this project, the spectral changes associated with the porphyrin-analyte interaction were measured using a coated photoresistor. Photoresistors are made from semiconductor materials and have light sensitive properties. They can be found in many types and sizes, as depicted in figure 5.3. Additionally, the spectral sensitivity of three photoresistor materials, CdS, CdSe and Cd(S.Se.), are presented in figure 5.3. Their different relative sensitivity and its corresponding wavelength response depend on the materials of the photoresistor.
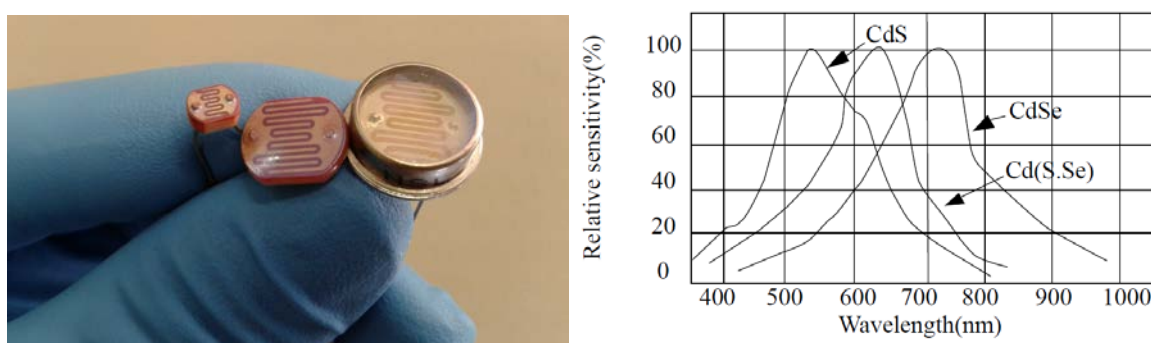
Figure 5.3: Left: Three different cadmium selenide sized photoresistors coated with porphyrin; Right: Resistor spectral response of different semiconductors: Cadmium sulphide (CdS), cadmium selenide (CdSe) and a combination of them.

To test the ability of this photo device to detect analytes, a general purpose circuit, shown in figure 5.4 was developed. The circuit is composed of an operational amplifier (op amp) and

two voltage dividers. The op amp compares the signal between the two voltage dividers. One of the voltage dividers is the reference and has a fixed voltage (and its value can be adjusted with the resistors R_3 and R_4) and the other one changes its value depending on the illumination of the system (formed between the photo resistor X_3 and R_2).

As the name implies, a voltage divider divides the voltage among the components of the divider. To describe the general behaviour of the divider, suppose that the reference fixed voltage needs to be adjusted. The following equation describes the first voltage divider:

$$V_{out} = (V_{in}) \left(\frac{R_3}{R_3 + R_4} \right)$$
Eq. 5.1

Where V_{in} is the voltage provided by the source and V_{out} is voltage measured in the node between R_3 and R_4. To adjust the output voltage of the divider (V_{out}) to a fixed value, it is necessary to assign a value to either R_3 or R_4 and then solve equation 5.1.

For the second voltage divider, it is necessary to match the resistance value of the photoresistor X3 (when is illuminated by the LED) with R_2. The same mathematical principles are applied to this voltage divider, however the function of this divider is not to assist with a voltage reference but to measure the optical changes of the porphyrin induced by the analyte. The photoresistor will change its resistance value depending upon the illumination it receives the output of this divider will vary with illumination intensity received by the photoresistor. The intensity of this illumination will be determined by the interaction of the porphyrin with the vapour analyte because the porphyrin absorbance spectrum matches the LED emission spectrum.

In this case, the op amp is a voltage comparator; the device compares the fixed voltage of the two constant resistors and compares with the voltage divider integrated by R_2 and the photoresistor. When the inverted input is higher than the non-inverting one, the op amp gives the most negative voltage it can drop. On the contrary, when the non-inverting input has a higher voltage than the inverting one, the output of the op amp will be saturated at the highest positive voltage, which is the voltage of the source. A multimeter is used to measure the voltage at the output of the operational amplifier and is define in the figure as XMM1.
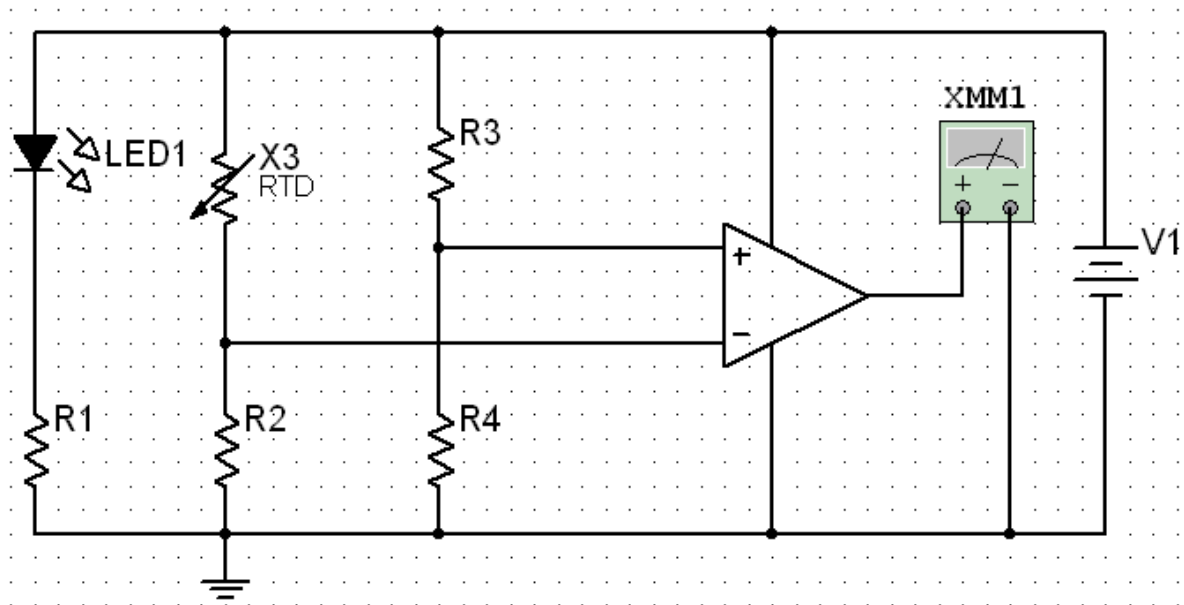
Figure 5.4: Detection circuit made by a LED and a photoresistor sensing pair.

Overall, the circuit was able to detect high concentrations of analyte vapours. The main disadvantage of this circuit is that the design is essentially binary and therefore only allows detecting one toxicity level: everything above that detection concentration will result in a single saturated response. This circuit is suitable to be used as a preventive alarm system which triggers after a certain predetermined amount of analyte is detected in the environment.

The circuit can easily be calibrated to detect different concentrations by adjusting the voltage reference following equation 5.1. Nevertheless, the sensor did not show a promising limit of detection, i.e. the concentrations needed to trigger the sensor were much higher than the ones presented in the other photo devices.

5.1.2.2 Photodiode

Photodiodes convert light into an electrical form which can be monitored. The photodiode junctions transforms the photon energy into an electrical signal by exciting carriers and therefore releasing them to conduct current within the semiconductor of the device [3].

When a photodiode is reverse biased, the operation mode is called photoconductive or photocurrent mode. Reverse biasing the diode reduces its capacitance, and hence improves bandwidth, but requires further circuit complexity to reduce noise performance. However, it

shows several advantages over the photovoltaic mode (zero bias) such as a better stability, lower temperature coefficient, higher speed, larger dynamic range and improved long wavelength response over the interior region [4]. The main disadvantage of using a photodiode in the photoconductive mode is the flow of dark current, i.e. the current that flows when no light is incident on the photodiode. Also, due to the reverse bias it is common to get flicker noise (also called pink noise) in the photodiode, characterized by $1/f$ in which the noise power is inversely proportional to f, the modulation frequency. The mechanisms that produce $1/f$ noise are poorly understood [5].

A circuit consisting of an LED as an emitter and a photodiode as a receptor (assisted by an op amp) is depicted in figure 5.5, the circuit shows a basic linear amplifier operation. The device must be operated with a small load resistance, so linearity can be reached. Linear operation is obtained if the load resistance is very low with respect to the dynamic resistance of the photodiode. In the circuit arrangement, negative-going input is at virtual ground; the dynamic resistance seen there by the photodiode is R1 divided by loop gain. Resistor R_2 can be omitted if the photocurrent is fairly high (its objective is just to balance off the effect of the offset current). For simplicity, consider the case when $R_1=R_2$. In order to measure the response of the circuit (voltage in the node corresponding to the output of the operational amplifier) a multimeter labelled as XMM1 in figure 5.5 was used.
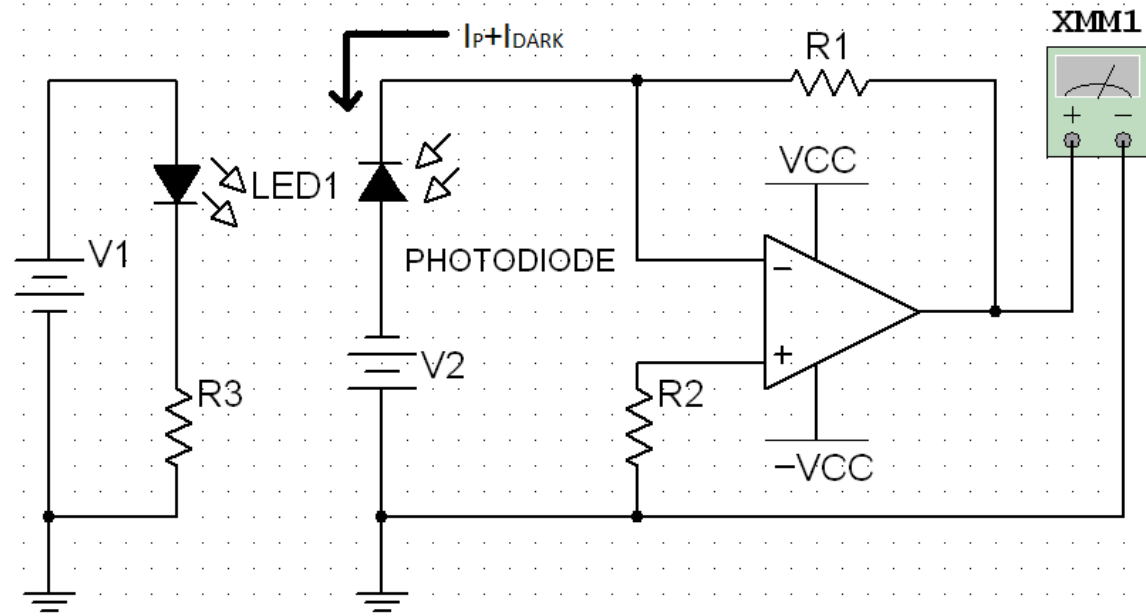
Figure 5.5: Linear response circuit made by a photodiode and a LED sensing pair. The voltage in the op amp will rise in response to the optical signal.

The following expression, equation 5.2, shows the behaviour of the circuit:

$$V_{out} = R_1(I_{dark} + I_P)$$ Eq. 5.2

The equation shows that the output voltage (V_{out}) increases in response to the optical signal, which is dependent of the photocurrent (I_P) and the dark current.

Despite the fact this circuit diagram now provides a voltage directly related to the illumination intensity and therefore analyte concentration the resulting spectral changes detected by the photodiode were not significantly greater than those observed using a photoresistor. On top of that, the design of the circuit for each LED is very time consuming and not always satisfactory; variables as the gain, the frequency bandwidth, noise and stability of the sensor are often competing with each other. To a more detailed description of it, consult the booked titled "Photodiode amplifiers: op amp solutions" by Jerald Graeme [3]. Therefore, a third and final optically active electronic component was tested. The application of phototransistors within the sensor system is presented in the following section.

5.1.2.3 Phototransistor

A phototransistor is an electronic photo sensitive device that transforms light into an electrical signal. In principle, a phototransistor is equivalent to a photodiode and a transistor put together in a single device. Essentially, the photo device is a bipolar transistor encased in a translucent case, so the photons can reach the base-collector junction. The phototransistor base terminal is exposed, and the photons striking the device excite carriers which subsequently activate the internal transistor. The produced electrons in the base-collector junction are injected into the base, and this current is amplified by the transistor.

Phototransistors are much more sensitive than photodiodes. On the other hand, phototransistors are slower (microseconds vs nanoseconds). Though, for this project that difference is irrelevant because the T_{90} and T_{50} response times of porphyrins are in the order of seconds, even when the phototransistor operates in microseconds, the electronics will still respond much faster than the sensing material therefore fulfilling the sampling requirements.

Generally, the phototransistor is operated either in switch (between the cut-off and saturated states) or active mode (in which the output of the device is proportional to the detected light in the environment). Figure 5.6 shows a circuit operated in the active mode. This is achieved when $V_{CC} > R_2 I_C$. To measure the response of the sensor, a multimeter was placed in the pin corresponding to the output of the op amp. The multimeter is represented in figure 5.6 and it is marked as XMM1.

182
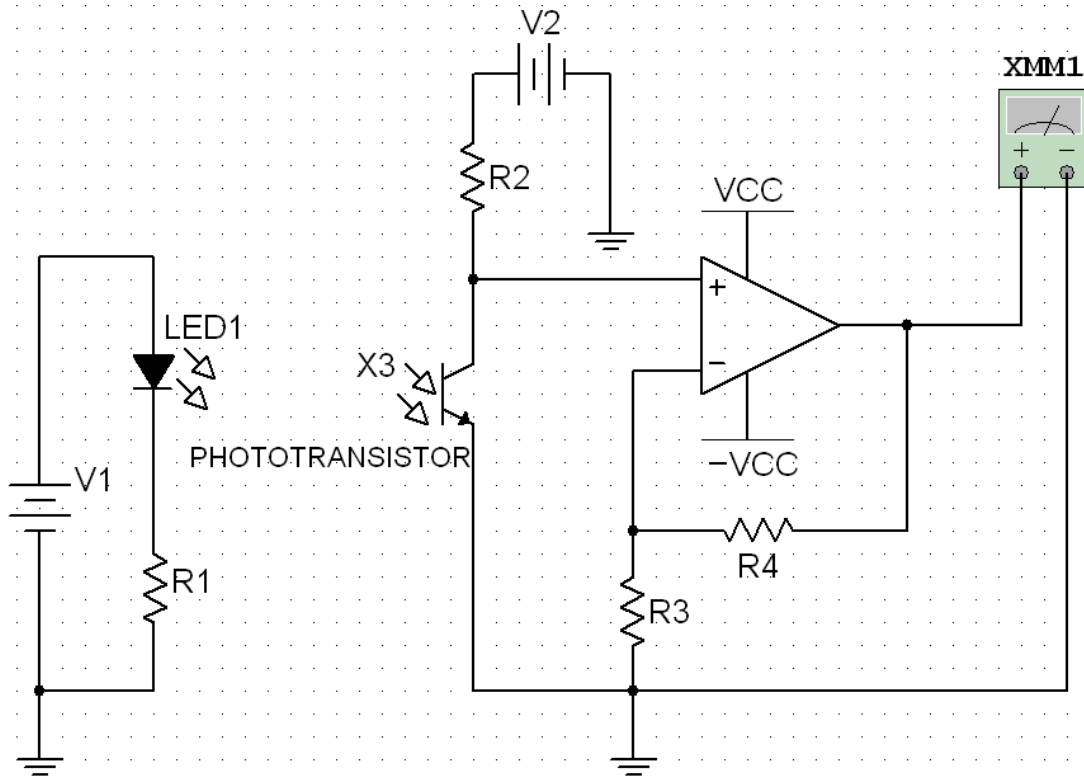
Figure 5.6: Sensing pair circuit consisting of a phototransistor and an LED. The op amp assist to amplify the photocurrent induced in the base of the phototransistor.

A potential divider consisting of the resistance R_2 and the phototransistor was used to provide an output which is proportional to the light intensity that comes into the photo device. A base current is generated under exposure to incident light, and the current then is amplified by the internal transistor which is then sent to the op amp.

In this circuit, the output goes from high to low, which means that the lower the light intensity detected by the phototransistor, the higher the output voltage. The op amp is operating as a non-inverting amplifier, which amplifies the photocurrent I_c of the device. The light intensity is proportional to the base current generated.

5.1.3. Variables of the system

In order to start characterizing the emitter-receiver pairs, it is necessary to consider the system variables such as the temperature, external illumination, distance between the components, bias of the elements and electrical compatibility of the devices.

5.1.3.1 Temperature

It is important to emphasise that temperature is one of the most important variables to be considered. All the semiconductor based photo devices used in this project, including the LEDs and the photo receivers, were found to have a variation in their responses depending on the temperature at which they were operated. As the temperature of a semiconductor is raised its vibration energy increases and so the average distance between atoms in the semiconductor crystal structure increases because of thermal expansion. This in turn modifies the size of the energy band gap. So as the temperature increases the energy difference between the conduction band and the valence band is reduced, thereby effecting the properties of the materials and hence the electrical responses of the emitter and receiver.

In order to avoid any temperature variations in the experiments, it is then essential to be able to regulate the temperature of the internal medium (inside the chamber), so the evaluation of the devices (emitter-receiver) can be carried out at the same conditions. So, under the same fixed temperature, similar devices must show a good repeatability. Note that high temperatures (above 80°C) can also lower the longevity of the devices.

5.1.3.2 External illumination

In order to establish an accurate set of optical measurements it is key to have a fixed reference, therefore, a medium that isolates the system from external sources of illumination is required. Light sources such as the sun or even the laboratory lights produce a non-constant external source of illumination; this could affect the response in the sensors by detecting stray light generating unwanted noise and causing an offset in the resulting voltage.

To avoid that optical noise, a zero stray illumination condition was required. For the first experiments, a series of black absorbent covers were used in order to get rid of the external light. In principle, the thick black material will absorb the light before it interferes with the sensor measurements. Figure 5.7 shows some of the covers for various previous prototypes.

Figure 5.7: Left: Different light isolators that kept the sensing pair away from undesired sources of illumination. Right: operating prototype of a Phototransistor-LED pair.

5.1.3.3 Distance between emitter and receiver

Another import parameter to be considered is the distance between the emitter and the receiver. This variable plays an important role in finding the optimum coupling for each emitter and receiver. The coupling characteristics of an emitter-receiver pair is represented in figure 5.8. The characterization graph depends on the combination of the emitted light in the circuit and the detecting device characteristics. To find the most adequate illumination and distance between the emitter and receiver it is necessary to investigate every pair individually.
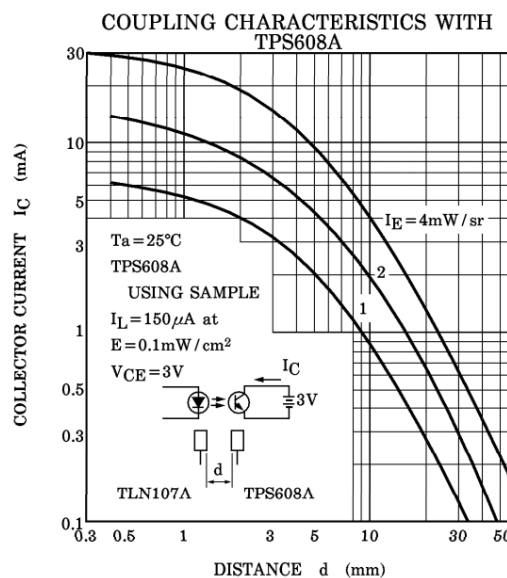
Figure 5.8: Coupling characteristics of an infrared emitter (TLN107A) with a phototransistor (TPS608B) [6].

To couple each pair, it is necessary to read the characteristic parameters shown in the data sheet of the devices. The information for each devices such as the minimum light current (I_L) of the photo detector along with the minimum radiant intensity (I_E) of the LED must be taken into consideration for the first set up. When the received light current in the photo detector (proportional to the amount of light) is small compared to the typical currents expressed in the data sheet, it is necessary to increase the radiant intensity I_E by pulse forward current or to augment the DC forward current of the LED.

Figure 5.8 describes the coupling characteristics of a phototransistor and a LED. As illustrated, the graph describes the inverse square law principle, which represents the correlation between the light intensity from a point source and distance and it can be represented as:

$$E = \frac{I_s}{d^2}$$ Eq. 5.3

Where E is the illuminance (total luminous flux incident per unit area), d is the distance between the source and the detector and I_s is the source intensity. Equation 5.3 states that the intensity per unit area is inversely proportional to the square of the distance from the source. Expressly, if you measure 25 W/cm^2 at 1 cm, you will measure 5 W/cm^2 at 2 cm.

5.1.3.4 LED characteristics

In this project, many LED were compared due to their different power performances, and mostly importantly because they differ from each other in their dominant emission wavelength. The characteristic colour of an LED depends on the band gap energy of the materials forming the junctions. Typically, the LEDs used in this work were located in the blue range, these LED devices are normally made with gallium nitride (GaN) on silicon carbide (SiC).

Figure 5.9 shows some of the LEDs used in this project in the blue range. Note that intensities were not taken into consideration, so the scale was normalized.
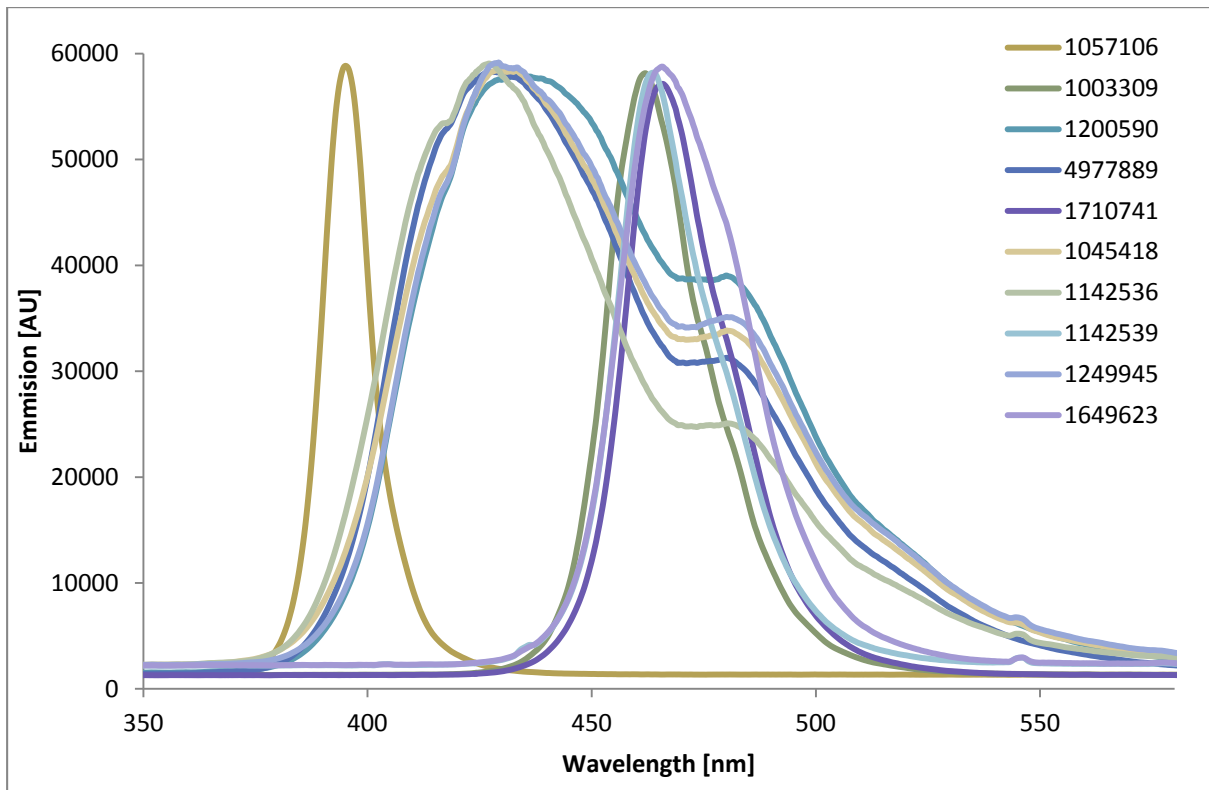
Figure 5.9: Variety of LEDs with a dominant wavelength peak located from 395 to 470 nm.

It is evident that the dominant wavelength from one device to another varies by a few nanometres in some of the cases. Also, the shape of the curve is not always regular; the appearance of a shoulder can be observed in some of the LEDs emission spectra.

In order to operate correctly the LED, it is necessary to estimate the optimal resistance in the emitter circuit, which can be easily calculated using the following formula:

$$R = \frac{V_S - V_F}{I_F} \qquad \text{Eq. 5.4}$$

Where R is the optimal resistance, V_S is the supply voltage, V_F is the forward voltage (also known as voltage drop) and I_F is the current flowing through the LED.

Similarly, if the bias applied to the device is not the adequate; the performance of the device will be not satisfactory: If the current is excessive, the LED may burn out; and if there current is not large enough, it may not energize the device properly. To show the principle, the transmittance spectrum a blue LED was measured at a fix distance, varying the bias voltage in the power source. Figure 5.10, shows the results of the experiment.
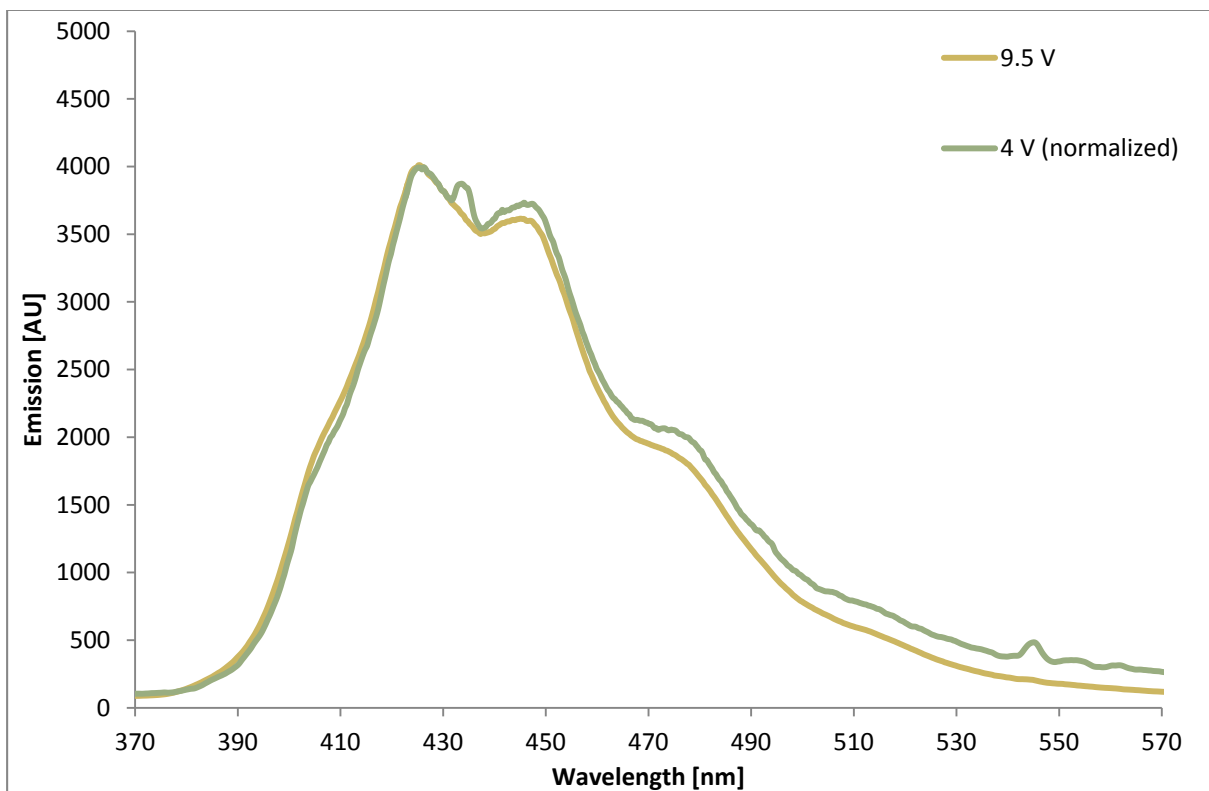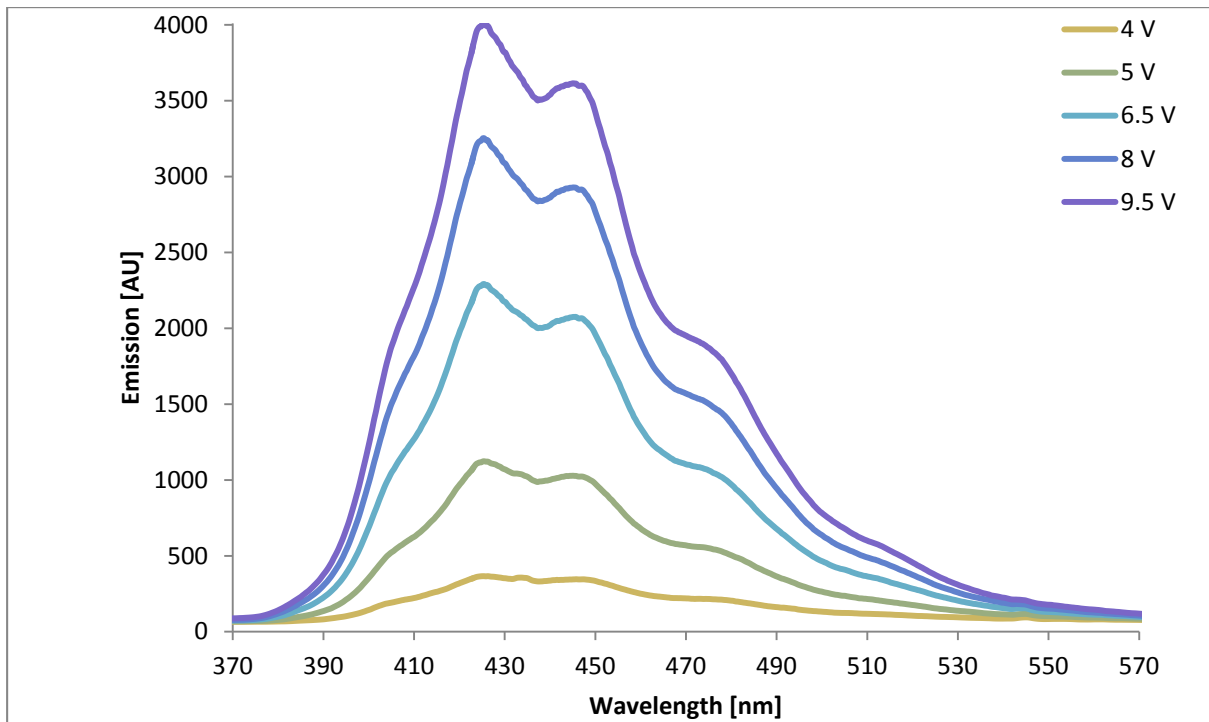
Figure 5.10: Top: Emission spectrum of a blue LED model: 1249945 at different voltage bias. Bottom: Emission spectrum blue LED (1249945) at 9.5 v and 4 v (normalized).

Figure 5.10 shows that the emission of the LED increases with higher voltages. In appearance, the shape of the characteristic curve is the same for all the bias voltages; however, when the

emission is normalized the spectral response is different (as observed in figure 5.10). When the LED is biased with 4 v, two shoulders at 432 and 545 nm appears. Once the LED is biased with more than 6 volts, the shape no longer changes, just the scale. It is possible that the radiative combination rate changes at different bias, leading to a modified emission spectrum; however, the causes of this effect are still unclear [7].

5.1.4. Optimization of the system: developing the proto-type chamber

The following section shows some proto-type gas exposure chambers that were fabricated in order to perform vapour sensing measurements. Each model was intended to be used as a final version of the emitter-receiver vapour delivery system; however, some problems arose in each these early proto-types. The problems encountered in these models suggested new design considerations for the fabrication of the final chamber.

5.1.4.1 Syringe proto-type

The first proto-type was made with the intention of measuring some analytes but taking into consideration the importance of the distance between the sensing pair. A syringe was used as the basis for the chamber, the tip where the needle was originally placed was clipped off. The plunger was drilled and two additional metal terminals were placed in holes drilled through the black plastic plunger seal. In addition, some holes were drilled in the main barrel of the syringe, so the vapours could enter to the space between the sensing pair. Figure 5.11 shows a photograph of the syringe proto-type.

Figure 5.11: Photos of the syringe proto-type, which allowed easy variation of the LED-receiver distance.

One of the most important characteristics of the system is that the plastic is transparent, so the distance between the emitter and the receiver can be effortlessly seen. On top of that, the barrel already contains marks which facilitate the measuring process.

The main problem with this proto-type is that due to its simplicity, the model does not allow a controlled vapour delivery, which is crucial for the project. Furthermore, the prime material is plastic, which can be melted with common substances used in the laboratory (as in the case of chloroform).

5.1.4.2 Glass apparatus proto-type

The next proto-types were made in order to eliminate the design inconveniences presented in the syringe model, i.e. the vapour amount could be controlled easily and the material of the chamber was not as reactive to chemicals when compared to plastic.

Two proto-types were fabricated by the workshop of the University of Sheffield. Both models were made by the same material, but differ in the gas terminals positions. One proto-type has the inlet and outlet of gas aligned and the other does not. It was believed that the position

190

would affect the time in which the chamber was filled with the exposed toxic gases. Figure 5.12 illustrates the models.
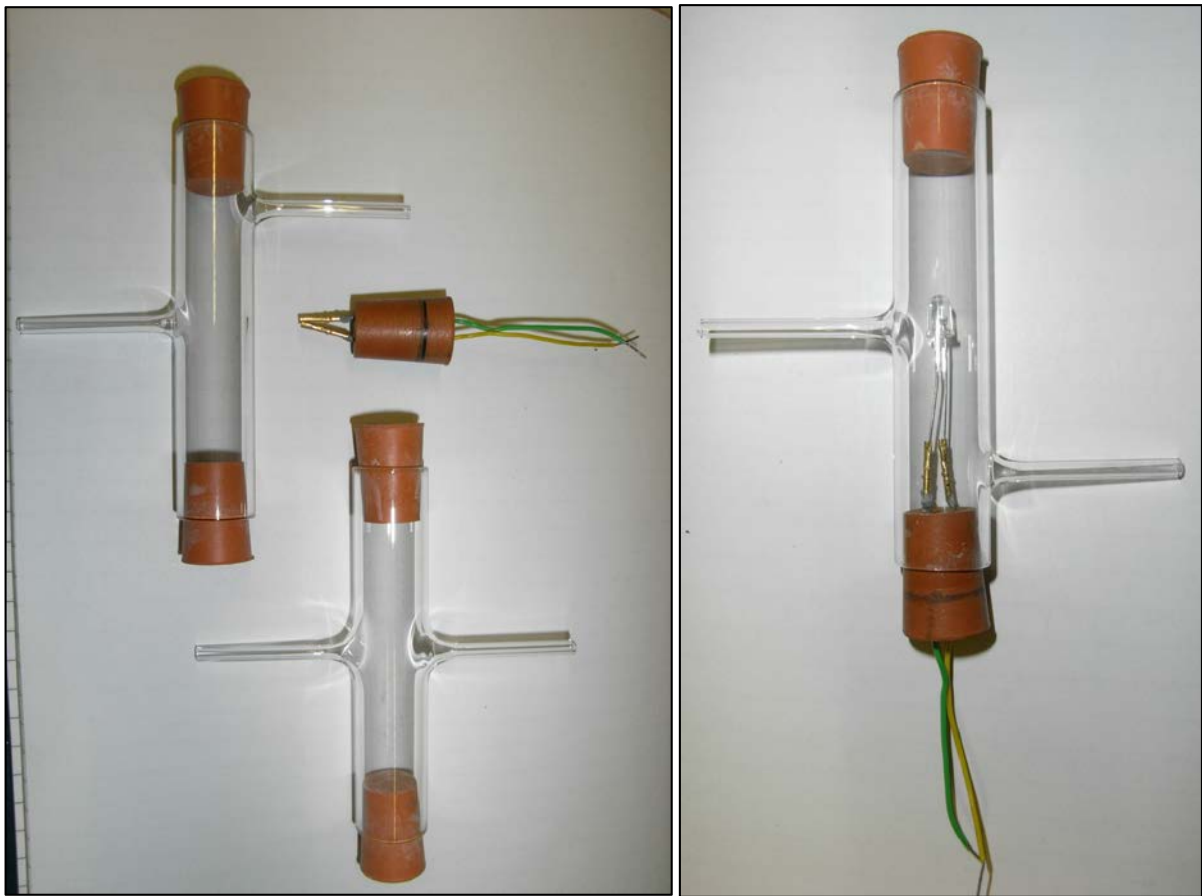
Figure 5.12: Left: Two different glass proto-types; right: Phototransistor connected to one of the extremes, the metal terminals were embedded in the rubber bung.

This model presented the advantage of being able to deliver vapour at known volumes/concentrations. The delivery of the gas was controlled using the automated valves described in section 3.5.1e. Nevertheless, after the first set of measurements it was observed that the results had a poor repeatability. They seemed to work fine once the chamber was sealed with the rubber bungs, but every time the operation was repeated (when the rubber was removed and put in place again) the results were different, even when the sensing pair and the circuitry were the same.

The problem appeared to be related with the alignment of the emitter and receiver, i.e. the precise alignment of the emitter and the receiver. To the naked eye, the problem was not perceptible, but reading closely on the datasheets of the devices it was noticeable that a few

degrees of misalignment could lead to significant variations of light intensity detected by the phototransistor and likewise, a different relative sensitivity to the LED. It is worth mentioning that the misalignment effect is more likely to occur with a longer distance.

Figure 5.13 shows the relative sensitivity of a sensing pair conformed of a phototransistor and a LED. They both have a similar characteristic curves describing the sensitivity vs the angular displacement. In general terms, the higher the degree of displacement, the less effective the sensor pair will be.
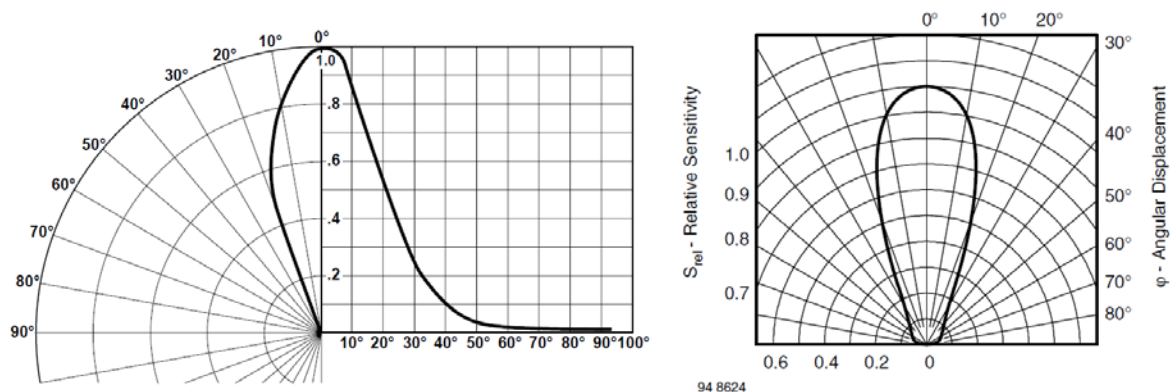
Figure 5.13: Left: relative luminous intensity vs angular displacement of an LED (1003309) Right: Relative sensitivity vs angular displacement of a phototransistor (TEPT5600).

Suppose than the emitter has an angular displacement of 10 degrees, as a result, the emission of the LED will be reduced by approximately 18 percent. If the phototransistor also has a degree of displacement in an opposite direction (-10 degrees) with respect to the sensing axis, the phototransistor will decrease its response by 10 percent. Putting the results all together, it is evident that the alignment of the devices is a critical and the effect is even more devastating if the distance between the emitter and receiver is increased, because they will also follow the inverse square law.

Other disadvantages of the glass model is that it was not possible to control the temperature of the interior of the chamber, so the results varied from one measurement to another because the temperature in which the experiments were carried out was not always constant. The performance of the electronic devices are temperature dependant.

In the interest of having a rapid recovery of the sensor, it is important to implement a heating system that may be able to induce desorption of the sensing material. So, it is desirable not

only to keep a constant temperature inside the chamber, but also to be able to increase the temperature systematically during the recovery of the sensor.

On the next chamber proto-type, all the design problems presented on the previous models were corrected. So, in the final proto-type, all the considerations learnt from the early trials were implemented and taken into consideration before the blueprints were handed to the workshop.

5.1.5. Design of the vapour chamber

The final version of the chamber resolved all the problems presented in the early models. The design was inspired by previous design of gas exposure ring similar to the one used for the porphyrin on glass samples in the previous chapter. It is noticeable that the design is much more burly compared to the other proto-types. This previous design of chamber is shown in figure 5.14. The chamber is mostly made of steel and the lid is heavy enough to seal the chamber only by its weight.

The only inconveniences of this chamber is that the space inside the chamber is big, and therefore it takes a long time (relative to the new design shown in figure 5.15) to fill the chamber with gas. This system was last used in 2011 by the Nano Material Engineering Group (NMEG).
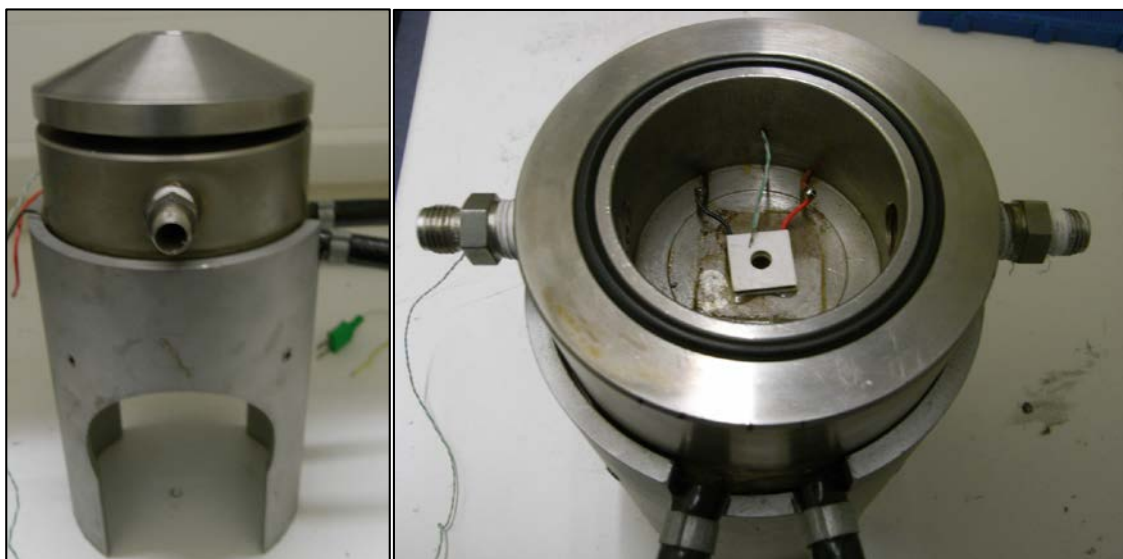
Figure 5.14: Steel vapour chamber, last used in 2011 by the NMEG.

The next series of figures, fig 5.15, 5.16 and 5.17, shows the pictures of the final gas delivery system. The arrows in the figures indicate key parts of the anatomy of the chamber.

One of the most important characteristics of the new gas ring is that its small size allow it to be filled with gas really quickly. Also, it is possible to exchange the traditional UV-Vis delivery and collection fibres for an LED and phototransistor. So a particular porphyrin-analyte case can be analysed using both systems, and because the system characteristics are exactly the same, they can be directly comparable with each other.

Importantly, a heating system that helps to induce desorption was implemented: A Peltier plate with a hole in the centre was installed to let the chamber to operate at a fixed temperature, and in addition, a thermocouple was also coupled with the Peltier, so the temperature could be measured by the user.

Other features, such as the distance between the emitter and the receiver can be easily adjusted using knobs placed in the outer part of chamber. Likewise, the threads located in the base and the lid are aligned; so when the electronic devices are set in the interior of the chamber, they are already aligned.
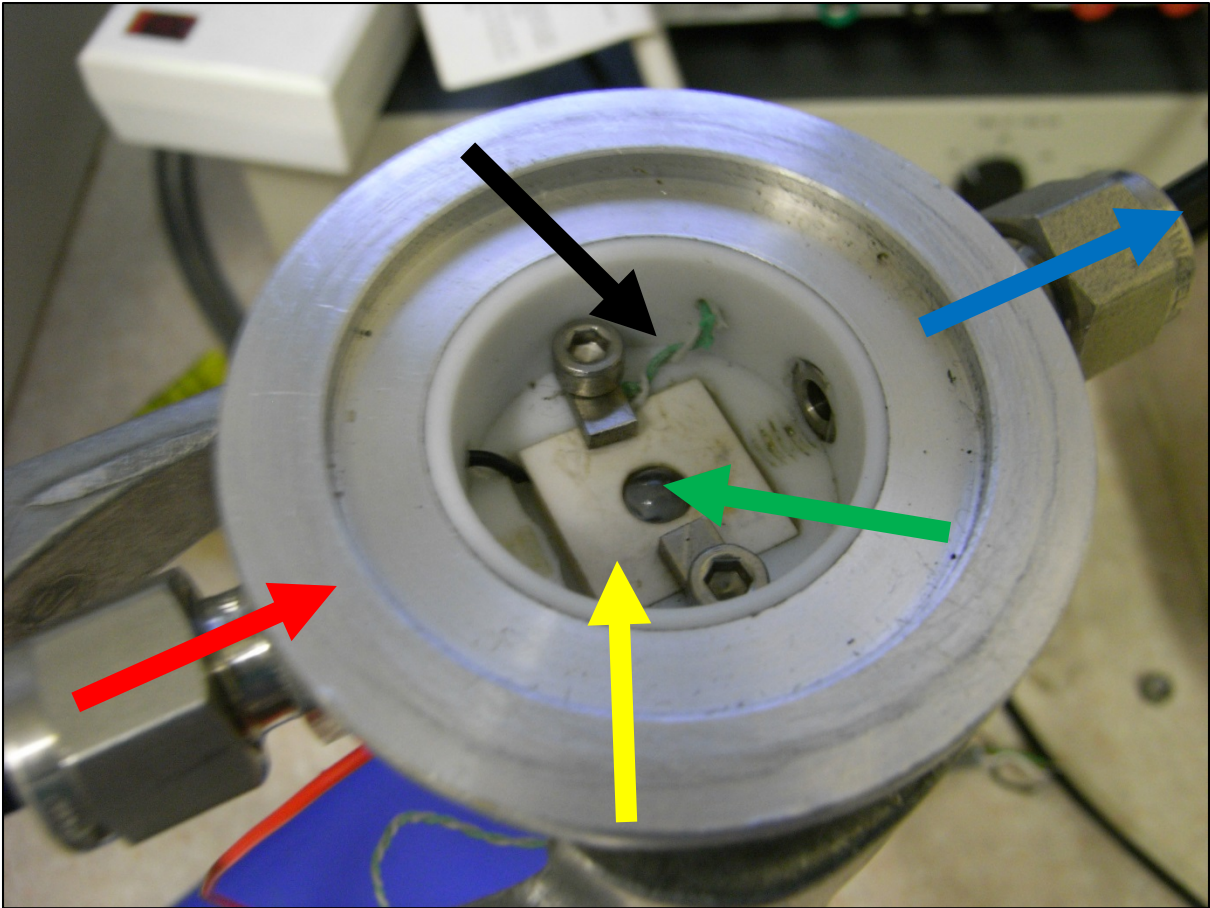
Figure 5.15: Photograph of the base of the chamber: red - vapour inlet, yellow – Peltier plate, black - thermocouple, green – emitter/receiver, blue – vapour outlet.
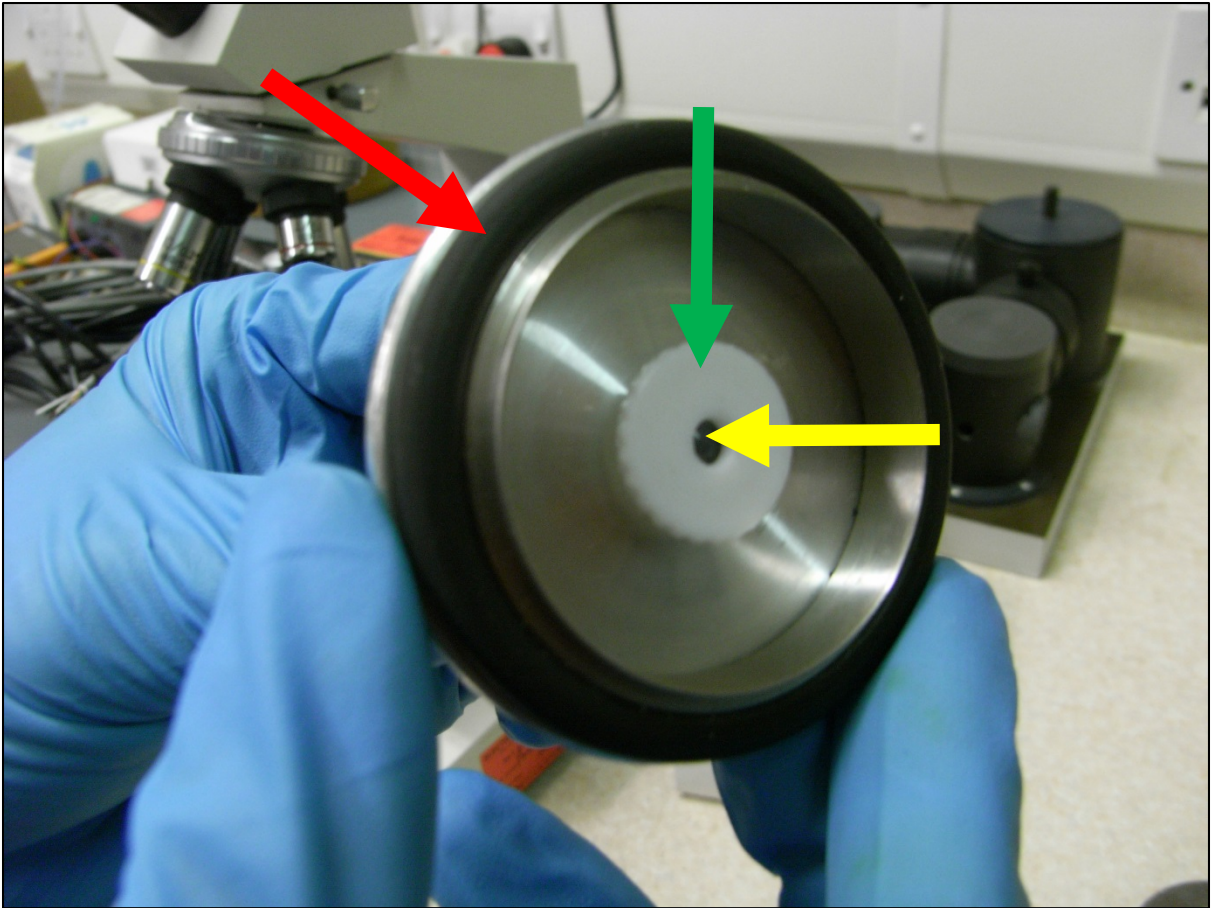
Figure 5.16: Lid of the chamber: red – sealing rubber ring, yellow – emitter/receiver, green – light cover.
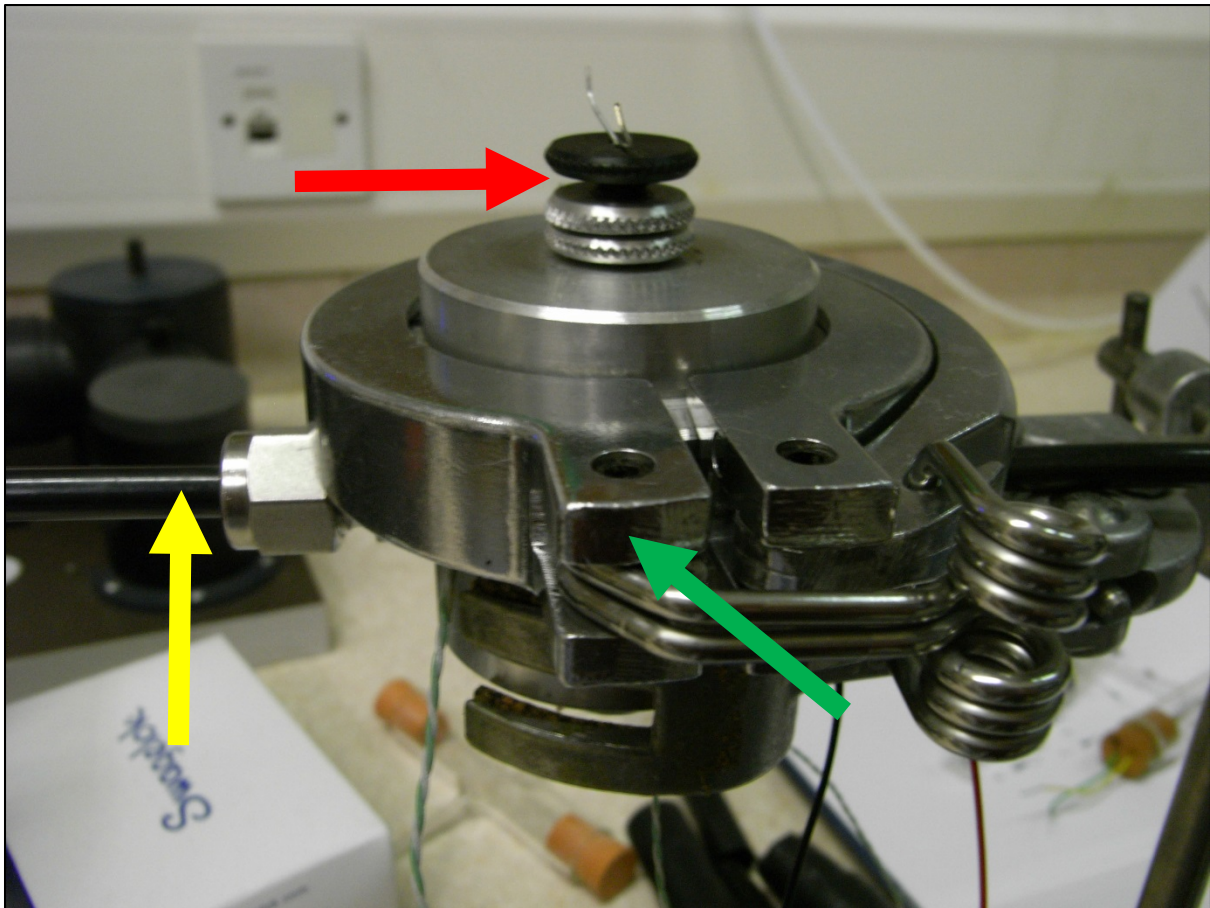
Figure 5.17: Sealed chamber: yellow – black tubes, red – distance adjuster knobs, green – cast clamp.

Overall, the characteristics of the final chamber design can be stated:

- ✓ Possible to change between the two systems (LED - Phototransistor) and UV-Vis.

- ✓ Small interior which allows rapid filling of the chamber.

- ✓ The emitter and receiver are well aligned.

- ✓ Accurate control of the vapour delivery (concentration of the analyte).

- ✓ Optically isolation from other sources of illumination.

- ✓ It is possible to change the distance between the emitter and the receiver.

- ✓ A Peltier plate allows a rapid recovery of the sensor by heating the chamber.

- ✓ The temperature is controlled so effects due to variation of the temperature within the electronic devices can be monitored and understood.

Section 2: Proto-type considerations

In this section, an optoelectronic system will be tested using the prototype gas sensing chamber designed and discussed at the end of the previous section. The system incorporates a light emitting diode (LED) as an emitter and a phototransistor (PX) as a receiver. To start measuring the molecular absorbance events and therefore determine the concentration of analyte present, it is necessary to conduct various control experiments and to understand the internal sensing variables involved in a PX-LED system. In this section, the results from the prototype sensor system are presented showing that it is able to detect vapour.

5.2.1. Phototransistor standardization and error estimation

An ambient light phototransistor was selected above other receivers in order to enable a single device to be used for several different porphyrins. The phototransistor was chosen due to its uniform response in the range from 400 to 500 nm, which is the wavelength range in which most porphyrins exhibit changes in their absorption spectra due to the exposure to analytes. This wavelength range (from 400 to 500 nm) corresponds to the Soret band absorbance of the porphyrins of interest. Chapter 4 offers an insight of the spectral changes produced by analytes for different porphyrin-analyte complexes.

The Vishay ambient light sensor, model TEPT5600, was then selected to track the changes of absorbance of the porphyrins upon exposure to analytes, figure 5.18 shows the characteristics of the PX at room temperature.

The error was estimated by considering the magnitude of the external noise of the signal. The variation in the sensor signal under steady conditions produced a background noise oscillation in the measured voltage of 2 mV peak-to-peak.
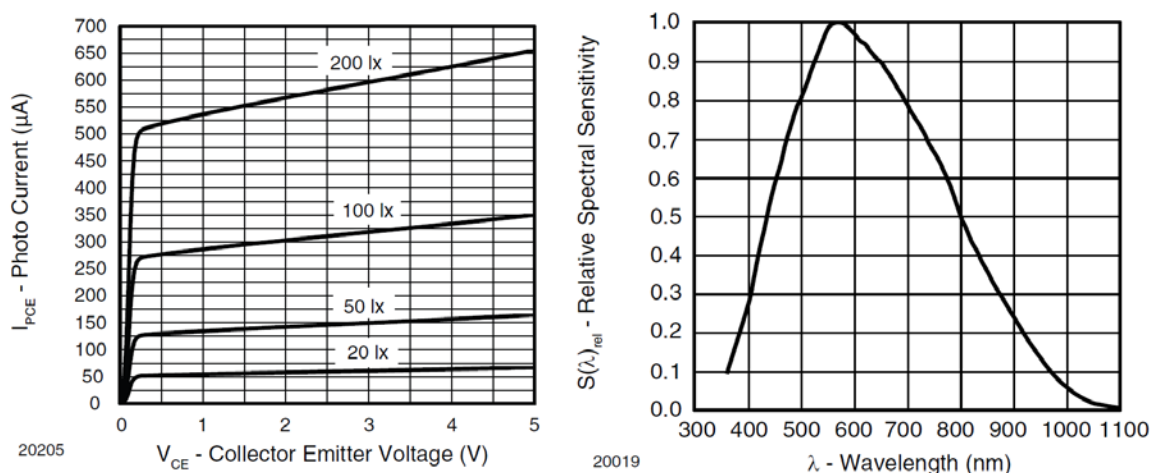
Figure 5.18: Characteristics of the selected phototransistor (Vishay-TEPT5600) measured at room temperature.

5.2.2. Control experiments

Before starting the measurements in the proto-type sensor, it is necessary to conduct a series of control experiments to monitor the possible effects of the analyte in the PX-LED when the sensing material is absent. This control experiment must be effectuated for every analyte presented in this work in order to confirm the absence of any possible effects of the vapours in the sensor. So, it verifies that the absorption of the LED was induced by the porphyrin and not by the analyte itself. In figure 5.19, an LED with no porphyrin coating was placed in the chamber and exposed to 255 ppm of hydrogen chloride (HCl). As a result, little scattering due do the presence of the analyte and noise within the UV-Vis was observed, but no significant spectral changes were detected. Figure 5.19 shows that the scattering caused by the HCl produce little modification in the shape of the characteristic emission, in fact the lines between the two plots are overlapped and is hard to distinguish a difference between each other.
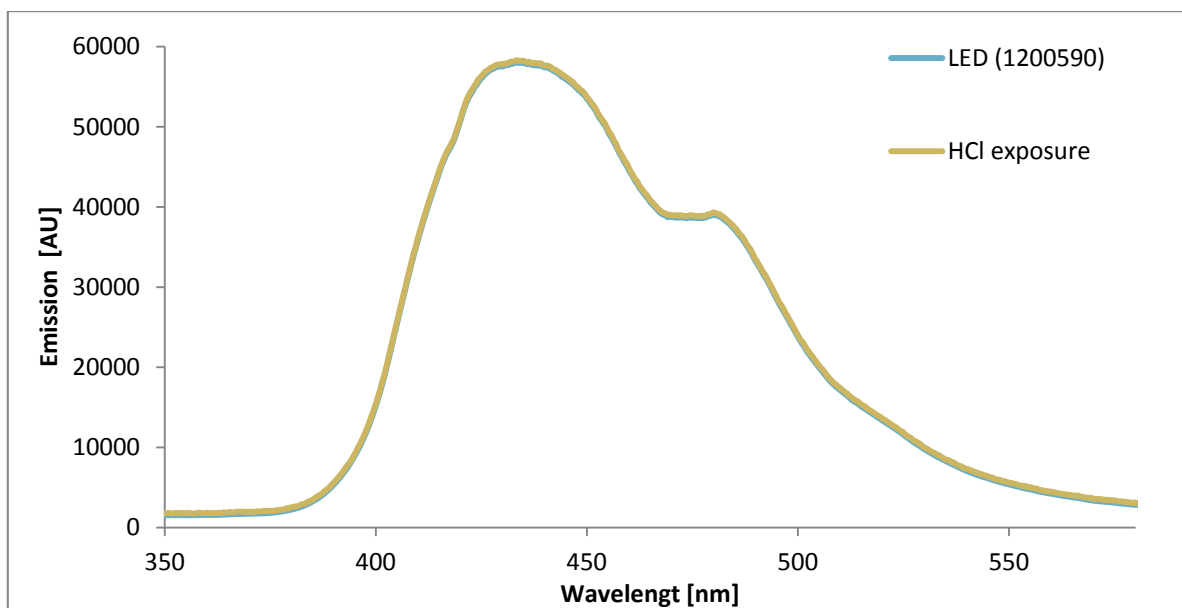
Figure 5.19: Very small changes are observed due to scattering of the analyte or noise within the UV-Vis spectrometer. The concentration of 255 ppm of HCl does not change the emission spectrum of the LED.

In addition to that, a different experiment must be carried out but this time using the PX-LED pair (with no porphyrin as a sensing material). For this second experiment the signal in the proto-type must remain at the same voltage over time before and after the exposure of the vapour to prove that no electrical or optical oscillations exist in the system. Assuming the PX-LED pair shows no response to the vapour, the deposition of the porphyrin can proceed. This can be either on the surface of the emitter, the receiver or on a transparent substrate placed between the sensing pair. An example of the PX-LED control experiment can be found in section 5.3.2.

5.2.3. Electronic filter

A digital filter is a system that processes an input using algorithms in order to enhance or reduce certain aspects of the signal. For this project, it is important to filter the sensor response after it has been recorded to remove electronic noise from the signal and facilitate easier analysis and interpretation of the true signal.

The use of a digital filter was selected because it has well-known advantages over the classical analog filters [8]. One of the greatest advantages of a digital filter is that it is easy to boost or supress certain frequencies and therefore remove unwanted electronic noise [9]. Other advantages of digital filters are that arithmetic operations to the signals can be easy

implemented and also they are immune to temperature or humidity variations (as compared to the analog filters).

Taking that into consideration, a smoothing filter was designed using system design software. The application was built in Labview, a visual programming software. The signal from the sensor (collector voltage in the PX) was recorded using a 14-Bit, 48 kS/s National Instruments data acquisition device (model NI-USB-6009). The data acquisition device and associated software performed an analog to digital conversion to measure and save the electrical signal of the PX on the computer as a digital file (*txt).

After the data is recorded, the file containing the data was subsequently processed by the digital filter software, which was written in Labview. Figure 5.20 shows an screenshot of the designed filter: the top image corresponds to the front panel (where the inputs and the outputs of the sensor signal are displayed) and the bottom corresponds to the block diagram (which is where the user writes the visual code). The digital filter algorithm is applied after the signal has been recorded, so it does not work on real time.

The filter control software was developed with the objective of smoothing the signal of the proto-type. The filter software reads the original file, and then it splits the information into two rows of data; corresponding to the time and response. The raw data corresponding to the time is not treated, whereas the data corresponding to the signal of the sensor is treated using a smoothing filter algorithm.

The smoothing filter function is generalized moving average algorithm. The function used for the filter was based on the Savitzky-Golay algorithm, which improves the signal to noise ratio without greatly distorting the shape of the original signal. The Labview filter function smooths a noisy signal using a convolution process by fitting successive sub-sets of adjacent data points by the method of linear least squares minimization [10].

After the response of the sensor is treated by the algorithm, the arrays corresponding to the treated data and time are merged and plotted in the front panel of the software. As a result, the original and treated data can be visualized in the front panel of LabView. The Labview application then allows the processed data to be exported into a text file, which can be read by spreadsheet applications, such as Microsoft Excel.

In figure 5.20 an early data set of a noisy signal is processed by the electronic filter. The signal corresponds to a series of exposure-recovery cycles of MgEHO 3 LB sample (deposited at 15 mN/m) when measuring 5.39 ppm of NO_2. However, the signal is shifted because the chamber was not properly sealed, so the light measurements depend not only on the vapour concentration, but also in the variation of the light in the environment. The sensitivity to the external sources of lights caused a high distortion of the signal. To avoid that problem the vapour inlet and outlet of the chamber were covered with opaque black tubes in order to prevent the variations of the light intensity measurements produced by the changes in the sun and laboratory light intensities. Figure 5.17 shows a picture of the black tubes incorporated into the chamber.

The bottom half of figure 5.20 shows the LabView graphical programming block diagram, which defines the procedures that the signal passes through before being processed and saved. On the top of the figure, a screen shoot of the front panel of the software is shown. The red line represents the data before being treated, whereas the white line represents the treated (smoothed) response. It is noticeable that the noise is greatly reduced after treating the signal by the Savitzky-Golay algorithm. Noticeably, the original data (red line) is noisier and hence thicker than the treated data (white line). The filter process then is useful to assist with the data analysis and hence to facilitate the data interpretation.

Figure 5.20: Front panel (top) and block diagram (bottom) of the filter designed in LabView. The front panel represents the signal before (red line) and after (white line) the signal treatment. The block diagram represents the programming code of the digital filter.

5.2.4. Sensing mechanism principle

In previous experiments in the last chapter, EHO deposited into a transparent glass was exposed to NO_2. It is thought that free base porphyrins upon exposure to gases such as Cl_2, HCl and NO_2 undergo similar spectral changes due to the similar protonation reactions happening in the central ring of the porphyrin [11].

In order to analyse the interaction between HCl and EHO, 100 µl of stock EHO solution with a concentration of 1.3 g/l was poured in a transparent cuvette containing 1 ml of chloroform resulting in an EHO solution of 0.118 g/l. After recording the initial EHO absorbance spectrum, 100 µl of HCl was mixed in the cuvette and a new spectrum was recorded. The result induced by the HCl shown a significant spectral change in the original spectrum of the porphyrin, these changes can be observed in figure 5.21. The most notorious spectral changes occurs in the

reduction of the Soret band intensity at 424 nm approximately, and the appearance of a new strong band at 462 nm.
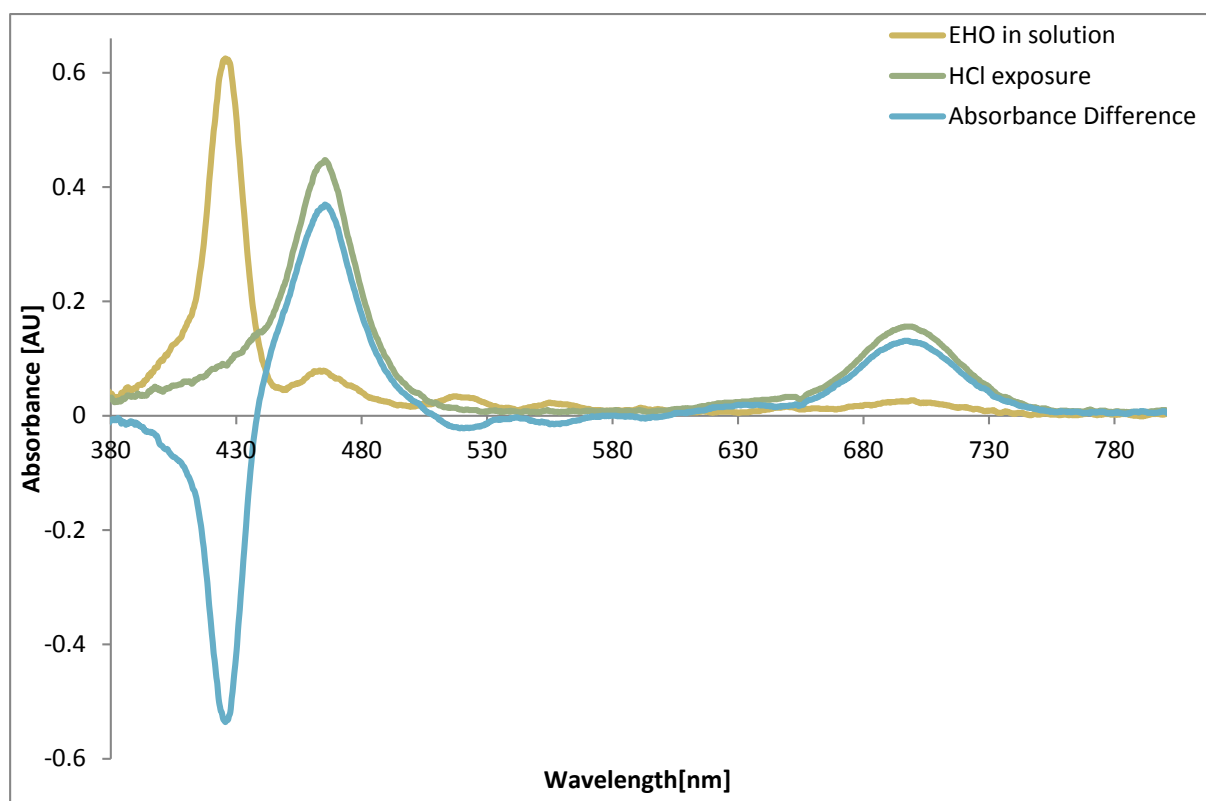
Figure 5.21: Spectrum of EHO solution with a concentration of 0.118 mg/ml before and after 100 μl of HCl were mixed in the solution. The corresponding change in absorbance (absorbance difference) is a mathematical representation of the exposed spectrum subtracted from the unexposed spectrum.

With the objective of showing the sensing mechanism of an emitter-receiver photo device using EHO as a sensing material to detect HCl vapours, two LEDs with dominant peaks at 395 nm and 461 were selected as a source of light. Both LEDs were be considered as a possible light source because their emission is found in a wavelength range from 380 to 500 nm, which is the range at which EHO exhibits its largest change in absorbance upon exposure to HCl.

Furthermore, two phototransistors were deposited with a different number of porphyrin layers. The photo detectors were coated with 10 and 35 layers of EHO, both of them, using the following fabrication parameters: 250 μl spread onto the trough from a solution of concentration of 1.3 mg/ml, target pressure: 15 mN/m, barrier speed: 50 cm^2/min. Previous studies have shown that a range from 10 to 40 deposited layers are the optimum number for the fabrication of glass substrate samples for the detection of nitrogen dioxide [11].

To demonstrate the sensing principle, figure 5.22 shows the emission of the two LEDs and the absorption difference induced by HCl. The absorption difference in solution gives us a clue of how will the absorbance spectra change when the porphyrin is protonated in the phototransistor substrate. Note how close the peak of the LED emission wavelength located at 461 nm is in relation to the main of the peak of absorbance difference located at 464 nm for the porphyrin-HCl interaction. In comparison, the LED located at 395 nm has only a very small overlap with the lower wavelength negative absorbance difference located at 424 nm; to display the intercepting region between these two spectra, an inverted version of the absorbance difference was also plotted. The intercepting region for the 395 nm LED and the EHO-HCl difference spectrum is located at 408 nm approximately.
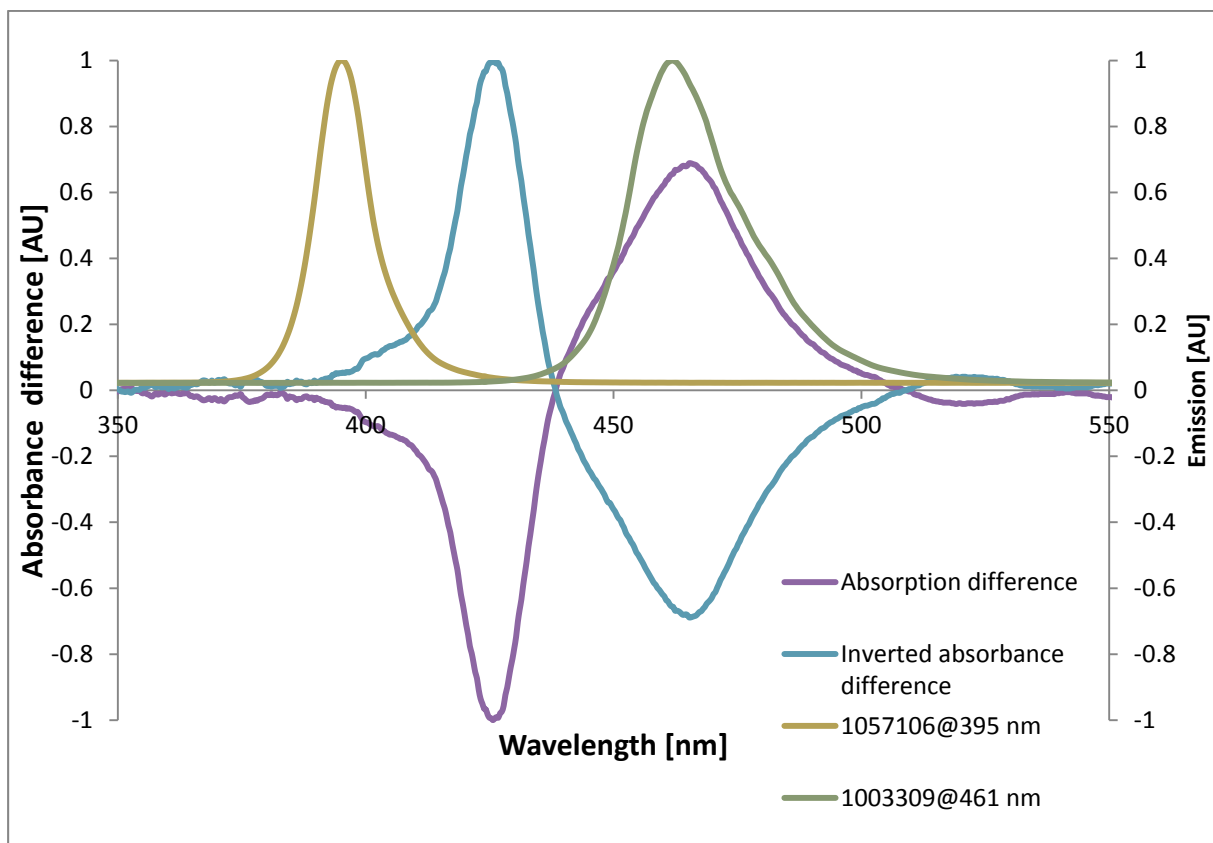
Figure 5.22: Emission spectra of the LEDs and absorbance difference of the EHO exposed to HCl in solution. The LEDs exhibit their higher emission peak at 395 nm (model 1057106) and 461 nm (model 1003309). The absorption difference is a mathematical representation of the exposed absorbance spectrum minus the initial absorbance spectrum of EHO.

The two coated phototransistors, containing 10 and 35 deposited layers respectively, were positioned in the chamber (one at a time) as were the two LEDs (peak emission at 395 nm

and 465 nm) in turn. The 4 different PX-LED pairs were used to detect 255 ppm of HCl. Figure 5.23 shows the four possible cases of pairing the PX-LEDs and the response after being exposed to the toxic gas.
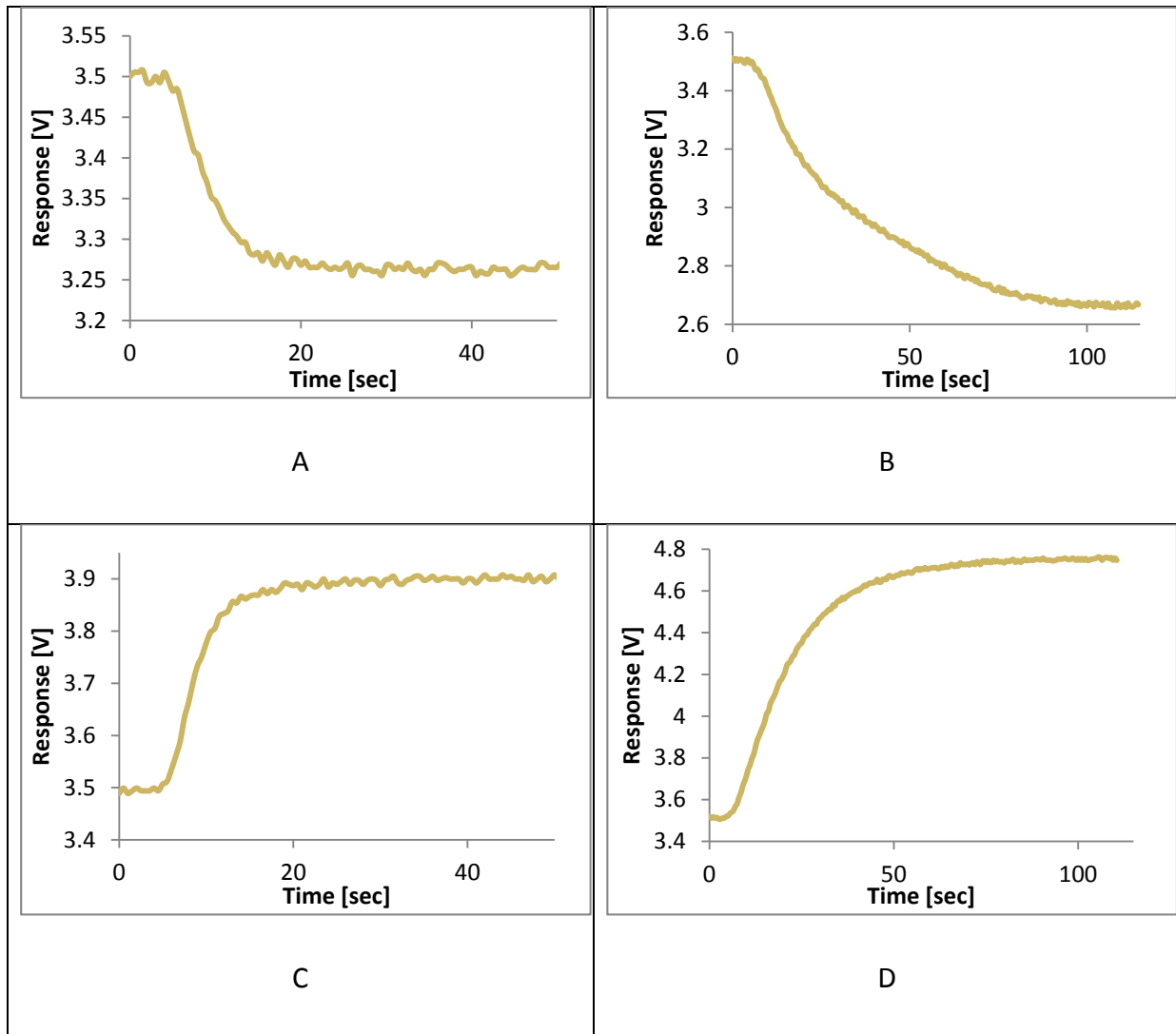
Figure 5.23: Response of the LED-PX pairs when exposed to 255 ppm of HCl.

A) LED model 1057106 (395 nm) – 10 EHO layers, deposited at 15 π. ΔV=3.26-3.5 V= -0.24V

B) LED model 1057106 (395 nm) – 35 EHO layers, deposited at 15 π. ΔV=2.66-3.5 V=-0.84V

C) LED model 1003309 (461 nm) – 10 EHO layers, deposited at 15 π. ΔV=3.9-3.5 V= 0.4V

D) LED model 1003309 (461 nm) – 35 EHO layers, deposited at 15 π. ΔV=4.75-3.5 V=1.25V

Unsurprisingly, the response of the sensor (i.e. the voltage change measured in V) is larger when a larger number of deposited layers are presented. Strictly speaking, when more porphyrin is deposited, there is more absorbance because there are more available sites for the analyte to bind.

On the other hand, it is unmistakeable that the sensor response time t_{90} is higher when more deposited porphyrin layers are presented. By way of explanation, the adsorption of the analyte is limited by the diffusion though the greater number of porphyrin layers present. In other words, the access to the available sites becomes harder as the analyte penetrates in underneath porphyrin layers, and as a result, the diffusion takes more time to be completed.

The configuration of the electronic circuit powering the PX was set such that the response of the PX remains constant with a fixed amount of light. The voltage goes from high to low with light, which means that the response is low at a maximum light intensity.

The LED with a peak emission located at 461 nm has a positive response in voltage after the exposure to HCl. According to figure 5.23(c and d), the absorbance increases approximately at this range of wavelength, and the effect is perceived as a reduction of light in the sensor. The reduction of light makes the sensor to go from its pre-exposure voltage to a higher voltage corresponding to a lower light intensity, so this PX-LED pair behaves as a transducer that characterizes the absorption events that occurs in the porphyrin layers.

A similar effect happens when the LED with a peak emission located at 395 nm is the source of light in the system. However, in this case the response not only is smaller than the one presented in the other LED, but also the response has a negative numerical response. The fact that the symbol is opposite is due to the change in absorbance, in which is reduced in the wavelength range corresponding to the light source. This PX-LED pair is monitoring the decrease in the absorption band at 461 nm rather than the increase in the 426 nm Soret peak as was the case for the previous pairing. In this case, the effect is opposite, i.e. the absorbance decreases in the LED range, and that is perceived as an increase in light in the phototransistor, so the response is negative. In addition, because the emission peak of the LED has a poor overlap with the maximum absorbance change difference, the response is significantly smaller in magnitude.

It is important to point out that the response of the PX is not a measurement of the single spectral change (induced by the analyte) presented at the peak emission of the LED. Strictly speaking, the response of the PX is a function of the wavelength of the emission spectrum of the LED and of the PX properties, such as the band gap of the materials of which the PX is made (the relative spectral sensitivity of the PX is described in figure 5.18b). So the response of the PX involves an integral response of all the wavelengths presented in the emission spectrum of the LED. Additionally, the responses in the photo detector differ from one wavelength to another, so the responses corresponding to a specific wavelength must be scaled according to its relative spectral sensitivity in the phototransistor. Nevertheless, this simple approximation permits to predict the behaviour of the prototype and helps to understand the sensing mechanism of the sensor.

5.2.5 Limiting the LED range of wavelengths

To analyse the spectrum of the porphyrins and its interrelated absorbance spectral changes caused by an analyte exposure, it is informative to characterize the sensing materials using traditional UV-Vis spectroscopy which provides a full spectral analysis of the reaction, and therefore helps in terms of understanding the underlying science. However, for most sensor applications the desired output that is required is a single variable which corresponds to the concentration of the analyte present. Therefore in order to minimise the complexity of the sensor design and keep the associated costs down it is necessary to simplify the sensor response to the most elementary terms.

In section 5.2.4 it was mentioned that the response of the PX depends on the incident radiation (in this case, on the wavelength range at which the LED emits light). Certainly an LED that emits at a wide range of wavelengths (as in the case of a pure light LED) will induce a proportional response in the PX within that range; however, the fact that the LED covers a wide wavelength range does not necessary means that it is a good candidate to pair it with the photo detector. Looked at a different way, the higher the radiation range, the higher the change in absorbance of the sensing material and the sensor will be able to detect a in a wider spectral range. However the absorbance difference is not an absolute value, the sensor can detect a positive or negative change in absorbance so the sum of the different wavelengths can cancel each other out and the overall response of the sensor could be null. To

demonstrate this principle, a glass substrate was coated with three LS EHO (38%)/calixarene[8]arene(62%) (molar ratio) layers using the following fabrication parameters: target pressure: 15 mN/m, barrier speed: 50 cm²/min.

Figure 5.24 shows the emission of an LED with a dominant peak located at 430 nm. Later, the calixarene/porphyrin glass sample was placed between the LED and the UV-Vis, reducing the detected emission. The spectrum produced by placing the sample in the chamber is smaller in size not only because the glass substrate produce an increase in scattering effect due to surface reflections but also because the porphyrin absorbs light and changes the shape of the characteristic curve of the spectrum detected. Later, the sample was exposed to 20.68 ppt of acetic acid which generates a change in the wavelengths the film absorbs and therefore a change in the spectrum observed.
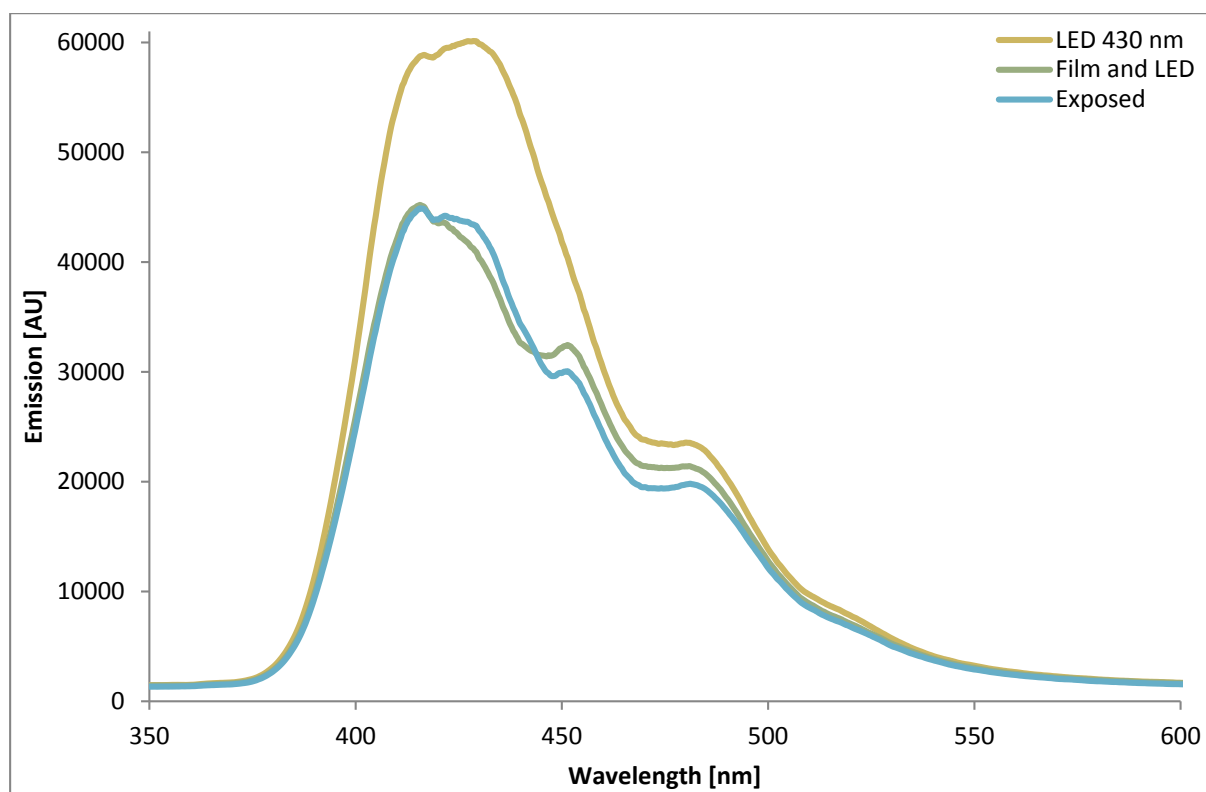
Figure 5.24: Emission of the LED with a peak emission located at 430 nm. Afterwards, a glass EHO/calixarene sample with three LS EHO deposited at 15 mN/m was placed in the chamber and subsequently exposed to 20.68 ppt of acetic acid.

Afterwards, the LED was replaced with the white light source more typically used when doing UV-Vis spectroscopy, so the absorbance spectrum of the glass substrate could be analysed once the sample has been exposed to the vapour analyte.

Figure 5.25 shows the spectrum difference of the EHO/calixarene LS sample when exposed to 20.68 ppt of acetic acid. In the same graph, the emission of an LED with a dominant peak emission located at 430 nm is also plotted. The operational wavelength at which the LED emits ranges from 375 to 575 nm. Note that the arbitrary units in the LED emission allow the graph to be re-scaled, therefore it can be directly compared with the absorbance difference in the film.
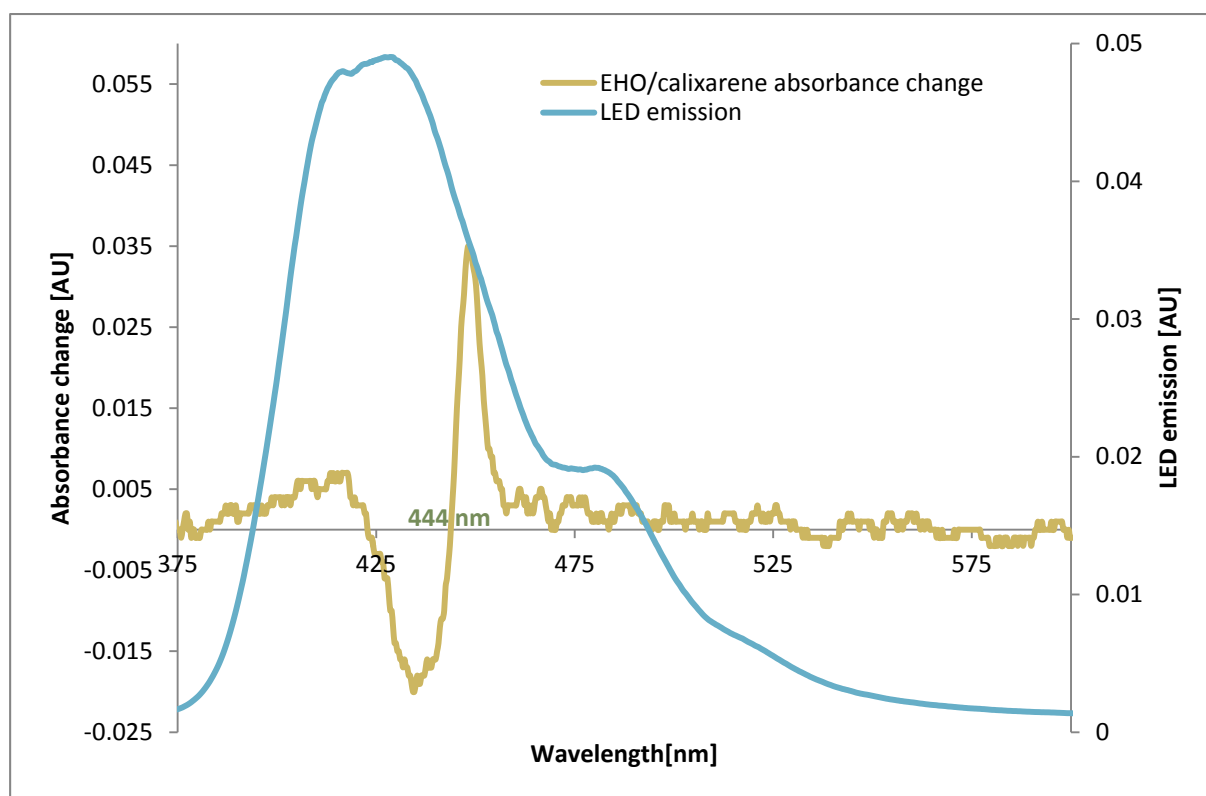
Figure 5.25: Change in absorbance of the EHO/calixarene sample with three LS EHO deposited at 15 mN/m upon exposure to 20.68 ppt of acetic acid. The blue line represents the emission of the LED with a dominant peak emission located at 430 nm.

The point noted here is that when evaluating a response using an emitter-receiver scheme, the response reported by the sensor is a summation of all the responses presented at different wavelengths, and since they can have either positive or negative responses, they can cancel each other. In other words, the response of the sensor will detect just a little

variation of light in this case because in the range of the emitted light provided by the LED the large positive signal is partially cancelled by the negative signal because some upon exposure the absorbance at some wavelengths is reduced but at other it is increased.

Figure 5.25 shows that the LED emits in a range corresponding to a positive and negative change in the porphyrin absorbance, so the responses cancel each other out for that wavelength range. Then, for this particular case, it would be necessary to select a LED that emits at wavelengths above or below the cross point of 444 nm only (as depicted in figure 5.25), so the absorbance differences do not cancel each other. In this manner, the obtained response would be either positive or negative.

So, the appropriate strategy to obtain a higher response is to focus in a single narrow range of wavelengths, which corresponds to either a large decrement or a large increment in absorbance upon exposure. Within this narrow range it is preferable to ensure that the absorbance increases and decreases do not cancel each other out.

It is important to mention that with the interest of reducing the emission range of wavelengths in LEDs, optical filters were incorporated into the chamber. The plastic filters were set between the emitter and receiver in order to selectively filter light and reduce the range of wavelengths of the light source. However, it of was found that some of the more corrosive analytes (such as acids and halogenated compounds) damaged or dissolved the plastic filters once they were in contact with them.

In addition, other alternatives such as coloured glass filters were considered. However, due to the limited space in the chamber it was not possible to fit them into the chamber.

Section 3: Detection of alcohols using the proto-type system

In the previous chapter, it was shown that the change in absorbance induced by alcohols in MgEHO was not easily detected using the traditional UV-Vis spectrometer. To show the potential of the proto-type sensor system developed in this chapter, the detection of the same analytes will be investigated using an LED-phototransistor (LED-PX) circuit. The Freundlich Adsorption model will be used to describe the response of the phototransistor when exposed to the different concentration of the alcohol. Additionally, the enthalpy of absorption will be calculated to describe the force interaction between the porphyrin and the analyte. The work presented in this part, was published in the Journal of Sensors and Actuators B: Chemical. [12]

5.3.1. Sample preparation and circuit configuration

In the interest of detecting the vapour of different analytes, an LED and a phototransistor (PX) will be paired to detect methanol, 2-propanol, octanol, ethanol and 2-methyl-2-butanol (2M2B). A Multicomp LED, model SPC-F005 was chosen among other because its dominant intensity wavelength corresponds to the maximum absorbance change of MgEHO when exposed to alcohols. The dominant intensity of the blue LED is located at a wavelength of 430 nm.

A phototransistor (model TEPT5600) was coated with 10 layers of MgEHO with the following fabrication parameters: 150 µl spread onto the trough from a solution of concentration of 1.75 mg/ml, target pressure: 15 mN/m, barrier speed: 50 cm2/min.

The configuration of the circuit was such that the resulting voltage was low with light, and high at zero illumination. An operational amplifier (741) was used to assist with the amplification of the signal perceived by the phototransistor, as described in figure 5.6.

An increase in the sensor voltage can be interpreted as a reduction in the incident emitted light reaching the PX. The proportionality of the response of the sensor in volts and to light intensity incident on the PX can be described by the equation:

$$\Delta V \propto -\Delta I \qquad\qquad\qquad\qquad \text{Eq. 5.5}$$

5.3.2. Sensor Measurements

The LED was biased at a fixed voltage, so the light intensity detected by the PX remained constant. Despite the fact that the LED was supposed to provide a constant amount of light, the variation in the sensing pair under these nominally steady conditions produced a background noise oscillation in the measured voltage of 2 mV peak to peak. The emission from the LED corresponds to a narrow band of wavelengths that overlap the Soret peak of the MgEHO.

For the case of the detection of alcohols using MgEHO, the spectral changes are very subtle, as observed in the previous chapter (see figures 2.45 and 2.46 of chapter 4 section IV). The fact that the optical change in absorbance is minor shows the advantage of incorporating a sensing pair to amplify the signal difference produced by the analyte.

Figure 5.26 shows a series of cycles when the MgEHO sensing pair is exposed to 2-methyl-2-butanol (2M2B). In the figure, the exposure is represented in the unshaded area in which the temperature is set at 25°C and the sensor is exposed to the vapour analyte for 300 seconds. During the recovery, two different processes are carried out: heating up (shaded red) and cooling down (shaded blue) the interior of the chamber. The red coloured areas represent the heating up in which the porphyrin desorbs the analyte, at this stage the sensor is heated to 65°C whilst being flushed with clean dry nitrogen. After the heating up, a period of cooling down allows the sensor to go back to its initial state before the exposure of alcohol, whilst still being flushed by nitrogen. The cooling down is represented as blue coloured areas, during these 450 seconds the electronic devices cool off and go back to its initial operational temperature. The response of the sensing pair is reproducible over the cycles, showing the reliability of the system. In the figure, it can be observed that the voltage goes from a low to a high state, which means that the phototransistor perceives a decrease of light, or in other words, an increase in the absorption in the sensing range of wavelengths. The voltage goes from 3.842 v to 3.860 V, giving a voltage difference (ΔV) of 18 mV between the exposure and recovery stages that represents the response of the sensor when exposed to 50 ppt of 2M2B.
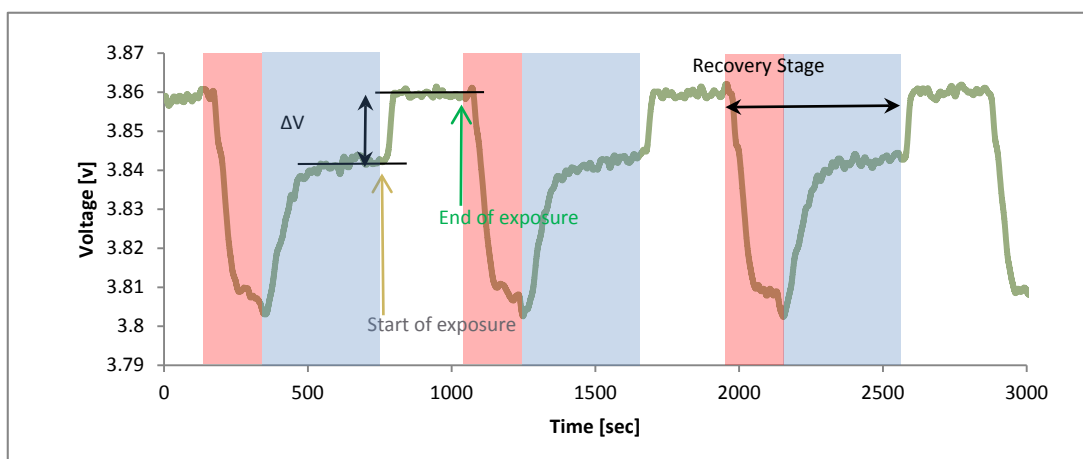
Figure 5.26: Response in the MgEHO coated phototransistor corresponding to the absorbance located at 430 nm as a function of time during exposure to 50 ppt of 2M2B.

Figure 5.27 shows the response of the sensor when clean dry nitrogen is flushed during the exposure instead of alcohol vapour. The cycle was produced under the same conditions, i.e same exposure/recovery times and same temperature variations. The objective of this control experiment was to show the repeatability of the sensor during the temperature fluctuations and also, to prove that no response was shown when nitrogen is flushed into the chamber throughout. No spectral difference is observed and therefore the voltage response remains constant during the exposure to nitrogen. However, the sensing pair voltage reference changes decreases when the system is heated from 25°C to 65°C. This is attributed to the effects of the temperature variation upon the response of the phototransistor, and therefore these negative voltage spikes are ignored.
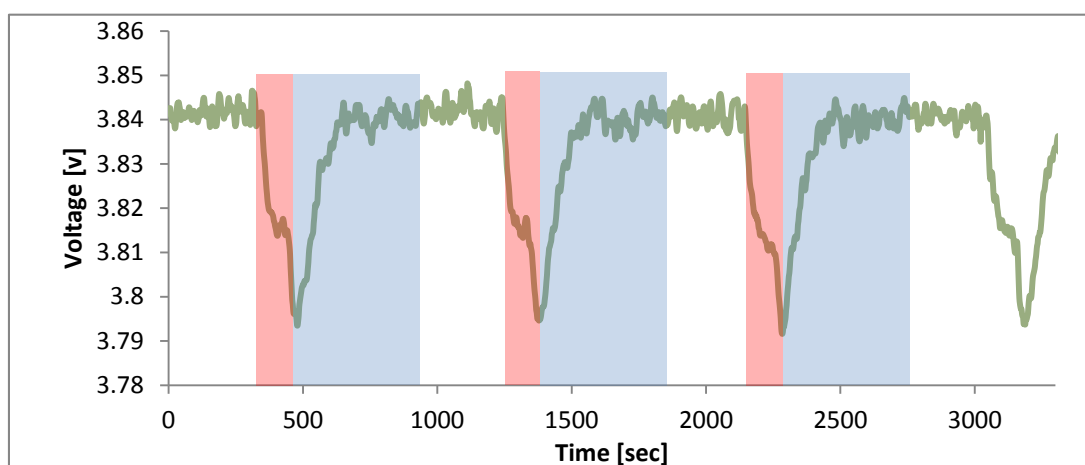
Figure 5.27: Effects of temperature in the MgEHO coated phototransistor. No voltage response was observed between the exposure and recovery stages.

The rise in temperature in the sensing pair causes a decrease in the voltage reference. The emission intensity in the LED and the relative sensitivity in the phototransistor vary depending on the working temperature. The effect of heating up the system changes the sensing characteristics of the circuit; to fully understand the effect of temperature in the sensing pair, it is necessary to extend this work to the study of semiconductors.

The offset caused in the phototransistor can explicated in terms of charge carriers, which are responsible for the current through the photo detector. At high temperatures more electrons will move from the valence to the conduction band because they will have enough thermal energy to be promoted to the higher energy conducting band. As a result of the thermal excitation, an increase in charge carriers will lead to a lower output from the photo detector. Due to the complexity of the system, the offset produced by temperature was not analysed in the extension of this study.

5.3.2.1 Response to alcohols

The sensor was designed to detect optical changes located at 430 nm. Due to the characteristics of the sensing pair, the optical change is amplified by the phototransistor and after that, amplified once more by the operational amplifier. The coated MgEHO phototransistor and LED pair was able to detect alcohols, because they all have a maximum change in absorbance at approximately 430 nm. All the alcohols were in liquid form and were transformed into vapour by flushing nitrogen trough the headspace of a vessel container partially filled with the required alcohol at a known temperature.

The phototransistor response depends on the relative spectral sensitivity at a specific wavelength, and since the maximum spectral change induced by alcohols in MgEHO is found at different wavelengths the response will be different to the various analytes. Figure 2.45 in chapter 4 section IV shows the subtle spectral difference of MgEHO when exposed to alcohols. Because the sensor is designed to detect optical changes at 430 nm, the response will be optimized at that particular wavelength. The fact that the overall amplification of the sensor response depends on the wavelength and the maximum absorbance changes occurs at different wavelengths gives the system a nonlinear response. This is an important

consideration as becomes clear when trying to fit an appropriate adsorption model to using the sensor response data.

The concentration of the analyte was controlled by adjusting the temperature in the water bath. A temperature of 40°C was set at the water bath for all the different alcohols, and their relative concentrations were calculated using Antoine coefficients to characterize the vapour pressure vs temperature characteristics. Table 5.1 shows the concentration of the alcohol and its corresponding sensor response.

Alcohol	Concentration [ppt]	Sensor response [mv]
Ethanol	176	5.2
Methanol	350	7
Octanol	26	7.1
Propanol	68	11.5
2M2B	50	17.9

Table 5.1: Response of the sensing pair to various alcohol vapours.

It is evident that the small change in the absorption spectrum induced by the alcohols gives a different response in the sensor, even when spectral difference in the maximum peaks between analytes differs by just a few nanometres. In other words, the match between the maximum absorbance difference and the sensing range in the PX/LED is more critical than the concentration of the vapour itself. For instance, the maximum spectral response of methanol is located at 425 nm, whereas the one induced by 2M2B is at 430 nm. Consequently, 350 ppt of methanol were necessary to produce a response of 7 mv; on the other hand, 2M2B produced a higher sensor response with less concentration. So, the optical changes located at the maximum sensing wavelength sensitivity of the sensing pair (in this case 430 nm) will be amplified in a higher rate than ones that does not converge at that specific wavelength. For this reason, the particular case of 2M2B will be investigated in the following subsection.

The main disadvantage of this type of sensor is not being able to differentiate between alcohols. That is to say that the magnesium porphyrin exhibits cross sensitivity to more than

just one target vapour (the effect is defined in section 1.3). In a like manner, the sensing material has shown a response to other analytes such as amines and carboxylic acids, which also cause an energy shift in the delocalized electron system [13]. Therefore differentiating between these different types of analyte with a single sensing pair would not be possible.

To achieve selectivity between different analytes, it would be necessary to characterize the spectral responses at different wavelengths using other sensing pairs; so the change of absorbance induced by the analyte will not be limited to a single range of wavelengths and a single response, but instead, it may characterize a broader part of the porphyrin spectrum. However, to discriminate a specific kind of analyte it would be necessary not only to sense different wavelengths using the same sensing material but also it may need a cross responsive sensing material (a material that is also reactive to the sensed analyte).

In this case, phthalocyanine and manganese porphyrins could be used as cross responsive sensing elements. This sensing materials respond at different wavelengths and has been used by other researches [14, 15].

Therefore, a cross-responsive sensor array composed of different sensing pairs and sensing materials would be ideal to differentiate and quantify the analyte vapour. The higher the number of sensing pairs (in this case wavelength ranges) and cross responsive materials, the higher the discriminatory capacity and the accuracy of the sensor.

Nevertheless, the cross-responsive sensor array needs a cross-reactive recognition mechanism, and the complexity of the system increases with the number of sensing elements in the system, i.e. the number of wavelength ranges (sensing pairs) times the number of sensing materials. So this sensor array system may require the use of more sophisticated analysis to categorize and quantify the analytes, such as principal component analysis (PCA). PCA is a statistical procedure that is useful for the compression and classification of data, it reduces the dimensionality of a data set a new set of variables smaller than the original set of variables. In other words, PCA simplifies the data and categorize the responses.

Also the electronics involved in the system will require a peripheral interface controller (microcontroller) due to the number of outputs in the system and the necessary

interpretation of the signals. The PIC could control not only the conversion of signals from analog to digital, but also it can be programmed to show information about the analyte in an LCD display.

5.3.3. Concentration dependence and saturation of the sensor

To show the response to changes in the analyte concentration for this sensing pair, different concentrations of 2M2B were delivered into the chamber. The concentration was modulated by changing the temperature in the water bath in which the liquid analyte is placed. Figure 5.28 shows the response of the sensor after being exposed to the alcohol.
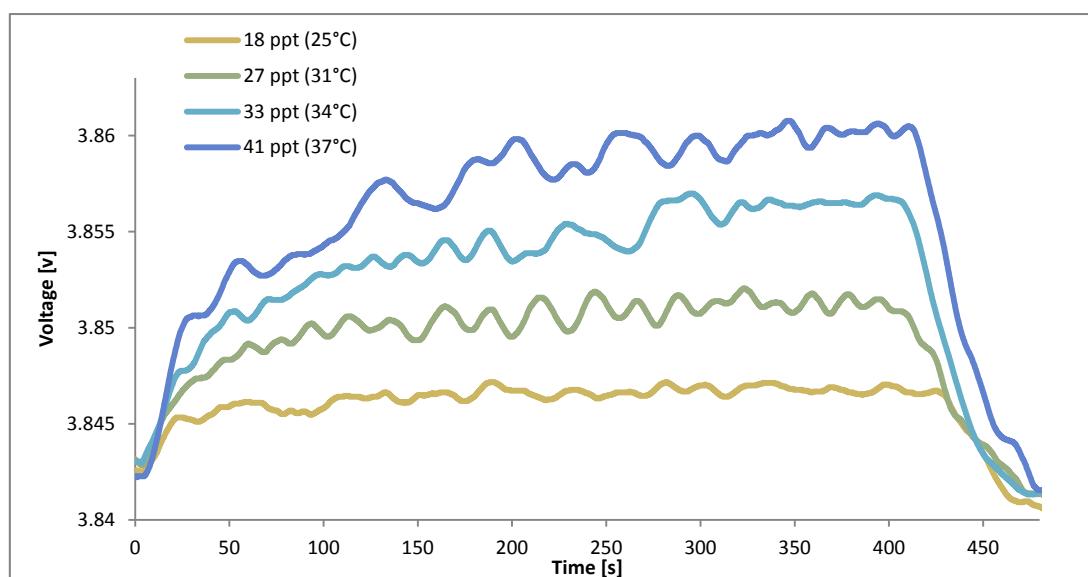
Figure 5.28: Voltage response of the sensor as a function of the concentration of 2M2B. The analyte concentration varies depending on the water bath temperature.

It was observed that for concentrations below 41 ppt, the response of the sensor increases with increasing concentration; this concentration/response relationship diverges slightly from linearity. For this range of concentrations (analytes temperatures from 0°C to 37°C), the response in the sensor progressively becomes stronger as the concentrations approaches 41 ppt. The concentration dependence is illustrated in Figure 5.29, in which the change in voltage of the sensor is plotted against the concentration of the vapour.

After 41 ppt (corresponding to alcohol at 37°C) the response of the sensor changed no more with increasing concentrations, in other words, the response remains constant. There are two possible explanations for this: either the sensor is saturated (all magnesium porphyrin

218

molecules available have interacted with the vapour analyte and consequently the sensor is saturated) or the delivered vapour is condensing in the pipework that connects the sensor to the analyte. In the interest of discarding one of the possibilities, an experiment using the Fourier Transform Infrared Spectroscopy (FTIR) apparatus (described in section 3.5.4) was performed and is reported in the following subsection.
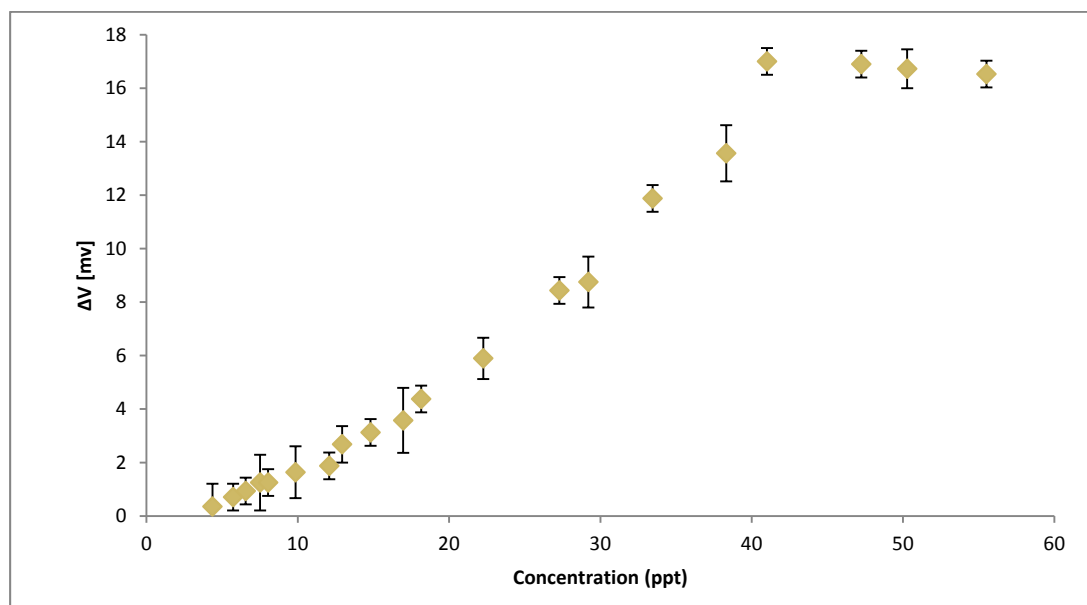
Figure 5.29: Concentration of 2M2B as a function of the change in voltage in the sensor.

5.3.3.1 Study of 2M2B condensation

Liquids can evaporate into gaseous forms, in the same way that gases can condensate back to their liquid form. When a liquid analyte is placed into a glass vessel an equilibrium exists between its gaseous and liquid phase. This balance in this equilibrium will depend upon the temperature of the liquid analyte and the gas temperature inside the glass vase container. It occurs because some particles in the analyte escape the liquid cohesive forces and enter the gaseous phase. Some of the molecules will have enough energy to enter the gaseous phase and this occurs at any temperature. So, this thermodynamic equilibrium occurs in a closed system. Within the confines of the temperature controlled water bath this equilibrium holds. However, when the vaporized analyte is flushed trough the tubes, the vapour cools down because there is a temperature difference between the hot analyte vapour and its surroundings (in this case, the laboratory temperature). This condensation effect arises when the vaporized analyte is compressed to its saturation limit or/and cooled down.

The IR absorption spectrum of the 2M2B was measured recreating the fabrication of vapour conditions implemented in the gas chamber. That is to say that the liquid analyte was placed in a sealed glass vase and was heated by a water bath. Figure 5.29 shows the absorbance of vapour produced varying the temperature of the analyte. The results of the FTIR experiment are presented in figure 5.30 in a wavelength range from 2750 to 3100 nm.
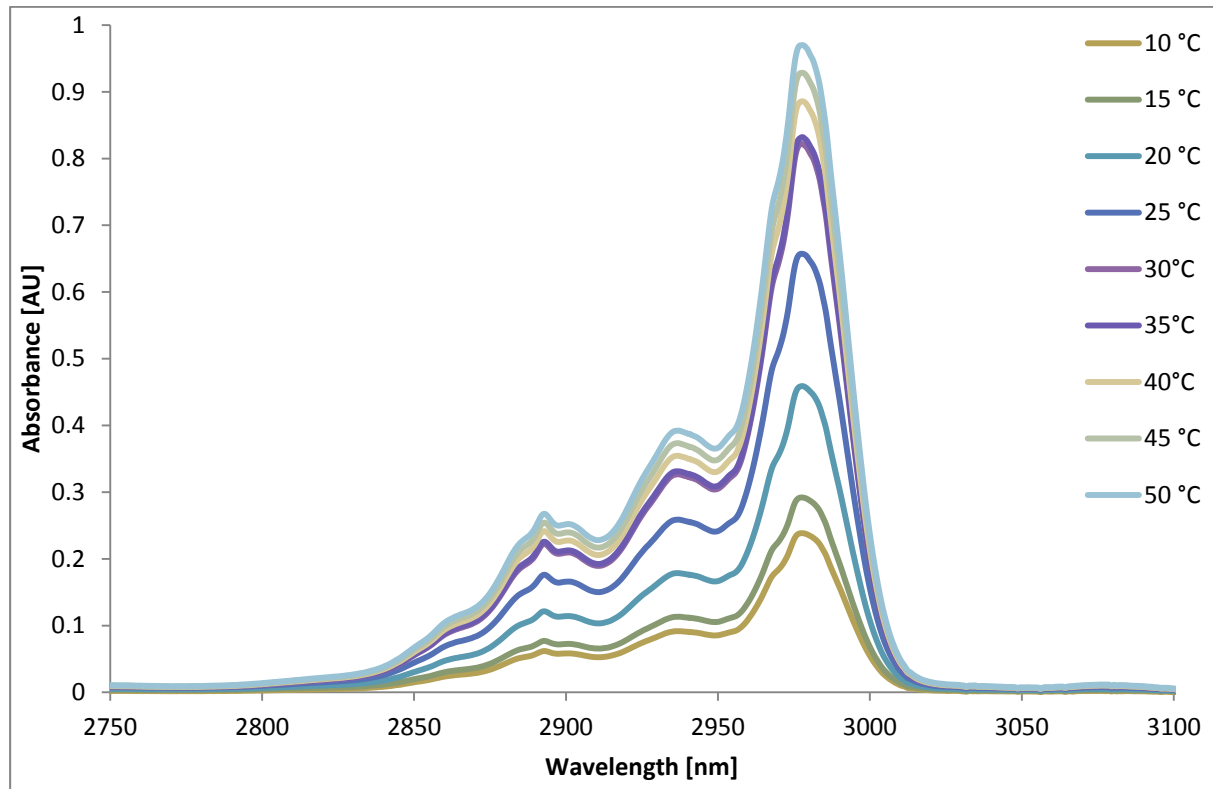
Figure 5.30: FTIR absorbance spectrum of 2M2B at different temperatures.

Figure 5.31 shows a graph of the absorbance of a 2977 nm wavelength vs temperature of the analyte in the water bath. The absorbance and the temperature in the analyte seems to be directly proportional at low temperatures as would be expected from the Beer-Lambert Law, however that linearity is not observed after the water bath exceeds 35 °C. Consequently, it can be concluded that the analyte condenses in the tubes at water bath temperatures above 35 °C. The condensation occurs above this water bath temperature because the vaporized analyte is not maintained at this elevated temperature. Cooling of the vapour by loss of heat to the lab environment and pipework reduce the saturation limit of the vapour so it being to condense on any available surface. Figure 5.29 shown that the saturation of the proto-type was achieved when the sensor is exposed to 41 ppt of 2M2B, which corresponds to a temperature of approximately 37°C in the water bath. Therefore, it can be inferred that the

saturation of the sensor occurs not because there are no more available porphyrin sites to bind with, but because the analyte vapour is being condensed and the concentration cannot be raised above 41 ppt. The higher concentration values reported in Figure 5.29 are not reliable and are a result of how the concentrations are calculated using the Antoine equations as described in section 3.5.1f.

To avoid the problem, either these higher concentration ranges should be avoided or the possibility of isolating thermally the pipework connecting the sensor to the analyte must be considered. Future experiments will contemplate that possibility.
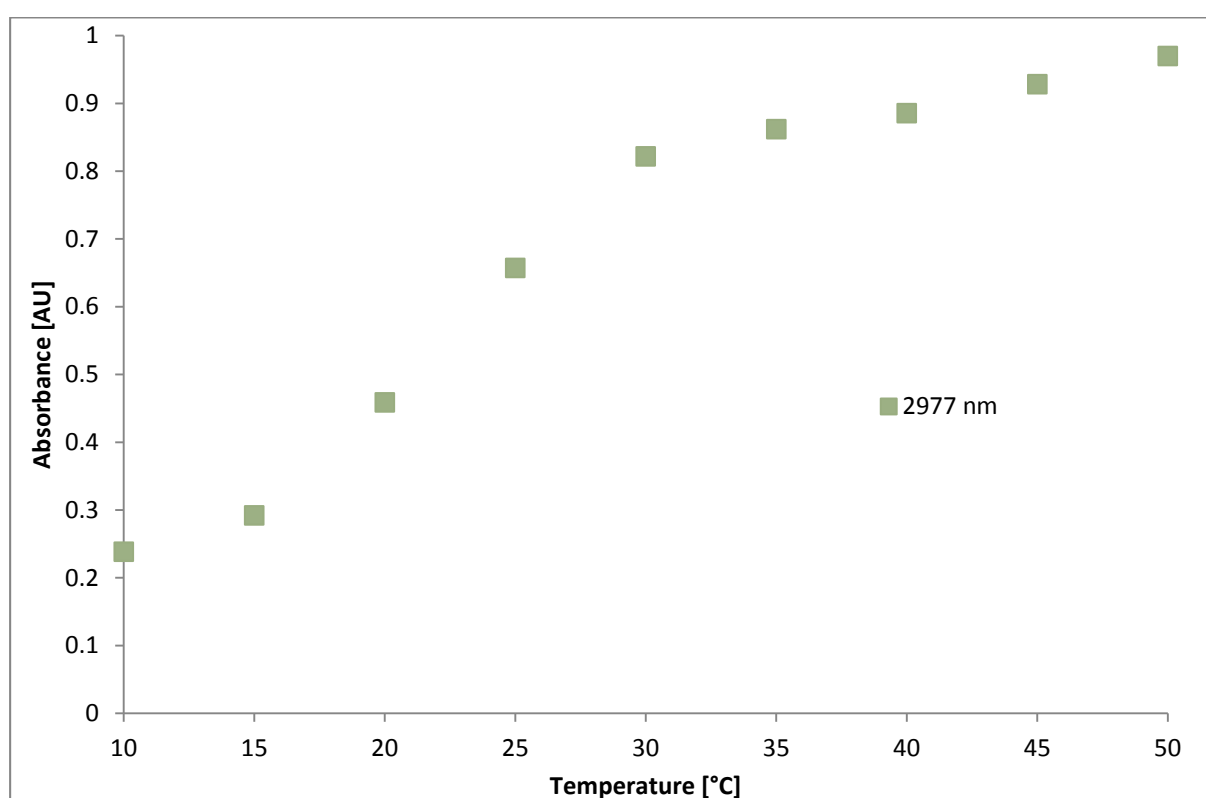
Figure 5.31: FTIR absorbance spectrum of 2M2B at a wavelength of 2977 nm.

5.3.4. Freundlich adsorption model

It is important to understand the adsorption behaviour of the vapour onto the porphyrin films deposited in the sensor. To express the adsorption of the analyte molecules a mathematical model of the system must be expressed. Initial attempts using the Langmuir absorption model and the BET absorption model were not successful in fitting the results from the LED-PX sensor. The Freundlich Adsorption isotherm was used to correlate the experimental data with

the equations of the model. By definition, the Freundlich Adsorption is an empirical model, so it is based on direct observation rather than theoretical assumptions.

The non-linear model characterizes the isothermal variation of adsorption of a vapour per unit mass of solid adsorbent as a function of pressure [16]. The Freundlich model can be described with the following equation:

$$\frac{x}{m} = kp^{\frac{1}{n}}$$

Eq. 5.6

Where x is the mass of adsorbate (analyte) and m is the mass of adsorbent (porphyrin) at an equilibrium pressure p. k is an indicator of adsorption capacity and the term $1/n$ denotes the intensity of the relative adsorption; both, n and k are constants whose values depends upon the gas temperature and the adsorbent type.

To eliminate the exponential term in equation 5.6 a logarithm term was added, resulting in the following expression:

$$log\left(\frac{x}{m}\right) = log(k) + \frac{1}{n}log(p)$$

Eq. 5.7

Presuming that the concentration (c) is analogous to the pressure (p) and ΔV is proportional to x/m, a graph of a logarithmic term of the change in voltage in the sensor against the logarithmic term of the concentration was plotted. Figure 5.32 shows the plot of $log(\Delta V)$ vs $log(c)$ which leaded up to a straight line that denotes that the adsorption process coincides with the Freundlich adsorption model. The slope of the line is the empirical adsorption intensity $(1/n)$ and the intercept in the y axis is assimilated to the Freundlich sorption coefficient$(log(k))$.
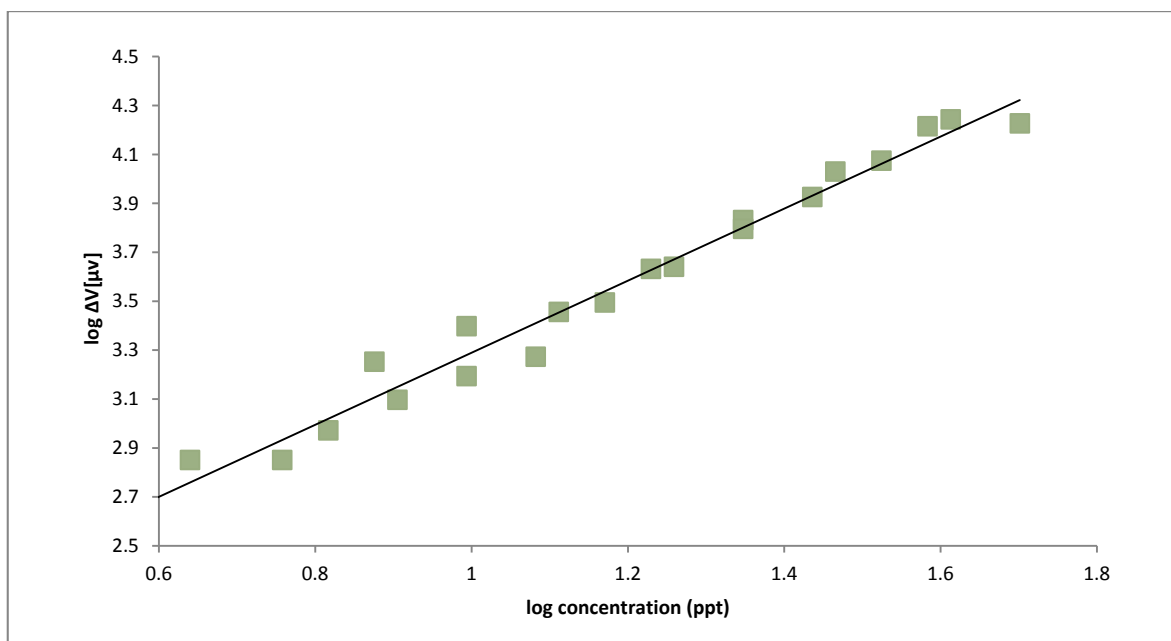
Figure 5.32: Concentration of 2M2B as a function of the voltage change in the phototransistor. The gaseous adsorption detected by the sensor was modelled using the empirical Freundlich model.

The Freundlich model can be expressed theoretically supposing that enthalpy of adsorption changes exponentially with the extent of surface coverage; assumption that is closer to reality than the classical Langmuir adsorption model. The model is classically used when considering heterogeneous surfaces where there is a distribution of interaction site enthalpies, and as such commonly yield up a gradient $1/n$ that is greater than unity. However, in this analysis the gradient is lower than unity. So, it can be inferred that the distribution in the interaction enthalpy for interactions between the analyte and the same porphyrin is not significant. Thus, it is hypothesized that the non-linearity observed in the system is not a consequence of the distribution of interaction enthalpies, but can be explained in terms of the number of available sites for adsorption increasing marginally upon exposure. Porphyrins tend to aggregate to each other when ligands are not present. When the porphyrin is exposed to suitable ligands, the aggregated molecules may separate, creating more available active sites for adsorption, resulting in the non-linear response revealed in the experimental data.

Alternatively, the non-linearity of the model can be attributed to the non-linear response of the phototransistor.

5.3.5. Temperature dependence and enthalpy of adsorption

Other than the sensor response as a function of the vapour concentration, it is also crucial to study the response of the sensing pair and its temperature dependence related to the rate of the chemical reaction between the porphyrin and the analyte. A series of cycles were effectuated varying the exposure temperature at a fixed concentration of 2M2B to observe the correlation between the optical response of the sensor and the temperature inside the chamber. Figure 5.33 shows five exposure/recovery cycles when the sensor was exposed to 30 ppt of 2M2B. The temperatures of exposure were 303, 313, 323, 333 and 343 °K whereas the temperature used to desorb the sensor was maintained at 348 K.

It is evident from figure 5.33 that the sensor voltage drops as the temperature increases, that is, the system does not return to the same base voltage at different temperatures. This effect is attributed to the temperature response of the sensing pair associated with the energy gap of the electronic devices in the semiconductor. Despite the fact that the temperature relocates to a new voltage reference, the variation in voltage between the pre and post exposure steady levels were taken as the sensor response values for its corresponding temperature.

As the temperature in the chamber increases the magnitude of the sensor response to the vapour exposure decreases because there is more thermic energy available in the system, which causes a different absorption/desorption rate. The figure also shows that the noise level is increased at higher temperatures, which causes an increase in the collector current in the phototransistor and consequently results in a worse signal-to-noise ratio.
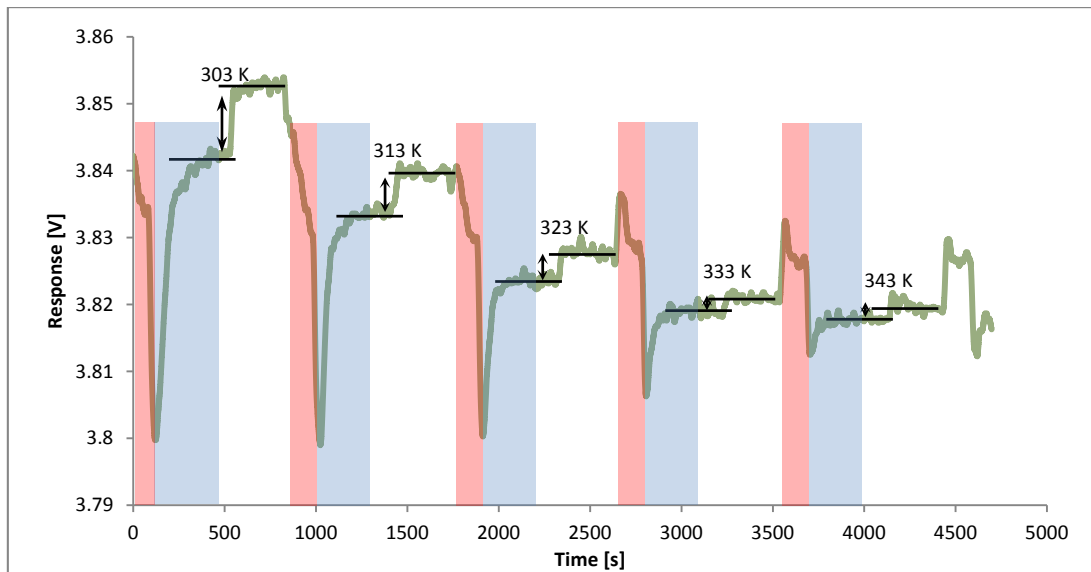
Figure 5.33: Sequence of exposure/recovery cycles carried out over a range of temperature.

It has been observed that the response of the sensor decreases as the temperature increases and the effect is related to the average time which an analyte molecule stays bound to a porphyrin binding site. In general, the time which a molecule remains bound is reduced with increasing temperature and therefore there are fewer vapour molecules absorbed onto the porphyrin layers.

The Arrhenius equation produced from this dataset describes the porphyrin-analyte interaction occurring at a temperature T in terms of a reaction rate k. The equation can be written as:

$$k = Ae^{-\left(\frac{E_a}{k_B T}\right)}$$

Eq. 5.8

Where k_B is the Boltzmann constant, A is a constant associated with the rate coefficient and the temperature and E_a is the activation energy. Since the reaction rate k is proportional to the sensor response, the equation can represented as:

$$\Delta Sensor\ Voltage = Be^{-\left(\frac{E_a}{k_B T}\right)}$$

Eq. 5.9

Where B is a constant. Equation 5.9 can be rewritten as:

$$\ln(\Delta Sensor\ Voltage) = -\left(\frac{E_a}{k_B}\right)\left(\frac{1}{T}\right) + \ln(b) \qquad \text{Eq. 5.10}$$

Consequently, when $\ln(\Delta Sensor\ Voltage)$ is plotted as a function of $1/T$ a correlation should result in a straight line, in which the gradient of the line is analogous to the enthalpy of adsorption. Figure 5.34 shows the Arrhenius plot of the sensing pair for the adsorption process involving MgEHO and 2M2B.
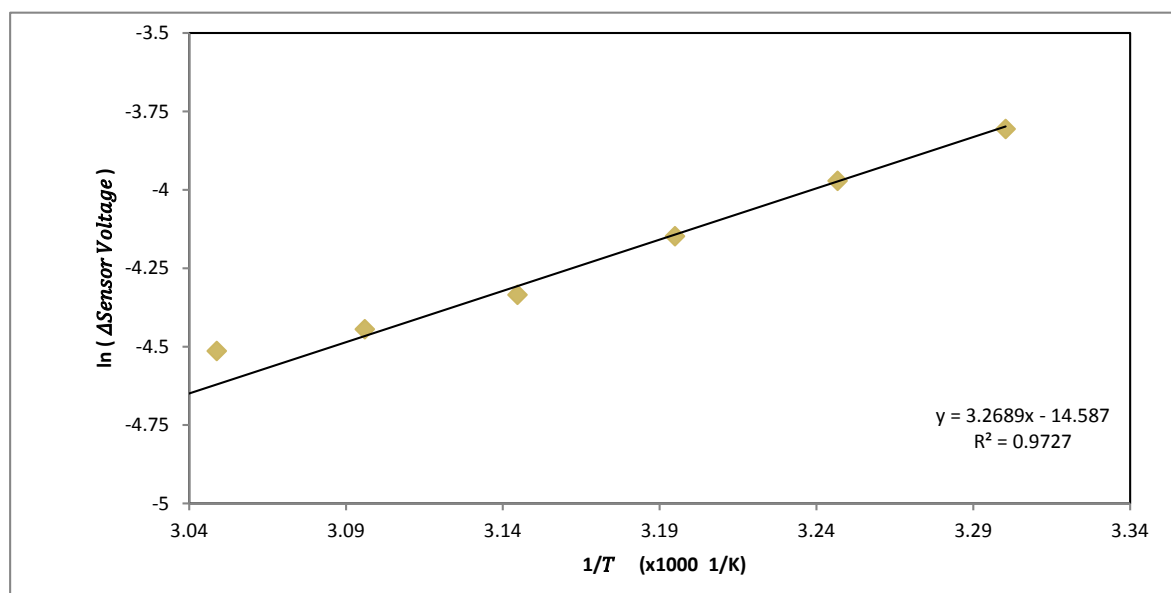
Figure 5.34: Arrhenius plot of a sensing pair exposed to 41 ppt of 2M2B.

The gradient of the Arrhenius plot is a correlation of the activation energy and the Boltzmann constant that can be expressed as E_a/k_B; the term is useful because it can lead us to the calculation of the enthalpy of adsorption of 0.28 eV. The value is similar to other analyte-porphyrin interactions, which are in the range of 0.2 to 1 eV, and is an indicator of a moderate recovery rate and sensitivity [5].

Conclusions, implications and future work

The objective of this chapter was to fabricate a cheap, small, simple and efficient system able to detect different vapour analytes. The gases can be detected using a photo receiver, an LED as a light source and an organic layer that changes their optical properties once it is exposed to the reactive analyte. The use of emitter-receiver pairs incorporating a thin film of porphyrin provides a colorimetric method to monitor analyte vapours.

Different systems were developed using a variety of photo detectors such as photo resistors, photo diodes and phototransistors. Despite the fact that all the sensors were able to detect gases, phototransistors showed a better performance because they allow a higher amplification of the sensor signal. The circuit used to measure the absorbance of porphyrin was made just using the emitter/receiver (sensing pair) and an op-amp that amplifies the signal one more time after the phototransistor, and is therefore very low cost. A data acquisition device was used to extract the data of the sensing circuit. The data was treated with a digital filter in order to reduce the noise of the system.

Various models of vapour chamber were also designed in order to have a controlled vapour delivery system and isolation from exterior sources of illumination. The first models had a poor designs and they had problems such as emitter/receiver misalignment and inaccurate control of the vapour delivery. The final chamber design fixed those problems and also incorporated other characteristics such as a temperature controller and the possibility of changing between two systems (phototransistor-LED and UV-Vis).

For a good sensor response, it is important to limit the wavelength of the LEDs, because if the change in absorbance of the porphyrin shows both a positive and a negative response in the range of the emission wavelength of the LED, the changes in absorbance could therefore cancel each other out. One inconvenience with LEDs is that their emission spectrum is not limited to a single wavelength, but a range of wavelengths. To improve the response by limiting the illumination range of wavelength it would be necessary to use a laser diode. Laser

diodes are semiconductor lasers in which the active medium is formed by a p-n junction of a semiconductor diode (similar to that found in an LED). However, contrary to LEDs, laserdiodes generate a single colour (i.e. monochromatic) so the wavelength range is dramatically reduced. Laser diodes are available in many different sizes, shapes and laser powers ranging from a few mW to hundreds of watts. The emitted wavelength depends mainly on the semiconductor material of the laser diode cavity and laser diodes are produced to cover the full visible spectrum from blue to red, and even beyond, with some emitting in the infrared. Common laser diodes can be found in the wavelength range from 360 to 2300 nm, which makes this device an ideal source of light because it covers most of the porphyrin spectrum [17]. Future experiments will contemplate the use of laser diodes instead of LEDs.

The main advantage of the PX-LED system is that is really flexible. The design of the various prototypes can be easily modified by matching the wavelength ranges of the electronic devices to the wavelength range that corresponds to the largest change in absorbance of a particular porphyrin-analyte complex. Another benefit of the prototype system is that the cost of the main components is very low. The total cost of the electronic components was £0.97, corresponding to the LED (£0.44) and phototransistor (£0.53) respectively. The devices were purchased through a global distributor of electronic components (Farnell UK). So far, the most expensive part of the gas sensing system is the steel chamber; however, a mass production of a suitably corrosion resistant plastic chamber would dramatically reduce the cost of the prototype. An approximate cost of the plastic piece was estimated, resulting in a cost from £2 to £4 (depending on the production volume). Therefore, it can be said that the marginal of cost of the prototype (electronic components and plastic chamber) would not exceed £5.

To show the capacity of the proto-type vapour sensor a PX-LED sensor was made using magnesium porphyrin as a sensitizer; the sensor exhibited a good repeatability and stable results. The magnitude of response of the alcohol-MgEHO complexes is relatively weak compared to other analyte-porphyrin complexes. In this manner, the detection of alcohol vapours using MgEHO was deliberately chosen to show the ability of the system to detect small changes in optical absorbance spectra. To illustrate the difference EHO was exposed to HCl and the response of the sensor was in the order of V (instead of millivolts as in the case

228

of MgEHO-2M2B) as depicted in figure 5.23.

The Mg-EHO sensor can detect concentrations of 2M2B ranging from 4.36 to 41 ppt. According to the FTIR study, the sensor reached saturation because the gas delivery system does not permit the concentration to be raised above 41 ppt reliably. The enthalpy of adsorption calculated for the 2M2B-MgEHO complex indicated a moderate rate of recovery.

The main inconvenience of the vapour sensing system is that the sensor is not able to differentiate between analytes. To make that happen, it is necessary to incorporate in a new sensing pair reactive materials that also induce optical changes when exposed to alcohols, such as phthalocyanines and metalloporphyrins. In addition to that, it is necessary to increase the number of sensing pair for all the materials in order to obtain more information about the sensed analyte. Further research should concentrate on developing a cheap robust proto-type sensor array using various sensing materials as the active sensing layers in different LED-PX sensing pairs, such that it is possible to discriminate between different chemical analytes.

References:

1.   Gutiérrez, A.F., *Proto-type vapour sensing using porphyrin molecular films* 2010, University of Leeds/University of Sheffield: UK.
2.   National Instruments. *Multisim*. 2014 17/09/2014]; Available from: http://www.ni.com/multisim/.
3.   Graeme, J.G., *Photodiode amplifiers: op amp solutions*. 1996: McGraw Hill.
4.   Gage, S., et al., *Optoelectronics/fiber-optics applications manual.* New York, McGraw-Hill Book Co., 1981. 376 p., 1981. **1**.
5.   Llopis, O., et al. *Photodiode 1/f noise and other types of less known baseband noises in optical telecommunications devices*. in *Proceedings of the 22th International Conference on Noise and Fluctuations*. 2013.
6.   Toshiba. *TLN107A Datasheet*. 2012 11/08/2014]; Available from: http://pdf.dzsc.com/88889/11594.pdf.
7.   Kim, C., et al., *Temperature-and bias-dependent study of photocurrent spectroscopy in an InGaN light-emitting diode operating near 400 nm.* 2010.
8.   National Instruments. *Designing Filters Using the NI LabVIEW Digital Filter Design Toolkit*. 2012 12/07/2014]; Available from: http://www.ni.com/white-paper/3237/en/.
9.   Mitra, S.K. and J.F. Kaiser, *Handbook for digital signal processing*. 1993: John Wiley & Sons, Inc.
10.   National Instruments. *Savitzky-Golay Filter VI*. 2014 13/08/2014]; Available from: http://zone.ni.com/reference/en-XX/help/371361H-01/lvanls/sgfil/.
11.   Richardson, T., et al., *Gas sensing properties of porphyrin assemblies prepared using ultra-fast LB deposition.* Colloids and Surfaces A: Physicochemical and Engineering Aspects, 2002. **198**: p. 843-857.
12.   Gutiérrez, A.F., et al., *A proto-type sensor for volatile organic compounds based on magnesium porphyrin molecular films.* Sensors and Actuators B: Chemical, 2014. **202**(0): p. 854-860.
13.   Dunbar, A.D., et al., *Investigation of free base, Mg, Sn, and Zn substituted porphyrin LB films as gas sensors for organic analytes.* The Journal of Physical Chemistry B, 2006. **110**(33): p. 16646-16651.
14.   Lvova, L., et al., *Detection of alcohols in beverages: An application of porphyrin-based Electronic tongue.* Sensors and Actuators B: Chemical, 2006. **118**(1): p. 439-447.
15.   Spadavecchia, J., et al., *Spin-coated thin films of metal porphyrin–phthalocyanine blend for an optochemical sensor of alcohol vapours.* Sensors and Actuators B: Chemical, 2004. **100**(1): p. 88-93.
16.   LeVan, M.D. and T. Vermeulen, *Binary Langmuir and Freundlich isotherms for ideal adsorbed solutions.* The Journal of Physical Chemistry, 1981. **85**(22): p. 3247-3250.
17.   Nakamura, S., *Laser diodes.* Optoelectronic properties of semiconductors and superlattices, 1999. **7**: p. 1-44.

Chapter 6: Study of the macroscopic expansion of porphyrin layers using a quartz crystal microbalance sensor.

In this section, a quartz crystal microbalance (QCM) will be mounted within a Pierce oscillator circuit with the intention of determining the mass of porphyrin deposited on the quartz crystal during an LB deposition process by measuring the change in frequency of the crystal resonator. An electronic oscillator is an electronic circuit that converts a direct current from a power source to an alternating current signal in a periodic oscillating signal.

The aim of the experiment is to correlate the expansion of the Langmuir monolayers with the protonation effect induced upon exposure to trifluoroacetic acid. The expansion of the monolayer will be explained in terms of the molecular orientation of the porphyrin molecules.

The results presented in this chapter have previously been published in an article entitled "Macroscopic expansion of tetraphenyl porphyrin Langmuir layers stimulated by protonation" [1]. The author of this thesis was responsible for the design and measurements related to the QCM aspects of this publication. In the production of this journal article, the late Dr. Richardson wrote the text of the published article.

6.1 Materials

6.1.1. Porphyrins

In this chapter, six free base tetra phenyl porphyrins were used to demonstrate how the side group variation in the chemical structure of the porphyrins affected the orientation of the molecules in the monolayer in response to protonation. Figure 6.1 shows the porphyrins selected for the study.
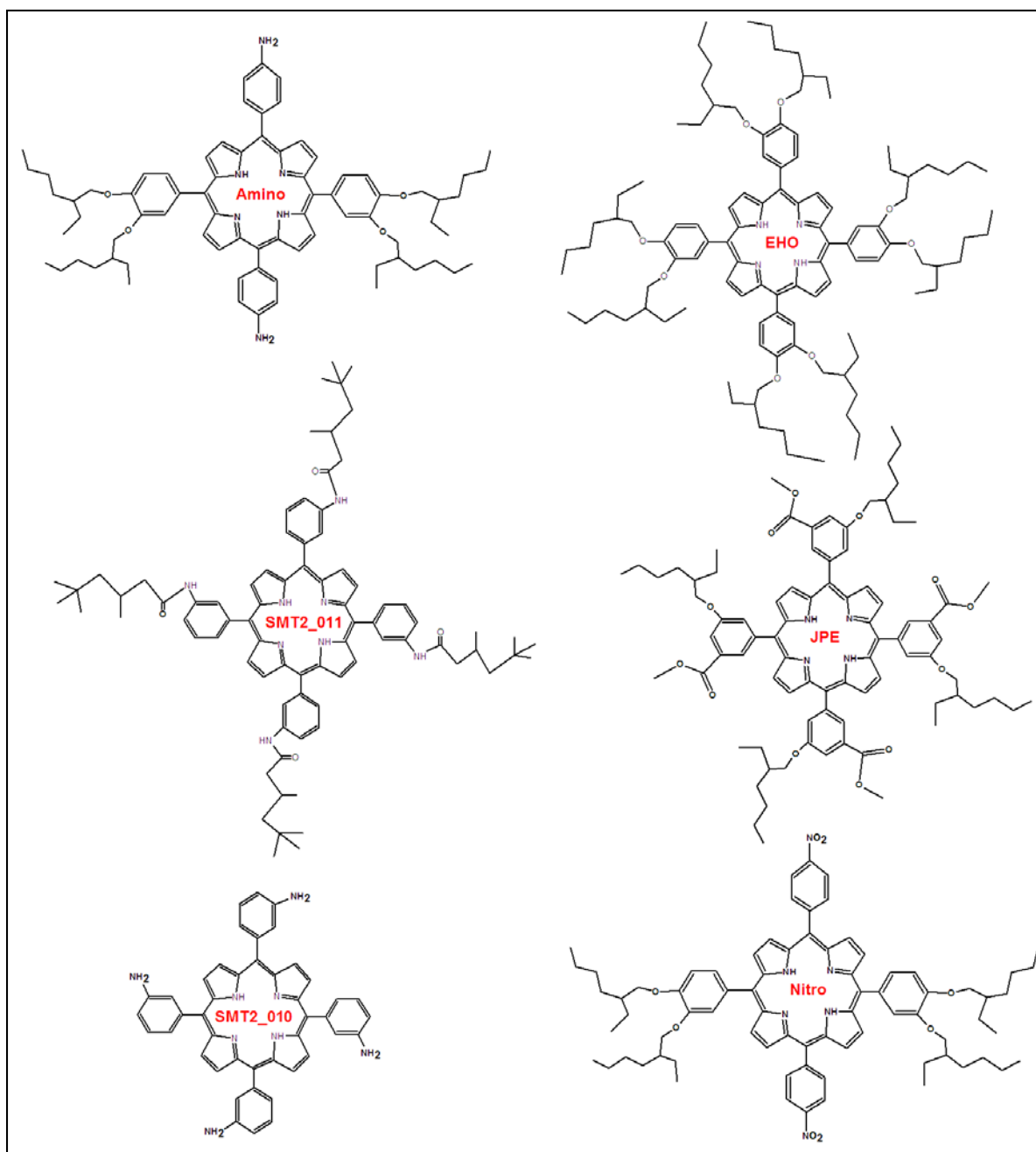
Figure 6.1: Molecular structures of the tetraphenyl porphyrins derivatives used in this study and the abbreviations used to refer to them.

6.1.2 Analyte

Trifluoroacetic acid (TFA) is an organic compound with a chemical formula of CF_3CO_2H. The compound is characterized by its remarkably strong fluorine-carbon bond. Previous studies have shown that TFA, along with other compounds such as HCl, NO_2 and Cl_2 induce protonation of the porphine ring in free base porphyrins [2].

6.1.3 Quartz Crystal

A 10 MHz quartz crystal model 151215-10 provided by SPI Supplies (USA) was used as a microbalance to characterize the deposited porphyrin layers. The electrodes in the crystal have a diameter of 0.201" and are made of gold and the diameter of the circular quartz crystal is 0.538". (See figure 6.12)

6.2 Experimental details

6.2.1 Pierce Oscillator

The Pierce oscillator is an electronic circuit that operates at the series resonant frequency of a quartz crystal in the range from 1 KHz to 30 MHz. Its fundamental limitation is the proper matching of the on-board Pierce oscillator with the quartz crystal. The design of the Pierce oscillator must comply two conditions: The phase shift in the whole circuit must be 0 or some integer multiple of 360° and the amplifier must overcome the losses of the feedback network [3]. Figure 6.2 shows a simplistic Pierce oscillator circuit incorporating a transistor to compensate for the high gain losses in the circuitry surrounding the crystal. 180° phase shift are provided by the capacitors C_2 and C_3 along with the quartz crystal and the opposing 180° are provided by the transistor.
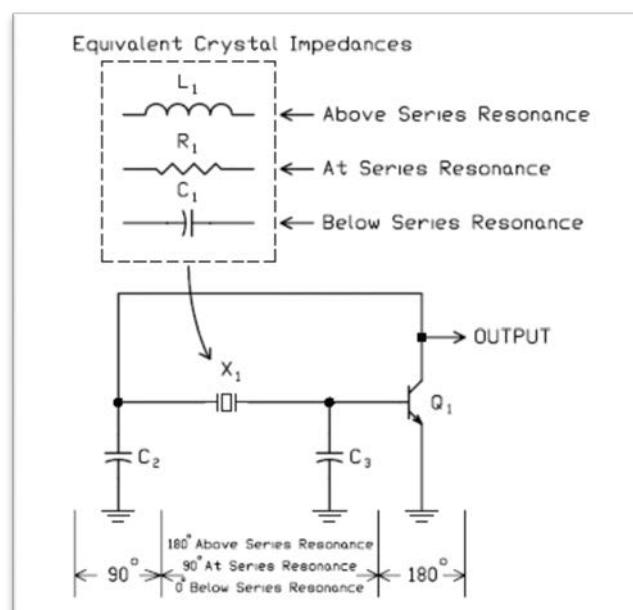

Figure 6.2: Ideal circuit of a Pierce crystal oscillator [4].

The load capacitance (C_L) is the external capacitance of the crystal within the feedback loop of the oscillator circuit. The quartz crystal expects to see and operate at this desired frequency. The circuit load capacitance is determined by the transistor internal capacitance, the capacitors C_2 and C_3 and stray capacitance (C_S).

The values of the external capacitors are selected to match the crystal load capacitance using the following equation [5]:

$$C_L = \frac{C_2 C_3}{C_2 + C_3} + C_S \qquad \text{Eq. 6.1}$$

When selecting values of C_2 and C_3, care must be taken to ensure that there are no oscillator start-up problems instigated. For example, although selecting large values will increase the frequency stability, it may also decrease the loop gain impacting the start-up.

6.2.2 Design

Figure 6.3 shows the Pierce oscillation circuit used to perform the experiments. A wideband transistor (model NPN BFR92) was used to match the gain and frequency of response required for the system.

The resistors connecting the input and output (R_1 and R_2 respectively) adjust the amplification of the transistor and control the amount of feedback. R_3 controls how fast the oscillator starts in which the value must be small enough to provide current to start the circuit oscillation, yet large enough to avoid overdriving the crystal. Capacitors C_1 and C_2 set the initial gain and crystal drive level.

The variable capacitor was incorporated to match the oscillator load capacitance to that of the selected quartz crystal.

The green box marked as XFC1 represents a frequency counter. The apparatus is connected to a single node, which is shared with R_1, R_2 and R_3.
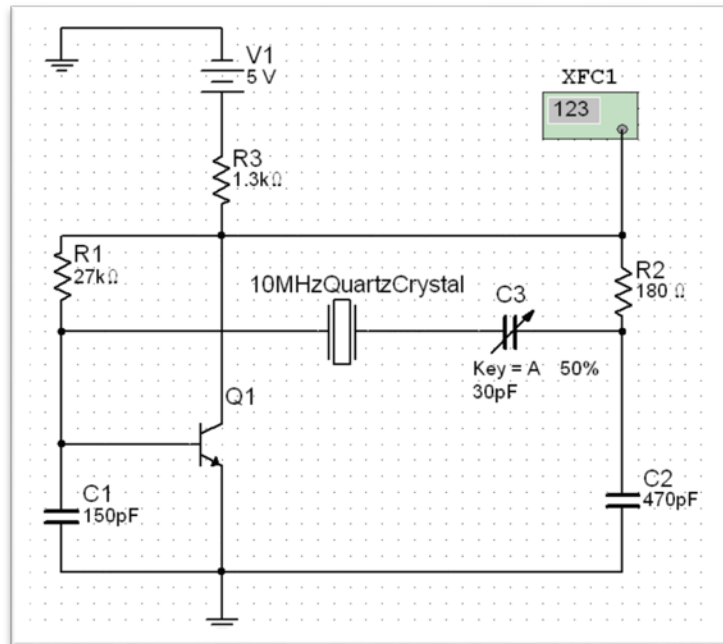
Figure 6.3: Pierce oscillator circuit used to carry out the experiments.

6.2.3 Faraday cage

Minimal interference in the circuit produced by external electric fields was obtained by using a Faraday cage to permit precise measurements to be made. The cage works as a shield against electrostatic charges and some types of electromagnetic radiation. The enclosure consists of a conducting shell to distribute the external radiation or electrical charge around the exterior of the cage, cancelling the subsequent effects in the interior of the cage. The conducting shield will protect the interior of the cage because no electric field is perceived by it, even when a strong external electric field is applied, the charges on the conducting shield rearrange themselves until the electric field inside is zero. In other words, the cage is immune to possible electromagnetic disturbances produced in the exterior of our system.

Figure 6.4 shows the Faraday cage used to isolate the Pierce circuit and the quartz crystal from strong electric fields or other electrical effects. For demonstrative purposes, the picture shows the cage with the oscillator circuit in the exterior and the enclosure of the case open.
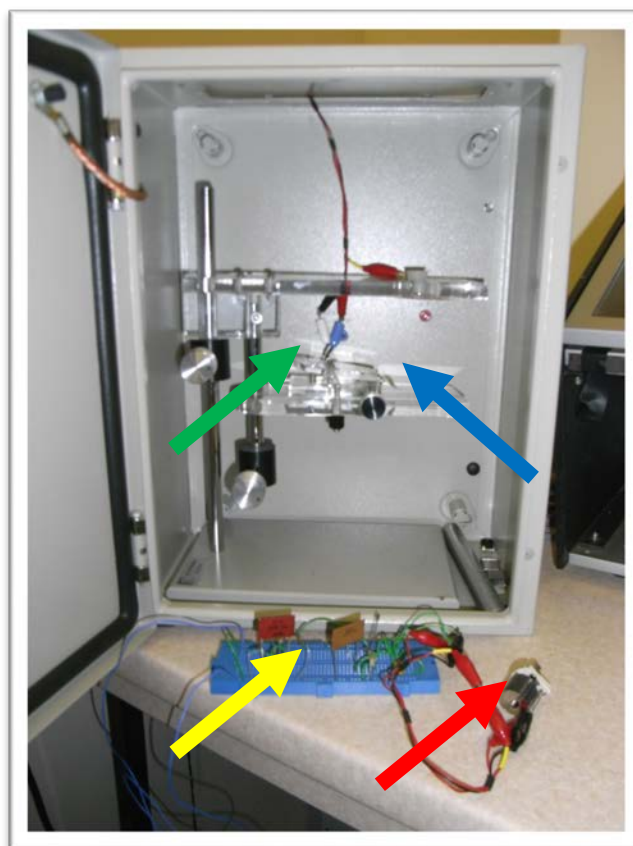
Figure 6.4: Open Faraday cage. Yellow: Pierce oscillator circuit, red: variable capacitor, blue: quartz crystal, green: crystal holder clip.

6.2.4 Control experiment

To verify that the oscillator circuit operates at the natural frequency of the quartz crystal and to corroborate its stability and accuracy after some mass has been added to the crystal, a control experiment was performed. To implement the test, 150 µl of stearic acid were spread on the air-water interface of a trough and later the barriers were compressed to a target pressure of 15 mN/m. The saturated fatty acid was selected because it forms fine and homogeneous organized monolayers, unlike some porphyrins that tend to aggregate and/or create rigid films [6]. A 2.4 GHz high resolution frequency counter (model: Veremall-DVM13MFC2) was used to measure the change in frequency of the crystal for every 4 deposited layers.

Figure 6.5 is a graph showing the relation between the frequency change and the number of deposited layers in the crystal. Figure 6.5 implies, the change in frequency is directly proportional to the number of layers. In figure 6.5, a trend line (the straight black line) is

drawn along with the R^2 value that proves that the plotted data is close to the fitted regression.
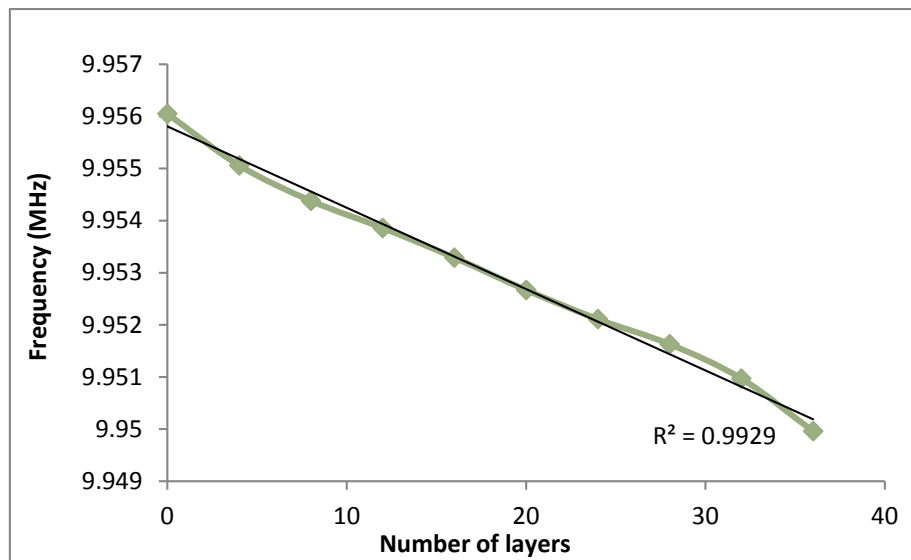

Figure 6.5: Frequency of the quartz crystal in the Pierce oscillator plotted against the number of layers of stearic acid deposited onto the quartz crystal at a target surface pressure of 15 mN/m.

Taking into consideration the fact that a certain number of layers of acetic acid resulted in a corresponding shift in the frequency, it can be inferred that the circuit is stable and can be used to quantify the deposited mass on the quartz crystal using the Sauerbrey equation. Alternatively, the results can be expressed in a plot relating the change in frequency versus the number of deposited layers, as shown in figure 6.6.
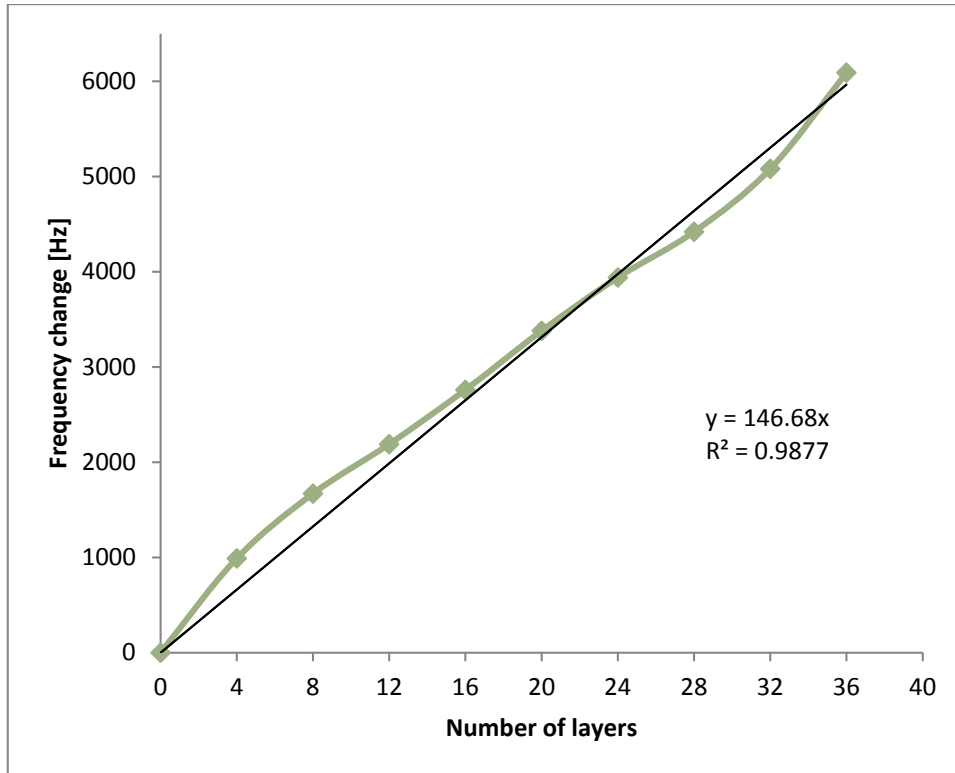
Figure 6.6: Frequency change versus number of stearic acid layers.

Having applied a straight line fit a slope corresponding to a change in frequency (Δf) of 146 Hz/layer can be extracted from figure 6.6. The Sauerbrey equation, described in section 3.5.3b, can be expressed as:

$$\Delta f = \frac{\Delta m}{A} k$$

Eq. 6.2

Where k represent a constant given by the resonant frequency, density and shear modulus of quartz. To correlate the change in frequency with the change of mass, it is necessary to calculate the value of the constant k for this QCM system. Assuming an area per molecule of 0.21 nm^2 for stearic acid [6] and rearranging equation 6.2:

$$K = \frac{W}{N_A \Delta f A} = \frac{284.5 \ g/mol}{(N_A)(146 \ Hz)(0.21 \ nm^2)} = 1.54 \frac{ng}{Hz \ cm^2}$$

Eq. 6.3

Equation 6.2 can now be simplified to:

$$\Delta m = K \Delta f$$

Eq. 6.4

Where K represents the crystal-dependent sensitivity factor, also known as the mass sensitivity constant. Using equation 6.4, now it is possible to obtain the corresponding change of mass for the QCM system. For this control experiment, the mass per unit area per layer corresponded to 226.38 ng/cm^2.

6.3 Results

6.3.1 Estimation of the expansion using the surface pressure – area isotherms

To investigate the protonation and subsequent expansion of the porphyrin whilst still on the surface of the Langmuir trough, the analyte was added in liquid form instead of exposing the porphyrin to it in its vapour form. In other words, to quantify the expansion effect in the monolayers, two isotherms were made for every porphyrin: the first one was prepared using a concentration of 0.3 mg/ml of the porphyrin in chloroform and the second one was a compound of the porphyrin with the same concentration plus 1 drop of TFA.

As anticipated, the acid free and exposed to acid solutions resulted in different isotherms. Clearly, the addition of TFA produced an alteration in the curve characteristics of the isotherm due to the protonation of the porphyrin, causing an expansion in the monolayer. Figure 6.7 shows the surface pressure versus area per molecule characteristics for EHO and EHO plus a drop of TFA.
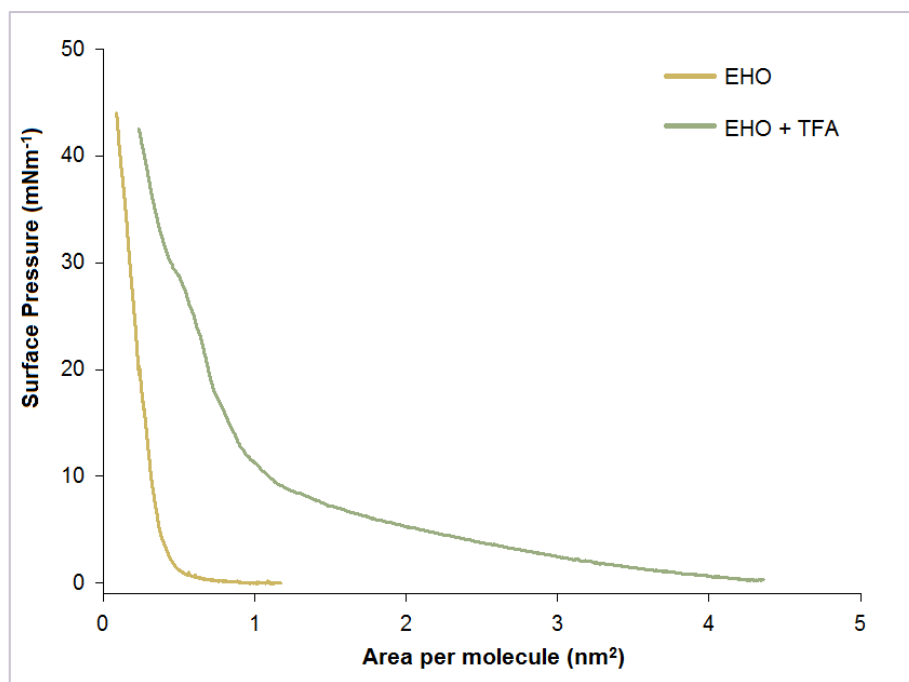
Figure 6.7: Isotherms for EHO and EHO with a drop of TFA. The addition of the acid produced protonation of the porphyrin, leading to a more expanded state.

The isotherms of the rest of the porphyrins were also recorded for their two respective solutions, acid free porphyrin and TFA/porphyrin solution. The comparison between these two isotherms, TFA treated and original, allowed an approximation of the degree of expansion of the monolayer, in response to addition of the acid.

The expansion level of the monolayer that could be achieved via exposure to TFA was quantifed by using the following equation to estimate the fractional expansion ratio (F_{exp}) of the monolayer.

$$F_{exp} = \frac{A - A_0}{A_0}$$

Eq. 6.5

The equation compares the monolayer area per molecule of its original state (A_0) with its exposed expanded area (A). Where a fractional expansion factor with a value of zero represents no areal difference induced by the acid and a negative value would imply contraction. To assign a valid expansion ratio, the areas must be taken at the same surface pressure. By way of explanation, the isotherms in figure 6.7 show that at a surface pressure of 5 mN/m the original solution has an area per molecule around 0.4 nm², whereas the TFA-treated reaches a larger area per molecule of approximately 2.4 nm².

240

For the pure EHO at the selected target pressure, it can be inferred that the porphyrin molecules are in a highly aggregated statement in which the molecules sit on the air-water interface in an edge-on configuration. Because the molecules are in a neutral electrical configuration, the situation permits a face to face grouping. Due to the absence of electrostatic interactions between the water and the porphyrin molecules, a strong overlap of the π electron system exists between the porphyrin molecules.

In the isotherm of the TFA-treated monolayer a larger value of the area per molecule is reached, indicating an expansion in the area of the Langmuir film. The effect is an indicator of a different orientation in which the porphyrin molecules lie face down towards the water. The addition of TFA in the EHO solution causes an alteration in the electrical properties of the thin film, and that leads to a different molecular orientation of the porphyrin on the water surface. Figure 6.8 shows how the addition of TFA causes an expansion in the surface area of the EHO. This is explained in terms of protons are captured by the porphine molecular core, producing di-cationic species. The protonation of the porphine causes Coulombic repulsion between the face to face formation of the EHO molecules and results in a new polar and charged molecular system with high affinity for water. The resulting protonated configuration leads to a less aggregated molecular conformation due to repulsion of electrically charged adjacent EHO molecules, causing a new orientation in which the plane of the water surface is parallel to the plane of the porphyrin ring, as depicted in figure 6.8.
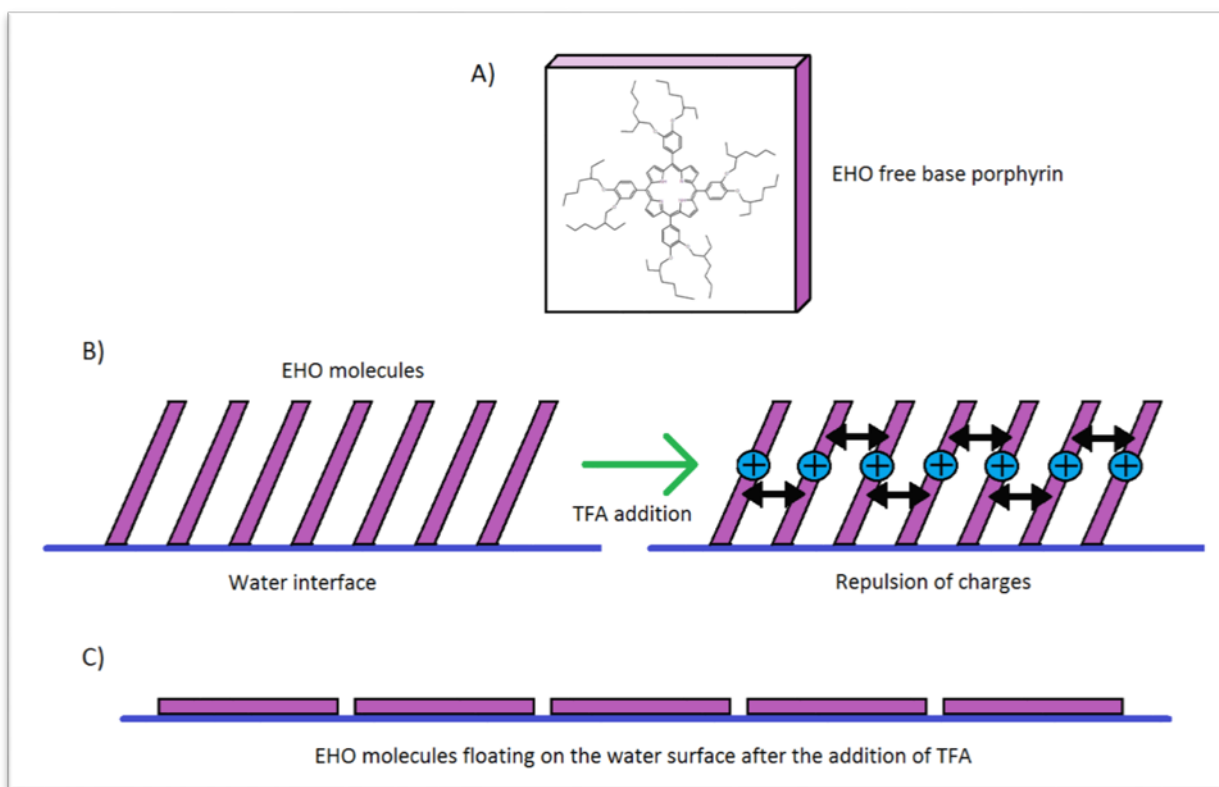
Figure 6.8: Theoretical portrayal of an EHO LB film on the water surface when exposed to TFA. A) Representation of a single EHO molecule, b) effect of the addition of TFA on the monolayer, c) new orientation of the porphyrin molecules after the exposure to TFA.

The fractional expansion factor for EHO was found to have a value of approximately 5 at a surface pressure of 5 mN/m, demonstrating a dramatic expansion of the LB film. Correspondingly, a similar isotherm investigation was carried out for the rest of the porphyrins to examine the expansion effect induced by TFA on porphyrins with different side groups. Figure 6.9 shows the fractional expansion factors of the six porphyrins used in this study measured consistently at a fixed target pressure of 5 mN/m. Noticeably, JPE reveals the smallest expansion factor which indicates only a small difference between its area per molecule in its exposed and unexposed states. On the other hand, EHO display the greatest F_{exp} value. The other porphyrins showed intermediate areal expansions upon exposure to TFA.
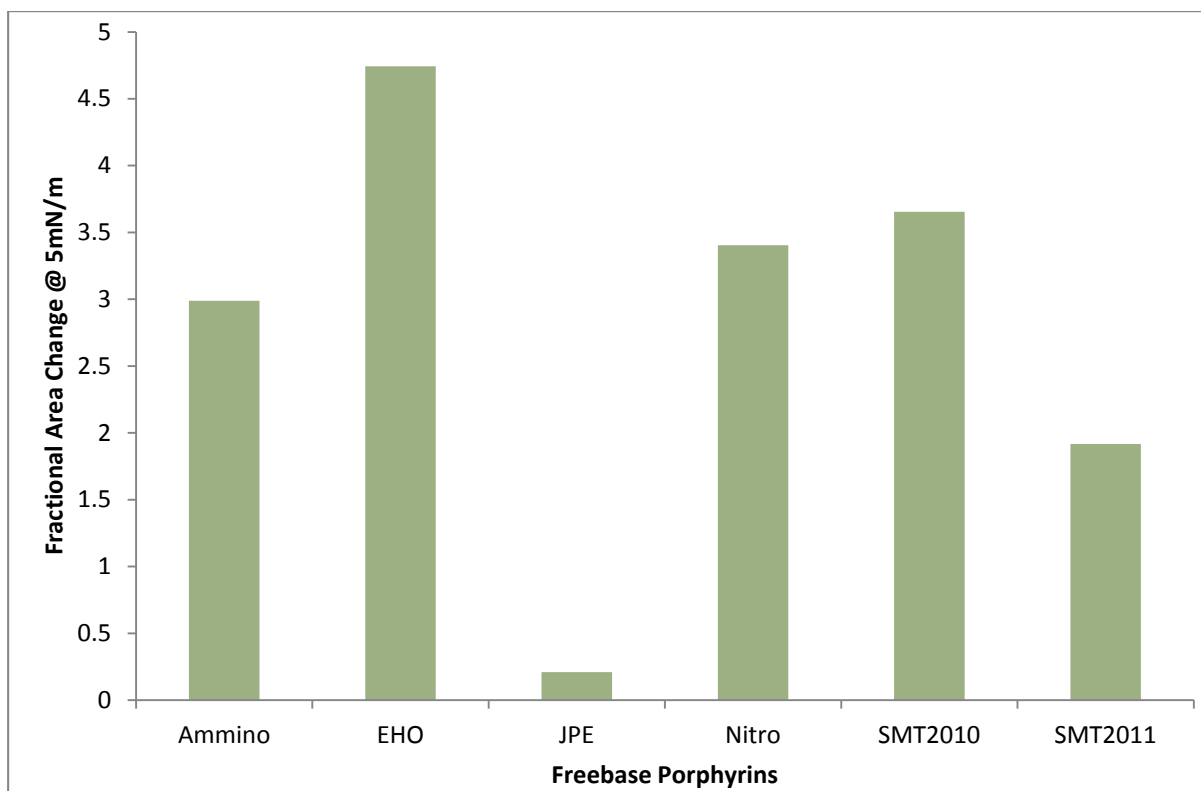
Figure 6.9: Fractional areal change induced by TFA for the tetra phenyl free base porphyrins.

The results for F_{exp} shown in figure 6.9 can be compared to a factor ϕ that associates the modelled area per molecule in a face down orientation (a_{mod}) derived from molecular modelling with the area per molecule within the pre-exposed edge on monolayer determine experimentally. Equation 6.6 describes the factor ϕ, in which a_{exp} is measured using the experimental isotherm data and a_{mod} is obtained by modelling the porphyrin molecules using a chemical structure drawing program that assigns a numerical value for its theoretical most expanded areal state.

$$\phi = \frac{a_{exp}}{a_{mod}}$$
<div style="text-align:right">Eq. 6.6</div>

When the value of ϕ is equal to unity it means that the modelled area and the experimental non TFA-treated area are numerically equivalent, but is also an indicator of the low degree of aggregation and implies a face down molecular orientation of the porphyrin without any exposure to the acid. Alternatively but less likely to happen, it can indicate that the aggregated porphyrin molecules remain unaffected after the addition of TFA. Brittle et. al exposed the free base porphyrins used in this study to several analytes; all of the materials responded to an acetic acid, which is a weaker acid than TFA [7].

In the same way, if 1 is much greater than the numerical value of ϕ this may suggest an aggregated monolayer that is affected by the exposure of TFA, expanding the area of the LB film.

Consequently, it is possible to make a direct comparison between the fractional area change (F_{exp}) and the factor ϕ in order to determine the capability for expansion for the free base porphyrins. A graph plotting these two terms, ϕ and F_{exp}, is depicted in Figure 6.10. The plot provides a clear visualization of the data, for instance the highest expansion effect is observed in EHO because its ϕ factor is extremely low, this situation is caused by the highly aggregated state of the porphyrin molecules within the monolayer prior to any TFA exposure. On the contrary, JPE exhibited the least expansion effect of all the free base materials, showing a ϕ factor close to 0.33. The two polar ester groups in the side group of JPE promote some anchoring between the water surface and the porphyrin molecules, consequently letting the JPE molecules arrange themselves in a face down orientation rather than a face to face orientation. The other materials in the in the study: SMT2_011, SMT2_010, nitro and ammino porphyrins, shown intermediary behaviour between that of JPE and EHO.
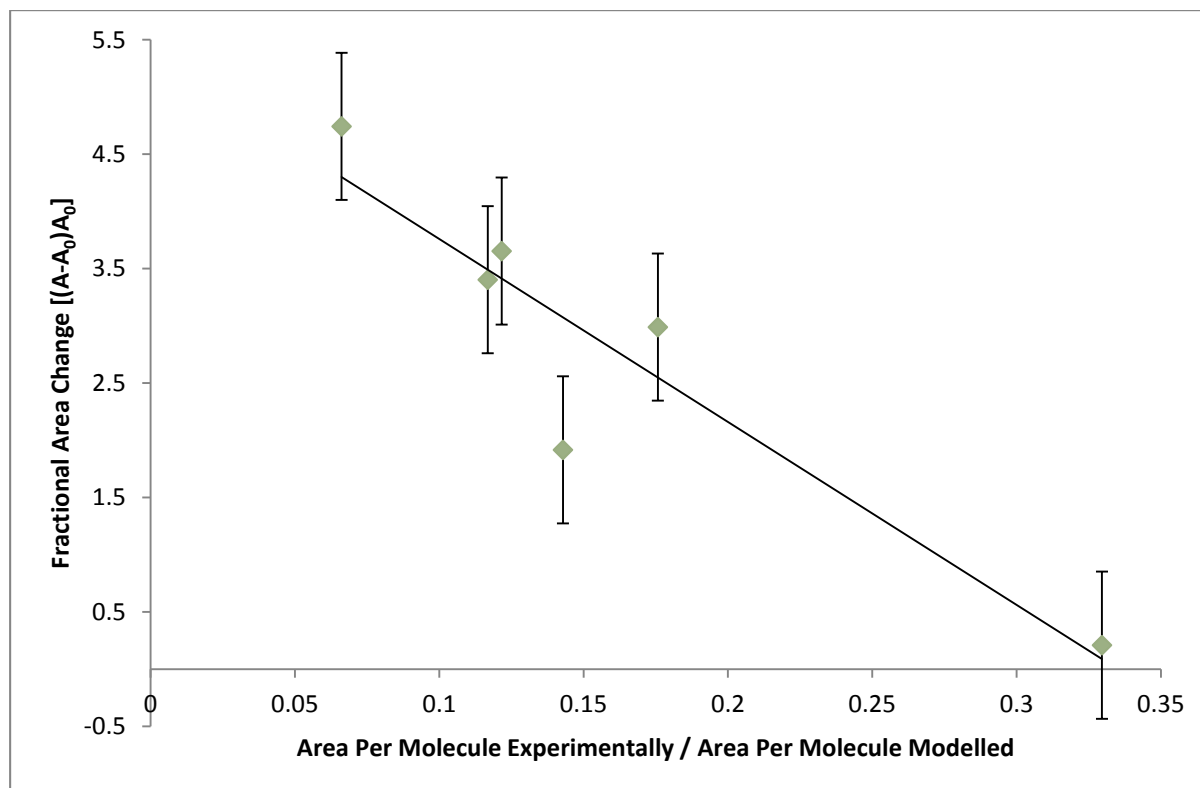

Figure 6.10: Plot of the fractional area change (F_{exp}) vs factor ϕ for the tetra phenyl porphyrins.

244

6.3.2 Estimation of the expansion using the Quartz Crystal Microbalance

The expansion effect in the LB films induced by the TFA was investigated further by depositing the porphyrin monolayers onto the quartz crystal, so the mass of the deposited materials could be quantified. The QCM system provides an accurate measurement of the mass of the films transferred onto the crystal surface, thus it is possible to compare the mass of the porphyrin for both TFA-treated and pre-exposed (original) monolayers.

In figure 6.11, both the TFA-treated film (expanded) and unaltered EHO film (unexpanded) after deposition on QCM crystals are presented as a function of the QCM frequency and the number of transferred layers. Undoubtedly, the addition of layers on the crystal produces a decrease in the frequency due to the increase of mass in the overall oscillating system. However, in the graph the slopes have a positive slope because the plot represents a frequency difference (as shown in figure 6.5 and 6.6).

The expanded and unexpanded graphs have very different gradients, 137 Hz/layer for the exposed, TFA-treated system and 347 Hz/layer for the unexpanded EHO porphyrin. The slopes represent the frequency change per layer (Δf), and therefore is possible to calculate the mass per unit area per layer ($\sigma_{\Delta f}$) using the equation 6.4. The resulting values for $\sigma_{\Delta f}$ were 211 ng/cm^2 for the TFA-treated and 534 ng/cm^2 for the EHO system.

Clearly, a higher mass per unit area for the non-exposed film is observed, which corresponds to the denser and more aggregated state hypothesised as compared with the TFA-treated film. The values for the mass per unit area per layer for exposed and non-exposed films are consistent and are congruent with the predicted molecular density obtained by the isotherms.
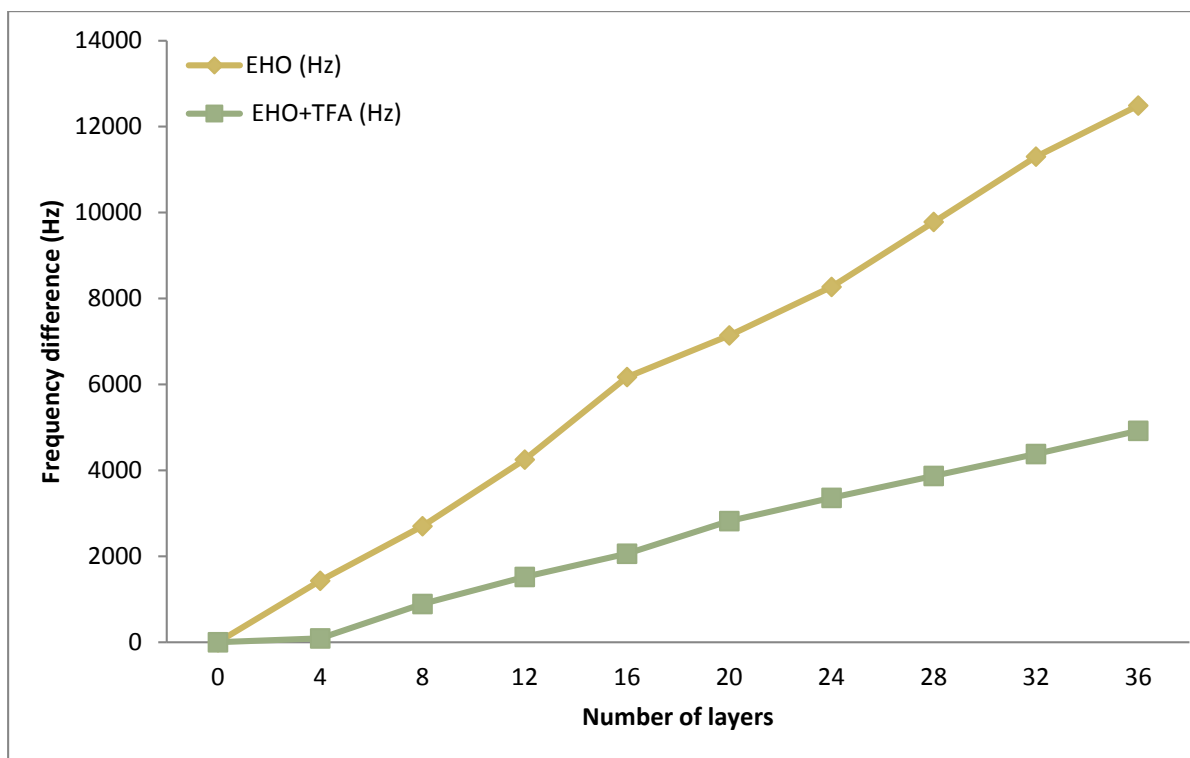
Figure 6.11: Frequency response of the QCM coated with porphyrin versus the number of deposited layers for EHO and EHO + TFA.

The mass per unit area per layer can be also estimated using the information displayed on the surface pressure – area isotherms, and it can be calculated by the following formula:

$$\sigma_\pi = \frac{W}{N_A a_{exp}}$$

Eq. 6.7

Where σ_π is the mass per unit area per layer, W is the mass of a single porphyrin molecule, N_A is the Avogadro constant and a_{exp} is the value of the expanded area per molecule at a certain target pressure plotted in the isotherm.

Table 6.1 shows a comparison of the mass per unit area per layer calculated by the isotherm at a surface pressure of 15 mN/m (σ_π) and the mass per unit area determined by the QCM oscillating system ($\sigma_{\Delta f}$). Noticeably, the values for $\sigma_{\Delta f}$ and σ_π are numerically similar for the acid-treated EHO system. However, for the non-exposed system the $\sigma_{\Delta f}$ value is lower than the anticipated which may suggest some degree of molecular reorganisation occurring during the deposition.

Materials	Frequency change per layer, Δf (Hz)	Area/molecule (15 mN/m), a_{exp}(nm^2)	Mass per unit area per layer, σ_π (ng/cm^2)	Mass per unit area per layer, $\sigma_{\Delta f}$ (ng/cm^2)
EHO	347	0.28	668	534
EHO + TFA	137	0.83	225	211

Table 6.1: Comparison of the mass per unit area per layer and frequency change per layer values for the non-exposed and exposed.

QCM investigations were conducted for the six free base porphyrins, however, only the materials JPE, SMT2_011 and EHO could be deposited on the gold electrodes of the QCM. Figure 6.12 shows the quartz crystals for Nitro and EHO after the deposition of 4 layers of their respective material. Although the original porphyrin solutions (0.3 mg/ml) exhibit its characteristic purple colour when the material is compressed on the water surface to 15 mN/m, the colour of the deposited quartz crystal suggest that no material has been transferred into the QCM. As a matter of fact, further measurements in the QCM proved that the deposition of the material was not reliable, clear indication of a non-consistent transfer ratio. There was not sufficient adhesion between the films of these two molecules and the gold QCM electrode for reliable transfer.
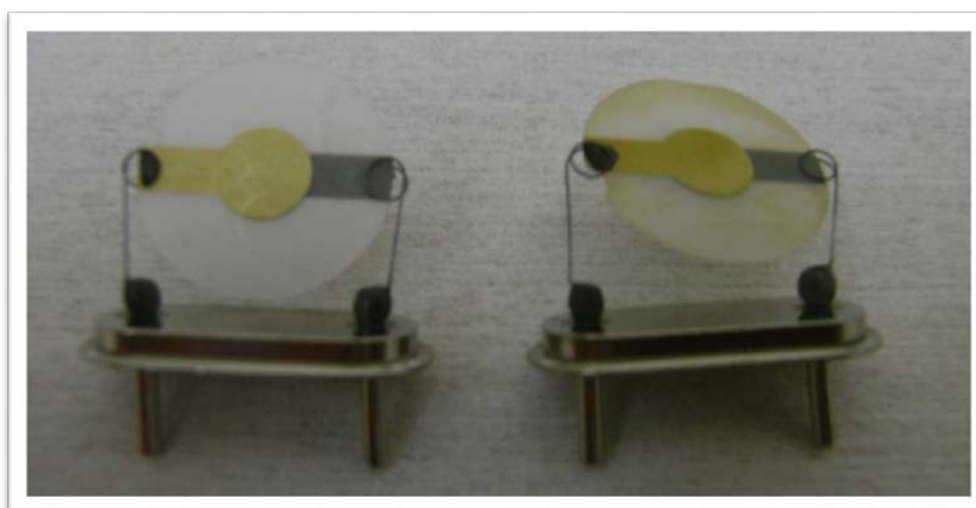

Figure 6.12: Comparison of the materials on the deposited quartz crystal. Nitro (left) shown no deposition in the electrodes, whereas EHO shown a perceptible change in the original QCM colour.

Figure 6.13 and 6.14 show the QCM measurements for SMT2_011 and JPE. Notice that for the case of SMT2_011, the deposition of the first 4 layers led to a very subtle change in frequency. However, after deposition of the material remained constant after that point for both the non-TFA treated and the TFA-treated systems.
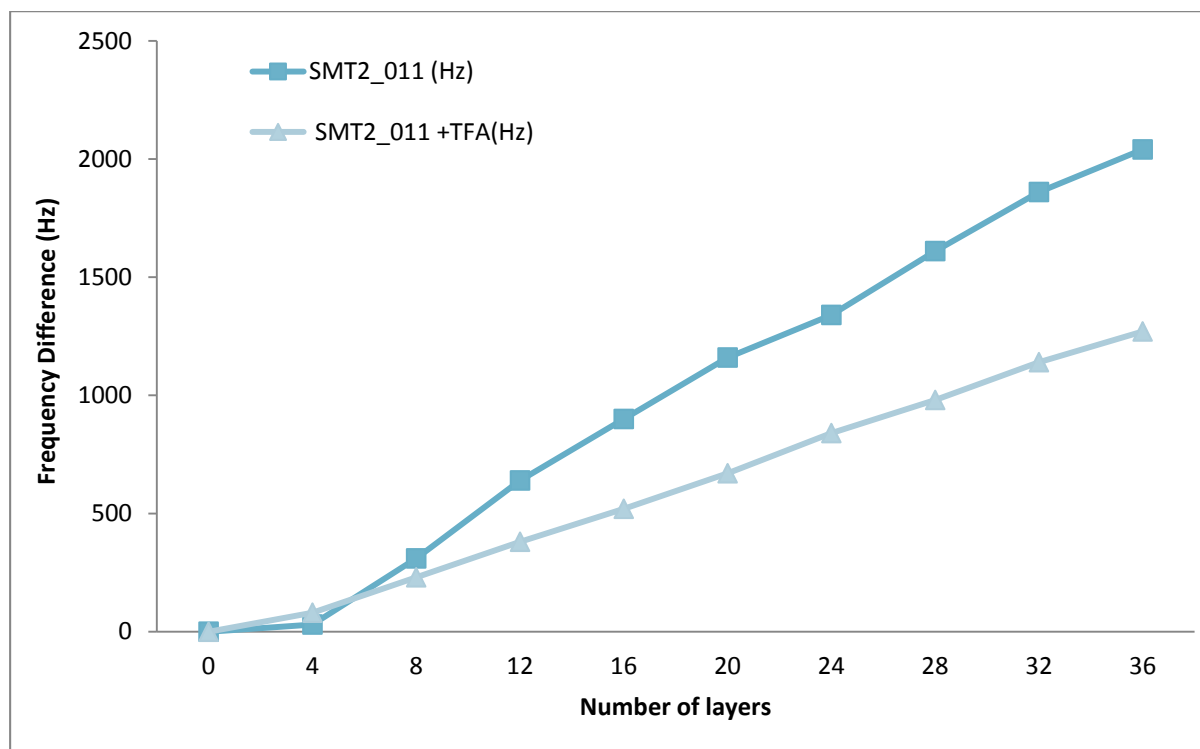

Figure 6.13: Frequency response of the QCM coated with porphyrin versus the number of deposited layers for SMT2_011 and SMT2_011 + TFA.
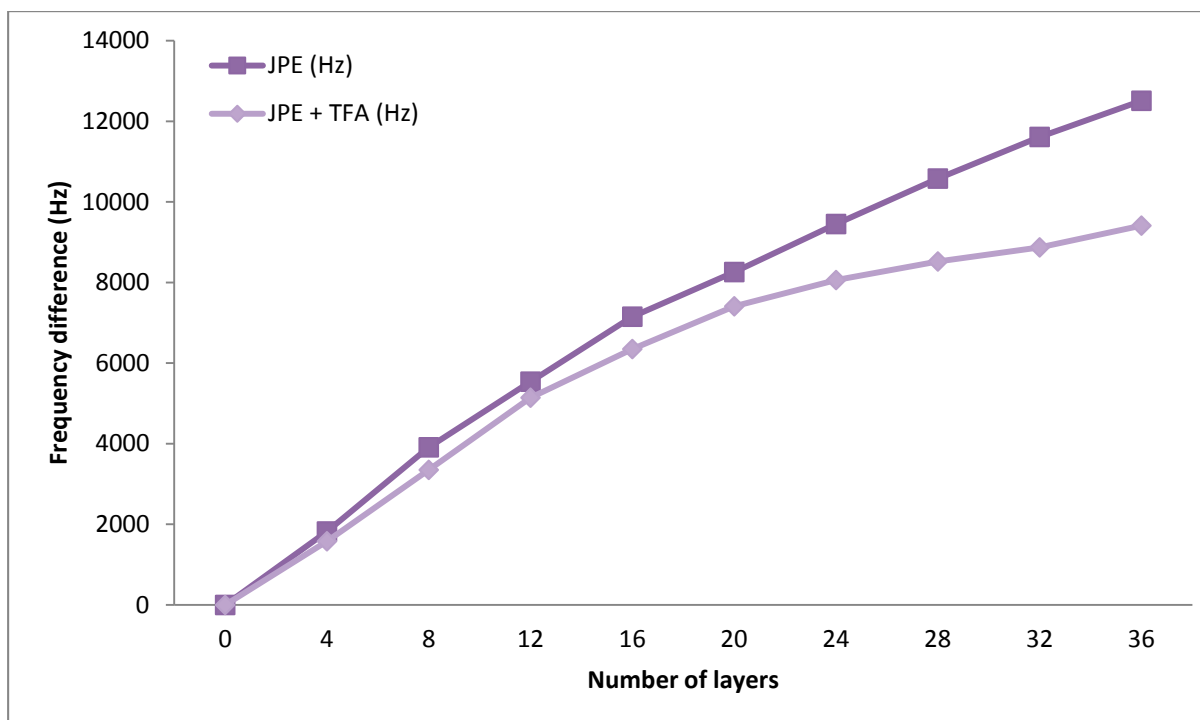
Figure 6.14: Frequency response of the QCM coated with porphyrin versus the number of deposited layers for JPE and JPE + TFA.

It is clear from figures 6.13 and 6.14 that JPE and SMT2_011 follow the same trend of EHO system, which justify the fact that when a less dense layer is transferred into the QCM the change in frequency is correspondingly lower, as in the case of the TFA-treated measurements. The QCM data for JPE, SMT2_011 and EHO also corroborate that the porphyrin lie on the water surface in an edge-on orientation and when the acid is added, protonation causes a molecular reordering in which the molecules adopt a face down orientation. That new orientation is less dense, and results in a smaller frequency change per layer, or in other words, in a less steep gradient of the plot describing the change in frequency vs number of layers.

Evidently, the inclination of the slopes for the exposed and non-exposed states of EHO varies from each other to a higher degree than that observed for JPE, in which the lines have a similar gradient. This is an indication of the effect caused by TFA in the monolayer. For instance, it is likely that some of the SMT2_011 molecules are in a partial face down configuration once they have been deposited on the water surface, so when the material is exposed to the acid its molecular arrangement will not change as greatly because the molecules are already lying

on the water in that way. In a more extreme case, the JPE molecules are already configured in that orientation, so when the TFA is added the change in area is minimal.

A correlation between the change in frequency of the two gradients of the different states and its corresponding mass change can be obtained by using a simplified version of the Sauerbrey equation:

$$\Delta f = f_0{}^2 b \Delta m \qquad \text{Eq. 6.8}$$

Where Δf is the change of frequency due to the deposition of the porphyrin on the QCM, f_0 is the resonant frequency of the quartz resonator, b is the material constant of the acoustic properties of the crystal, and Δm is the additional porphyrin mass.

For the particular case of the non-TFA treated porphyrin, equation 6.8 can be rearranged to show the increase of mass per transferred layer (Δm_P) as a function of the other variables as shown below:

$$\Delta m_P = \frac{\Delta f_P}{f_0{}^2 b} \qquad \text{Eq. 6.9}$$

Where the Δf_P represents the decrease of oscillation frequency per layer for the non-exposed porphyrin. Correspondingly, an equation that describes the exposed porphyrin can be represented by the following equation:

$$\Delta m_{P+TFA} = \frac{\Delta f_{P+TFA}}{f_0{}^2 b} \qquad \text{Eq. 6.10}$$

Where Δm_{P+TFA} and Δf_{P+TFA} are the corresponding mass increase per deposited layer and measured frequency decrease induced for the TFA-treated porphyrin system.

With the aim of being able to compare the decrease in oscillation frequency data of the QCM for the JPE, SMT2_011 and EHO, an equation relating the exposed and unexposed statements measured by the QCM system can be defined as:

$$\rho_{DL} = \frac{\Delta f_P}{\Delta f_{P+TFA}} = \frac{\Delta m_P}{\Delta m_{P+TFA}} \qquad \text{Eq. 6.11}$$

Where ρ_{DL} denotes the surface density lowering ratio; the term represents a measure of the reduction of mass per unit area per layer generated as a consequence of the interaction between the acid and the porphyrin, leading to the expansion of the monolayer.

In figure 6.15 a graph relating the density lowering ratio ρ_{DL} and the factor ϕ is shown. Noticeably EHO exhibits the higher ρ_{DL} ratio, with an approximate value of 2.5; correspondingly, its low ϕ verifies that the experimental data in the isotherms concurs with the results measured by the QCM.

On the other hand, JPE exhibits the lowest ρ_{DL} ratio which is close to unity, suggesting that the mass per unit area per layer is hardly affected by the acid, leading to a minimal areal expansion after the exposure to TFA. In like manner, those results can be compared with the data shown in the isotherms, and can be directly correlated with the factor ϕ. Finally, the porphyrin SMT2_011 shows an intermediary behaviour between EHO and JPE. The QCM results for SMT2_011 are also in agreement with its corresponding value for the factor ϕ.
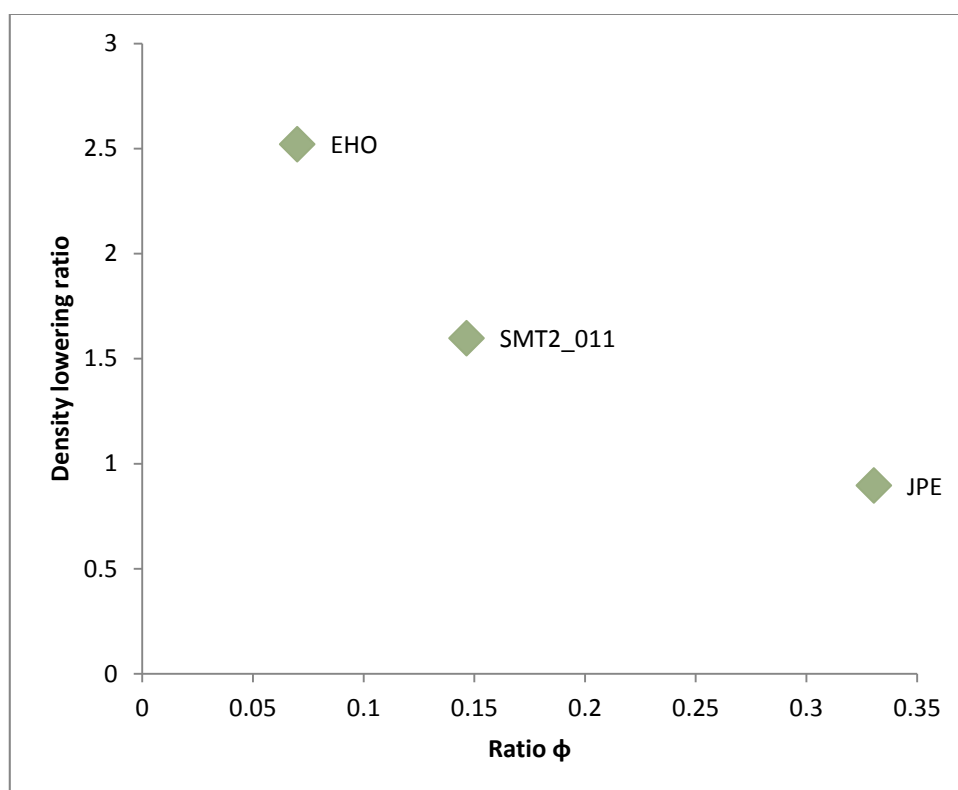

Figure 6.15: Representation of the JPE, SMT2_011 and EHO porphyrins in a ρ_{DL} vs ϕ plot.

Conclusions, implications and future work

A quartz crystal has been mounted in a Pierce oscillator circuit to build a QCM system. The calibration was performed using stearic acid, a saturated fatty acid that is well-known for forming homogenous organized monolayers. The calibration measurements lead to the calculation of the mass sensitivity constant, which allows to correlate directly the change in mass with the change in frequency using the Sauerbrey equation.

The QCM was used to measure the mass of the films transferred onto the crystal surface, thus it was possible to compare the mass of the porphyrin for both pre-exposed (original) and TFA-treated monolayers. TFA treated deposited monolayers shown a lower mass per unit area per layer, indicating that the density of the monolayer has been reduced upon exposure to the acid. This change in density can be seen as a molecular expansion induced by protonation, which can be explained in terms of the molecular orientation of the porphyrin molecules.

The areal expansion induced by TFA caused a different expansion rate in the materials. EHO showed the greatest expansion rate, changing from a face to face orientation (at which the material is highly aggregated) to a face down molecular orientation (with the porphine parallel to the water surface). JPE showed a low expansion rate, possibly because the molecules were already in a face down configuration. SMT2_011 showed an intermediate behaviour between JPE and EHO. Other porphyrins could not be transferred into the quartz crystal (there was not sufficient adhesion between the films and the gold electrodes).

The macroscopic expansion of the free base porphyrins implies that some sensing materials have the tendency to enlarge their molecular area when they are exposed to acids such as TFA, which suggest a change of orientation but more importantly, a reduction of aggregation.

Further experiments in this area should put emphasis on designing and/or identifying porphyrins that switch from one orientation to another, for which the orientation transition results in a larger difference in area per molecule within the monolayer. An attempt to reduce the aggregation of the free base porphyrins will be made by exposing the materials to TFA.

This would help to enhance our understanding the tendency of molecules to adopt a low energy conformation as a result to the exposure to a certain analytes.

References:

1. Brittle, S.A., et al., *Macroscopic expansion of tetraphenylporphyrin Langmuir layers stimulated by protonation.* Soft Matter, 2012. **8**(10): p. 2807-2811.
2. Richardson, T., et al., *Gas sensing properties of porphyrin assemblies prepared using ultra-fast LB deposition.* Colloids and Surfaces A: Physicochemical and Engineering Aspects, 2002. **198**: p. 843-857.
3. Aleaf, A., *A study of the Crystal Oscillator for CMOS-COPS® Devices.* 1986, Application Notes, AN400, Microchip Technology, Inc.
4. Bible, S., *Crystal Oscillator Basics and Crystal Selection for rfPICTM and PICmicro® Devices.* 2002, Application Notes, AN826, Microchip Technology, Inc.
5. Horowitz, P., W. Hill, and T.C. Hayes, *The art of electronics*. Vol. 2. 1989: Cambridge university press Cambridge.
6. Hardy, N.J., T.H. Richardson, and F. Grunfeld, *Minimising monolayer collapse on Langmuir troughs.* Colloids and Surfaces A: Physicochemical and Engineering Aspects, 2006. **284–285**(0): p. 202-206.
7. Brittle, S.A., et al., *Tuning free base tetraphenylporphyrins as optical sensing elements for volatile organic analytes.* Journal of Materials Chemistry, 2011. **21**(13): p. 4882-4887.

Chapter 7

Conclusions

7.1 Summary

The work in this thesis represents a study of the characterization of porphyrin derivatives. The absorption of UV-visible light provides an extremely useful tool to determine the interactions of molecules within thin organic films. An investigation of the changes in the visible absorption spectra of various porphyrin compounds in thin films and solution form upon exposure to analytes has shown distinctive responses. Each specific analyte produces a fingerprint which is subtly different in shape depending upon the porphyrin used. Different porphyrins permit different kinds of analytes to be detected. These fingerprints can be used to identify the presence of analytes for the different porphyrin-analyte complexes.

Although porphyrin solutions have shown reasonable, detectable responses to a range of analytes, it is convenient that the sensing materials are transferred to the solid state so that vapour analytes can be detected in a more practical manner.

As a method of comparing performance, typical sensing parameters, namely response to gas at different concentrations, t_{90} and representative figures of largest change in absorbance have been reported for the different porphyrin-analyte complexes tested within this research. Characterization techniques, such as Atomic Force Microscopy have offered a basic understanding of the molecular organization and formation of domains in the films.

In general terms, to obtain a good porphyrin based sensor it is necessary to select a material with a strongly coloured spectrum that is highly responsive to analytes; i.e., it induces a large wavelength shift and a large change in absorbance. To get a good response the binding between the porphyrin and the analyte must be strong enough to induce a noticeable spectral change, but not too strong to cause an irreversible state.

When depositing the porphyrin materials a good transfer to the solid substrate is always desirable, as indicated by a high transfer ratio. Therefore there must be suitable attractive interactions between the surface of the substrate of choice and the floating porphyrin layer.

Using LB/LS depositions, the ultra-fast deposition technique produced a highly porosity morphology in the film, enhancing the diffusion of analyte and response of the sensor.

A low density loosely packed film will have fewer available porphyrin sites to bind with analytes. On the contrary a highly packed film will have a higher number of molecules (and therefore more binding sites), but due to the high density of the film not all the sites may be accessible to the analyte because the porphyrins may be too close together. In the same way, the time of response of a sensor depends on the diffusion of the analyte vapour through the monolayers. Generally, the time of response is increased as the molecular weight of the diffusing analyte increases.

The response of the sensing materials varies depending on the electron donating/withdrawing properties of the substituted side groups attached to the porphyrins. Donating groups increase the electron density of the conjugated π system by bringing electrons towards the porphine ring. The incorporation of a donating side group attached to the porphyrin structure should facilitate the interaction with the analyte; however, the change in the electric properties also affects the porphyrin-porphyrin interactions, leading to a highly aggregated statement in some cases. Thus, an open structure along with strong electron donating properties within the side groups would be the best scenario for a sensor.

Reduction of aggregation in porphyrins can be reached by many methods. Calixarene was used as a host Langmuir film matrix material due to its outstanding film forming capability. Similarly a composite of TiO_2 was used as a host material, however its use is limited to the molecules containing certain side groups (such as carboxylic acids). Exposure to TFA also leaded to a reduction of aggregation.

The macroscopic expansion effect upon protonation was also studied for various free base porphyrins using a quartz crystal microbalance method. The tendency to adopt a lower energy conformation upon exposure to TFA (reorientation of the molecular configuration) in the monolayer of the sensing materials was corroborated by measuring the deposited mass on the quartz crystal.

The long term objective of this research field is incorporation of this technology into real devices capable of operating under a range of conditions. The fabrication of a portable,

efficient and inexpensive system was reported. The proto-type is able to detect a range of alcohols, exhibiting good repeatability and stable results. The main components of the proto-type are a light emitter and a photo detector coated with porphyrin which acts as a sensing material. The marginal cost of the electronic components of the proto-type did not exceed £5.

7.2 The thesis

The results obtained in the course of this research will be summarised in the following section. This thesis is divided into six different chapters. The first three chapters describe the basis of introduction, theory and experimental methods, the latter three chapters are the author's experimental work.

Chapter I: Introduction

A short outline of the impact of the project and the necessity of a new generation gas sensors is described. The definition of a sensor and few applications of gas sensors in different industries are also pointed out.

Chapter II: Background Theory

The second chapter described the type of gas sensors currently available and discussed some adsorption models vital to interface interaction of materials. The electronic orbital theory was briefly described, along with the description of the porphyrin molecule. The chapter also offers a recent research into gas sensor.

Chapter III: Experimental Techniques

The third chapter discussed aspects of the Langmuir Blodgett technique and Langmuir films, including concepts of surface tension, amphiphiles and cleanliness. It also encompassed the different techniques used to characterise the materials involved. Techniques like UV-Vis, and AFM have been discussed.

Chapter IV: Characterization and evaluation of porphyrins as optical sensing devices

A range of porphyrins, both metalled and free base, have shown response to a variety of analytes.

Section I: Zinc metallo porphyrins and amines

Zinc porphyrins have shown the ability to detect amine vapours. In solution, all the responses are fairly similar for all the sensing materials. However, once they have been deposited on a glass substrate the responses of the materials differ; the electrophilic nature of the side groups along with the physical dimensions of the molecule results in a different interaction between the porphyrin molecules and hence a different molecular organization on a substrate.

The hydroxyl group (-OH) in the moieties of SMT5_075 was expected to induce a strongest electron donating interaction with the amines, followed by the –OR in SMT2_028 and SMT5_075 and finally –NHCOR present in the SMT2_012 and SMT2_040. However, the LS films that were most responsive to the amine vapour analytes were not necessarily those with the most electron donating side groups. Instead it was found that the ones that had both electron donating side groups and showed an open structure performed best. It is possible that the stronger porphyrin-porphyrin interactions in the other materials led to a densely packed aggregated thin film, which limited the response of the sensor by sterically hindering access to the porphyrin binding sites.

Both AFM and isotherms studies indicated that porphyrins containing alkyl chains in their side groups (SMT2_040 and SMT2_012) exhibited an open structure. Those porphyrins had a better response because their structure allows the amine vapour to interact with the porphyrin ring. Primary amines induced the highest optical change or response, followed by secondary and lastly tertiary amines. The nitrogen lone pair of a primary amine is relatively exposed to bind to an accessible porphyrin site as compared to a tertiary amine, which exhibit a bulkier branched molecular structure. The t^{90} value of the porphyrin LS films increases as the size of the diffusing amine type increases.

Section II: Free base porphyrins and carboxylic acids

This section described the response of free base porphyrins when exposed to carboxylic acids. The concentration of the gaseous carboxylic acids was the dominating factor in determining the magnitude of the sensor response. Acetic acid caused the greatest response in all the sensing materials due to its high vapour pressure at 25°C meaning concentration of acetic acid during exposure was high. Some correlation between sensing performance, the concentration and the molecular size of the carboxylic acids has been noticed; clearly more research in this future should be aimed at characterising the film at different target pressures and attempting to quantify the surface to volume rations for each sample.

The porphyrins with a hydroxyl group at the end of the side group, SMT5_054 and SMT2_029, showed the highest responses to the acids. The difference between SMT5_054 and SMT2_029 is that the first one has two phenyl rings instead of one in their side groups. The AFM has shown that SMT5_054 has produced a fairly continuous thin film; however SMT2_029 shown a better sensor response, possibly because the electrons of the side groups are pushed towards the centre of the porphyrin, and that increases is tendency to protonate. Therefore it is clear that the formation of a uniform continuous does not necessarily mean they sensors response will be good. The addition of the extra benzene in the SMT5_054 makes the film structure better, but the dilution of the electron donating effect from the side groups makes the sensor significantly less sensitive. Therefore there is a trade-off between having closely packed molecules to get good absorbance and well-spaced molecules such that interactions occur easily. This understanding is consistent with the observation that the average t^{90} value of the free base porphyrin LS films increases as the molecular size of the diffusing carboxylic acid type increases. Acetic acid experiences a relatively easy diffusion through a dense LS film, whereas a long carboxylic acid has a lower diffusion due to the steric hindrance so it will struggle to diffuse into deeper layers, indicating that diffusion of the analyte gas molecules into the sensor films plays a fundamental role in determining the sensor response.

Section III: Nitrogen dioxide detection

i) The materials used in the first two sections of the chapter were used to detect NO_2. The response of the free base porphyrins when exposed to the gas were similar to the ones presented in carboxylic acids (where SMT5_053 showed the lowest response and SMT2_012

the highest), possibly because carboxylic acids and NO_2 interact with the porphyrins in a similar way so they both protonate the central ring of the free base porphyrins.

ii) The tendency of EHO to aggregate causes deposition difficulties and has been shown to have a detrimental effect on the gas sensing behaviour. The gas sensing behaviour of LB films of EHO was modified by incorporating calixarene onto the EHO films. This was achieved by mixing calixarene and EHO in solution and producing LB films from this blend. The calixarene-porphyrin enhanced the response of the sensor because it reduced the aggregation within the EHO film. This improvement in sensor response by preventing aggregation corroborates that idea that aggregation sterically hinder the sensing action of this class of molecule.

iii) Optically transparent free base porphyrin/TiO_2 composites were prepared in order to detect NO_2. The highly polar side groups of the carboxylic acid presented within the side groups of the porphyrins allowed the molecules to be anchored onto the TiO_2 rods. The highest responses were presented with the materials that have four phenyl groups with a carboxyl end in their side groups, T4CPP and T3CPP. The porphyrins with four carboxylic acid have the best response are securely anchored at 4 points to the TiO2 rods and therefore least capable of aggregating further confirming that excessive aggregation is detrimental to sensor performance.

Section IV: Alcohol detection

This section studied the alcohol gas-sensing properties of LS film assemblies of a magnesium porphyrin. The weak interaction between the analytes and the porphyrins produce a slight change in the absorbance spectrum of the material, which is difficult to visualize with the UV-Vis apparatus. The different magnesium-alcohol complexes were studied to demonstrate the advantages of using the proto-type described in chapter 5 section 3.

Chapter V: Proto-type vapour sensing using molecular films

The fifth chapter describes the sequential development of the construction of a proto-type able to detect vapour analytes. The proto-type is fabricated using electronic components that are commercially available.

Section I: Design of the proto-type

Sensing based on an optical response allows the construction of devices involving compact, low power LED-photo detector circuits. The change in the absorption of light (from an LED light source) by the organic layer can be detected using a photoresistor, photodiode or phototransistor as a light detector. The phototransistor-LED sensing pair has shown a superior performance for the gas sensing purposes because it allows a higher amplification of the sensor signal (which is analogue to the change of absorbance of the porphyrin upon exposure to the analyte).

The progressive development of the design of a vapour chamber to place the emitter-receiver sensing system was also described. The final design of the vapour chamber overcame the problems encountered in the early designs such as the alignment of the devices, optimal space inside the chamber (to fill the chamber with gas rapidly) and accurate control of the vapour delivery.

Section II: Proto-type considerations

An electronic filter was developed which reduced the noise in the sensor signal and facilitate easier analysis. The filter code was written on Labview, and it was based on the Savitzky-Golay algorithm.

The sensing mechanism was described in terms of fabrication parameters: a higher number of layers will produce a higher sensor response, however it may also increase the time of response of the sensor. To obtain a good sensing response the operating wavelengths of the PX and LED must coincide with the porphyrin-sensitive wavelengths for the system studied. Also, to obtain a higher response it is better to select a relatively narrow emission band in the LED to certify that the absorbance decreases and increases do not cancel each other out.

Section III: Detection of alcohols

A blue LED and a PX coated in MgEHO were matched and aligned within the designed gas chamber to detect alcohol vapours. The change in absorbance of the porphyrin spectrum upon exposure to the alcohols was analogue to the sensor response. The Freundlich adsorption model was used to describe the response of the phototransistor when exposed to the different concentration of the 2-methyl-2-butanol. The temperature dependence of the sensor was studied using the Arrhenius correlation model, the enthalpy of adsorption was calculated. This low cost sensor system was successfully used to detect different alcohol analytes in a reliable and repeatable way using a sensor response that was only weakly observable using the UV-vis setup previously employed with this class of sensor materials; therefore demonstrating that this approach to making a reliable reversible low cost gas sensor capable of detecting specific gaseous analytes is very promising and has the advantages of cost, simplicity and sensitivity over using full spectroscopic analysis.

Chapter VI: Quartz Crystal Microbalance

This chapter studied the formation of monolayers of various free base porphyrins and their corresponding reaction upon exposure to TFA. The interaction with TFA caused protonation of the porphyrin monolayers, altering the molecular orientation from a face-to-face orientation to a more face down orientation (parallel to the water surface). The change in orientation can be interpreted as a macroscopic expansion on the floating porphyrin layer. To quantify the expansion effect two sets of data corresponding to the isotherm (π-A) and QCM measurements were evaluated separately and subsequently merged in order to find a correlation between the two sets of experiments.

A Pierce oscillator circuit was designed to measure the mass deposited on a quartz crystal on both monolayers (original and TFA-treated). The Sauerbrey equation was used to correlate the changes in the oscillating frequency with the mass deposited on the quartz crystal. In all cases the TFA treated monolayers showed a lower mass per unit area per layer, demonstrating that the density of the monolayer has been reduced due to the change of molecular orientation upon the exposure to the acid.

EHO showed the highest expansion rate, demonstrating the most drastic areal expansion upon exposure to TFA. It was inferred that non-TFA treated EHO molecules are in a highly aggregated statement (in which the molecules sit on the air-water interface in a face to face configuration); whereas the TFA treated EHO molecules are in a more face down molecular orientation (parallel to the water surface). So, exposure to the acid proved to be an effective method to disaggregate the highly aggregated statement of EHO. It was theorized that JPE did not show a great expansion upon exposure to TFA because the molecules are already in a face down configuration. SMT2_011 shown an intermediate behaviour between JPE and EHO.

Appendix I

Appendix I lists all the porphyrins used in this work. The molecular structure of the porphyrins and the full chemical name of the sensing materials are given.

Appendix II

Appendix II is composed of three tables listing the properties of the analytes used in this work. The information obtained in the tables ranges from boiling points, saturated vapour pressures, densities to Antoine coefficients.
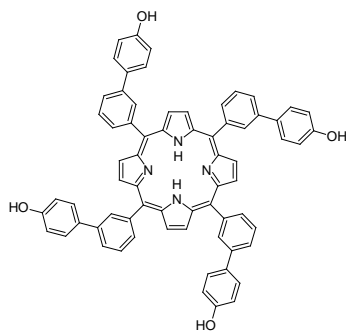
Appendix I

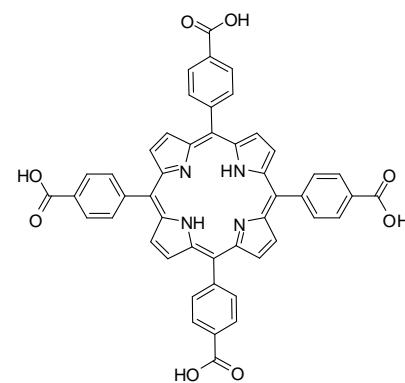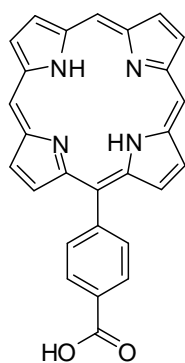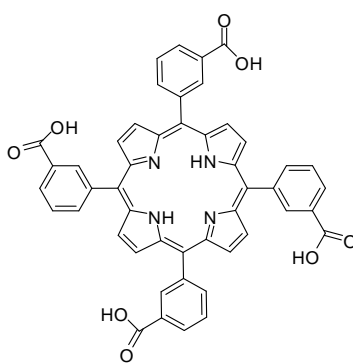# Materials List:

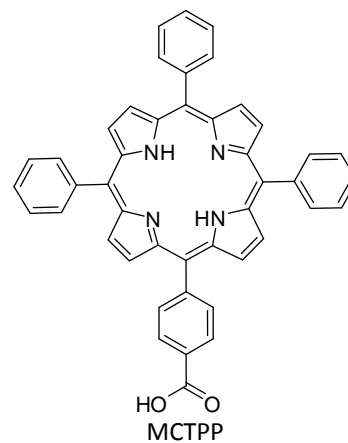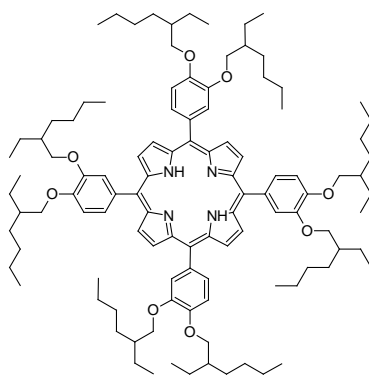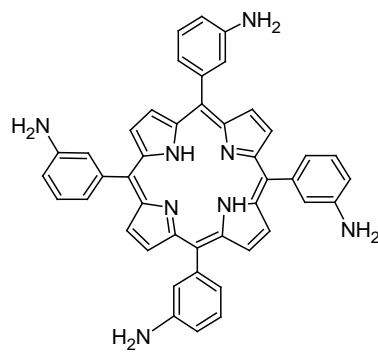<u>Free base porphyrins:</u>
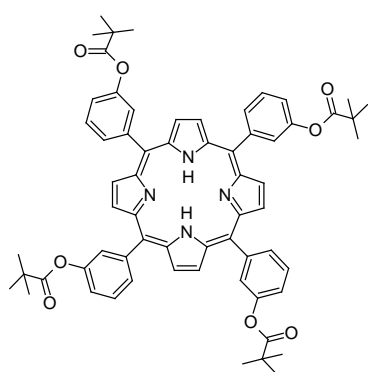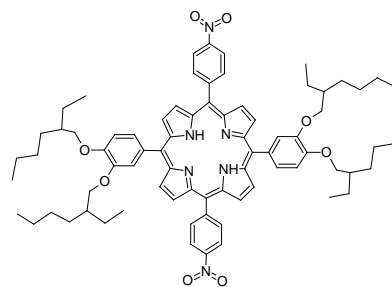
SMT2_076
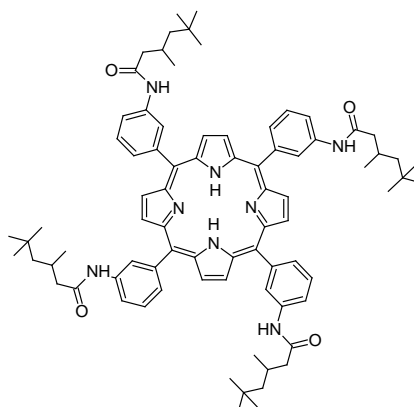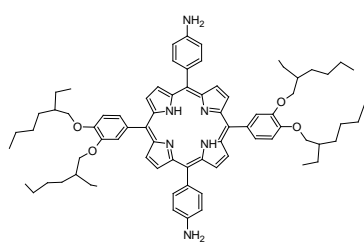
SMT2_011
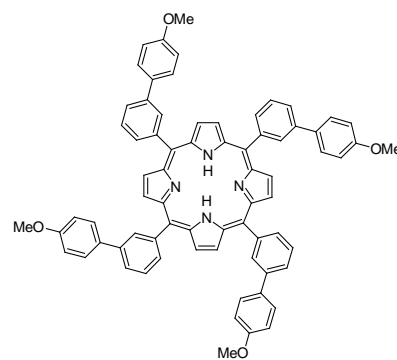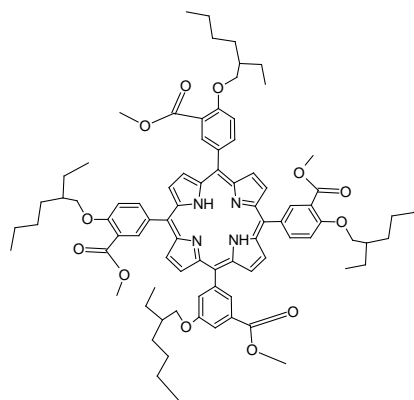
SMT5_053
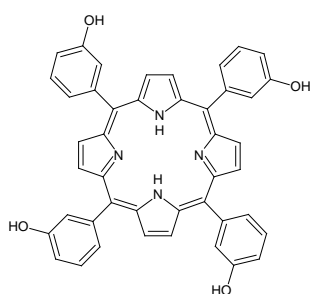
SMT2_029

SMT5_054
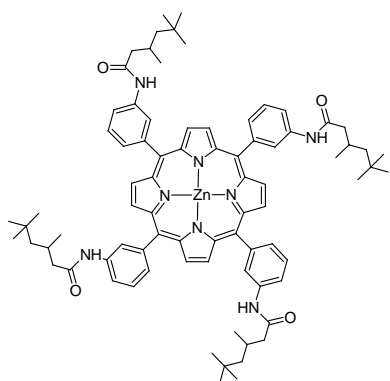
T4CPP (p-TCPP)

MCMPP

T3CPP (m-TCPP)

MCTPP

EHO

SMT2_010

Nitro

Ammino

JPE

266
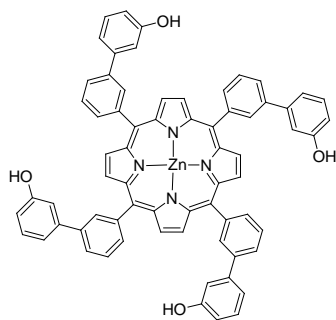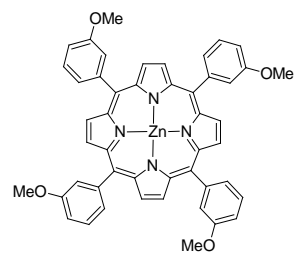
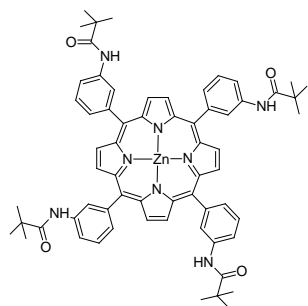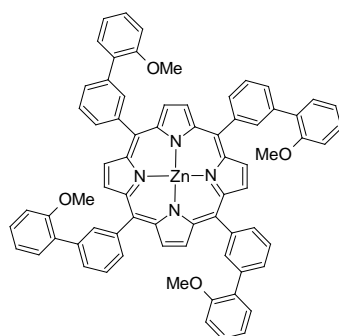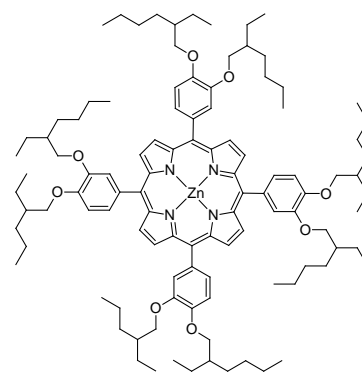Metallo-porphyrins:

SMT2_012
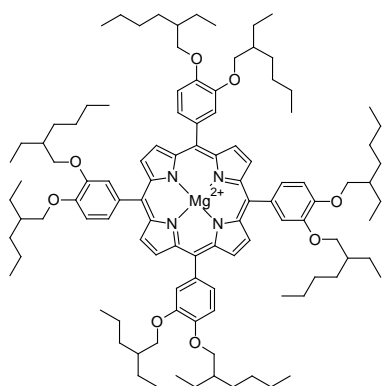

SMT5_016

SMT2_028

SMT2_040

SMT5_075

Zn-EHO

Mg-EHO

Porphyrin abbreviation name	Full descriptive name of the molecule
SMT2_076	5,10,15,20-tetrakis(3-phenyl 2,2-dimethylpropanoate)-21H,23H-porphyrin
SMT2_011	5,10,15,20-tetrakis(3-aminophenyl)-21H,23H-porphyrin
SMT5_053	5,10,15,20-tetrakis(biphenyl-4-methoxy)-21H,23H-porphyrin
SMT2_029	5,10,15,20-Tetra(3-hydroxyphenyl)-21H,23H-porphyrin[H_2-T(m-OH)P-P]
SMT5_054	5,10,15,20-tetrakis(biphenyl-4-ol)-21H,23H-porphyrin
T4CPP (p-TCPP)	5,10,15,20-tetrakis(3-carboxyphenyl)-21H,23H-porphyrin
MCMPP	5-(4-carboxyphenyl)21H,23H-porphyrin
T3CPP (m-TCPP)	5,10,15,20-tetrakis(4-carboxyphenyl)-21H,23H-porphyrin
MCTPP	5-(4-carboxyphenyl)10,15,20-triphenyl-21H,23H-porphyrin
EHO	5,10,15,20-tetrakis(3,4-bis[ethylhexyloxy]phenyl)-21H,23H-porphine
SMT2_010	5,10,15,20-tetrakis-(3-3,5,5-trimethyl-N-phenylhexanamide)-21H, 23H-porphine
Nitro	5,15-bis(4-nitrophenyl)-10,20-bis[3,4-bis(2-ethylhexyloxy)phenyl]-21H, 23H-porphine
Ammino	5,15-bis(4-aminophenyl)-10,20-bis3,4-bis(2-ethylhexyloxy) phenyl]-21H,23H-porphine
JPE	5,10,15,20-tetrakis[3,ethylhexyloxy-5-methoxycarbonylphenyl]-21H,23H-porphine
SMT2_012	Zinc(II) 5,10,15,20-Tetrakis(3,5,5-trimethyl-N-phenylhexanamide) porphyrin
SMT5_016	5,10,15,20-tetrakis-(biphenyl-3-ol)porphyrin zinc(II)
SMT2_028	5,10,15,20-Tetrakis(3-methoxyphenyl)porphyrin zinc(II)
SMT2_040	Zinc(II) 5,10,15-20-Tetrakis(2,2-dimethyl-N-phenylpropanamide) porphyrin
SMT5_075	5,10,15,20-tetrakis-(biphenyl-2-methoxy)porphyrin zinc(II)
ZnEHO	5,10,15,20-tetrakis[3,4-bis(2-ethylhexyloxy)phenyl]-21H,23H-porphinato zinc(II)
MgEHO	5,10,15,20-tetrakis[3,4-bis(2-ethylhexyloxy)phenyl]-21H,23H-porphyrinato magnesium (II)

Table A1.1: List of the porphyrins used in this work.

Appendix II: Physical properties of analytes

Mol. Formula	Name	Boiling Point (°C)	Density (g/mol)	Vapour pressure: temperature in °C for the indicated pressure					
				1 Pa	10 Pa	100 Pa	1 kPa	10 kPa	100 kPa
$C_2H_4O_2$	Acetic acid	118.1	60.052	-42.8 s	-26.7 s	-8 s	14.2 s	55.9	117.5
$C_3H_6O_2$	Propionic acid	141.1	74.078			0 e	35.1	79.9	140.8
$C_4H_8O_2$	Butyric acid	164	88.105			12.9	52.2	101.4	163.3
$C_5H_{10}O_2$	Valeric acid	186	102.132	-7.4	15.3	42.7	76.3	122.1	185.7
$C_6H_{12}O_2$	Hexanoic acid	202	116.158		33 e	59 e	93 e	139.3	204.5
$C_2HF_3O_2$	Trifluoroacetic acid	72	114.023					16.8	71.4
$C_8H_{18}O$	Octanol	195	130.228	12 e	30 e	53 e	84 e	128.2	194.8
C_3H_8O	2-Propanol	82.5	60.095	-65 e	-49 e	-28 e	-1.3	33.6	82
$C_5H_{12}O$	2-Methyl-2-butanol	101	88.148			-5 e	17.7	50.6	101.7
C_2H_6O	Ethanol	78	46.068	-73 e	-56 e	-34 e	-7 e	29.2	78
CH_4O	Methanol	64.7	32.042	-87 e	-69 e	-47.5	-20.4	15.2	64.2
$C_{12}H_{27}N$	Tributylamine	216	185.35	-26 e	1 e	35 e	77.7	134.5	213.4
$C_8H_{19}N$	Dibutylamine	159	129.243	-37 e	-16 e	10 e	44 e	90.8	159.1
$C_8H_{19}N$	Octylamine	176	129.243	-57 e	-36 e	-9	25.5	72.2	139
C_7H_9N	Benzylamine	185	107.153			25.6	62.6	112.7	183.9
$C_4H_{11}N$	Butylamine	78	73.137			-46 e	-18.1	20	75.9

Table A2.1: Physical properties of the liquid analytes used in this work [1].

*s - Indicates that the substance is a solid at this temperature. **e - Indicates an extrapolation beyond the region where experimental measure exist.

Mol. Formula	Name	Antoine Coefficients for vapour pressure				
		A	B	C	T_{MIN} (°C)	T_{MAX} (°C)
$C_2H_4O_2$	Acetic acid	7.8152	1800.03	246.894	16	319.56
$C_3H_6O_2$	Propionic acid	7.6694	1727.17	219.512	-20.7	330.85
$C_4H_8O_2$	Butyric acid	7.687	1778.18	206.702	-5.2	354.85
$C_5H_{10}O_2$	Valeric acid	7.61722	1828.33	200.516	-34	377.85
$C_6H_{12}O_2$	Hexanoic acid	7.47273	1747.23	174.802	-3	393.85
$C_2HF_3O_2$	Trifluoroacetic acid	7.50596	1399.76	230.84	-15.25	218.1
$C_8H_{18}O$	Octanol	7.16033	1536.79	163.905	-15.5	379.35
C_3H_8O	2-Propanol	7.77374	1518.16	213.076	-73.15	263.56
$C_5H_{12}O$	2-Methyl-2-butanol	7.43675	1395.79	177.668	-70.15	291.85
C_2H_6O	Ethanol	8.13484	1662.48	238.131	-114.1	243.1
CH_4O	Methanol	8.09126	1582.91	239.096	-97.68	239.43
$C_{12}H_{27}N$	Tributylamine	7.68482	2143.4	-70.15	-70.14	370.85
$C_8H_{19}N$	Dibutylamine	7.48571	1694.45	209.117	-62	334.35
$C_8H_{19}N$	Octylamine	7.54133	1879.97	223.783	-0.4	353.85
C_7H_9N	Benzylamine	7.40339	1813.01	216.379	-46	410.35
$C_4H_{11}N$	Butylamine	7.213	1308.4	224.2	-14	100

Table A2.2: Antoine parameters for the calculation of the saturated vapour pressure [1].

Mol. Formula	Name	Density (g/mol)
NO_2	Nitrogen dioxide	46.006
N_2	Nitrogen	28.013

Table A2.3: Density of the gases used in this work [1].

Reference:

1.   Haynes, W.M., *CRC handbook of chemistry and physics*. 2012: CRC press.